

The role of Birkeland currents in the Dungey cycle

John Charles Coxon

Radio & Space Plasma Physics Group
Department of Physics & Astronomy
University of Leicester

*A thesis submitted to the University of Leicester
for the degree of Doctor of Philosophy*

January 2015

The role of Birkeland currents in the Dungey cycle

John Charles Coxon

Abstract

The interaction of the solar wind with the near-Earth environment forms Earth's magnetosphere and drives a process called the Dungey Cycle. Birkeland currents are required to transmit stress within the system. This thesis uses large-scale, statistical analysis (both temporal and spatial) to examine their magnitude and spatial extent in the context of the Dungey Cycle.

Active Magnetosphere and Planetary Electrodynamics Response Experiment (AMPERE) data are processed; the methodology is described and the success rate examined before the regions 1 and 2 Birkeland current magnitudes are explicitly compared to dayside and nightside reconnection rate for the first time. The magnitudes of the currents are well-correlated with both, suggesting that magnetic reconnection on day and nightside is driving higher Birkeland current magnitudes.

The behaviour of the R1 and R2 currents is examined in a superposed epoch analysis of 2900 substorms identified by SuperMAG. Both current systems increase in magnitude and spatial extent during the growth phase of a substorm, peaking shortly after expansion phase onset. This analysis yields new information about how the currents react to the substorm cycle.

A seasonal and a diurnal variation in the Birkeland current magnitudes is described and linked to the effect of ionospheric conductance; this is explored further, and it is found that currents are well-described by multiplying the dayside reconnection rate by an number representing the global variation of conductance with UT.

This thesis presents evidence that Birkeland current magnitudes are consistent with driving by ionospheric convection, which is in turn driven by magnetic reconnection on both the dayside and the nightside. It is also demonstrated that the current ovals measured by AMPERE expand and contract with magnetic reconnection as open flux is added to and removed from the polar cap. These insights are expanded upon with ideas for future research.

Declaration

The research presented in this thesis is the work of the author. Information which has been taken from external sources has been appropriately referenced. The following scientific papers have been published based on the work presented in this thesis:

Coxon, J. C., S. E. Milan, L. B. N. Clausen, B. J. Anderson and H. Korth (2014a), The magnitudes of the regions 1 and 2 Birkeland currents observed by AMPERE and their role in solar wind-magnetosphere-ionosphere coupling, *J. Geophys. Res. Space Physics*, doi:10.1002/2014JA020138.

Coxon, J. C., S. E. Milan, L. B. N. Clausen, B. J. Anderson and H. Korth (2014b), A superposed epoch analysis of the regions 1 and 2 Birkeland currents observed by AMPERE during substorms, *J. Geophys. Res. Space Physics*, doi:10.1002/2014JA020500.

Acknowledgements

This thesis would not have been possible without the help and support of so many people. I'd especially like to thank my fiancée, España; my parents, Ruth and Charles; my brother, George; and my supervisor, Steve: their support has been invaluable over the last three years. There are too many people to express my thanks in prose, so instead I've created two crosswords to express my gratitude to everyone who has been in and around Leicester for the last seven years, printed over the next three pages.

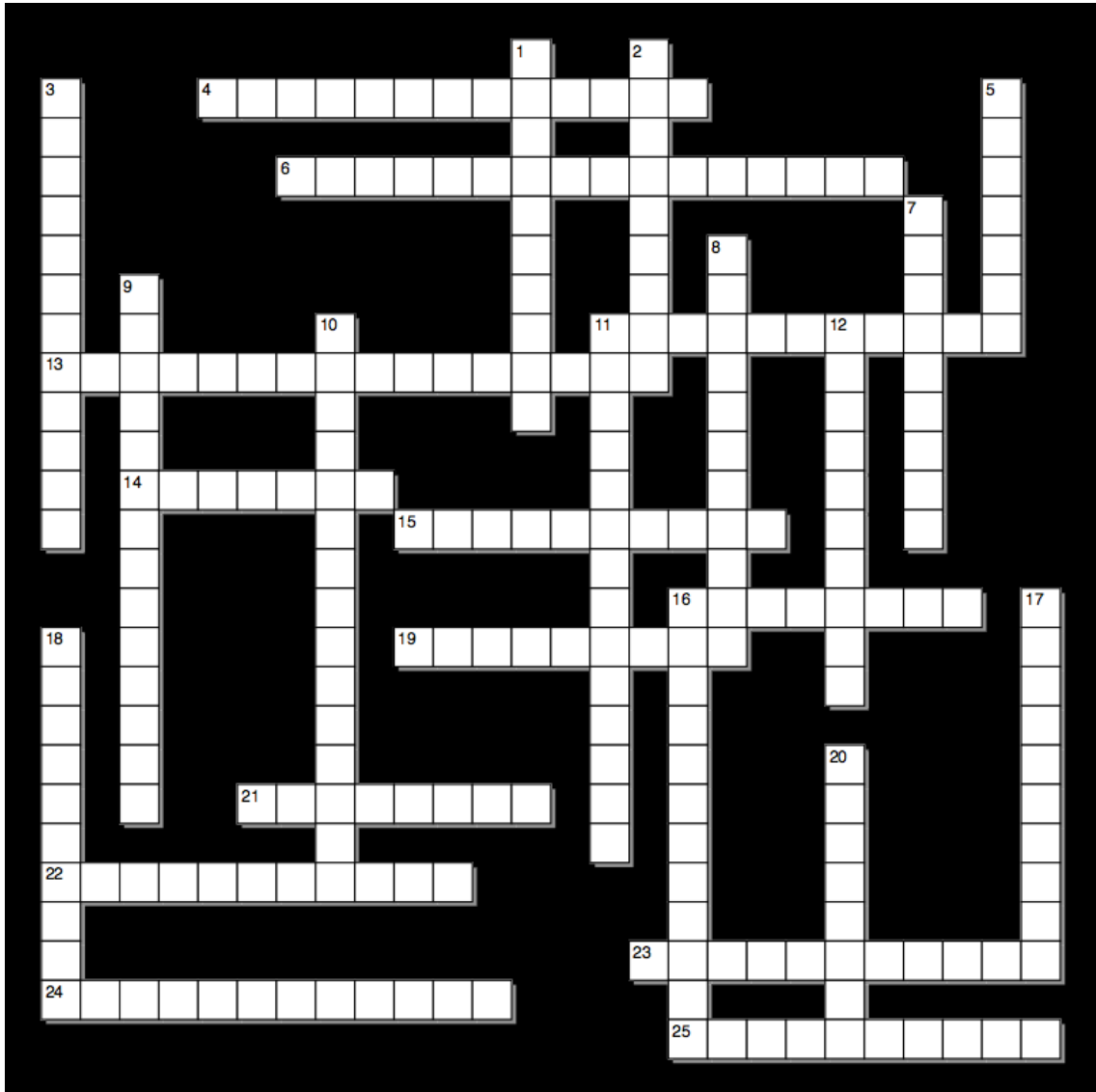


Figure 1: A crossword in which every answer is either a member of the RSPP or the wider MIST community. See Figure 3 for the solution.

Across 4. At the top of the fashion pyramid (7, 6). 6. Newest member of the family (5, 11). 11. Always cheers up a coffee meeting (5, 6). 13. New boss! (9, 7). 14. Can always be relied upon to have the shiniest toys (3, 4). 15. Internal examiner (4, 6). 16. Once got nine wickets and a run-out (3, 5). 19. Struggles to see sealions on the sea shore (3, 6). 21. Works on the best bit of Saturn (4, 4). 22. My PhD little sister! (5-8, 6). 23. Nickname like a Seinfeld character (5, 6). 24. Hair braider extraordinaire (5, 7). 25. Keeper of the emergency wine (5, 5).

Down 1. Makes exceedingly good cakes (5, 5). 2. External examiner (5, 4). 3. Happy that I've finally started using Python (5, 7). 5. Unwitting inaugurator of the beer club (3, 4). 7. The second-best T-shirt collection in the group (4, 5). 8. If I could put a cocktail emoji here, I would (6, 5). 9. People Magazine has a crossword too (9, 5). 10. President, cocktail club (8, 7). 11. Extremely punny man (5, 1'8). 12. Not a butcher or a candlestick maker (3, 7). 16. Most flatuent officemate (4, 8). 17. Second supervisor (4, 6). 18. Makes exceedingly good cakes (5, 5). 20. First seminar invitation (5, 3).

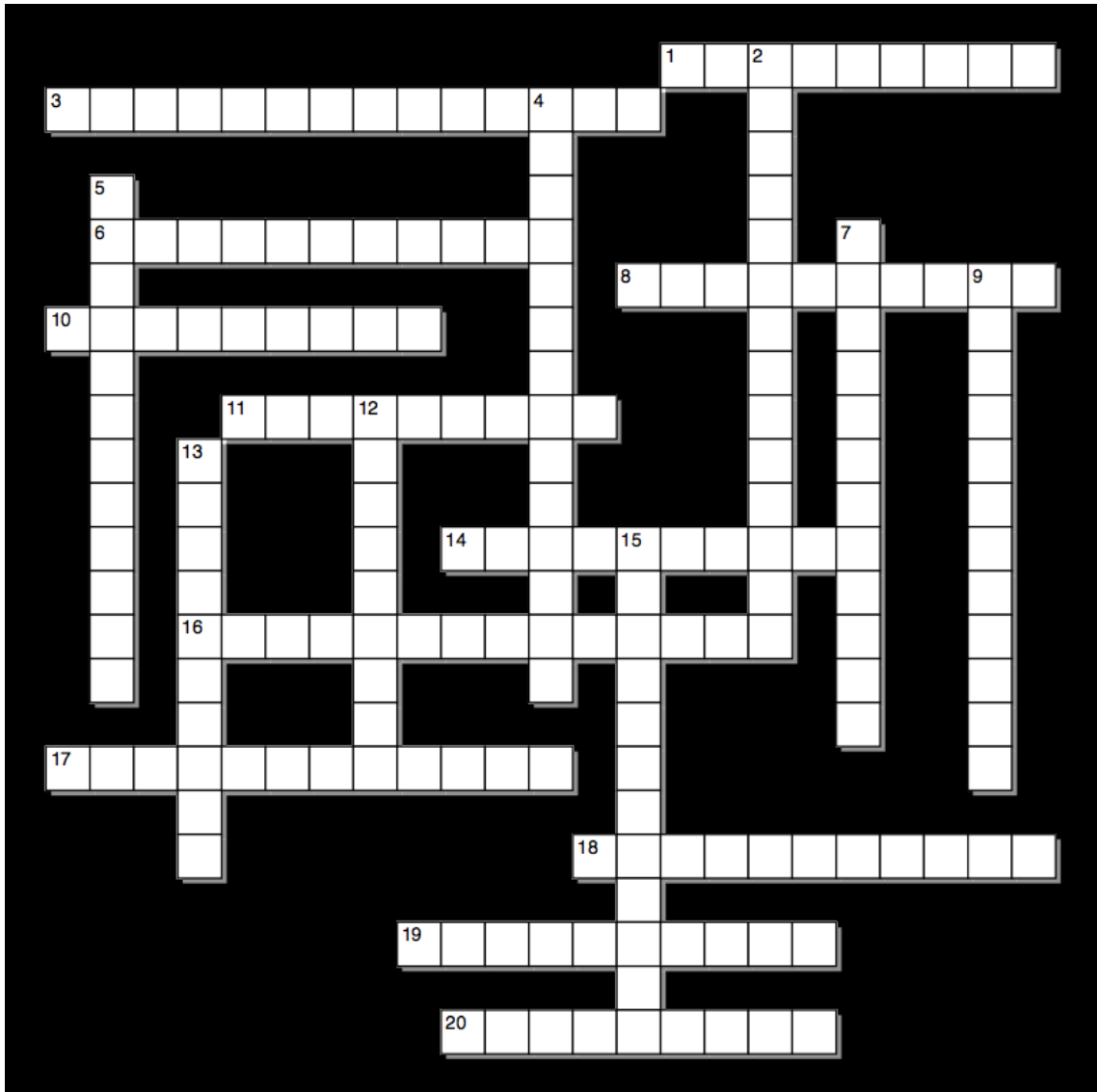


Figure 2: A crossword in which every answer is someone in Leicester (outside of work) who helped enhance my seven years there. See Figure 4 for the solution.

Across 1. Treasurer and all-round good egg (3, 6). 3. Book discusser (6, 8). 6. Introduced me to Netrunner (4, 7). 8. Proof that stoners are better housemates than alcoholics (4, 6). 10. Cat mum about to become a real mum (3, 6). 11. Best undergraduate cook (3, 6). 14. Consistent coffee companion, in his pre-evolved form (4, 6). 16. The other Mary Gee survivor (6, 8). 17. Panda (6, 6). 18. A housemate, in her pre-evolved form (6, 5). 19. Practitioner of the macarena (4, 6). 20. Princess (4, 5).

Down 2. Small, blond and deadly (7, 7). 4. Close friend and Nando's partner (7, 7). 5. Not allowed Galactus and Unicron (6, 6). 7. Overdosed on Netrunner (5, 7). 9. Fellow member of the SGC (6, 6). 12. Grandfather (4, 5). 13. First physicist I met in Leicester (5, 5). 15. Fellow President (4, 9).

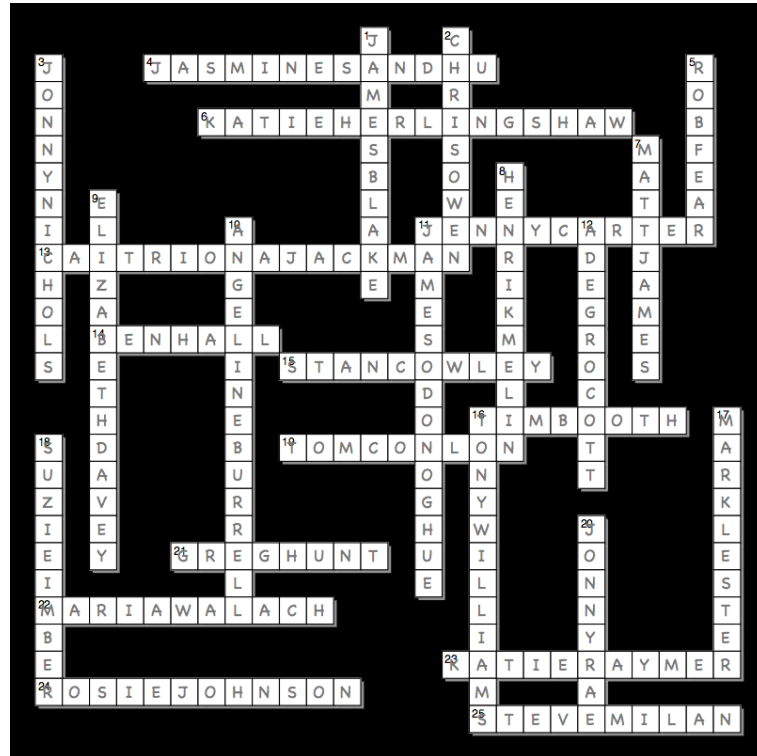


Figure 3: Solution to Figure 1.

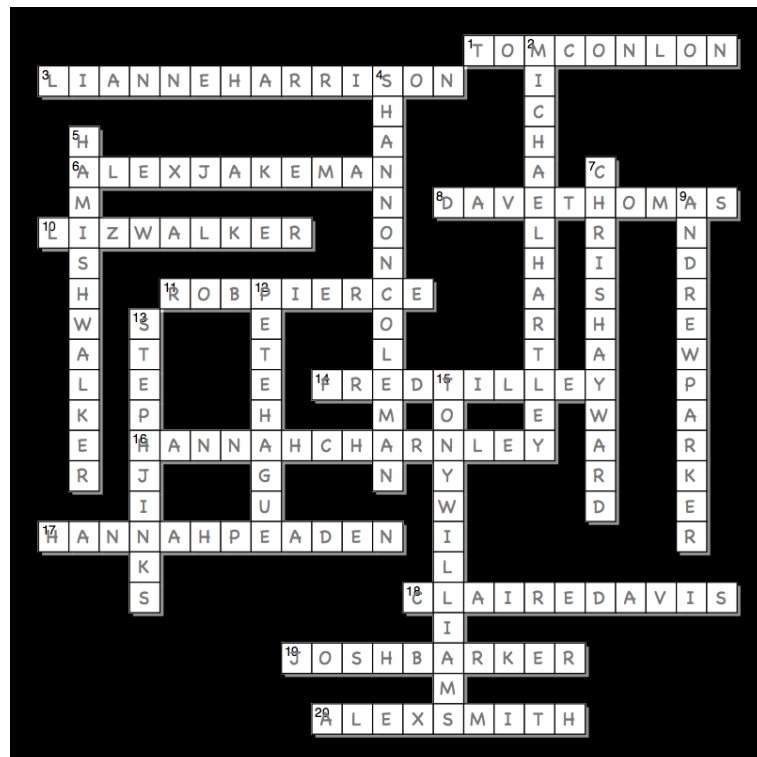


Figure 4: Solution to Figure 2.

Contents

Abstract	ii
Declaration	iii
Acknowledgements	iv
Contents	viii
List of figures	xii
List of tables	xiv
1 Introduction	1
1.1 Magnetohydrodynamics	2
1.1.1 Lorentz forces	3
1.1.2 Motion in a parallel magnetic field (gyromotion)	3
1.1.3 Motion in a convergent magnetic field (magnetic mirroring)	4
1.1.4 Motion with a parallel electric field	5
1.1.5 Motion with a perpendicular electric field (particle drift)	5
1.1.6 Frozen-in flow (Alfvén’s Theorem)	6
1.1.7 Equations of motion and Ohm’s Law	8
1.2 Magnetic Reconnection	10
1.3 The solar wind	11
1.4 The near-Earth environment	12
1.4.1 Particle motion in the ionosphere	15
1.5 Dungey cycle	17
1.6 Currents in the magnetosphere	21
1.6.1 The magnetopause	23
1.6.2 The magnetotail	25
1.6.3 The ring current	26
1.6.4 Hall and Pedersen currents	27
1.6.5 Birkeland currents	29

1.6.6	The substorm current wedge	34
1.7	Co-ordinate systems and conventions	36
1.7.1	Birkeland currents	36
1.7.2	Geomagnetic co-ordinates	36
1.7.3	AACGM co-ordinates	37
1.7.4	GSM co-ordinates	37
2	Literature review	38
2.1	Magnetospheric convection	38
2.1.1	The Dungey Cycle	38
2.1.2	The expanding/contracting polar cap paradigm (ECPC)	39
2.1.3	Quantifying the magnetic reconnection rate	42
2.2	Substorms	44
2.3	Birkeland currents	51
2.3.1	First measurements of Birkeland currents	52
2.3.2	The reaction of Birkeland currents to the solar wind	53
2.3.3	Seasonal and diurnal variations	58
2.3.3.1	Solar zenith angle dependence of ionospheric conduc-	
	tance	58
2.3.3.2	Solar zenith angle dependence of Birkeland currents	59
3	Instrumentation	62
3.1	AMPERE	62
3.1.1	The AMPERE processing method	63
3.1.2	Method for obtaining R1/R2 current magnitudes and locations	66
3.1.2.1	Success rates of this method	72
3.2	OMNI	74
3.2.1	Spacecraft	77
3.2.2	Indices	78
3.3	SuperMAG	79
4	Birkeland currents and their role in solar wind - magnetosphere -	
	ionosphere coupling	82
4.1	Introduction	82
4.2	Four day example of reconnection driving the Birkeland currents . . .	82
4.3	Current magnitude variations with magnetic reconnection rates on	
	the day and nightside	85
4.4	R1 and R2 variations with reconnection rate examined separately . .	89
4.5	Discussion	92
4.6	Conclusions	95

5	A superposed epoch analysis of the Birkeland currents during substorms	96
5.1	Introduction	96
5.2	Superposed epoch analysis	96
5.2.1	Quantifying the reaction of the coupled magnetosphere-ionosphere system to substorms	97
5.2.2	The variation of reactions to substorms given different levels of activity	99
5.2.2.1	Reconnection rate and magnetic indices	99
5.2.2.2	Current magnitudes	100
5.2.2.3	Latitude of current ovals	102
5.2.3	The variation of reactions to substorms with different seasons	104
5.3	Discussion	106
5.3.1	The reaction of the Birkeland currents to substorms	107
5.3.1.1	Spatial variations	107
5.3.1.2	Magnitude variations	107
5.3.2	Reactions varying with geomagnetic conditions	109
5.3.2.1	Signatures seen at small substorm onset colatitudes .	110
5.3.3	Reactions varying with season	110
5.4	Conclusions	111
6	An analysis of seasonal and diurnal variations in conductance-related Birkeland current strengths	115
6.1	Introduction	115
6.2	Birkeland current strengths 2010 – 2012	116
6.2.1	Mean monthly Birkeland current strengths	116
6.2.2	Mean diurnal Birkeland current strengths	120
6.2.3	Mean Birkeland current strengths as a function of solar zenith angle χ	123
6.2.3.1	Solar zenith angle χ over the auroral zone	123
6.2.3.2	Different relations between Birkeland current strengths and conductance	124
6.2.4	Comparison of net Birkeland current strengths with conductance	127
6.3	Discussion	128
6.3.1	Seasonal variation in conductance $\Xi(t)$	128
6.3.2	Variation in conductance $\Sigma(\chi)$	129
6.3.3	Differences in net currents	130
6.4	Conclusions	131

7 Conclusion and future work	132
7.1 Conclusion	132
7.2 Future work	134
References	136

List of Figures

1	Crossword featuring RSPP et al	v
2	Crossword featuring the rest of Leicester	vi
3	Solution to Figure 1	vii
4	Solution to Figure 2	vii
1.1	Illustration of $\mathbf{E} \times \mathbf{B}$ drift	6
1.2	Magnetic reconnection	11
1.3	The Parker Spiral	12
1.4	The Structure of the Magnetosphere	13
1.5	The Dungey cycle	17
1.6	Magnetospheric convection	19
1.7	Ionospheric convection and the induced electric field	20
1.8	Asymmetries in ionospheric convection associated with IMF B_y	20
1.9	Currents flowing due to field lines flowing across the polar cap	21
1.10	Currents flowing due to field lines in Dungey cycle flows	22
1.11	Chapman-Ferraro currents	24
1.12	Cross-tail currents	25
1.13	Pedersen currents	28
1.14	Hall, Pedersen and Birkeland currents in the ionosphere	30
1.15	Fukushima's theorem	32
1.16	Earth's large-scale current circuit	33
1.17	Cowling conductivity	35
1.18	Auroral and substorm electrojets	35
2.1	Modelled effect of reconnection on the size of the polar cap	41
2.2	Observations of an auroral substorm	46
2.3	Evolution of a plasmoid over time	48
2.4	Travelling Compression Region due to a plasmoid	49
2.5	Model of the classic substorm current wedge	50
2.6	Model of the 'two-loop' substorm current wedge	51
2.7	The large-scale picture of the R1 and R2 Birkeland current systems	53
2.8	Electric fields in the ionosphere due to convection	54

2.9	Observations of Birkeland currents with IMF clock angle	56
2.10	Variation in HMB with $F_{10.7}$	61
3.1	Stages of AMPERE data	66
3.2	Example of Equation 3.11 fitted to AMPERE data	67
3.3	A sinusoid illustrated with parameters from Equation 3.11	68
3.4	Example of Equation 3.12 fitted to AMPERE data	69
3.5	AMPERE current density, location and magnitude	71
3.6	Number of fits and current magnitude vs MLT	72
3.7	Number of fits against dayside reconnection rate (north)	75
3.8	Number of fits against dayside reconnection rate (south)	76
3.9	SuperMAG-detected magnetic perturbations	79
3.10	Histogram showing substorm onset binned by l_1	81
4.1	Temporal plot of Birkeland currents, Φ_D and AL	84
4.2	Scatter plots of J_1 and J_2 against Φ_D and AL index over a four-day period	86
4.3	J_1 versus J_2 , colour-coded by number of data, Φ_D and AL	87
4.4	J_1 versus J_2 , colour-coded by standard deviation of Φ_D and AL	88
4.5	J_1 and J_2 versus Φ_D and AL, colour-coded	90
4.6	Φ_D versus AL, colour-coded by J	91
4.7	Φ_D versus AL, colour-coded by number of data	91
5.1	Superposed epoch analysis on 2900 substorms	98
5.2	Binned superposed epoch analysis of Φ_D and SML and SMU	101
5.3	Binned superposed epoch analysis of J_1 and J_2	103
5.4	Binned superposed epoch analysis of l_1 and l_2	105
5.5	Superposed epoch analysis on substorms in the northern summer	113
5.6	Superposed epoch analysis on substorms in the southern summer	114
6.1	Seasonal variation of Birkeland current magnitudes	117
6.2	Dayside reconnection rates predicted using seasonal current magnitudes	119
6.3	Monthly and hourly variation in current magnitudes	121
6.4	Monthly and hourly variation in solar zenith angle	122
6.5	Modelled currents with conductance as a cosine function	125
6.6	Modelled currents with conductance as a linear function	126
6.7	Dependence on zenith angle of dawnside net currents	127
6.8	Dependence on zenith angle of duskside net currents	127

List of Tables

6.1 Seasonal maxima and minima	121
--	-----

Chapter 1

Introduction

The knowledge gained, since 1896, in radio-activity has favoured the view to which I gave expression in that year, namely, that magnetic disturbances on the Earth, and aurora borealis, are due to corpuscular rays emitted by the Sun. – Kristian Birkeland, 1908

This thesis is concerned with electric currents flowing in the magnetosphere, which arise due to Ampère's law in the near-Earth environment. The thesis focuses on those currents which flow along magnetic field lines, electro-dynamically linking the ionosphere to the magnetopause (at the far edge of the magnetosphere) and the ring current (in the inner magnetosphere). These field-aligned currents were first hypothesised by Birkeland (1908) and the broad structure of the currents was inferred by Iijima and Potemra (1976a, 1978); they are now known as Birkeland currents.

This thesis is also concerned with magnetic reconnection, which is the process by which the magnetic field embedded into the solar wind becomes interconnected with the terrestrial magnetic field, leading to solar wind plasma entering the magnetosphere and also driving convection in the ionosphere and magnetosphere. The cycle in which magnetic reconnection occurs is called the Dungey cycle (Dungey, 1961), and this gives rise to the expanding/contracting polar cap (ECPC) paradigm (Cowley and Lockwood, 1992).

Birkeland currents and their characteristics are an active area of research. Most of the work that has been done to examine these currents has relied on inferences from sparse data sets, usually consisting of single spacecraft measurements averaged over a long period of time (e.g. Iijima and Potemra, 1978). In addition, the reaction of the currents to magnetic reconnection is not yet fully understood, and neither is the way in which these currents behave during substorms. It is known that the

currents are affected by the ionospheric conductance, and by extension the solar zenith angle and particle precipitation, but this has not been well quantified, and the way in which the currents react to changes in both conductance and reconnection simultaneously is not clear. The work presented in this thesis aims to address these open questions, providing new insights into the way in which the Birkeland current paradigm relates to the ECPC paradigm.

This first chapter introduces the mathematics which underpin the magnetosphere, known as magnetohydrodynamics, before also giving an outline of the solar wind and the structure of the magnetosphere. The Dungey cycle is introduced and the current systems that flow throughout the magnetosphere are outlined, so as to give the reader the context required to better understand the research. The second chapter is a review of the literature relevant to the research in this thesis, and the third chapter is a description of the instrumentation that was used to undertake it. The fourth, fifth and sixth chapters address open questions in the field of Birkeland currents, exploring the relationship between the currents flowing and magnetic reconnection. The seventh chapter, the conclusion, provides an overview of the central findings of the thesis, before outlining future work and questions still unanswered.

1.1 Magnetohydrodynamics

A plasma is a gas which is comprised of electrically charged particles, but which itself is electrically neutral when considered as a whole: this property is called quasineutrality. For the purposes of some of the mathematics that follows, it will be assumed that plasmas are also collisionless, and that the effect of particles colliding can be neglected. (Later in the chapter, it will be necessary to reintroduce collisions.) Fundamental when considering electromagnetism are Maxwell's equations (Grant and Phillips, 1990):

$$\nabla \cdot \mathbf{E} = \frac{\rho_q}{\epsilon_0} \quad (1.1)$$

$$\nabla \cdot \mathbf{B} = 0 \quad (1.2)$$

$$\nabla \times \mathbf{E} = -\frac{\partial \mathbf{B}}{\partial t} \quad (1.3)$$

$$\nabla \times \mathbf{B} = \mu_0 \mathbf{j} + \mu_0 \epsilon_0 \frac{\partial \mathbf{E}}{\partial t} \quad (1.4)$$

These equations are Gauss' law (1.1), the law of no monopoles (1.2), Faraday's law (1.3) and Ampère's law (1.4). In the above equations, the electric field is \mathbf{E} in volts per metre; the charge density is ρ_q in Coulombs per cubic metre; the permittivity

of free space $\epsilon_0 = 8.854 \times 10^{-12}$ farads per metre; the magnetic field is \mathbf{B} in Teslas; the current density is \mathbf{j} in Ampères per square metre, and the permeability of free space $\mu_0 = 4\pi \times 10^{-7}$ Henries per metre.

1.1.1 Lorentz forces

Lorentz forces F_L act on charged particles (Grant and Phillips, 1990), accelerating them according to the electromagnetic environment. Where q is the charge of the particle in coulombs, and \mathbf{v} is the velocity of the particle in metres per second, the force that acts on a particle due to the background electric and magnetic fields is

$$\mathbf{F}_L = q(\mathbf{E} + \mathbf{v} \times \mathbf{B}). \quad (1.5)$$

The total force acting on a particle may be considered by adding a term \mathbf{F}_g to Equation 1.5 which describes the non-electromagnetic forces acting on the particle (Kivelson, 1995). This total force can then be used to calculate the rate of change of momentum $m\mathbf{v}$

$$m \frac{d\mathbf{v}}{dt} = q(\mathbf{E} + \mathbf{v} \times \mathbf{B}) + \mathbf{F}_g. \quad (1.6)$$

1.1.2 Motion in a parallel magnetic field (gyromotion)

Imagine a particle moving in a region of magnetic field \mathbf{B} . The Lorentz force acts on that particle perpendicular to the magnetic field \mathbf{B} and the particle velocity \mathbf{v} . Therefore the particle moves perpendicular to the magnetic field lines with a circular motion called gyromotion. Equating the Lorentz force $qv_{\perp}B$ with the centripetal force mv_{\perp}^2/r gives the gyroradius (Baumjohann and Treumann, 1997; Kivelson, 1995),

$$\rho_c = \frac{mv_{\perp}}{qB}. \quad (1.7)$$

Dividing the distance travelled by the particle (the circumference) by its velocity gives the gyroperiod

$$\tau_c = \frac{2\pi m}{qB} \quad (1.8)$$

which can then be used to find the gyrofrequency

$$\Omega_c = \frac{qB}{m}. \quad (1.9)$$

1.1.3 Motion in a convergent magnetic field (magnetic mirroring)

If a magnetic field converges, and a particle travels in this magnetic field in the direction of increasing field strength, the Lorentz force (Equation 1.5), which acts perpendicular to \mathbf{B} , has a component pointing away from the direction of travel. This will cause the particle to accelerate in the opposite direction to its initial velocity, eventually causing it to be reflected from the magnetic field; this reflection is called magnetic mirroring. The point at which a particle mirrors is deduced by using the first adiabatic invariant

$$\Rightarrow \frac{v_{\perp}^2}{B} = \text{const} = \frac{v_{\perp 0}^2}{B_0} \quad (1.10)$$

in which the subscripted zeroes indicate the values at $t = 0$. The first adiabatic invariant is conserved during the particle motion, which can be used to determine the point at which particles mirror along the field lines

$$B_m = B_0 \left(\frac{v}{v_{\perp 0}} \right)^2. \quad (1.11)$$

The pitch angle α can also be used to quantify the particle motion. The pitch angle is defined by the angle between the vector of the particle's velocity and the direction of the magnetic field, and is given by

$$\tan \alpha = \frac{v \sin \alpha}{v \cos \alpha} = \frac{v_{\perp}}{v_{\parallel}}. \quad (1.12)$$

Thus, the first adiabatic invariant (Equation 1.10) becomes

$$\frac{v^2 \sin^2 \alpha}{B} = \text{const}. \quad (1.13)$$

v is constant, so as $B \rightarrow B_m$, $\alpha \rightarrow \pi/2$. The result of Equation 1.13 can be utilised to write

$$\frac{v^2 \sin^2 \alpha}{B} = \frac{v^2}{B_m} \quad (1.14)$$

such that if α can be measured at some field strength B , the magnetic mirror point B_m may be calculated.

1.1.4 Motion with a parallel electric field

In the case where the electric field is absent, the velocity of the particle along the magnetic field will be constant. The introduction of an electric field means this is no longer necessarily true. Suppose an electric field \mathbf{E} is introduced which has some component \mathbf{E}_{\parallel} which is parallel to the magnetic field \mathbf{B} , which is defined to be in the z direction. Then, the time derivative of the velocity of the particle in z is

$$\frac{dv_z}{dt} = \frac{qE_{\parallel}}{m}. \quad (1.15)$$

This can be integrated with respect to t to find the velocity along z of the particle as a result of the applied \mathbf{E}_{\parallel} . The dependence of v_z upon q means that positively charged particles move in the direction of the parallel electric field and negatively charged particles move in the opposite direction. Eventually, this will create an electric field due to charge separation which will be exactly opposite to \mathbf{E}_{\parallel} . As the first field causes the particles to move, the second field will become larger until eventually the two are in equilibrium. The net electric field parallel to \mathbf{B} has become zero. As a result,

$$\mathbf{E}_{\parallel} = \mathbf{0} \quad (1.16)$$

is often valid in the case of space plasmas (Kivelson, 1995). However, this is not always the case: this thesis is concerned with Birkeland currents flowing along the magnetic field lines, and their existence requires that \mathbf{E}_{\parallel} is not zero. This will be discussed in greater detail in Section 1.6.5.

1.1.5 Motion with a perpendicular electric field (particle drift)

The presence of an electric field perpendicular to the magnetic field gives an additional velocity called the drift velocity (Baumjohann and Treumann, 1997), illustrated in Figure 1.1 and given by

$$\mathbf{v}_E = \frac{\mathbf{E} \times \mathbf{B}}{B^2}. \quad (1.17)$$

This equation does not depend on charge or mass, and particles of different charge and mass will move at the same velocity due to this effect. The total drift velocity of the particle will include any velocity along the magnetic field, such that the total velocity

$$\mathbf{v} = \frac{\mathbf{E} \times \mathbf{B}}{B^2} + v_z \hat{\mathbf{B}}. \quad (1.18)$$

If the frame is transformed to one moving with the bulk plasma motion, the particles simply gyrate in circles; the particles gyrate due to the magnetic field as before, but feel no effect from an electric field, and there is no drift in this frame. As such, if there is a bulk drift of plasma perpendicular to \mathbf{B} in the reference frame under consideration, then there is a perpendicular electric field given by

$$\mathbf{E} = -\mathbf{v} \times \mathbf{B}. \quad (1.19)$$

It can be shown that Equation 1.19 and Equation 1.18 are equivalent by crossing Equation 1.19 with \mathbf{B} .

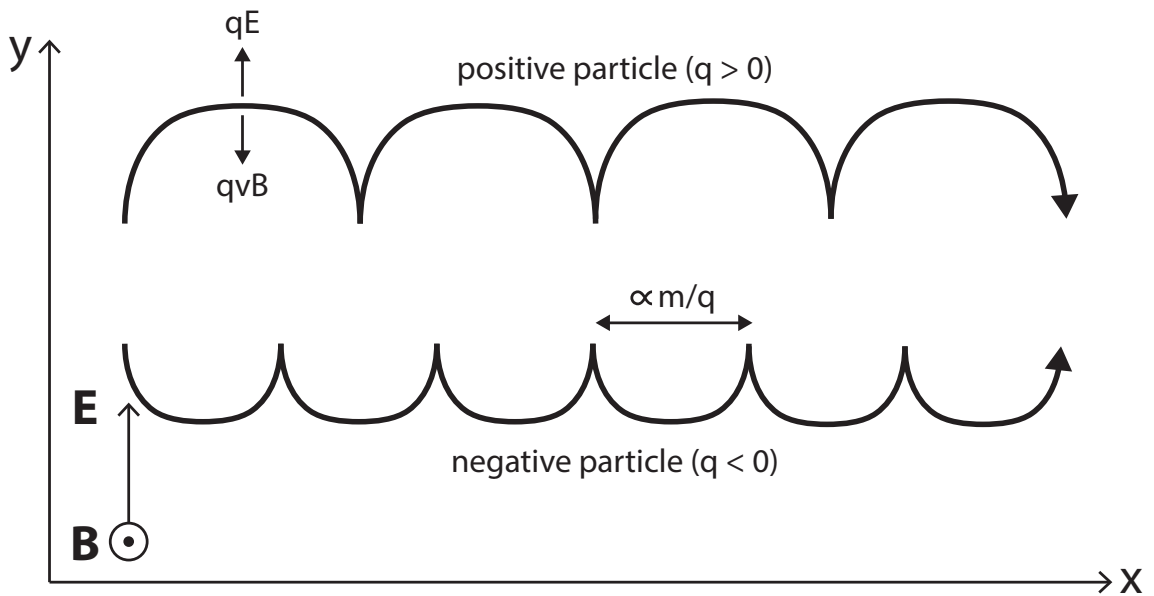


Figure 1.1: A diagram illustrating the motion of particles undergoing $\mathbf{E} \times \mathbf{B}$ drift, creating a net motion in the direction of $\mathbf{E} \times \mathbf{B}$.

1.1.6 Frozen-in flow (Alfvén's Theorem)

Consider an electric field and a magnetic field which vary slowly in time and space relative to the gyroradii and gyrofrequency. Faraday's Law (Equation 1.3) holds true and from Equation 1.16 the electric field is perpendicular to the magnetic field. Particle motion is comprised of v_{\parallel} and v_{\perp} , which are linked by the first adiabatic invariant (Equation 1.10), and a drift velocity as given by Equation 1.17.

Combining Equation 1.19 and Faraday's Law gives

$$\frac{\partial \mathbf{B}}{\partial t} = \nabla \times (\mathbf{v} \times \mathbf{B}) \quad (1.20)$$

This result can be used to show Alfvén's Theorem, or the frozen-in flow approximation, which states that, in a plasma, the centre of gyration of each particle is located on a particular field line; the particles are thus said to be frozen to the field line (Baumjohann and Treumann, 1997). As a result, when the field line moves, it carries these frozen-in particles with it; when the particles move, they drag the field line along with them. This approximation means that particles frozen to different field lines cannot mix together; the plasma population associated with a magnetic field cannot mix with particles in a different magnetic field unless the approximation breaks down (Hughes, 1995).

There are two types of drift motion that can lead to the violation of Alfvén's Theorem (Baumjohann and Treumann, 1997). The first case which causes the approximation to break down is when the magnetic field strength perpendicular to the field varies on spatial scales comparable to a gyroradius. The Grad-B drift is given by

$$\begin{aligned}\mathbf{v}_{\nabla B} &= \frac{mv_{\perp}^2}{2qB^3} \mathbf{B} \times \nabla B, \\ \mathbf{v}_{\nabla B} &= \frac{W_{\perp}}{qB^3} \mathbf{B} \times \nabla B\end{aligned}\tag{1.21}$$

where W_{\perp} is the perpendicular energy. The velocity is proportional to the gradient of the field, so that the velocity is small for weakly-varying magnetic fields, but becomes large enough to break the approximation with larger variations. The drift is larger for more energetic particles, and oppositely charged particles will move in opposite directions as a result of the dependence on q .

The other motion which can lead to the break-down of the frozen-in flux approximation is curvature drift, which occurs when particles move along curved magnetic field lines. This curvature drift is given by

$$\begin{aligned}\mathbf{v} &= \frac{mv_{\parallel}^2}{qR_c^2 B^2} \mathbf{R}_c \times \mathbf{B}, \\ \mathbf{v} &= \frac{2W_{\parallel}}{qR_c^2 B^2} \mathbf{R}_c \times \mathbf{B}\end{aligned}\tag{1.22}$$

where \mathbf{R}_c is the local radius of curvature. This drift velocity is larger for smaller radii of curvature. As with the Grad-B drift velocity, it is charge- and energy-dependent.

The frozen-in flow approximation holds when $\mathbf{E} \times \mathbf{B}$ drift dominates over the ∇B and curvature drifts. In a weakly-varying magnetic field with little curvature, or for a particle population that has low energies, Alfvén's theorem will be a good approximation; when the spatial scales of the variation are comparable to a gyroradius, the

frozen-in flow approximation will break down.

1.1.7 Equations of motion and Ohm's Law

Consider the fluid equations of motion. For ions,

$$n_i m_i \frac{d\mathbf{V}_i}{dt} = n_i m_i \mathbf{g} - \nabla P_i + (n_i e \mathbf{E} + n_i e \mathbf{v}_i \times \mathbf{B}) + \mathbf{F}_{ie}, \quad (1.23)$$

$$\mathbf{F}_{ie} = n_i \nu_{ie} m_i (\mathbf{V}_e - \mathbf{V}_i).$$

where n_i is the ion number density, m_i is the mass of the ions, ∇P_i is the ion pressure gradient, ν_{ie} is the collision frequency and \mathbf{V}_i is the bulk ion velocity. (It should be noted that the assumption of a collisionless plasma is no longer employed, as suggested by the presence of the collision frequency).

In the fluid equation of motion for electrons, these three quantities are substituted with their corresponding values for electrons, while the sign of the \mathbf{F}_{ie} term becomes negative (i.e. $\mathbf{F}_{ie} = -\mathbf{F}_{ei}$). The first term on the right-hand side is the gravitational force; the second term is the pressure gradient; the third term, in brackets, is the Lorentz force on the particles as a whole, and the last term is the frictional coupling between the ions and electrons. Assuming quasineutrality ($n_i = n_e$), assuming that $\rho_q \mathbf{E} \ll \mathbf{j} \times \mathbf{B}$ (which is valid in non-relativistic situations), and adding the ion and electron forms of this equation yield the momentum equation,

$$\rho \frac{d\mathbf{V}}{dt} = \rho \mathbf{g} - \nabla P + e(n_i \mathbf{V}_i - n \mathbf{V}_e) \times \mathbf{B} \quad (1.24)$$

$$= \rho \mathbf{g} - \nabla P + \mathbf{j} \times \mathbf{B}$$

where the first term is the force due to gravity, the second term is the force due to pressure, and the third term is the force due to the electromagnetic field, equal to $\mathbf{j} \times \mathbf{B}$. Subtracting the electron equation multiplied by m_i from the ion equation multiplied by m_e , the gravitational term is cancelled, and

$$\mathbf{E} = -\mathbf{V} \times \mathbf{B} + \frac{\mathbf{j}}{\sigma} + \frac{1}{ne} \mathbf{j} \times \mathbf{B} - \frac{1}{ne} \nabla P_e - \frac{m_e}{ne^2} \frac{\partial \mathbf{j}}{\partial t} \quad (1.25)$$

where σ is the conductivity, given by

$$\frac{q^2 n}{\nu_{ie} m_e}. \quad (1.26)$$

This is the Generalised Ohm's Law, which, in this form, gives the electric field inside the plasma. The first term is the convective motion term, the second is the

collision term, the third is the Hall term, the fourth is the pressure gradient term, and the fifth is the rate of change of the current. Note that the inclusion of a term describing particle collision means that the assumption of a collisionless plasma has been relaxed. The latter three terms can generally be neglected (Kivelson, 1995), so this can be rewritten to say

$$\mathbf{j} = \sigma(\mathbf{E} + \mathbf{V} \times \mathbf{B}). \quad (1.27)$$

There is a $\mathbf{j} \times \mathbf{B}$ term in Equation 1.25, and the curl of Ampère's Law can be taken such that

$$\begin{aligned} \mathbf{F} = \mathbf{j} \times \mathbf{B} &= \frac{1}{\mu_0}(\nabla \times \mathbf{B}) \times \mathbf{B}, \\ \mathbf{j} \times \mathbf{B} &= \frac{1}{\mu_0}(\mathbf{B} \cdot \nabla)\mathbf{B} - \nabla \left(\frac{\mathbf{B}^2}{2\mu_0} \right). \end{aligned} \quad (1.28)$$

The first term on the right-hand side is the magnetic tension force, and the second term is the magnetic pressure force, which combine to give the force due to electromagnetism. These terms imply that the force acts to straighten bends and smooth gradients in the magnetic field. By using Faraday's law, it can be shown that

$$\frac{\partial \mathbf{B}}{\partial t} = \nabla \times (\mathbf{V} \times \mathbf{B}) + \frac{1}{\mu_0 \sigma} \nabla^2 \mathbf{B} \quad (1.29)$$

where the first part of the right-hand side is due to convection and the second part is due to diffusion (Baumjohann and Treumann, 1997). In addition to the gradient and curvature drifts discussed in Section 1.1.6, the diffusion term causes the frozen-in flux approximation to become invalid due to collisions; when the diffusion term is large, the plasma will not be frozen onto magnetic field lines. This can be expressed by dividing the convective term by the diffusion term, resulting in the magnetic Reynolds number

$$R_m = \mu_0 \sigma V L \quad (1.30)$$

where σ is conductivity, V is the average plasma velocity perpendicular to the magnetic field, and L is the scale length of changes of the field and flow. When R_m is large, the convection dominates and frozen-in flow is a good approximation; when it is small, the diffusion term is important and therefore Alfvén's theorem no longer holds true.

Ampère's law implies that, if there are two different magnetic fields (with two different frozen-in plasmas) which are next to one another, there will be a current sheet separating the two. The frozen-in approximation breaks down inside such

a current sheet; the magnetic Reynolds number equals unity at the edges of the current sheet, and the thickness of the current sheet adjusts to balance the diffusion and convection. This allows particles from the two different plasmas to encounter one another and providing an area in which magnetic reconnection (introduced in Section 1.2) can occur (Hughes, 1995).

1.2 Magnetic Reconnection

In this section, the phenomenon of magnetic reconnection is outlined and the way in which it governs the interaction between the terrestrial magnetosphere and the solar wind is then explored (Section 1.5). In Sections 1.1.6 and 1.1.7, the frozen-in flow approximation has been described and those times at which it breaks down explained. In a current sheet, which is a thin region separating two regions of plasmas frozen onto their respective magnetic fields, the spatial scales under consideration are comparable to a gyroradius. Therefore within the current sheet, the magnetic field and plasma are not frozen to one another. This allows magnetic field lines to diffuse through the current sheet, where magnetic annihilation can occur, heating the plasma (Parker, 1957; Sweet, 1958; Petschek, 1964).

When the current sheet separates two magnetic fields that are not parallel, this diffusion of the magnetic field lines through the sheet can lead to the two magnetic fields interconnecting, in a process called magnetic reconnection illustrated in Figure 1.2. The newly-connected magnetic field lines, subject to magnetic tension, contract. The tension accelerates the particles on the field lines, and the contraction of the field lines leads to them moving away from the site of reconnection along the current sheet, which allows more magnetic field lines to reconnect at the same location.

An example of a place in which this process occurs is the magnetopause (Dungey, 1961), discussed in more detail in Section 1.6.1. Earth's field points north, and so magnetic reconnection can occur on the dayside when the IMF has a component in the southward direction. Once interconnected, the open field lines link the solar wind and the IMF to the magnetosphere and the terrestrial magnetic field. Then, on the nightside, magnetic reconnection can again occur, disconnecting the IMF from the terrestrial magnetic field and resulting in closed field lines. Closed field lines have footprints in the auroral oval in each hemisphere, whereas open field lines have a footprint in the polar cap (the region bounded by the auroral oval). This is discussed in more detail in Section 1.5.

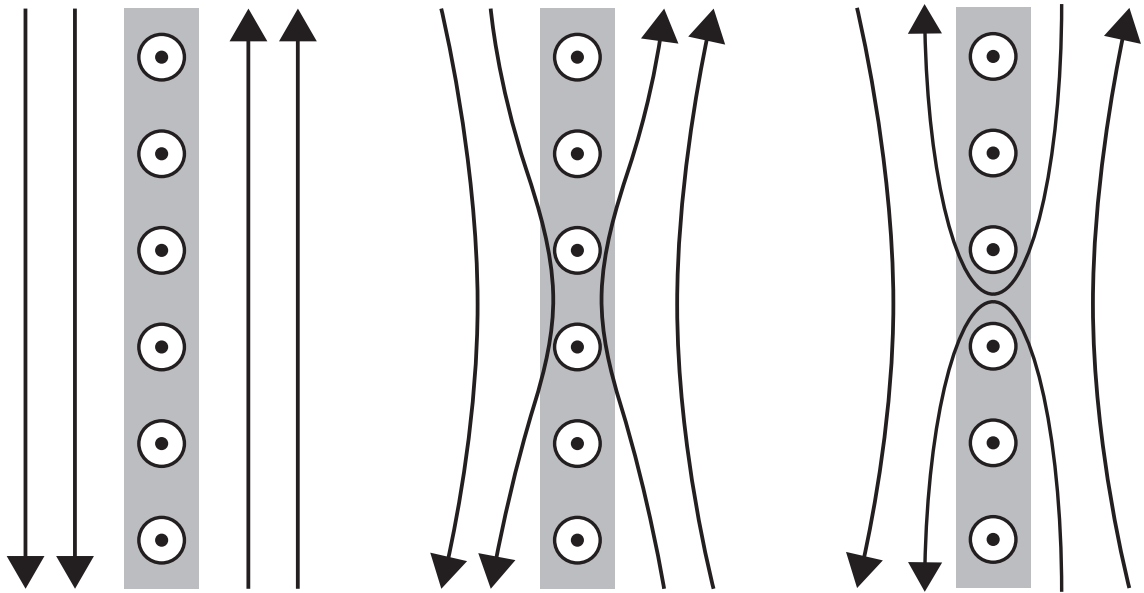


Figure 1.2: Illustration of oppositely directed field lines diffusing through a current sheet (shown coming out of the page, in grey) and reconnecting.

1.3 The solar wind

The solar wind is the name given to the combination of a stream of charged particles which flows radially outward from the Sun, and a magnetic field which is embedded within it called the interplanetary magnetic field (IMF). The influence of the Sun on Earth's geomagnetic activity was first hypothesised in the nineteenth century (Carrington, 1859; Birkeland, 1908). The solar wind occurs because of the pressure differential between the Sun and the interstellar space surrounding it, which causes a supersonic outflowing of solar particles from the Sun into the surrounding space. The solar wind has a typical speed of 450 km s^{-1} with a magnetic field strength of approximately 7 nT and electron and proton densities of 6.6 cm^{-3} and 7.1 cm^{-3} at a distance of 1 AU (Hundhausen, 1995).

The structure of the solar wind was inferred by Parker (1958) based on the postulations Biermann (1957) made by looking at cometary tails. As plasma is emitted near-radially from the Sun at a constant speed, the Sun rotates; this leads to the magnetic field frozen into the packets of plasma being threaded through those packets in a spiral known as the Parker spiral. Figure 1.3 shows the geometry of the Parker spiral, which leads to a 45° angle between the IMF and the Sun-Earth line at 1 AU (Parker, 1958; Hundhausen, 1995). The IMF was first discovered by Pioneer V (Coleman *et al.*, 1960).

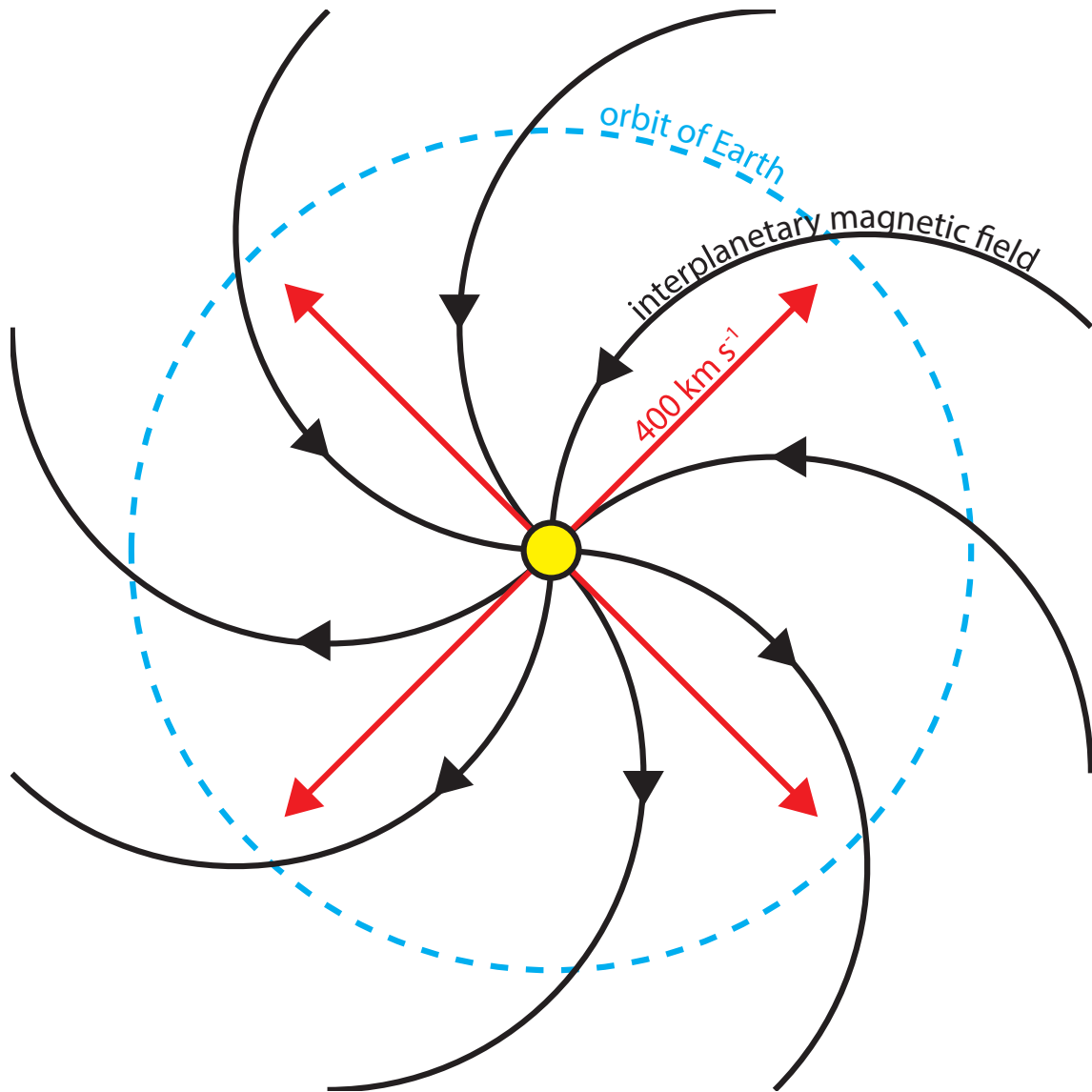


Figure 1.3: The spiral IMF caused by the rotation of the Sun and a radial expansion of the solar wind. Based on figures from Parker (1958) and Hundhausen (1995).

1.4 The near-Earth environment

The structure of the near-Earth environment is a result of the interaction between the planet and the solar wind and IMF. The region of space near Earth consists of the magnetosphere, the magnetopause, the magnetosheath and the bow shock (Figure 1.4). The magnetosheath consists of shocked solar wind plasma, and then there are several plasma populations within the magnetosphere: the magnetotail lobes, the plasma sheet (and plasma sheet boundary layer), the plasmasphere, and the radiation belts. This section aims to introduce the basic spatial structure of the magnetosphere and its surroundings, to provide context for the research in this thesis.

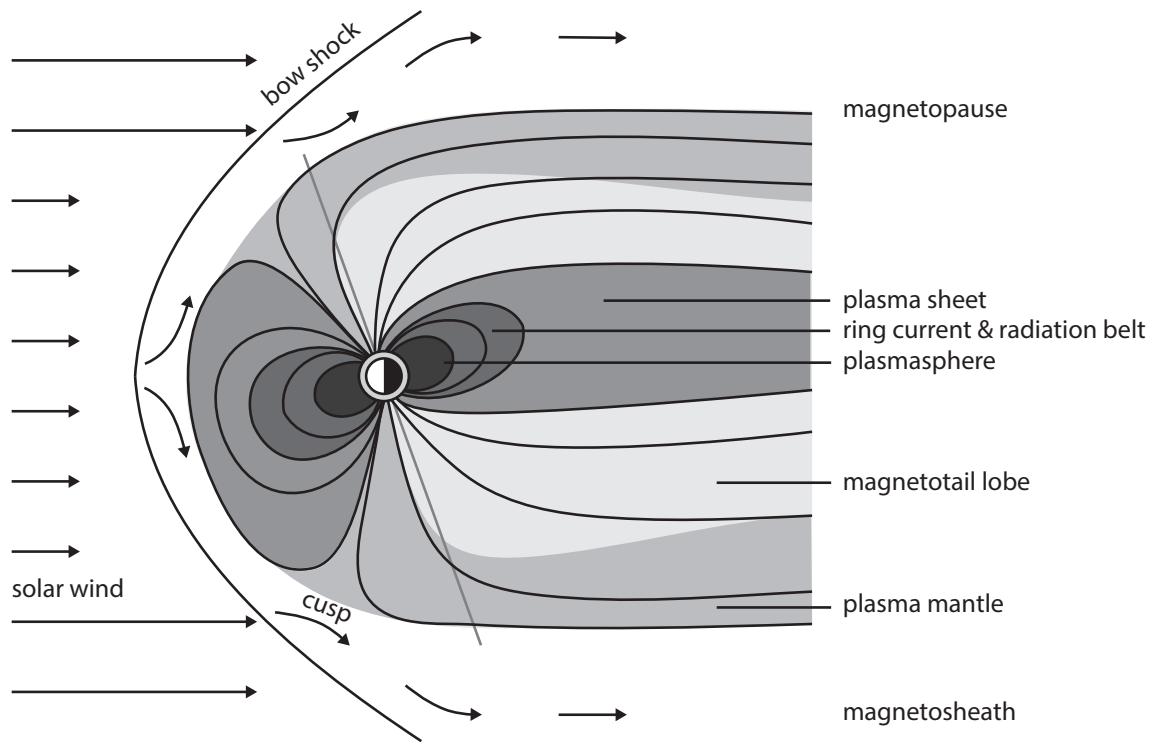


Figure 1.4: A diagram illustrating Earth and the constituent parts of its magnetosphere, adapted from Bahnsen (1978).

The magnetosphere is the name given to the region of space which contains Earth's magnetic field. Where the frozen-in approximation is valid, plasma frozen onto the IMF cannot mix with plasma frozen onto Earth's magnetic field, and so the solar wind flows around the magnetosphere. Sunward of the magnetosphere is the bow shock, which is the point at which the solar wind is slowed from supersonic to subsonic velocities by the obstacle in the flow (Earth's magnetosphere). The bow shock gives rise to a region of shocked solar wind plasma, which is called the magnetosheath (Schunk, 1983). Earthward of the bow shock and the magnetosheath, representing the edge of the magnetosphere, is the magnetopause (Chapman and Ferraro, 1931a,b). The magnetopause is the boundary between this (shocked) solar wind plasma and the magnetospheric plasma, and is therefore also the boundary between the IMF and the planetary magnetic field; this implies a current sheet (Hughes, 1995), which will be explored in more detail later (Section 1.6.1).

When reconnection occurs, the interplanetary magnetic field lines interconnect with the planetary field lines (Dungey, 1961), allowing solar wind plasma to flow towards the pole; the region in which this occurs is known as the cusp. These particles undergo mirroring close to Earth, and then travel away from the planet along the field line; by this time, the field line has moved around the planet. Thus the plasma becomes part of the plasma mantle (also called the high-latitude boundary

layer), streaming antisunward before reconnection in the distant tail converts this plasma into earthward streams which mirror at Earth. The plasma in the mantle is less dense than in the magnetosheath, flowing almost aligned with the field lines in the tail, but with a small inward flow due to the Dungey cycle, which results in it becoming thicker downstream (Vasyliunas, 1983).

When the Earthward streams and tailward streams are present together, the distribution is thermalised; the streaming energy of the plasma is converted to thermal energy, resulting in the hot, slow-flowing plasma sheet. As a result of the inflow of the field lines during the plasma's time of flight to the Earth, the outermost boundary consists of Earthward streaming plasma, and the tailward streams exist inward of that boundary. The plasma sheet is relatively densely populated with hot ions and electrons and lies on closed magnetic field lines (Wolf, 1995). Between the plasma mantle and the plasma sheet lie the magnetotail lobes and the plasma sheet boundary layer. The lobes are on open field lines, and are associated with cool plasma (flowing up from the ionosphere) and a low plasma density. In between the central plasma sheet and the tail lobes lies the plasma sheet boundary layer (PSBL). This is thought to be on closed field lines, and has a particle density between that of the lobes and central plasma sheet. It is formed of plasma which has just been accelerated in a reconnection region; magnetotail reconnection starts with plasma inflow from the lobes, and the plasma earthward of the reconnection site streams towards the planet along the field lines, mirroring at the Earth and creating earthward and anti-earthward flows observed on the PSBL (Hughes, 1995). On the other side of the reconnection site, the plasma is frozen to field lines which have been disconnected from Earth, in a structure called a plasmoid which is also sometimes found in the tail.

Closer to the planet, the radiation belts are found. The radiation belts are comprised of particles moving along the magnetic field lines, being mirrored at either end (Section 1.1.3); as a result, these structures are aligned with the magnetic field (Wolf, 1983). The particles that comprise the radiation belts are found up to a radial distance of $6R_E$, where R_E is the radius of Earth, equal to 6371 km. The density along the field line is not constant, with particles being lost due to interactions with the neutrals in the atmosphere at the ends of each field line. The radiation belts are home to the ions which predominantly carry the ring current (discussed in more detail in Section 1.6.3), as well as electrons which are responsible for the penetrating radiation that spacecraft experience in this region (Wolf, 1995). The electrons in the radiation belts appear in two belts: one closer to Earth (the inner belt) and one further away (the outer belt). The ions are not bifurcated in this manner, with no corresponding minimum observed in the ion flux.

The plasmasphere is a dense region of cold plasma which has a sharp boundary at $3 - 5R_E$, and whose population is replenished by the polar wind, which is the result of an ionospheric plasma population with energies large enough to escape the planet flowing upward at the poles. There is a separatrix between the hot plasma which makes up the plasma sheet and the cold plasma comprising the plasmasphere, which is called the plasmopause. The motion of plasmasphere plasma is controlled by corotation with Earth (which results in eastward motion), while the motion of the plasma sheet is controlled by Dungey cycle convection (which results in sunward motion). On the dawn side of Earth, eastward and sunward are the same direction; on the dusk side, the two are oppositely directed. There is a point on the dusk meridian at which each of the processes cancel the effect of the other, resulting in stagnant plasma at a radial distance of approximately $4 R_E$ (Baumjohann and Treumann, 1997).

The region of Earth's atmosphere known as the ionosphere is so called because it is the region of the atmosphere in which the particles are partly ionised and in which, therefore, the interaction of charged particles is an important consideration. The ionosphere has a peak in electron density at 250 km but has substructure leading to regions known as the D, E, and F regions; the E region lies between 90 km and 130 km, with D below and F above (Luhmann, 1995). The topside of the ionosphere lies above 800 km, with plasma beginning to flow from the ionosphere with a speed that increases with temperature, forming the polar wind (Schunk, 1983). The particle motions and collisions in the ionosphere lead to Hall and Pedersen currents flowing; these currents will be discussed qualitatively in Section 1.6.4 but it is useful to consider the particle motion quantitatively first.

1.4.1 Particle motion in the ionosphere

The particle motion in the ionosphere and the currents which arise as a result of this motion will now be considered. In the ionosphere, the plasma collides with the background population of neutrals, meaning that the plasma cannot be assumed to be collisionless. The equations of motion can be found from the Lorentz force such that

$$m_i \frac{d\mathbf{V}_i}{dt} = e\mathbf{E} + e\mathbf{V}_i \times \mathbf{B} + m_i\nu_i(\mathbf{U} - \mathbf{V}_i) \quad (\text{ions}), \quad (1.31a)$$

$$m_e \frac{d\mathbf{V}_e}{dt} = -e\mathbf{E} - e\mathbf{V}_e \times \mathbf{B} + m_e\nu_e(\mathbf{U} - \mathbf{V}_e) \quad (\text{electrons}), \quad (1.31b)$$

where ν is the collision frequency, m is the mass of a particle and the reference frame in which the neutrals are at rest is chosen, so $\mathbf{U} = \mathbf{0}$. The electric field and

magnetic field are assumed to be uniform and described by $\mathbf{B} = B\hat{\mathbf{z}}$ and $\mathbf{E} = E\hat{\mathbf{y}}$. Assuming the fluid moves at a constant velocity, $d\mathbf{V}/dt = \mathbf{0}$ (treating the plasma as a fluid means the gyromotions of the particles can be neglected). Now, considering just the ions, the ion bulk velocity is given by

$$\mathbf{V}_i = v_{ix}\hat{\mathbf{x}} + v_{iy}\hat{\mathbf{y}}. \quad (1.32)$$

Therefore, equations for the bulk motion in the $\hat{\mathbf{x}}$ and $\hat{\mathbf{y}}$ direction can be derived:

$$\hat{\mathbf{x}}: 0 = ev_{iy}B - m_i\nu_i v_{ix}, \quad (1.33a)$$

$$\hat{\mathbf{y}}: 0 = eE - ev_{ix}B - m_i\nu_i v_{iy}. \quad (1.33b)$$

Then the gyrofrequency $\Omega_i = eB/m_i$ may be used to find the current flowing

$$v_{ix} = (1 + \Omega_c^2\nu_i^2)^{-1} \frac{E}{B}, \quad (1.34)$$

$$\Rightarrow j_x = nev_{ix} = \frac{ne}{B} (1 + \Omega_c^2\nu_i^2)^{-1} E = \sigma_{ix}E. \quad (1.35)$$

This yields the current flowing as a result of the ions in the ionosphere in the direction $\hat{\mathbf{x}}$. A similar logic can be used to find the current in $\hat{\mathbf{y}}$ by rearranging Equation 1.33b to find v_{iy} and then substituting that into Equation 1.33a. The Hall current is the total current flowing in $\hat{\mathbf{x}}$, perpendicular to \mathbf{E} and \mathbf{B} , and the Pedersen current is the total current flowing in $\hat{\mathbf{y}}$, parallel to \mathbf{E} and perpendicular to \mathbf{B} . If the reciprocal in Equation 1.35 is evaluated and then the expression is divided by Ω_i before being added to the electron contribution, the Hall and Pedersen currents are given by

$$\text{Hall: } j_x = \left(\frac{ne^2}{m_i} \frac{\Omega_i}{\Omega_i^2 + \nu_i^2} - \frac{ne^2}{m_e} \frac{\Omega_e}{\Omega_e^2 + \nu_e^2} \right) E = \sigma_H E, \quad (1.36)$$

$$\text{Pedersen: } j_y = \left(\frac{ne^2}{m_i} \frac{\nu_i}{\Omega_i^2 + \nu_i^2} - \frac{ne^2}{m_e} \frac{\nu_e}{\Omega_e^2 + \nu_e^2} \right) E = \sigma_P E, \quad (1.37)$$

as given by Baumjohann and Treumann (1997). This means that the total ionospheric current is given by

$$\mathbf{j} = \sigma_P \mathbf{E} + \sigma_H \frac{\mathbf{E} \times \mathbf{B}}{B} \quad (1.38)$$

where the first vector expression has a magnitude of $\sigma_P E$ and direction of $\hat{\mathbf{E}}$ and the second has a magnitude of $\sigma_H E$ in the direction of $\hat{\mathbf{E}} \times \hat{\mathbf{B}}$. The Hall and Pedersen currents are discussed qualitatively in Section 1.6.4.

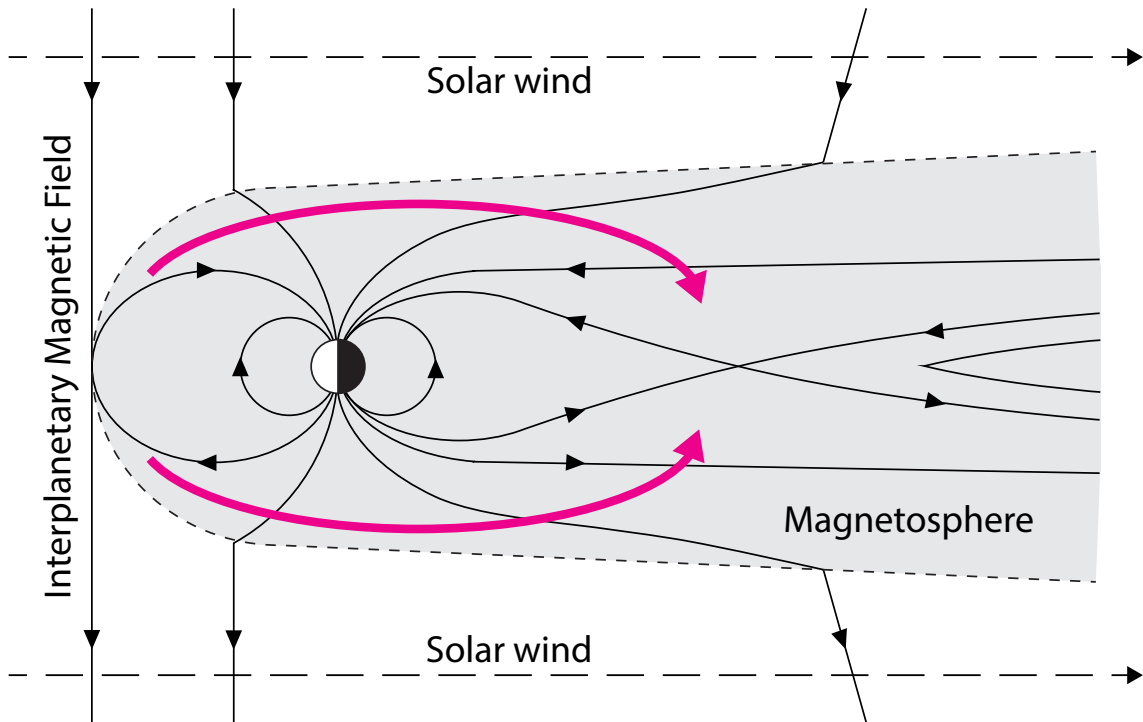


Figure 1.5: Magnetic field lines from the IMF and Earth interconnect at the nose of the magnetopause (on the left of the diagram). The newly opened field lines move antisunward as indicated by the pink arrows (top and bottom). They are pushed towards the centre of the magnetotail, where nightside reconnection takes place; the newly closed field lines then move sunward around the flanks of the planet so that the cycle can begin again.

1.5 Dungey cycle

The Dungey cycle, proposed by Dungey (1961), is the circulation of Earth's magnetic field and plasma caused by magnetic reconnection between the IMF (frozen into the solar wind) and the terrestrial magnetic field. This is one of the most important theories underpinning the field of solar-terrestrial physics, and it is possible to use this framework to evaluate the phenomena that occur within Earth's magnetosphere. In the Dungey cycle, IMF field lines interconnect with Earth's field during magnetic reconnection on the dayside of Earth, becoming 'open'. The newly opened flux tubes move sunward across the polar cap before being pushed towards the centre of the magnetotail, where nightside reconnection occurs, closing the magnetic field lines. These field lines then move sunward around the flanks of Earth, returning to the dayside so that the process can begin again. This picture of the magnetosphere is illustrated in Figure 1.5.

Dayside reconnection causes a redistribution of magnetic flux, which in turn leads to an imbalance between solar wind ram pressure and magnetospheric magnetic pressure; the magnetic flux in the magnetosphere moves in order to reach a new equilibrium, leading to closed flux tubes moving sunward around the flanks of the

planet and open flux tubes moving away from the Sun, crossing the polar cap in the antisunward direction. The IMF is frozen into the solar wind which is flowing past the planet, so the interconnected ends of the field lines also move downstream. The magnetotail, on the nightside of the planet, has a pressure exerted upon it by the solar wind flowing around the magnetosphere. This pressure causes the field lines to be pushed inwards, meaning a plasma motion towards the centre of the tail. This plasma motion inwards, and the magnetic field pointing to and from Earth, leads to a duskward electric field (Equation 1.19), leading to a Poynting vector as a result of \mathbf{E} and \mathbf{B} , given by

$$\mathbf{S} = \frac{\mathbf{E} \times \mathbf{B}}{\mu_0} \quad (1.39)$$

which means \mathbf{S} points towards the centre of the magnetotail. Therefore there must be a net flow of energy inwards; this energy accelerates the particle population in the central magnetotail, heating the plasma sheet.

This process can be seen in Figure 1.6, which illustrates the way in which the magnetopause changes shape after a field line interconnects, making the magnetopause blunter and causing the lobes to flare (as indicated by the grey arrows in panel b). The nose will experience larger magnetic pressure from within, and the lobes will experience larger ram pressure from the solar wind, leading to the nose being pushed outwards and the lobes being pushed inwards (in the opposite direction to the grey arrows) until equilibrium is restored. This leads the newly opened flux (and newly closed flux) to be pushed inwards, towards the centre of the tail (as can be seen in panel d). In the polar region, newly opened flux causes the boundary of the polar cap to move equatorward (panel f). Then, when flux is newly closed, the polar cap boundary moves poleward. Then, as more flux is closed, the closed flux moves sunward around the flanks to complete the cycle.

Considering the magnetic field \mathbf{B} pointing into (out of) the northern (southern) hemisphere, the plasma motion as a result of the convection \mathbf{V} will result in an electric field (Equation 1.19), which acts in the duskward direction for the region of antisunward plasma flow and the dawnward direction for sunward plasma flow. This electric field is illustrated using coloured arrows in Figure 1.7.

It should be noted that asymmetries in the ionospheric convection arise due to the dawn-dusk component of the IMF, B_y . This component of the IMF leads to magnetic tension forces acting in the dawn-dusk direction (Hughes, 1995), and consequently, the ionospheric convection pattern is asymmetrical about the noon-midnight meridian (Cowley *et al.*, 1991). These characteristics are illustrated in Figure 1.8.

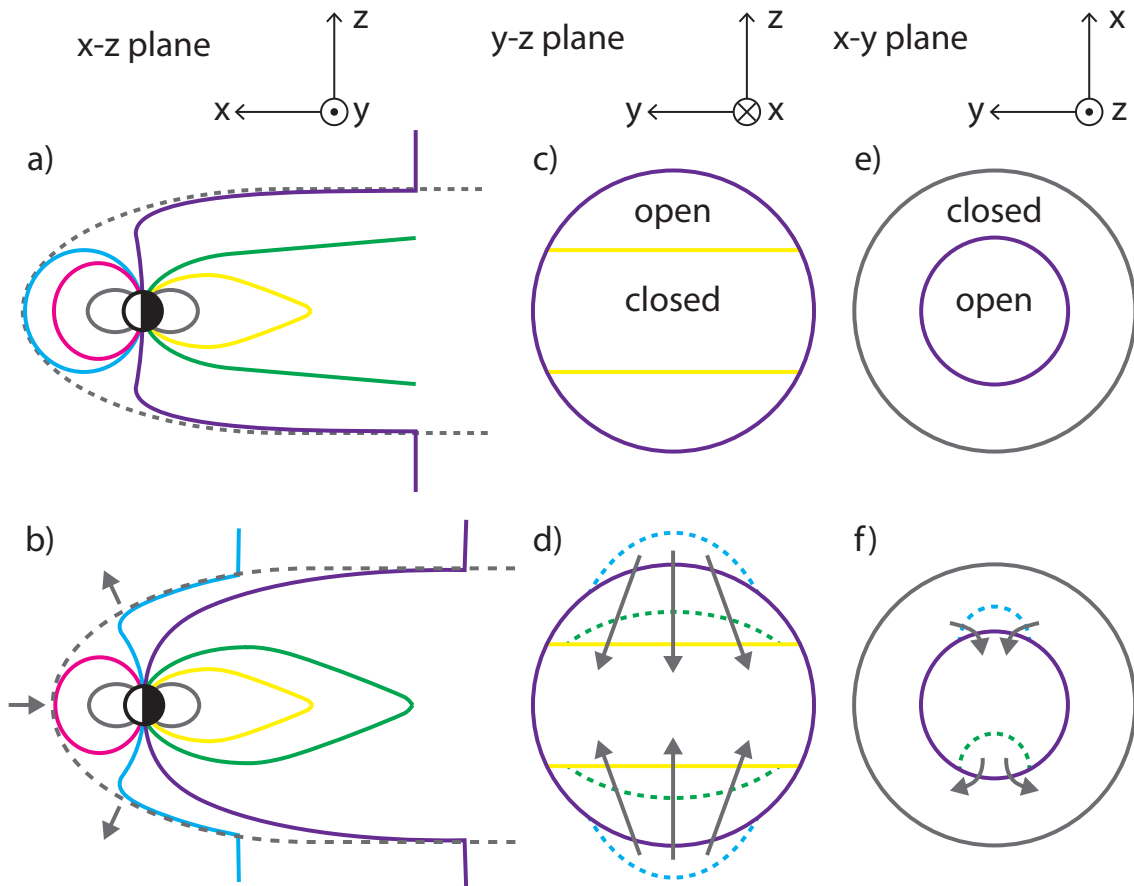


Figure 1.6: The way in which magnetic reconnection drives convection in the magnetosphere, sketched schematically. The left-hand panels show the magnetosphere, seen from the dusk side; the central panels show the magnetotail, seen from downstream; the right-hand panels show the polar cap and surrounding region, seen from above. The top panels show the situation before two field lines are opened and closed; the bottom panel shows the effect of the reconnection that occurs. Colours are used to illustrate how the field lines are interconnected between the top and the bottom panels; the blue field line is opened and the green is closed between the top and bottom of the diagram. The pink and yellow field lines are closed throughout, and the purple field line is open throughout. Grey arrows in panel b show how the magnetopause has moved in comparison to panel a, and show the motion of the plasma in panels d and f.

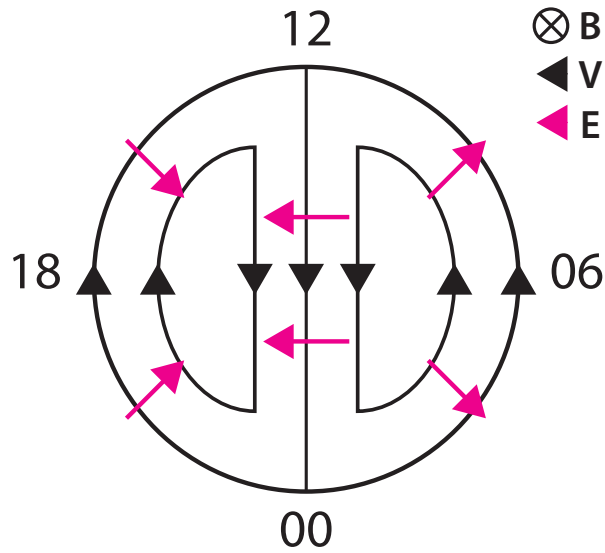


Figure 1.7: A schematic sketch of ionospheric convection in the northern hemisphere. The plasma streamlines are drawn in black and the magnetic field flows into the page. Application of Equation 1.19 yields the electric field illustrated by the coloured arrows.

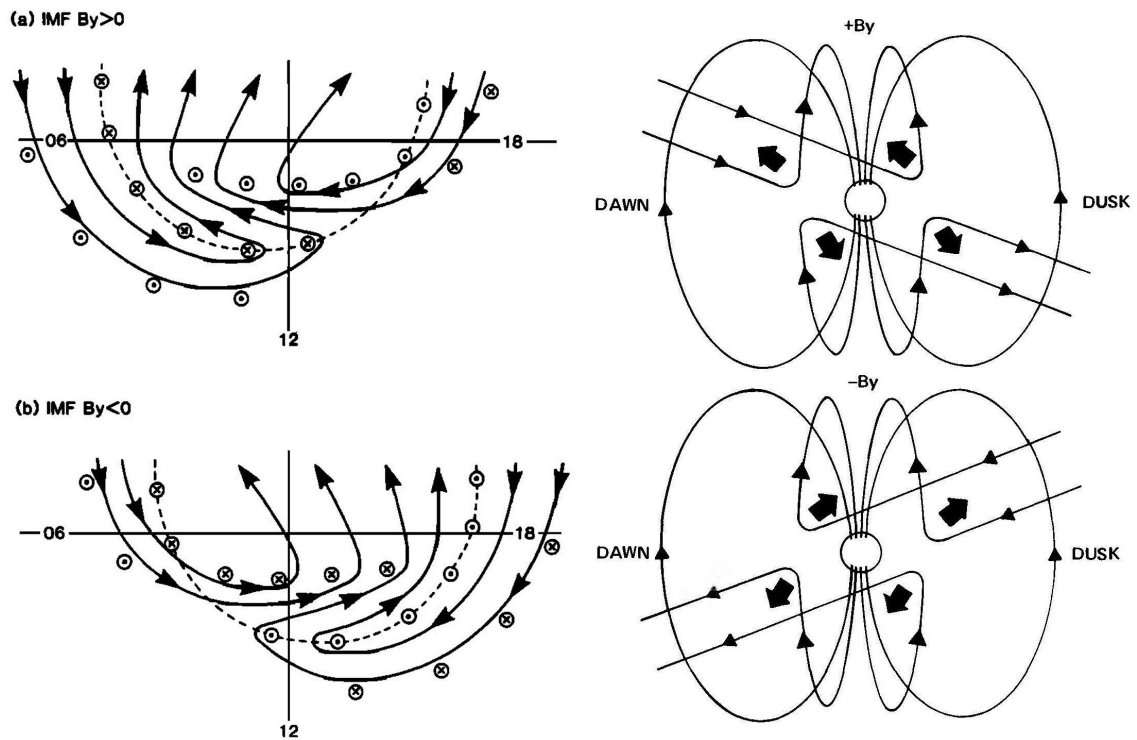


Figure 1.8: A diagram comprised of a figure from Cowley *et al.* (1991) (left) and another from Hughes (1995) (right) showing asymmetries associated with positive (top) and negative (bottom) IMF B_y . The left-hand diagrams show how ionospheric convection patterns are changed by the B_y component; the right-hand diagrams show the direction in which magnetic tension (illustrated as thick black arrows) will tend to pull newly reconnected field lines.

1.6 Currents in the magnetosphere

Earth's magnetosphere contains several current systems. Where there is an interface between Earth's magnetic field and the IMF, at the magnetopause, there is a curl in \mathbf{B} and so a current flows to satisfy Ampère's law; currents also flow in places where there is a curl in \mathbf{B} within the magnetosphere (for example, the magnetotail). Also, Equation 1.28 means that where a force acts on the magnetic field, there must be a current flowing.

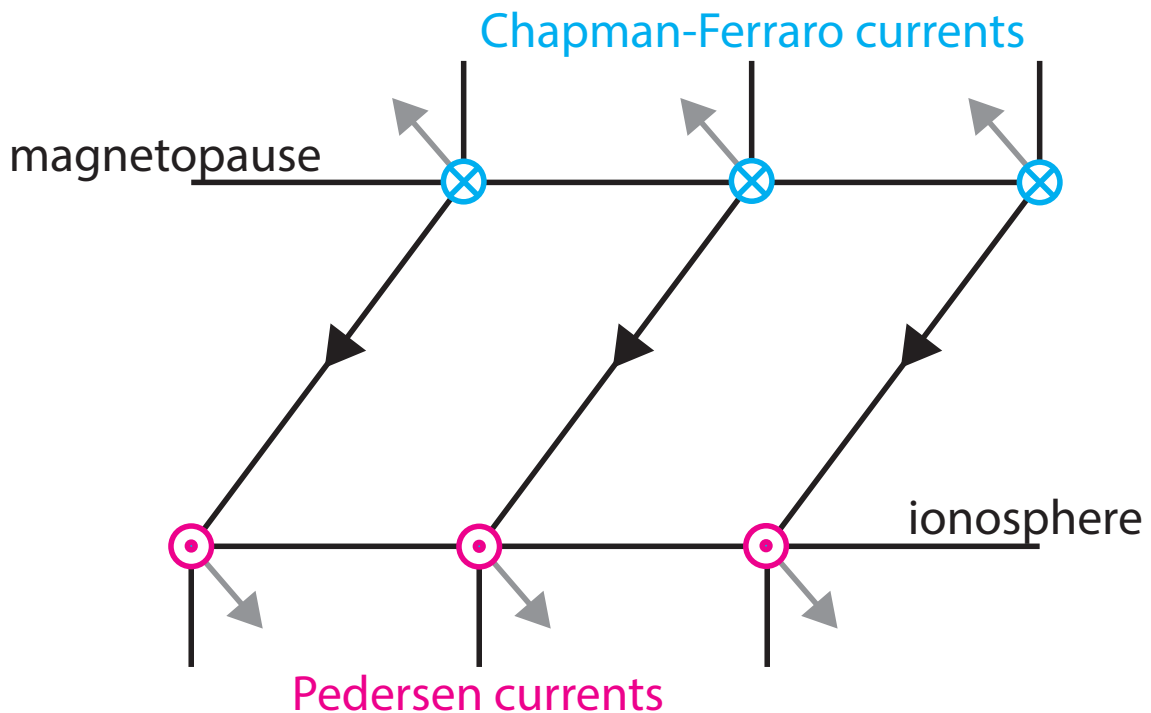


Figure 1.9: A schematic sketch of field lines flowing antisunward across the northern polar cap (to the right, in the diagram), causing them to bend as illustrated. Examination of Equation 1.28 means that currents must be flowing as a result of the magnetic tension (grey arrows) acting on these field lines, and these currents are illustrated in blue (magnetopause, or Chapman-Ferraro, currents) and pink (Pedersen currents). These two currents must be closed by a current flowing between the two, which are the Birkeland currents flowing along the field lines.

Ions flowing antisunward across the polar cap drag field lines with them due to the frozen-in flux approximation. The field lines are pulled from the magnetospheric side, with their feet dragging in the ionosphere due to ion-neutral collisions. Consequently, the field lines are tilted between the magnetopause and where they drag, which leads to the situation illustrated in Figure 1.9. The field lines are vertical at the bottom of the page (corresponding to the non-conducting region beneath the ionosphere). The consequent bends in the magnetic field lead to magnetic tension forces which act to try to straighten these bends; this thus leads to magnetopause currents and Pedersen currents as a result of Equation 1.28; these two currents are

illustrated in Figure 1.9. These two current systems must be closed by a third current system, which is the Birkeland currents flowing along the field lines to close the circuit.

Another way in which it can be seen that magnetopause currents are caused by magnetic tension forces is illustrated in Figure 1.10, which shows the magnetosphere, the magnetopause current (blue) and the cross-tail current (pink). Field lines flowing antisunward because of the Dungey cycle are bent; these field lines experience a magnetic tension force which acts in the direction which would reduce the bend. Consequently, magnetopause currents flow.

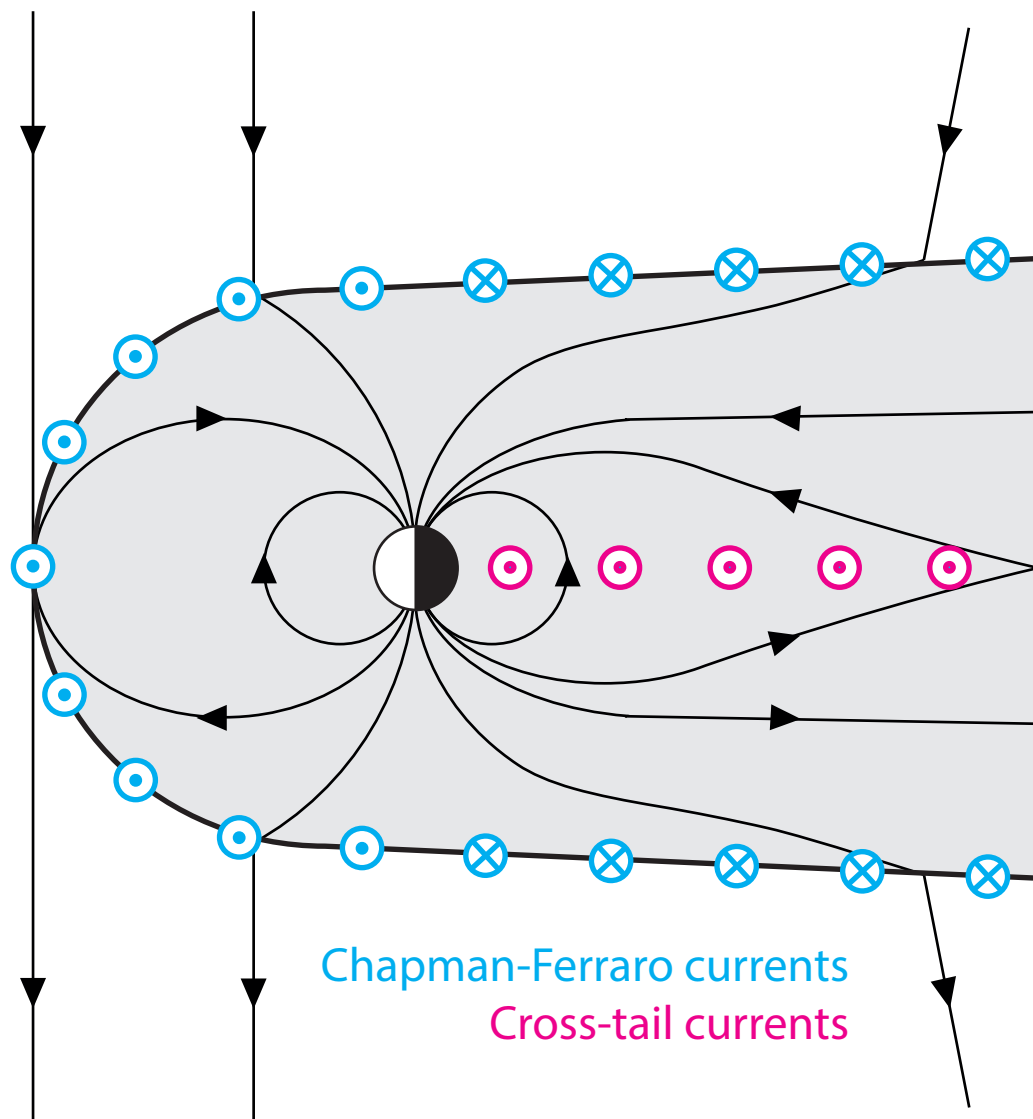


Figure 1.10: A schematic sketch of the magnetosphere seen in the x - z plane, with the magnetopause (Chapman-Ferraro) currents drawn in blue and cross-tail currents drawn in pink. In this diagram, field lines flow antisunward due to the Dungey cycle, and magnetic tension forces act on the field lines as they bend. Those field lines still on the dayside experience an antisunward magnetic tension; the field lines on the nightside experience a sunward magnetic tension. Consequently, magnetopause currents flow.

1.6.1 The magnetopause

The magnetopause is a current sheet that defines the outer edge of the magnetosphere, and separates the magnetosphere from the shocked solar wind in the magnetosheath. Its location is dictated by stress balance between the solar wind ram pressure on the outside and magnetic pressure on the inside; the magnetopause is located at the point where the forces exerted as a result of these pressures are in equilibrium. The magnetopause currents are also called the Chapman-Ferraro currents, as they were first theorised by Chapman and Ferraro (1931a,b).

These magnetopause currents can be explained in terms of solar wind particles impinging upon the magnetic field of Earth. Imagine that electrons and protons from the solar wind are moving with a velocity in the direction perpendicular to both the planetary magnetic field lines and the magnetopause. As these particles enter the magnetic field \mathbf{B} , they will experience a Lorentz force (as given by Equation 1.5) such that $\mathbf{F} = q(\mathbf{v} \times \mathbf{B})$. This force will accelerate the particle and thus change the direction of its velocity. Since \mathbf{F} acts perpendicular to \mathbf{v} at all times, this causes the particle to gyrate (see Section 1.1.2), completing half a gyration before leaving the area of space in which it encountered \mathbf{B} ; when this occurs, there is no Lorentz force and so the particle will continue moving in the opposite direction. This is illustrated in Figure 1.11.

The gyration performed by the particles leads to velocity with two components: the first component, in the original direction of motion, perpendicular to both the magnetic field lines and the magnetopause; and the second component, in the direction of the magnetopause. Since \mathbf{F} is dependent on q , the solar wind particles will experience opposite forces depending on their polarities, and thus will gyrate in different directions. This leads to a net motion of positive particles in one direction along the magnetopause and a net motion of negative particles in the opposite direction along the magnetopause, causing a current to flow in the direction of the positive charges. This current is the Chapman-Ferraro current which flows along the magnetopause; the magnetic perturbations from these currents Earthwards of the magnetopause are in the same direction as Earth's magnetic field.

It should be noted that the direction of the gyration will also be affected by the direction of \mathbf{B} in that region of the magnetopause. In the region of the magnetopause adjacent to closed magnetic field lines on the dayside, this will give rise to a current flowing from dawn to dusk, whereas the region of the magnetopause adjacent to open field lines will give rise to currents flowing from dusk to dawn; this motion gives rise to the current required by Ampère's law. At times of a high solar wind pressure incident on the magnetopause, it will be compressed, increasing the current

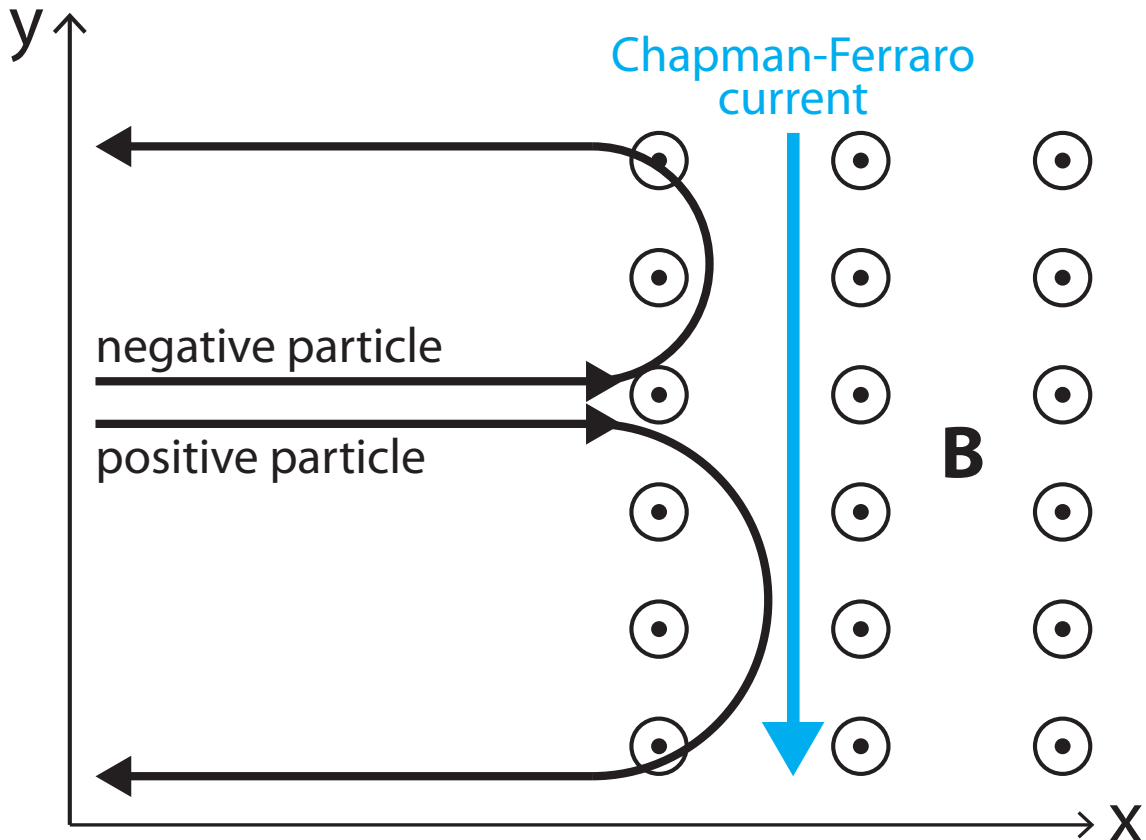


Figure 1.11: The motion of positive and negatively charged particles as they encounter Earth's magnetic field, gyrate once and leave the magnetic field travelling in the opposite direction. The Chapman-Ferraro current that forms as a result of this process is indicated in blue.

magnitudes in an event called a sudden impulse (Nishida and Cahill, 1964).

The assumptions inherent in the above description cause limitations. The positively charged solar wind particles will penetrate deeper into the magnetopause than the electrons due to the fact that the gyroradius ρ_c is dependent on the particle mass (Equation 1.7), causing an electric field gradient perpendicular to the plane of the magnetopause. Other assumptions are that there is no IMF (which is a poor assumption), nor any terrestrial plasma. The above treatment implies that the current sheet will be of a gyroradius in length scale, whereas it is known that the magnetopause is far thicker (e.g. Berchem and Russell, 1982, and references therein). In fact, the magnetopause can be shown to be significantly more complex than the picture described here, but the currents flowing are the aspect of interest in this thesis and thus there is no need to consider the particle interactions beyond the simplified version above.

1.6.2 The magnetotail

The tail current sheet is in the centre of the magnetotail, and separates the two lobes. The northern lobe is entirely populated by field lines directed towards the north pole and therefore towards Earth, whereas the southern lobe is entirely populated by field lines directed away from the south pole and therefore towards the tail. This means that the two lobes contain oppositely-directed magnetic fields, and this discontinuity implies a current sheet must be present. Any dipolarisation of the magnetic field in this region will reduce the current flowing in this sheet, which will be of importance in Section 1.6.6 (Baumjohann and Treumann, 1997).

The current intensity may be discovered by applying Ampère's law across the current sheet. Thus, if j is the current intensity (the current per length) of the plasma sheet and B_T is the magnetic field strength in the tail, $\mu_0 j = \Delta B = 2B_T$. Setting $B_T = 20 \text{ nT}$ (Siscoe *et al.*, 1984), $J = 0.03 \text{ A m}^{-1}$. This is a small current intensity, but the magnetotail is many R_E in length (Dungey, 1965); to put it in units more appropriate in scale, the current intensity $J = 2 \times 10^5 \text{ A}/R_E$ (Hughes, 1995).

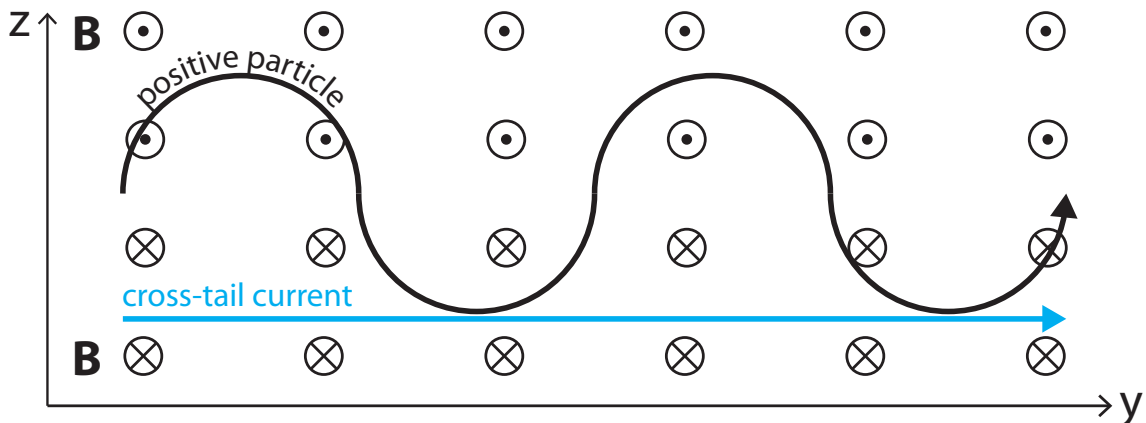


Figure 1.12: The motion of a positive particle in the discontinuity between the northern and southern lobes of the magnetotail. The cross-tail current that forms as a result of this particle motion is indicated in blue.

To examine this from the perspective of particle motion, consider a particle gyrating around a magnetic field line in the magnetotail. Now suppose that such a particle is gyrating around a field line which is close to the discontinuity between the northern and southern lobes. If the particle is positive and it starts in a region of magnetic field which points out of the page in the x direction, it will gyrate clockwise in the y, z plane around a field line. As it gyrates, the particle will cross the discontinuity between the lobes, and will now be in a magnetic field which now points into the page, causing it to gyrate anticlockwise. Half a gyration later, it will

have crossed the discontinuity again and will now be gyrating clockwise as before.

This generates no net motion in the z direction but causes a net motion in the y motion along the discontinuity. Since a negative particle will gyrate in opposite directions at each stage, the net motion is in the opposite direction for positively and negatively charged particles, causing a current to flow along the discontinuity between the two magnetic fields in the direction of the positive particle motion, causing the current sheet in the magnetotail to flow westwards, from dawn to dusk (Hughes, 1995). The currents are illustrated in Figure 1.12. Magnetic perturbations from these currents act in the same direction as the magnetic fields on either side of the current sheet.

1.6.3 The ring current

The ring current is carried by particles in the radiation belt, but not every radiation belt particle contributes to the current; instead, it is mostly carried by ions, due to their higher energies (Wolf, 1995). In the inner magnetosphere, the gradient of Earth's dipolar magnetic field is large, and as a result these particles undergo gradient-curvature drift (Equations 1.21 and 1.22); positive particles drift westwards and negative particles drift eastwards. Combined with a magnetisation current caused by spatial gradients in particle pressure, this results in the ring current.

Particle precipitation during a geomagnetic storm will lead to the ring current increasing in magnitude until the rate of the addition of particles is equal to the particle loss rate; when the geomagnetic storm abates, the ring current therefore decreases in magnitude as particles are lost (McPherron, 1995). The magnetic perturbations associated with the ring current reinforce the magnetic field outside the radiation belts but act in the opposite sense to the magnetic field inside the belts, thus enlarging the magnetosphere.

If it is assumed that the plasma sheet close to Earth has an inner edge (the plasmopause) which exactly follows a contour of constant magnetic field, then the particles in the plasma all drift at the same velocity and so the ring current closes self-consistently. However, not only is this a poor assumption, but as a result of the magnetospheric and ionospheric convection described earlier, it is known that there is an electric field which acts duskward across the magnetosphere. Such an electric field will induce $\mathbf{E} \times \mathbf{B}$ drift such that the plasma population will drift sunward across the system, which means that there will be an intrusion of the plasma closer to Earth on the nightside of the planet, leading to an area of higher density along a contour of constant field. This will lead to particle drift, meaning that a current

will flow westward, with positive charge building up on the dusk side and negative charge building up on the dawn side. This current must be closed in order to prevent the charge building up; therefore, a current flows from the dusk side of the bump to the ionosphere, and a current flows from the ionosphere to the dawn side of the bump (Wolf, 1995). These are Birkeland currents, which will be discussed in more detail in Section 1.6.5. The electric field which is formed as a result of the Earthward intrusion acts in the opposite direction to the electric field as a result of the convection.

1.6.4 Hall and Pedersen currents

The particle motion that gives rise to the Hall and Pedersen currents was introduced in Section 1.4.1, in which it was shown that particles undergo $\mathbf{E} \times \mathbf{B}$ drift with a velocity that is independent of their charge (Equation 1.17). Since this results in all particles moving in the same direction, no currents arise from this considered in isolation. However, once the collisions with neutral particles in Earth's ionosphere are considered, currents do arise as a result of $\mathbf{E} \times \mathbf{B}$ drift; these currents are the Hall and Pedersen currents respectively. This section discusses the Hall and Pedersen currents qualitatively, expanding upon the quantitative treatment in Section 1.4.1.

As protons and electrons move in the ionosphere, they collide with neutral particles, interrupting their $\mathbf{E} \times \mathbf{B}$ drift. However, ions have a larger cross-section of interaction and are therefore more likely to collide with neutral particles than the electrons also moving in the ionosphere. This means that there is a total deceleration of ions in the direction of the $\mathbf{E} \times \mathbf{B}$ drift which is larger than the total deceleration of electrons in the same direction. It can be seen from Equations 1.36 and 1.37 that this is dependent on the ratio ν/Ω .

This disparity in the rate of flow of charge leads to a current, which flows in the opposite direction to the $\mathbf{E} \times \mathbf{B}$ drift causing the current as a result of the fact that the ions collide more often and therefore, in the reference frame of the electron motion, the ions are moving opposite to the direction of the drift (Carlson and Egeland, 1995; Baumjohann and Treumann, 1997). This describes the Hall current, which is therefore perpendicular to both the electric field \mathbf{E} and the magnetic field \mathbf{B} in the ionosphere and, as a result, flows in the same direction but in the opposite sense to the ionospheric convection pattern. Since the ionospheric convection pattern is a continuous system, in the case of uniform conductivity the Hall current system is a closed circuit, sketched schematically in Figure 1.18a.

The collision of charges with neutral particles also interrupts the ongoing gy-

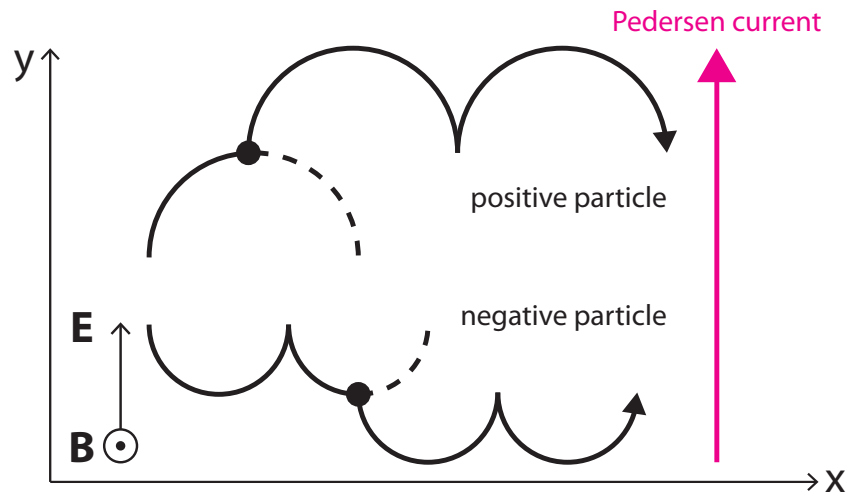


Figure 1.13: Particle motion interrupted by collisions with neutrals in the ionosphere, leading to a net motion of positive particles in the direction of \mathbf{E} and negative particles in the opposite direction. The resulting Pedersen current is shown in pink.

romotion. As plasma particles are brought to a stop by the collision, they begin accelerating again as a result of the Lorentz force; ions are accelerated in the direction of the electric field \mathbf{E} and electrons in the opposite direction. Because the Lorentz force is a function of q , this results in negative particles moving in one direction and positive particles moving in the other direction, meaning a net current occurs in the direction of the electric field (Baumjohann and Treumann, 1997; Carlson and Egeland, 1995); this current is the Pedersen current, and the particle motion is illustrated in Figure 1.13. It can be seen by considering the electric field in the ionosphere (Figure 1.7) that this current system is not closed; there is a source in the centre of the dawn convection cell and a sink within the dusk convection cell, alongside a second sink/source equatorward of the cell (dawn/dusk respectively), which will be considered later.

The Hall and Pedersen currents arise as a result of neutrals in the atmosphere, and therefore the density of these neutrals has an effect on the strength of the currents flowing; this can be seen by examination of Equations 1.36 and 1.37, both of which are dependent on the collision frequency ν , which is in turn dependent on neutral density. The neutral density increases sharply with decreasing altitude such that the ion-neutral collision frequency also increases rapidly, with the ratio of ν/Ω reaching 1 at 125 km. Above this altitude, the ratio is small and the ion $\mathbf{E} \times \mathbf{B}$ drift is not substantially retarded, while the mobility of the ions in the \mathbf{E} direction is proportional to ν_i/Ω_i ; below this altitude, the drift in the $\mathbf{E} \times \mathbf{B}$ direction becomes negligible and the ion mobility in the direction of the electric field is inversely proportional to ν_i/Ω_i , decreasing with decreasing altitude (Cowley, 2000).

A similar situation arises in the case of electrons, but the ratio ν_e/Ω_e remains small throughout the ionosphere where appreciable plasma densities are found (above an altitude of 90 km). As a result, the electrons $\mathbf{E} \times \mathbf{B}$ drift at all ionospheric heights. This results in a Pedersen current in the direction of \mathbf{E} , dominant above 125 km where both ions and electrons $\mathbf{E} \times \mathbf{B}$ drift but the ions also move in \mathbf{E} . It also results in a Hall current in the $-\mathbf{E} \times \mathbf{B}$ direction, dominant below 125 km where the electrons are still drifting but the ion drift becomes increasingly retarded.

The Hall currents can be observed using ground magnetometer data, and this can be used to sense ionospheric convection patterns, because the measured Hall currents will be in the opposite direction to the plasma flow. The Hall currents flow sunward across the polar cap and flow antisunward on the flanks of the polar cap; the Hall currents flowing in the flanks are also called the auroral electrojets. The Hall currents on the dawn side comprise the westward electrojet, and the dusk side is the eastward electrojet. This overall current system has names other than the Hall current system; some have termed it the S_D (solar disturbance) current system (Chapman and Bartels, 1940; Milone and Wilson, 2008), while others have called it the DP-2 (type 2 polar disturbance) current system (Obayashi, 1967; Nishida, 1968; McPherron, 1995; Kikuchi *et al.*, 1996).

This pattern implies a plasma flow which is antisunward across the polar cap but sunward in the two electrojets, which is the expected ionospheric convection pattern (see Section 1.5 and 2.1). In fact, when the magnetosphere forces frozen-in ionospheric plasma across the neutral atmosphere, the forces generated by the (principally Pedersen) currents act to cancel the drag forces that arise. The Hall and Pedersen currents in the dayside ionosphere are of a conductivity ~ 10 mho whereas on the nightside they are reliant on the precipitating plasma from the magnetosphere and thus may vary by an order of magnitude. Hall conductivities are usually 2-4 times higher than those of the Pedersen currents (Baker *et al.*, 1996).

1.6.5 Birkeland currents

Field-aligned currents are named the Birkeland currents for Kristian Birkeland, who hypothesised their existence (Birkeland, 1908, 1913). The consideration of the Hall and Pedersen currents above can be used to infer the presence of field-aligned currents in the ionosphere, by considering the current closure that occurs. As noted in Section 1.6.4, the Hall currents close self-consistently, assuming uniform conductance, but the Pedersen currents do not. Consequently, currents are needed to close the Pedersen current system, and the Hall current system at times of non-uniform conductance. The field-aligned current density J_{\parallel} in A m^{-2} flowing into or out of the

ionosphere is the divergence of the ionospheric height-integrated current intensity flowing in the ionosphere \mathbf{J}_\perp in A m^{-1} , such that

$$\begin{aligned}\frac{\partial \mathbf{B}}{\partial t} &= \mathbf{0}, \\ \mathbf{E} &= -\nabla \phi, \\ \mathbf{J}_\perp &= \Sigma_P \mathbf{E} + \Sigma_H (\hat{\mathbf{B}} \times \mathbf{E}), \\ J_\parallel &= \nabla \cdot \mathbf{J}_\perp = \Sigma_P \nabla^2 \phi + \nabla \phi \cdot \nabla \Sigma_P + (\nabla \phi \times \hat{\mathbf{B}}) \cdot \nabla \Sigma_H.\end{aligned}\quad (1.40)$$

The field-aligned currents that flow to and from the source/sink in the convection cells are the Region 1 Birkeland currents (also called the R1 currents); the currents which flow to and from the sink/source on the equatorward side of the cells are the Region 2 (R2) Birkeland currents. By definition, therefore, the R1 currents are always polewards of the R2 currents. The footprints of the Birkeland currents, alongside the Hall and Pedersen currents, are illustrated in Figure 1.14.

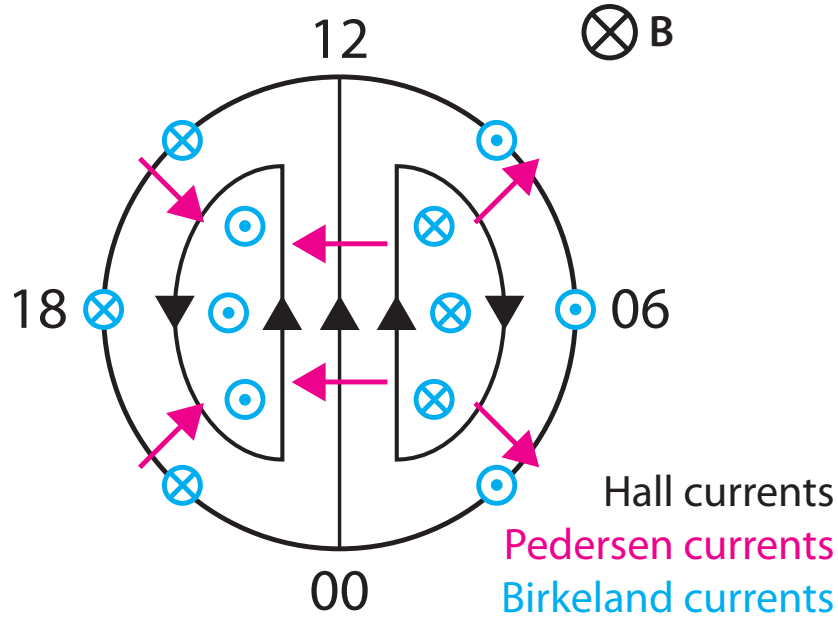


Figure 1.14: A schematic sketch of ionospheric current systems in the northern hemisphere. The Hall currents are drawn in black and flow oppositely to the plasma streamlines in Figure 1.7; the Pedersen currents flow in the same sense as the electric field and are illustrated in pink. The Birkeland currents flow into and out of the ionosphere, as shown by the blue circles.

Since the R1 currents flow to areas in the middle of the convection cells, they flow on field lines which are approximately colocated with the open/closed field line boundary (OCB), and can be seen to close at the magnetopause (Section 1.6.1), thus electrostatically linking the magnetopause to the ionosphere; the R2 currents are equatorward of the OCB, in the region of the ionosphere populated by closed field lines, and map to the partial ring current (Section 1.6.3), linking the inner

magnetosphere to the ionosphere. It can also be seen that R1 currents flow along this boundary by considering the shear between closed field lines, which are dipolarised, and open field lines, which are not; this implies a current sheet as a result of the frozen-in approximation and Ampère's Law.

Upward currents are associated with electrons moving downward, whereas downward currents are associated with electrons moving upward and ions moving downward (Ohtani *et al.*, 2009, and references therein). Downward moving electrons/protons will mean the presence of electron/proton aurora at the base of the currents. In the case where there are not enough particles to supply currents, there will be a potential drop along the field line, partially decoupling the ionosphere and magnetosphere. In the case of downward currents, there is a plentiful supply of electrons in the ionosphere to carry the current, but upward currents must be carried by either upward-flowing ionospheric ions (which is problematic due to their relatively high mass) or electrons from the magnetosphere; if there is only a small number of electrons available, those electrons that carry the current are accelerated by the potential drop (since $j = nev$); more accelerated electrons lead to more energetic collisions and thus more brilliant aurora. The voltage implied by a field-aligned current can be found using the Knight relation (Knight, 1973; Lyons, 1980), which implies that the electrostatic potential energy is up to an order of magnitude larger than the electron thermal energy; a relativistic form has also been derived by Cowley (2006).

In Section 1.6.4, it was noted that the Hall currents can be measured with ground magnetometers. However, if a field-aligned current flows vertically into the ionosphere, it creates a magnetic perturbation which encircles the field line; Pedersen currents, flowing away from the footprints of the field-aligned currents, also create magnetic perturbations. Fukushima's theorem (Fukushima, 1969, 1976) states that, from the ground, the magnetic perturbations act oppositely to the perturbation as a result of the field-aligned current in the case of uniform conductivity, making it impossible to make ground-based observations of these currents. (From above the Pedersen currents, the magnetic perturbations reinforce the perturbation as a result of the field-aligned currents.) This is illustrated in Figure 1.15, in which magnetic perturbations are coloured; those due to Birkeland currents are blue, and those due to Pedersen currents are pink. Assuming vertical field-aligned currents and uniform conductivity, the total Pedersen current will be equal to the total field-aligned current, thus meaning that the perturbations cancel perfectly. If the field-aligned currents have a non-vertical component, this will create a magnetic perturbation which could be measured on the ground.

Since it has been noted that, above the Pedersen currents, the perturbations from

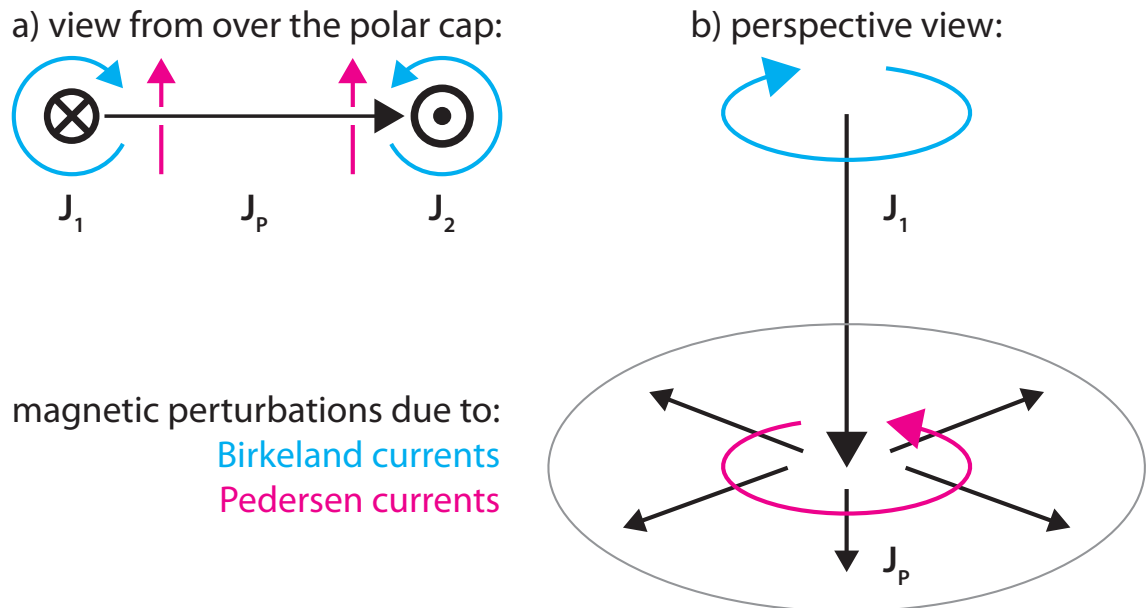


Figure 1.15: a) A Pedersen current closing two Birkeland currents flowing into and out of the page, seen from above the polar cap. b) A Birkeland current flowing into the ionosphere, and Pedersen currents flowing from its base. Blue arrows show the magnetic perturbations caused by the Birkeland current flowing, and pink arrows show those from Pedersen currents; the two cancel each other out, yielding Fukushima's theorem.

the Pedersen and field-aligned currents act in the same direction, it is instructive to examine the magnetopause currents. The magnetic perturbations caused Earthward of the Chapman-Ferraro currents act in the same direction as the perturbations due to the Pedersen and field-aligned currents. In this manner, a Poynting flux (Equation 1.39) is implied by the magnetic perturbations and the electric field (acting in the direction of the Pedersen currents) which acts towards the ionosphere from the magnetopause (Cowley, 2000).

Now that the Birkeland currents have been described, the large-scale current circuit for Earth may be explained. Chapman-Ferraro currents induced in the magnetopause close in two ways; either through the magnetotail and back through the Chapman-Ferraro system, or through R1 Birkeland currents linking the magnetopause to the ionosphere. In the latter case, Pedersen currents then flow, linking the footprint of the R1 current on the dawn side to the R2 currents. The R2 currents link the ionosphere to the partial ring current in the inner magnetosphere, with the partial ring current providing the bridge between the dawn and dusk R2 currents. The Pedersen current system links the dusk footprint of the R2 current back to the R1 current system, such that currents flow from the ionosphere back to the magnetopause, which can be seen in Figure 1.16. Since the magnetopause currents can close through the tail and back to the magnetopause the question of how much current closes through the Birkeland current system and how much current

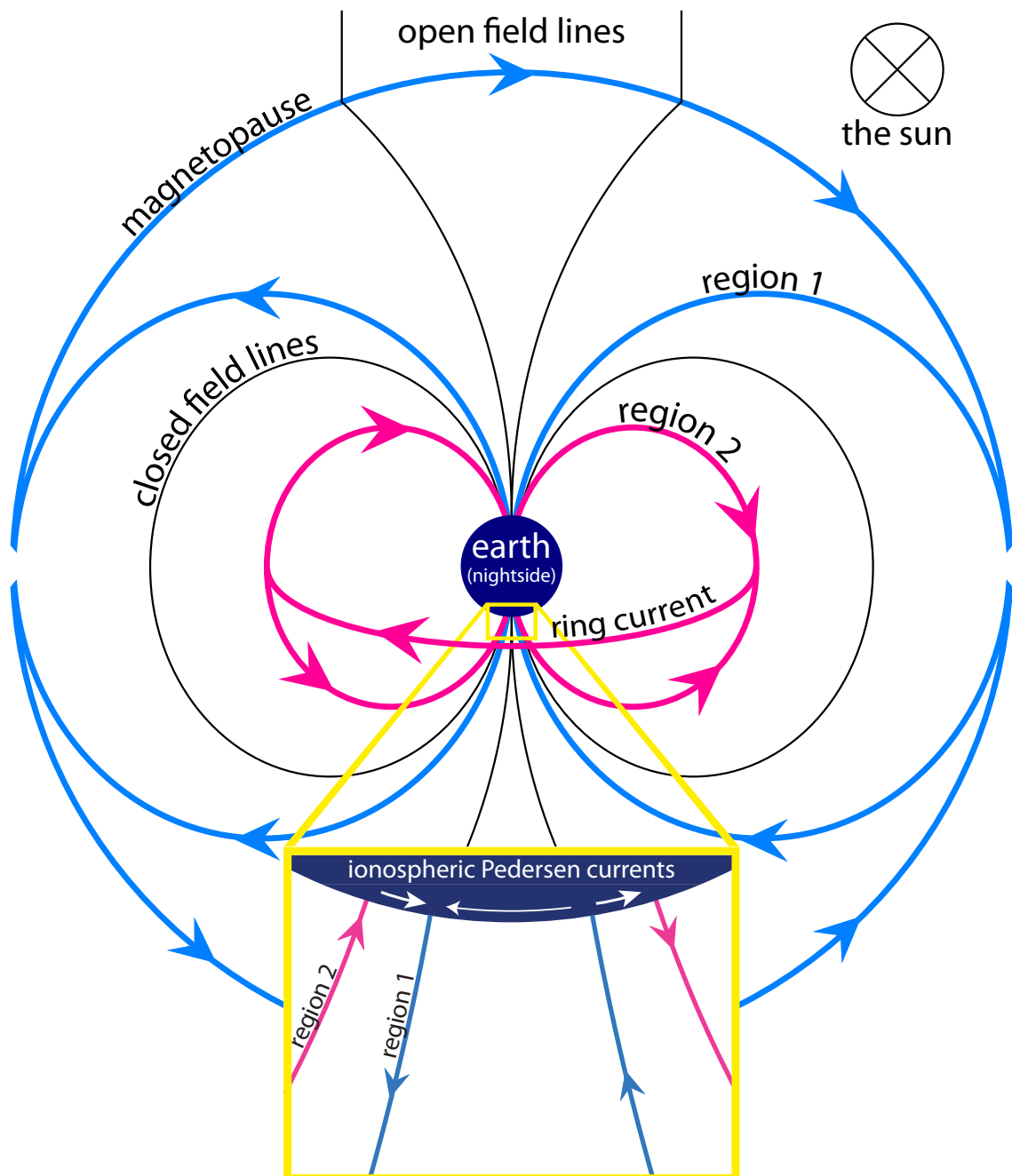


Figure 1.16: A diagram drawn looking towards the Sun. It shows the region 1, region 2, Pedersen, magnetopause (Chapman-Ferraro) and ring currents as well as illustrating the location of open and closed terrestrial magnetic field lines. The arrow showing Pedersen current flow across the polar cap is smaller than the arrows for the auroral zone to indicate the relative strength of the Pedersen currents (not to scale). It can be seen from this image how the region 1 current sheet corresponds to the open/closed field line boundary, or OCB.

closes through the magnetotail/magnetopause system, why this is so, and what (if anything) causes this ratio to change, are all open questions.

1.6.6 The substorm current wedge

The substorm current wedge (SCW) forms during the expansion phase of a substorm (see Section 2.2). Because it was not possible to determine whether or not it was confined to the ionosphere, it was originally known as the substorm electrojet. Work later showed that the substorm electrojet in the ionosphere is accompanied by field-aligned currents which electrodynamically link the substorm electrojet to reconnection events in the magnetotail (the evolution of theories on current systems during substorms is presented in Chapter 2). The ionospheric substorm electrojet has also been termed the DP-1 current system (Obayashi, 1967; Nishida, 1968; McPherron, 1995) and consists of a westward current which flows across the midnight sector on the nightside of Earth, coincident with an auroral bulge which occurs during a substorm.

During a substorm, there is a collapse of the magnetic field as a dipolarisation occurs, with magnetic reconnection occurring in the centre of the magnetotail; this change of magnetic configuration leads to a shear in the magnetic field between dipolarised field in the substorm-disturbed region and undipolarised field on the other side, leading to R1 current due to Ampère's Law. Therefore current flows from the magnetotail to the ionosphere; this current balances the disruption in the cross-tail current (described in Section 1.6.2) due to the dipolarisation process, which would otherwise lead to a build-up of charge on the dawn side of the dipolarisation (Baumjohann and Treumann, 1997).

Meanwhile, in the ionosphere, the high-conductivity auroral bulge is associated with equatorward, antisunward plasma motion, which creates a westward electric field. The high conductivity thus drives an intense westward Pedersen current and poleward Hall current; this Hall current is not closed at its poleward and equatorward edges, and thus an equatorward polarisation electric field develops which drives an equatorward Pedersen current (cancelling the initial Hall current) and a westward Hall current (Cowley, 2000); this is shown in Figure 1.17 (Egeland *et al.*, 1973). This enhanced conductivity, known as Cowling conductivity, leads to an intense westward electrojet being driven; some authors have noted that the question of why the Hall currents generated by this electric field are not closed through field-aligned currents at the poleward and equatorward edges has not yet been answered (Cowley, 2000).

Region 1 currents flow from the dawn side of the dipolarised magnetotail to the dawn side of the electrojet, and on the dusk side, from the electrojet to the magnetotail. The new westward electrojet is illustrated in Figure 1.18b.

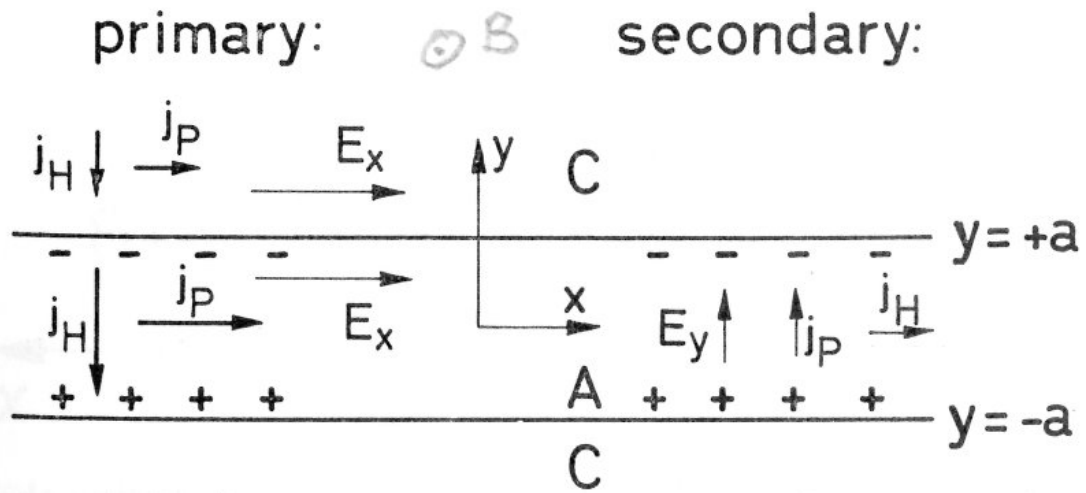


Figure 1.17: Diagram showing the primary (left-hand side) and secondary (right-hand side) currents which give rise to an enhanced westward electrojet, taken from Egeland *et al.* (1973).

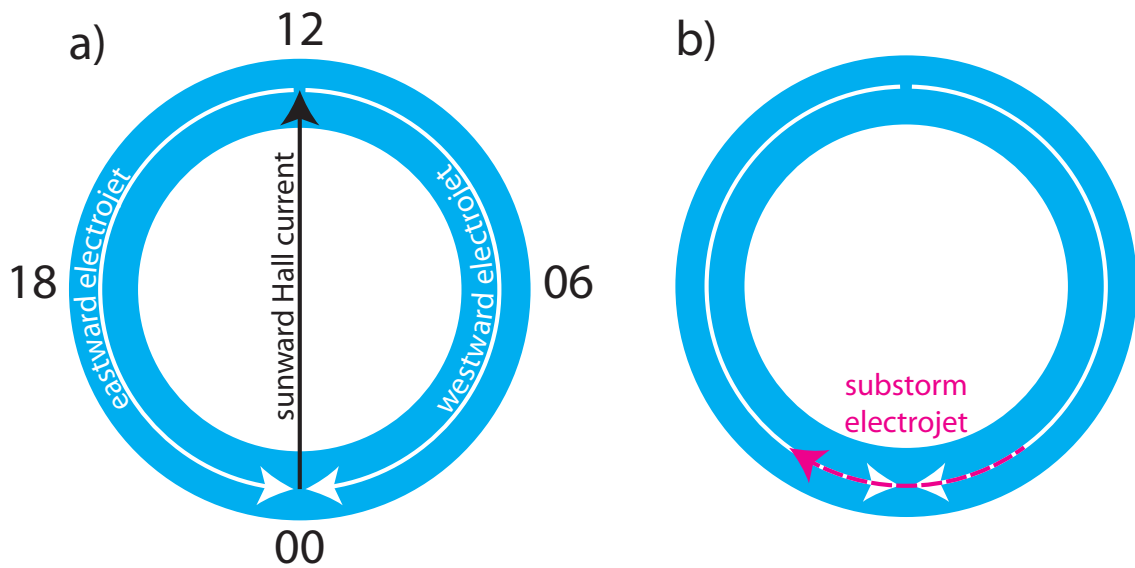


Figure 1.18: a) A schematic to illustrate the Hall currents in the ionosphere, comprised of the eastward and westward electrojets and a current across the polar cap. b) A schematic showing how the electrojets are altered by the substorm electrojet.

1.7 Co-ordinate systems and conventions

1.7.1 Birkeland currents

Birkeland currents are described such that currents flowing out of the ionosphere are positive currents and currents flowing into the ionosphere are negative currents. This convention is adopted widely in the literature, and is therefore also adopted in this thesis.

There are three values associated with any Birkeland current flow across some region of Earth:

Current density The current density is measured in $\mu\text{A m}^{-2}$ and is a measure of the current flowing per area. This is one of the variables given in the AMPERE dataset described in Section 3.1.

Current intensity The current intensity is measured in mA m^{-1} and is employed when the thickness of a current sheet is known but the longitudinal extent of the current sheet is not known; this situation often arises during single spacecraft passes across a region of flowing Birkeland current. This variable is not used in the data analysis in this thesis, but is used by other authors and therefore it appears in Chapter 2.

Current magnitude Current magnitude is measured in A and is the current density integrated across the relevant area, as described in Section 3.1; it is the primary measurement of Birkeland current employed during this thesis.

1.7.2 Geomagnetic co-ordinates

Geomagnetic (MAG) co-ordinates are defined with the z axis parallel to the magnetic dipole axis, as given by the International Geomagnetic Reference Field, or IGRF (Finlay *et al.*, 2010). The y -axis is defined perpendicular to the geographic poles, and the x -axis completes the right-handed set (Kivelson and Russell, 1995). Co-ordinates in this system are often given in magnetic colatitude and magnetic local time, where magnetic colatitude is the number of degrees south of the north magnetic pole, and magnetic local time is the time at that point on Earth (such that noon is in the direction of the sun).

1.7.3 AACGM co-ordinates

Altitude-Adjusted Corrected Geomagnetic (AACGM) co-ordinates are based on the MAG co-ordinates outlined in Section 1.7.2 and the work of Baker and Wing (1989), and are derived using the IGRF (Finlay *et al.*, 2010). These are the co-ordinates in which the AMPERE data described in Section 3.1 are made available. They are defined such that a magnetic field line has the same magnetic latitude and magnetic local time across its entire extent; the footprint in the northern hemisphere of such a field-line is defined so that the AACGM co-ordinate at an altitude of zero is the same as the geographic co-ordinate. Then, the latitude and longitude are kept constant along the field line as the altitude increases. The AMPERE dataset is described using AACGM co-ordinates at an altitude of 780 km.

1.7.4 GSM co-ordinates

Geocentric Solar Magnetospheric (GSM) co-ordinates are defined such that the x axis is a line connecting the centre of Earth with the centre of the Sun. Then, the y axis is defined to be perpendicular to the magnetic dipole, so that the x - z plane contains the magnetic dipole. The positive z -axis is selected such that it is positive in the same sense as the northern magnetic pole (Kivelson and Russell, 1995).

Chapter 2

Literature review

The first aspect of the literature to be reviewed is magnetospheric convection, and how it is affected by magnetic reconnection on the dayside and the nightside. This will result in a more detailed explanation of how the predictions made by the Dungey Cycle were tested and verified against observations, as well as discussing the expanding/contracting polar cap (ECPC) paradigm and various attempts to parameterise the dayside reconnection rate. Substorms will be discussed, and their role in the ECPC paradigm explored, in Section 2.2. After reviewing the literature on magnetospheric convection, the research that has been undertaken regarding the Birkeland currents will be reviewed in Section 2.3. Although they are the focus of this thesis, reviewing the literature on Birkeland currents last allows for the review to go into more detail on the reaction of the Birkeland currents to the Dungey Cycle and ECPC paradigm, to substorms, and to changes in the solar illumination.

2.1 Magnetospheric convection

2.1.1 The Dungey Cycle

It was suggested as early as 1896 that the aurora were caused by rays emitted by the Sun, impinging on the Earth's magnetic field (Birkeland, 1908) and this picture was expanded upon with the theory that the aurora might be caused by particles accelerated at points of neutral magnetic field forming an interface between the Earth's magnetic field and the IMF (Dungey, 1953). The discovery of the IMF by Pioneer V (Coleman *et al.*, 1960) led Dungey (1961) to suggest a mechanism by which particles could be accelerated on the dayside and the nightside of Earth by magnetic reconnection (see Section 1.5 and Figure 1.5). This model required an

approximately southward IMF, and the predicted equipotentials of electric field in the ionosphere as a result of the model was found to match the observed ionospheric current system. Both the voltage and flow across the polar cap have been examined with respect to southward IMF, which has been shown to drive a twin-cell convection pattern (Cauffman and Gurnett, 1972; Heppner, 1972, 1977; Volland, 1978; Cowley, 1982, 1984; Foster, 1983; Lockwood, 1991) whereas strong northward IMF drives a more complex pattern known as reverse-cell convection (Huang *et al.*, 2000; Imber *et al.*, 2006; Grocott *et al.*, 2012). The length of time it takes a field line to cross the polar cap can be combined with the solar wind speed to estimate the length of the longest open field lines in the magnetotail, which Dungey (1965) estimated were $10^3 R_E$ long, given a residence time of approximately 4 hours.

An alternative theory to the Dungey Cycle was suggested which proposed that the observed ionospheric convection could be explained via a viscous interaction between the solar wind and magnetosphere (Axford and Hines, 1961). Work has shown that this process might also play a role in the geomagnetic activity observed at Earth, although to a much lesser extent than the Dungey Cycle (Cowley, 1982), and observations of low but non-zero transpolar voltage at times of no dayside reconnection (Reiff *et al.*, 1981; Reiff and Burch, 1985) were attributed to this viscous interaction (Cowley and Lockwood, 1992). It has since been suggested that the observations of non-zero transpolar voltages may be a result of nightside reconnection (Milan, 2004), but recent papers shy away from eliminating the viscous process from consideration (Milan *et al.*, 2012).

2.1.2 The expanding/contracting polar cap paradigm (ECPC)

Early work conducted on the Dungey Cycle and solar wind-magnetosphere coupling did not focus on the temporal variability of magnetic reconnection beyond analyses of the transpolar flow. Indeed, the majority of models that looked at ionospheric convection considered it as a steady-state process (Lockwood and Cowley, 1992) with little consideration of imbalances between magnetic reconnection on the dayside and the nightside. Examinations of the cusp (Kamide *et al.*, 1976) and the auroral oval (Vorobjev *et al.*, 1976) showed that equatorward motions in both were linked to southward turnings of the IMF, and Holzer and Slavin (1978) suggested that magnetic reconnection could affect the size of the dayside and nightside magnetosphere. Siscoe and Huang (1985) noted that over long timescales, magnetic reconnection on the dayside and nightside would dominate at different times, suggesting that the polar cap changed size in reaction.

This work led to the proposal of the expanding/contracting polar cap paradigm (Cowley and Lockwood, 1992), also called the ECPC. In this model, it was demonstrated that a southward turning of the IMF would lead to the expansion of the polar cap as dayside reconnection added open magnetic field lines to the magnetosphere. They theorised that nightside reconnection would begin after some delay, and that this would stop the polar cap from further expansion and, as the dayside reconnection waned, lead the polar cap to contract; this process is illustrated in Figure 2.1. In this model, the difference between the dayside reconnection rate Φ_D and the nightside reconnection rate Φ_N (both measured in volts) gives the rate of expansion of the polar cap:

$$\frac{dF_{PC}}{dt} = \Phi_D - \Phi_N \quad (2.1)$$

This means that the rate of expansion of the polar cap after a southward turning in the IMF can be used to estimate the dayside reconnection rate assuming $\Phi_N = 0$ V (Milan *et al.*, 2012).

The nightside reconnection process was discussed by Cowley and Lockwood (1992) and Lockwood and Cowley (1992), who surmised that substorms were the primary mechanism which results in the closure of magnetic flux on the nightside of the planet. They noted that the observations which had resulted in the description of a three-phase substorm cycle would result from their model of the expanding/contracting polar cap. The substorm growth phase is coincident with the expansion of the polar cap driven by the dominating dayside reconnection, whereas the substorm expansion phase is coincident with the contraction of the polar cap driven by dominating nightside reconnection. These phases are explored in more detail in Section 2.2.

Evidence for the ECPC paradigm has been presented by a number of authors (Milan *et al.*, 2003, 2007, 2008). It is necessary to find ways of measuring either F_{PC} or dF_{PC}/dt in order to explore the ECPC paradigm by measuring the relative strengths of Φ_D and Φ_N (Equation 2.1). In order to do this effectively, proxies for the size of the polar cap are used in order to quantify dF_{PC}/dt ; this means that measurements can be made with continuous temporal coverage and good spatial coverage. The dim area inside the auroral oval has been used as a proxy for the open flux content of the magnetosphere, alongside demarcations between high and low fluxes of high-energy particles (Milan *et al.*, 2003). Since the global ionospheric convection patterns become larger when the polar cap larger, another proxy utilised is the Heppner-Maynard boundary, which represents the equatorward boundary of ionospheric convection (Imber *et al.*, 2013a). Early observations of the Birkeland currents showed they moved equatorward with enhanced geomagnetic activity (Zmuda *et al.*, 1970; Iijima and Potemra, 1978), and although Green *et al.* (2009) suggested

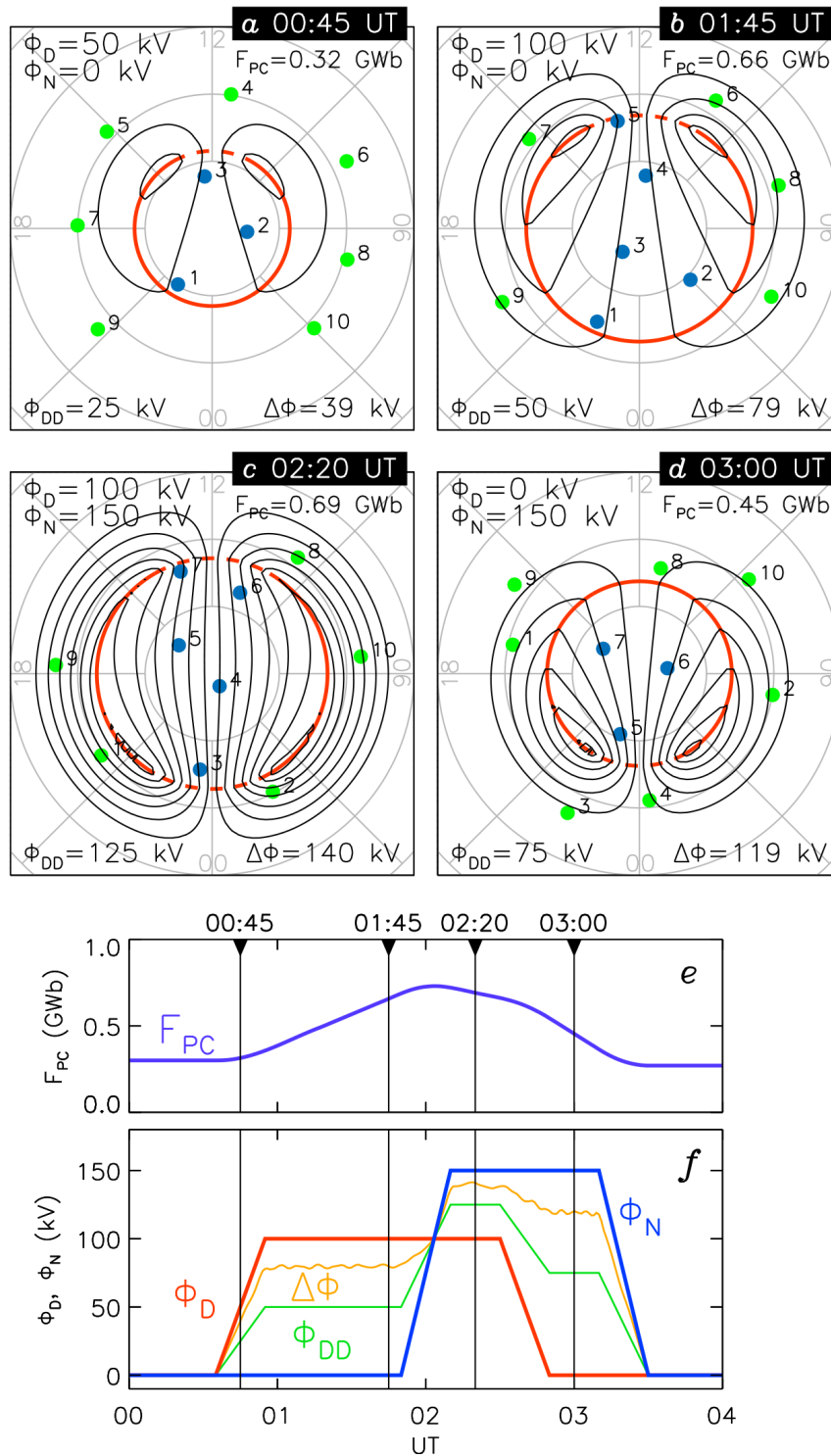


Figure 2.1: A model interval of dayside and nightside reconnection and the effect it has on the ionosphere. Panels a-d consist of a red circle to illustrate the open/closed field line boundary (OCB) and black lines to illustrate the electrostatic potential pattern (in contours of 10 kV). The dashed red line is where reconnection is active; the black lines are equivalent to plasma streamlines; and the blue/green dots are the footprints of open/closed magnetic field lines respectively. The intervals depicted by these panels are given in panels e and f. Panel e is a plot of the size of the polar cap, and panel f is a plot which shows the dayside and nightside reconnection rates (Φ_D and Φ_N in red and blue respectively). Panel f also depicts the dawn-dusk cross-polar cap potential Φ_{DD} and the difference between maximum and minimum in the convection pattern $\Delta\Phi$. It can be seen in this diagram that reconnection drives convection in the ionosphere and that the polar cap expands when $\Phi_D > \Phi_N$ and contracts when $\Phi_D < \Phi_N$. Adapted from Milan *et al.* (2012).

that the R1 current oval may not be colocated with the OCB in the winter hemisphere, recent results from Clausen *et al.* (2012, 2013b) have shown that the R1 current oval can also be used as a proxy for the location of the region of open flux.

2.1.3 Quantifying the magnetic reconnection rate

It was realised that magnetic reconnection would occur at the low-latitude magnetopause during periods of southward IMF (Dungey, 1961), resulting in the presence of a transpolar voltage and also transpolar flows as a result of reconnection-driven convection (Cowley, 1984). Prior to the ECPC paradigm and the realisation that transpolar voltage was not equivalent to the dayside reconnection voltage (Cowley and Lockwood, 1992; Milan, 2004; Milan *et al.*, 2009b), authors looked at the speed of ionospheric convection with the IMF (Heppner, 1972) as well as attempting to quantify the transpolar voltage in terms of solar wind parameters (Gonzalez and Mozer, 1974; Reiff *et al.*, 1981; Doyle and Burke, 1983; Wygant *et al.*, 1983; Cowley, 1984) and also used merging at the magnetopause to estimate the flux transfer rate (Holzer *et al.*, 1986). Other authors have approached this problem in the context of energy coupling rather than magnetic reconnection by using comparisons with geomagnetic indices (Burton *et al.*, 1975; Perreault and Akasofu, 1978; Kan and Lee, 1979; Vasyliunas *et al.*, 1982; Scurry and Russell, 1991; Newell *et al.*, 2007; Borovsky and Birn, 2014). The size of the polar cap has also been employed, with authors using both the value itself (Newell *et al.*, 2007) and the time derivative (Milan *et al.*, 2012).

These parameterisations are also called coupling functions, and have employed combinations of contributions from the IMF strength in the GSM y and z directions B_Y and B_Z ; the velocity of the solar wind V_{sw} ; and the density of the solar wind N_{sw} (amongst others). The transverse component of the IMF B_{\perp} is given by

$$B_{\perp}^2 = B_Y^2 + B_Z^2. \quad (2.2)$$

and the electric field transverse to the solar wind flow is given by $V_{sw}B_{\perp}$, which has been used in reconnection functions for some time (Cowley, 1984), with the angle between the y and z components θ realised to play a role in the efficiency of reconnection (Petschek, 1966; Sonnerup, 1974). The reconnection electric field becomes the reconnection voltage when multiplied by some effective length scale L_{eff} ; this length can be thought of as the width of the magnetic flux which impinges on and reconnects at the magnetopause (Milan *et al.*, 2012). Early considerations also included the Mach number and density in the calculation of reconnection (Va-

syliunas *et al.*, 1982), but papers found that this had little effect on reconnection rate (Scurry and Russell, 1991), and recent papers have not found a dependence of dayside reconnection rate on solar wind density (Newell *et al.*, 2007; Milan *et al.*, 2012).

Turning now to magnetic reconnection on the nightside of Earth, it has been found that the rate of the contraction of the polar cap caused by nightside reconnection in the magnetotail is approximately proportional to the flow of the westward electrojet (Holzer *et al.*, 1986), which is unsurprising in the context of a westward electrojet driven by substorms as described in Section 1.6.6. Since the AL index is a measure of the maximum intensity of the westward electrojet, this means that the AL index can be used as a proxy for the nightside reconnection rate. More recently, work has been done to estimate the nightside reconnection by using estimates of dayside reconnection rate (Holzer *et al.*, 1986; Milan *et al.*, 2007) to forecast the expected expansion of the polar cap, and then assuming that nightside reconnection is responsible for any disparity between forecast and observation. Using this method, it was demonstrated that nightside reconnection operates in bursts at an average rate of ~ 85 kV (Milan *et al.*, 2007). This demonstrated that magnetic reconnection on the nightside is a bursty process, with no evidence for low-level nightside reconnection between substorm events, supporting the picture of the substorm as the primary mechanism for nightside reconnection in the ECPC paradigm (Cowley and Lockwood, 1992).

During periods when nightside reconnection is not occurring, the time derivative of the open flux in the polar cap will be equal to the dayside magnetic reconnection rate (Cowley and Lockwood, 1992). Milan *et al.* (2012) calculated the open flux in the magnetosphere by analysing IMAGE pictures of the auroral oval, and then used this to obtain the time derivative of the open flux. They included contributions from B_Y , B_Z , V_{sw} , N_{sw} and iterated towards the best fit to the data; using this method they found that the solar wind density did not contribute significantly to the dayside magnetic reconnection rate, and arrived at the formula:

$$\Phi_D = L_{\text{eff}}(V_{sw})V_{sw}B_{\perp} \sin^{\frac{9}{2}}\left(\frac{\theta}{2}\right) \quad (2.3)$$

In the above equation $L_{\text{eff}}(V_{sw})$ is an effective length scale, given by

$$L_{\text{eff}}(V_{sw}) = 3.8R_E \left(\frac{V_{sw}}{4 \times 10^5 \text{ m s}^{-1}}\right)^{\frac{1}{3}}. \quad (2.4)$$

V_{sw} is the solar wind speed, θ is the clock angle between the IMF vector projected into the GSM Y - Z plane and Z axis and R_E is the radius of Earth. The data used

by Milan *et al.* (2012) was OMNI data shifted to the bow shock; no additional shift to the magnetopause was performed.

More recently, it has been suggested by Borovsky and Birn (2014) that the magnetic reconnection rate should not depend on the solar wind electric field, because they expect local reconnection rate to be governed by local plasma parameters near the reconnection site. They concluded that modifying existing estimates by replacing $v_{sw}B_{\perp}$ with $v_{sw}|B|$ would yield an increase in accuracy of these functions. They compare several existing coupling functions (Kan and Lee, 1979; Wygant *et al.*, 1983; Newell *et al.*, 2007) with eight different geomagnetic indices (including AE , AU , AL , Kp and Dst) both with and without the proposed modification, finding a higher correlation coefficient in the changed functions. However, when the modification is applied and then tested against the time derivative of the open flux in the polar cap, the correlation decreases (Milan, 2014, private communication), suggesting that although Borovsky and Birn (2014)'s function may measure coupling in some sense it does not give the instantaneous dayside reconnection rate.

This section demonstrates that there are a number of different parameterisations of Φ_D . Throughout the rest of this thesis, the estimate of Milan *et al.* (2012), from Equations 2.3 and 2.4, is employed. This function is chosen because it has achieved the best fit of any of the available options to the time derivative of open flux in the polar cap.

2.2 Substorms

Substorms have been theorised to be nightside reconnection events which occur in the magnetotail (Russell and McPherron, 1973a; Baker *et al.*, 1996). Consequently, a review of substorm observations and theory is necessary in order to explain how substorms relate to the ECPC paradigm described above.

Substorms were observed in polar magnetic perturbations by Birkeland (1908), who referred to them as polar elementary storms; later it was noted that these storms occurred within geomagnetic storms by Akasofu and Chapman (1961) who referred to them as DP substorms, although they have also been called magnetospheric substorms. Substorms could wax and wane multiple times within a single geomagnetic storm, hence the name. It was also found that auroral substorms, sometimes called auroral displays in the early days (Elvey, 1957), occurred which were coincident with these magnetic substorms (Akasofu, 1964). Initial reports of substorms described them as having two phases, called the 'expansion phase' and the 'recovery phase' (Akasofu, 1964). Later work established the concept of the 'growth phase', a third

phase theorised to occur prior to the expansion phase (McPherron, 1970). The term ‘quiet phase’ has been used to refer to periods of time between substorms (Akasofu, 1964).

Early descriptions of substorms were given in terms of the auroral activity which occurs during a substorm, and the early observations of substorms recorded by Akasofu (1964) are shown in Figure 2.2. The auroral substorm consists mostly of the expansion phase and recovery phase; an auroral substorm lasts between one and three hours, with the expansion phase lasting up to 30 minutes. During an auroral substorm, the equatormost quiet arc around midnight suddenly brightens and expands polewards (hence the term expansion phase), with the arc becoming disrupted and forming rays, folds and other structure. The auroral breakup is the point at which the equatormost arc is the brightest (Akasofu, 1964), just prior to the disruption of the arc, and is associated with a large negative bay in AL index. Smaller brightenings of higher-latitude arcs are known as pseudo-breakups and are associated with smaller bays prior to the main bay (Elvey, 1957). The aurora rapidly moves towards the pole, with the speed related to the intensity of the substorm. The aurora eventually reaches the polemost point, and structures within the aurora move rapidly westward in a phenomenon called the westward travelling surge, associated with the substorm electrojet in the ionosphere (Akasofu *et al.*, 1966; Rostoker *et al.*, 1970, 1980). After this, the substorm enters the recovery phase, in which the activity dies down and the ionosphere returns to its pre-substorm state. At this point the recovery of the negative bays in the magnetometers is observed (Baker *et al.*, 1996).

The magnetospheric substorm starts with the growth phase (McPherron, 1970) in which dayside reconnection (Baker *et al.*, 1996) leads to the erosion of the dayside magnetosphere and the addition of magnetic flux to the magnetotail, as energy is stored in the lobes of the tail. The growth phase is also marked by the formation of a partial ring current on the nightside of Earth (Cummings and Coleman, 1968; Cummings *et al.*, 1968) and the ionospheric footprint of the cusp field lines moving equatorward (McPherron, 1972; McPherron *et al.*, 1973). The substorm growth phase can therefore be seen as the expanding polar cap in the ECPC paradigm, with magnetic flux being interconnected at the dayside of the planet and the entire polar cap moving equatorward, including the cusp (McPherron *et al.*, 1973; Cowley and Lockwood, 1992).

The onset of nightside reconnection marks the start of the substorm expansion phase, leading up to open magnetic flux being closed in the magnetotail. The substorm expansion phase can therefore be seen as the contracting polar cap in the ECPC paradigm, with magnetic flux being reconnected at the nightside of the planet and therefore closed, with the polar cap boundary moving poleward. This agrees

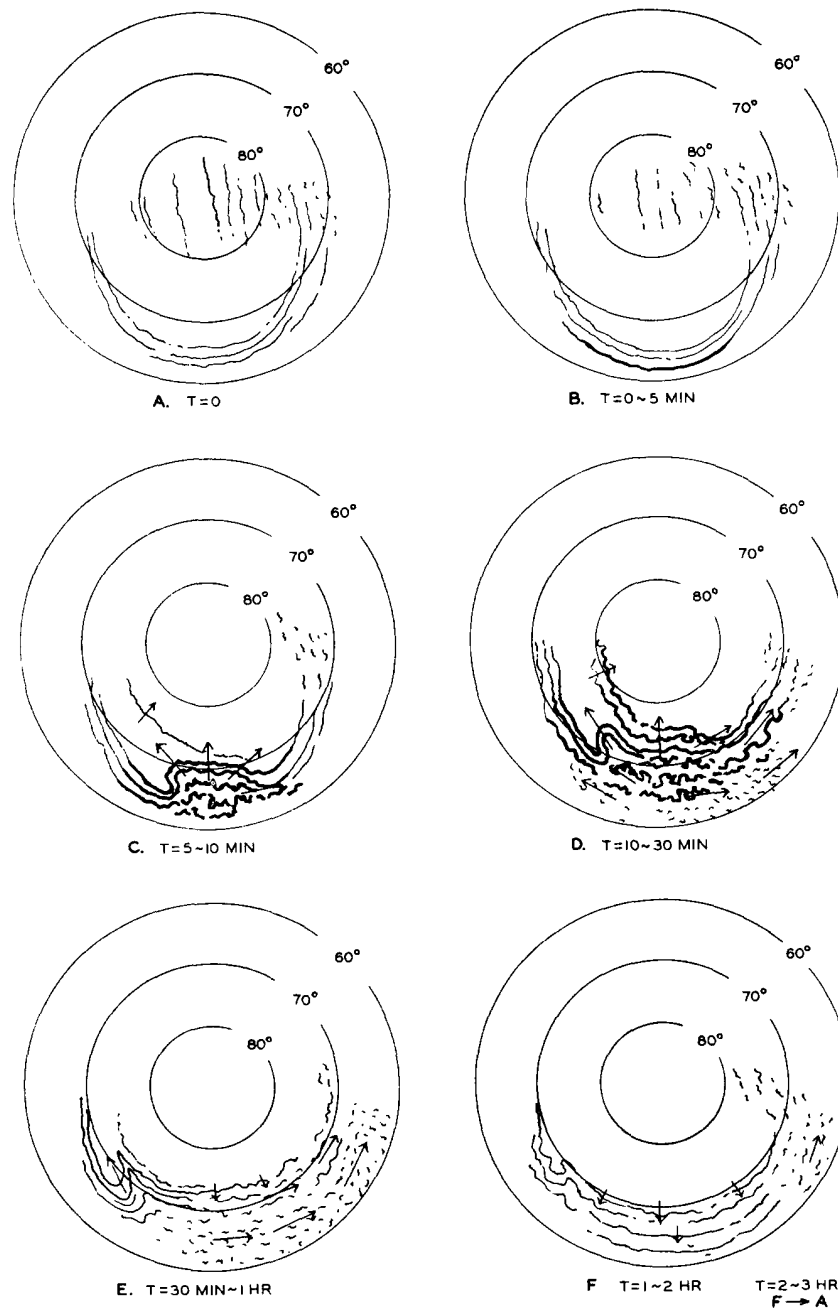


Figure 2.2: The original diagram of the auroral forms observed during a substorm, taken from Akasofu (1964).

with observations in which the aurora moves poleward during an auroral substorm, since the auroral oval can be used as a proxy for the polar cap (Milan *et al.*, 2003). If there is no dayside reconnection occurring, the end of the auroral substorm is the point at which the aurora reaches its polemost point (Akasofu, 1964), which marks the end of nightside reconnection; if reconnection is happening on the dayside, the polemost point will be the point at which $\Phi_N < \Phi_D$.

The method by which open magnetic flux is reconnected during a substorm has been theorised to be the formation of a near-Earth neutral line, or NENL (Russell and McPherron, 1973a; Baker *et al.*, 1996), which is illustrated in Figure 2.3. There is a point in the magnetotail at a distance of at least $20 R_E$ at which reconnection can occur (Baker *et al.*, 1996), which leads to a dipolarisation of the magnetic field at $6\text{--}10 R_E$ (McPherron *et al.*, 1973). This leads to substantial amounts of plasma downtail of the reconnection site being ejected downstream; these are called plasmoids and have previously been observed (Baker *et al.*, 1987; Slavin *et al.*, 1992). These plasmoids are bulges in the tail plasma sheet which move rapidly downstream from the planet; they can be detected either by spacecraft in the plasma sheet at the time of the ejection (Hones *et al.*, 1984; Scholer *et al.*, 1984) or by observing signatures in the lobes known as travelling compression regions, shown in Figure 2.4 (Slavin *et al.*, 1984).

It is known that the auroral zone contains an eastward electrojet and a westward electrojet in the dusk and dawn sectors respectively (this is part of the Hall current system). Observations of the currents during substorms led to the conclusion that the current system simultaneous with a substorm could not be solely ionospheric but probably included a component which flowed along magnetic field lines, inward in the dawn sector and outward in the dusk sector (Akasofu and Meng, 1969; Meng and Akasofu, 1969; Kamide and Akasofu, 1976). This current system was closed in the ionosphere by the extension of the westward electrojet, a phenomenon called the westward travelling surge associated with upward flowing current caused by electron precipitation (Rothwell *et al.*, 1984). The westward electrojet extends such that it impinges on the eastward electrojet, sketched schematically in Figure 1.18 and discussed in more detail later.

The upward and downward currents flowing on each side of the substorm electrojet are thought to be the result of a disruption in the cross-tail current sheet drawn in Figure 2.5 (Clauer and McPherron, 1974; Yang *et al.*, 2012); this system has become known as the substorm current wedge (SCW). The current sheet disruption is associated with a dipolarisation of the field lines in the tail at a radius of $6\text{--}10 R_E$ (McPherron *et al.*, 1973; Forsyth *et al.*, 2014). Barfield *et al.* (1986) concluded that the disruption, the intensification of the Birkeland currents, and the

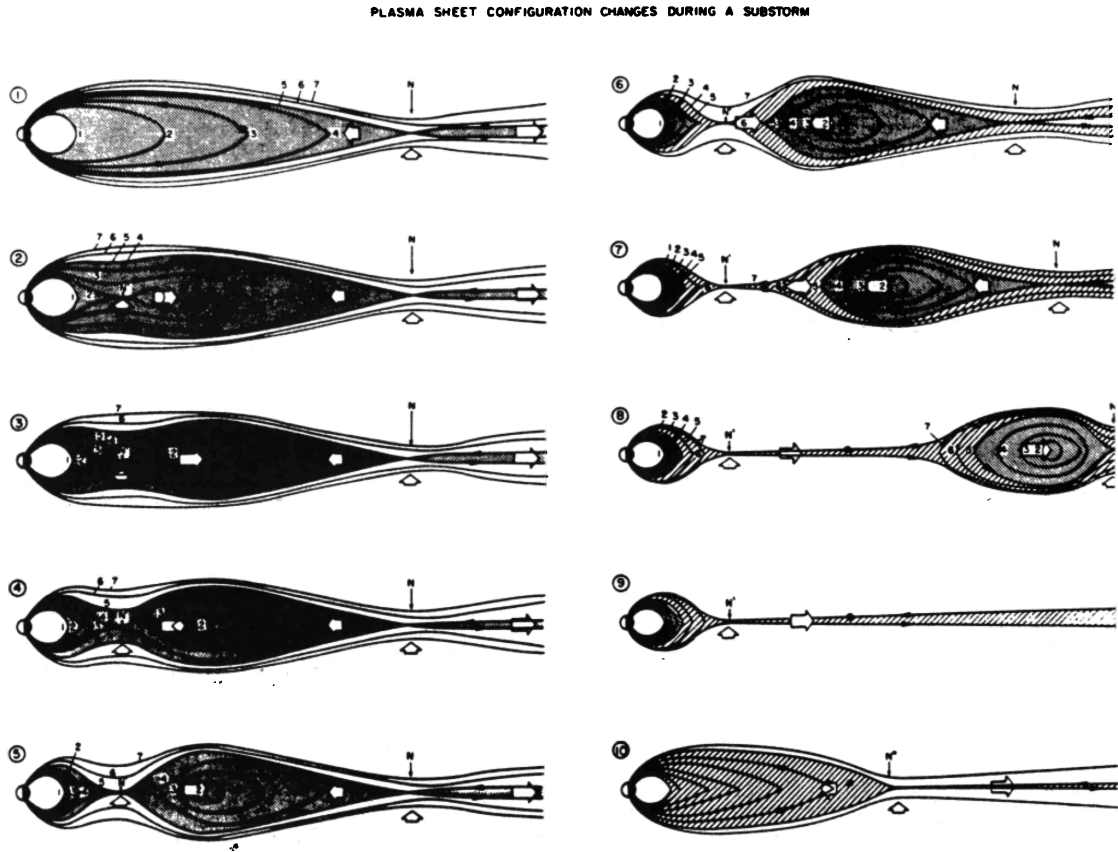


Figure 2.3: Schematic diagrams of the time evolution of a substorm in the magnetotail, including the formation of a plasmoid. From Baker *et al.* (1996).

observed electrojet were initiated at the onset of the substorm expansion phase; Dynamics Explorer data also show a wedge-shaped system (Hoffman *et al.*, 1994). It has been shown that the simple model of one upward and one downward field-aligned current, combined with a cross-tail disruption and a substorm electrojet, accurately replicates ground magnetometer data (Bonnevier *et al.*, 1970; Horning *et al.*, 1974; Cramoysan *et al.*, 1995).

A superposed epoch analysis of the Birkeland current densities through a substorm shows that they increase through the epoch and peak at approximately the point of expansion phase onset (Clausen *et al.*, 2013b). Work has also suggested that the open flux content of the magnetosphere is linked to the intensity of a substorm; authors have concluded that more energy is released by substorms that occur during times of high open flux (Akasofu, 1975, 2013; Kamide *et al.*, 1999) and it has been observed that the polar cap contracts by a larger amount in a substorm at these times, indicating that more open flux is closed by these substorms (Milan *et al.*, 2009a; Clausen *et al.*, 2013b).

Initial theories treated the SCW as a wedge of one upward and one downward

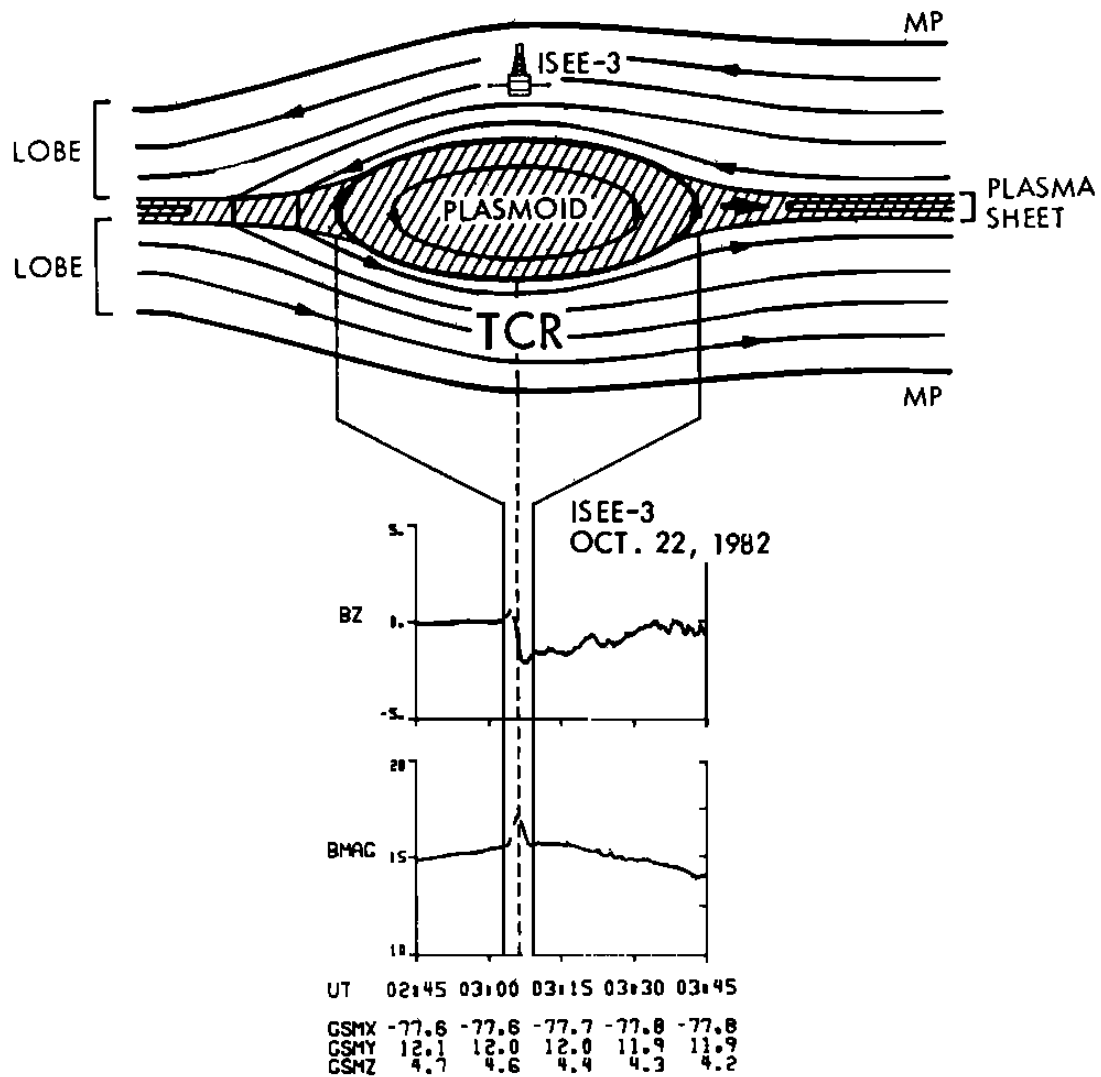


Figure 2.4: A schematic diagram of a plasmoid moving through the magnetotail compared to ISEE-3 measurements of a Travelling Compression Region (TCR). From Slavin *et al.* (1984).

current, and thus only observed in the Region 1 Birkeland currents. Recently, however, observations have suggested that this is an oversimplification. It has been suggested that the SCW is seen both in Region 1 and Region 2 Birkeland currents (Clausen *et al.*, 2013b; Murphy *et al.*, 2013), in what some authors have termed a two-loop or two-wedge model drawn in Figure 2.6 (Sergeev *et al.*, 2011, 2014). Furthermore, auroral structure seen during substorms is complex (Elvey, 1957; Akasofu, 1964; Sandahl *et al.*, 2011), and complex auroral structure has been linked to small-scale field-aligned current flow (Lanchester *et al.*, 2001; Otto *et al.*, 2003), indicating that the SCW may also contain many small-scale field-aligned currents, something that has been confirmed by observation (Forsyth *et al.*, 2014). As a result, it can be inferred that the SCW is the large-scale average of a more complex system.

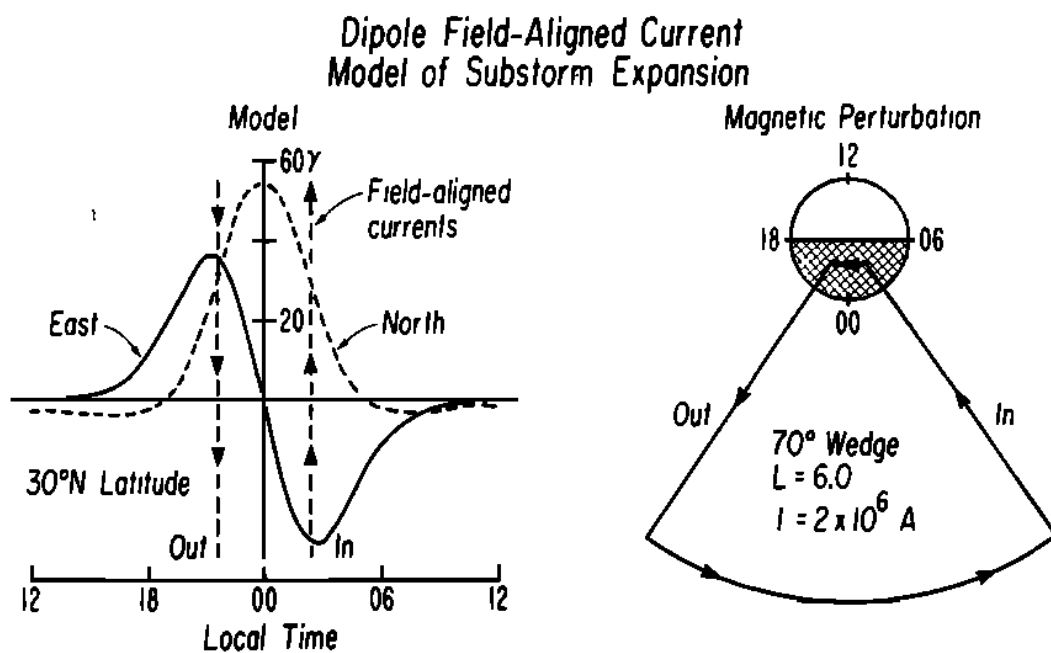
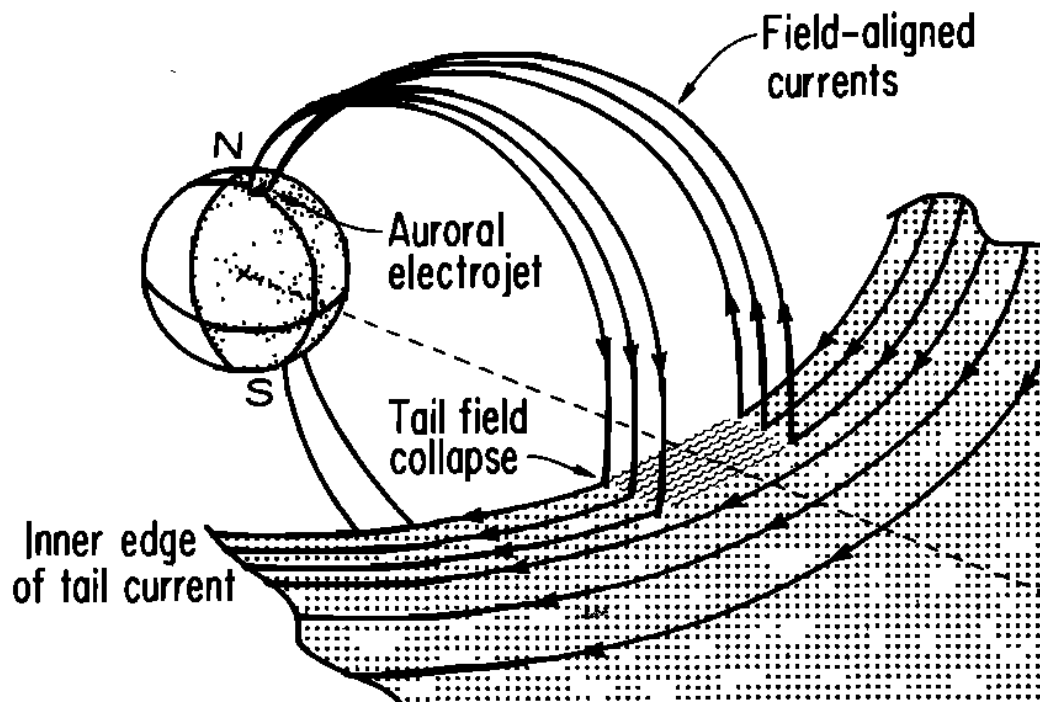


Figure 2.5: A diagram to illustrate the classic substorm current wedge, which flows through the R1 current system as a result of a disruption of the cross-tail current sheet. The top and bottom-right illustrations show this schematically from different perspectives, whilst the bottom-left illustration shows the magnetic perturbation measured as a result of this system at different MLTs. Adapted from McPherron *et al.* (1973); Clauer and McPherron (1974).

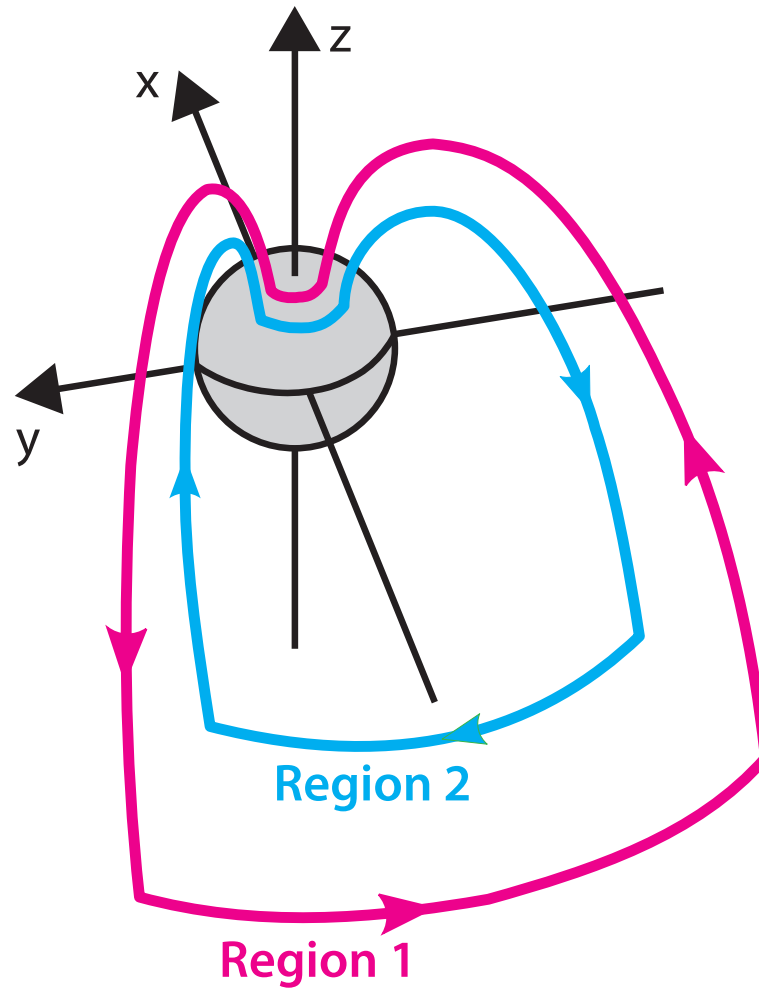


Figure 2.6: A schematic diagram to illustrate the ‘two-loop’ substorm current wedge, which flows through both the R1 and R2 current systems. Adapted from Sergeev *et al.* (2014).

2.3 Birkeland currents

The primary focus of this thesis, Birkeland currents are the currents which flow along the magnetic field lines in Earth’s magnetosphere, and were originally proposed by Birkeland (1908, 1913). The first evidence for field-aligned currents was detected by Zmuda *et al.* (1966), and the structure of the currents was inferred by Iijima and Potemra (1976a) from single spacecraft measurements. This was done by using Ampère’s Law to obtain the current density based on magnetic perturbations measured by the Triad spacecraft, and taking many orbits to draw conclusions about the large-scale structure of the currents based on averaged measurements over a period of over a year. This section explores the research that has been done on Birkeland currents, both in terms of their structure and in terms of their reaction to reconnection and the evolution of the currents during substorms.

2.3.1 First measurements of Birkeland currents

Field-aligned currents were first suggested by Birkeland (1908, 1913) and were theorised to flow within the auroral arcs by Boström (1964, 1966). It is known that the magnetic field perturbations as a result of Pedersen currents and from Birkeland currents flowing in the ionosphere cancel each other out on the Earth's surface in the case of vertical field-aligned currents (Fukushima, 1969, 1976), and so the Birkeland currents were first detected using spacecraft data. Zmuda *et al.* (1966) observed magnetic perturbations at an altitude of 1100 km in data from Satellite 1963 38C, which were interpreted by Cummings and Dessler (1967) as field-aligned currents. These observations were followed by the discovery that the currents moved equatorward with geomagnetic activity (Zmuda *et al.*, 1970), and Zmuda *et al.* (1974) suggested that the motion of the Birkeland currents, and the motion of the associated magnetic perturbations, induced electric fields parallel to the main geomagnetic field.

Armstrong and Zmuda (1970) found that the currents were comprised of two current sheets, and after Armstrong and Zmuda (1973) discussed early measurements of the currents using data from the Triad satellite, observations of flows of the currents at different magnetic local times were made (Zmuda and Armstrong, 1974a,b). It was noted that the polemost boundary of the flowing currents was coincident with the polemost auroral boundary and that the eastward electrojet flowed in a region bounded by Birkeland currents (Armstrong *et al.*, 1975). The first picture of the large-scale current patterns, plotted in Figure 2.7, was inferred from Triad data averaged over a long period by Iijima and Potemra (1976a, 1978), who discovered that there were two current ovals. These ovals were each comprised of current which flowed in opposite directions on either side of the noon-midnight meridian. The poleward oval was termed the Region 1 Birkeland current (R1), whereas the equatorward oval was termed Region 2 (R2); R1 was said to map to the magnetopause, whereas R2 mapped to the partial ring current; this mapping has been broadly verified more recently by Tsyganenko and Stern (1996), who pointed out that R1 currents near midnight map to the magnetotail. Measurements of the Birkeland currents have suggested that the magnitude of R1 current $J_1 \sim 1.6$ MA and the magnitude of the R2 current $J_2 \sim 1.1$ MA at quiescent times, whereas R1 ~ 2.7 MA and R2 ~ 2.5 MA during active periods (Iijima and Potemra, 1978; Cowley, 2000).

The R0 current system was said to be poleward of R1 in the noon sector (Iijima and Potemra, 1976b) and flowed in the opposite direction, although some authors have said that it is just an extension of the R1 oval from the other side of the

noon-midnight meridian (Iijima and Potemra, 1978; McDiarmid *et al.*, 1979; de la Beaujardiere *et al.*, 1993). Another Birkeland current system called the NBZ system has been shown to exist during northward IMF which is found on the dayside of Earth, poleward of R1; these currents flow in the opposite direction to R1 in the dawn and dusk flanks (Araki *et al.*, 1984; Iijima *et al.*, 1984; Zanetti *et al.*, 1984; Stauning, 2002) and are associated with the ionospheric convection pattern observed during northward IMF (Huang *et al.*, 2000; Imber *et al.*, 2006; Grocott *et al.*, 2012). Ohtani *et al.* (1995) presented evidence for a fourth current system poleward of the R0 currents which had the same polarity as R1 on the dawn and dusk flanks and was found in the pre-noon sector; this was attributed to reversals of convection due to the interaction of different convection patterns during strongly negative B_Y .

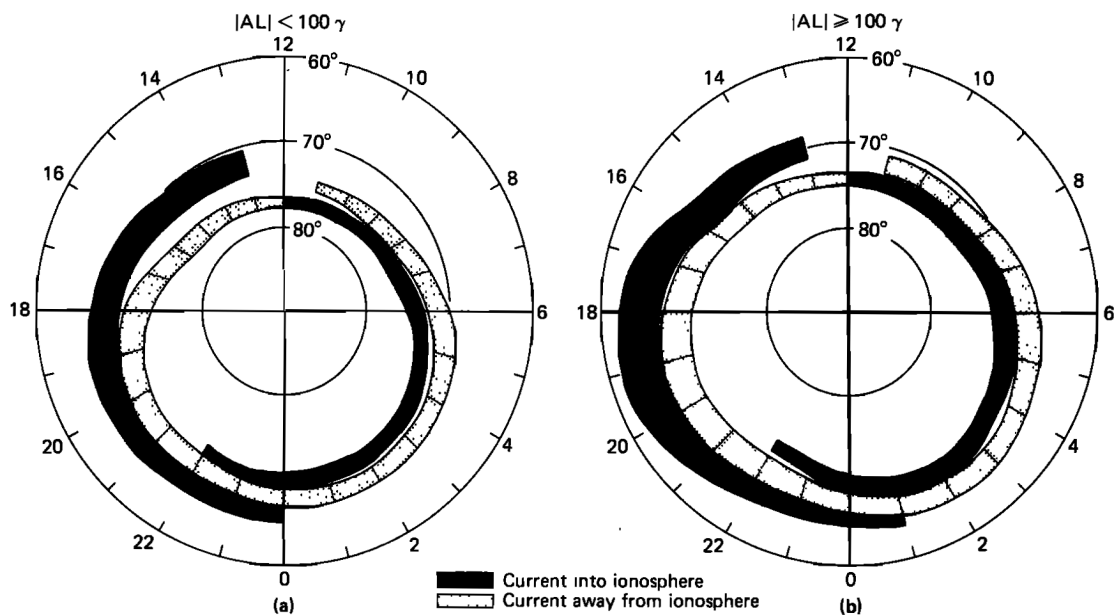


Figure 2.7: A diagram which illustrates the early large-scale observations made using the Triad satellite of the large-scale Birkeland current systems under quiet conditions (left) and active conditions (right). The R1 currents are on the poleward edge and the R2 currents are on the equatorward edge. Adapted from Iijima and Potemra (1978).

2.3.2 The reaction of Birkeland currents to the solar wind

As discussed in Section 2.1.2, the R1 currents flow coincident with the OCB (Clausen *et al.*, 2013b), so that the location of the current oval can be used as a proxy for the size of the polar cap. It has been established in Section 2.1.2 that the polar cap expands and contracts with magnetic reconnection on the dayside and nightside respectively (Cowley and Lockwood, 1992), and this is seen in the movement of the current ovals with changes in the solar wind conditions (Clausen *et al.*, 2012).

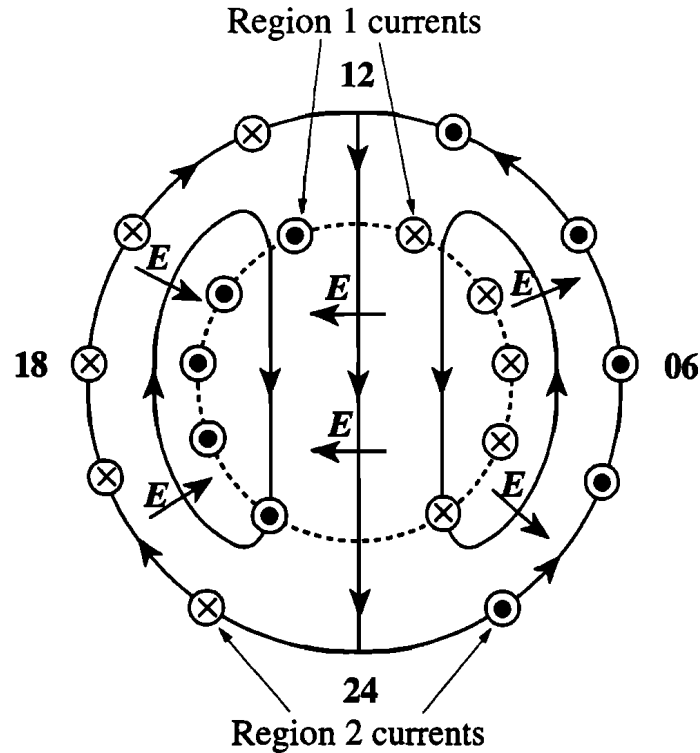


Figure 2.8: Ionospheric convection as a result of the Dungey Cycle where the solid arrows are plasma streamlines and the dashed line is the OCB. It can be found that the electric field \mathbf{E} is as illustrated by considering Equation 1.19 with the given convection and a magnetic field coming out of the page. The Hall current flows opposite to the particle motion, and the Pedersen current flows in the direction of \mathbf{E} . The result is the need for a source of current within the dawn convection cell and a sink of current at dusk, which is provided by the Region 1 Birkeland currents coming into and out of the page (shown by the crossed and dotted circles respectively). There is also a sink and source required equatorward of the cells on the dawn and dusk sides respectively, which is provided by the Region 2 currents. Adapted from Cowley (2000).

As has been noted, reconnection on the dayside and the nightside drives twin-cell ionospheric convection (Cowley and Lockwood, 1992; Milan, 2004). The vorticity in the ionosphere as a result of this pattern is associated with field-aligned current flow, as shown in Figure 2.8 (Cowley, 2000), and has been used by many authors as a method of using ground-based observations to study the field-aligned currents with SABRE (Freeman *et al.*, 1990) and SuperDARN (Sofko *et al.*, 1995; McWilliams *et al.*, 2001; Chisham *et al.*, 2009), although it has been found that satellite observations disagree with SuperDARN estimates of the currents where the SuperDARN returns are poor (Green *et al.*, 2006). Further to the realisation that a combination of ionospheric flow vorticity and ionospheric conductivity gradients can be used to infer the current flows, Milan (2013) modelled the Birkeland currents flowing by extending models of the convection driven by the ECPC paradigm (Freeman and Southwood, 1988). Milan (2013) specifies the magnetic reconnection rates Φ_D and Φ_N and then calculates the model current flows (given assumed Hall and Pedersen

conductances). In this model, the currents are found to depend on the transpolar voltage (the average of the dayside and nightside reconnection voltages), with currents on the dayside being stronger when dayside reconnection dominates and the same being true for the nightside.

The dependence of currents on ionospheric convection indicates that southward IMF should drive larger currents, and this has been found experimentally by taking sparse datasets and averaging them over long timescales. It was found that southward turnings of the IMF drive strengthened field-aligned currents in addition to strengthened electrojets within a few minutes (Rostoker *et al.*, 1982). Investigations were performed using methods relying on ground-based magnetograms (Kern, 1966; Kamide *et al.*, 1981) which found that the extent and the intensity of the Birkeland currents decreased as B_Z became positive (Friis-Christensen *et al.*, 1985; Feldstein and Levitin, 1986). Since Fukushima (1969, 1976) showed that, if the Birkeland currents are vertical, they cannot be discerned from ground-based data, these studies look at the horizontal component of the Birkeland currents flowing.

Models have been constructed using Dynamics Explorer 2 data over two years (Weimer, 2001) and with data from Magsat (six months) and Ørsted (two years) (Papitashvili, 2002) which show that the currents are stronger during southward IMF and during the summer; it was also shown that asymmetries in the current patterns arise as a result of B_Y . Juusola *et al.* (2009) used five years of CHAMP data to show that field-aligned currents increase in intensity with more southward IMF, solar wind dynamic pressure and the merging electric field, whilst He *et al.* (2012) integrated ten years of data from the CHAMP satellite into a model of field-aligned currents that used empirical orthogonal functions (MFACE) to show that B_Z drives the R1 and R2 pattern associated with twin-cell convection, B_Y drives modifications to the pattern around noon and midnight, and the timescale of the reaction of the currents to solar wind driving is 20 minutes (He *et al.*, 2012).

CHAMP data have also been used alongside SuperDARN data to construct average maps of the Birkeland currents and the ionospheric convection for different IMF configurations (Juusola *et al.*, 2014). It was reported that the current pattern showed the traditional R1 and R2 picture for southward IMF associated with twin-cell convection, whereas during northward IMF the current system shows the NBZ and R1 currents associated with reverse-cell convection (Iijima *et al.*, 1984; Imber *et al.*, 2006; Grocott *et al.*, 2012). Alongside the IMF orientation driving of the current patterns, the amplitude of the IMF was found to drive the magnitudes of the currents flowing.

Zheng *et al.* (2006) found that an increase in polar cap potential resulted in

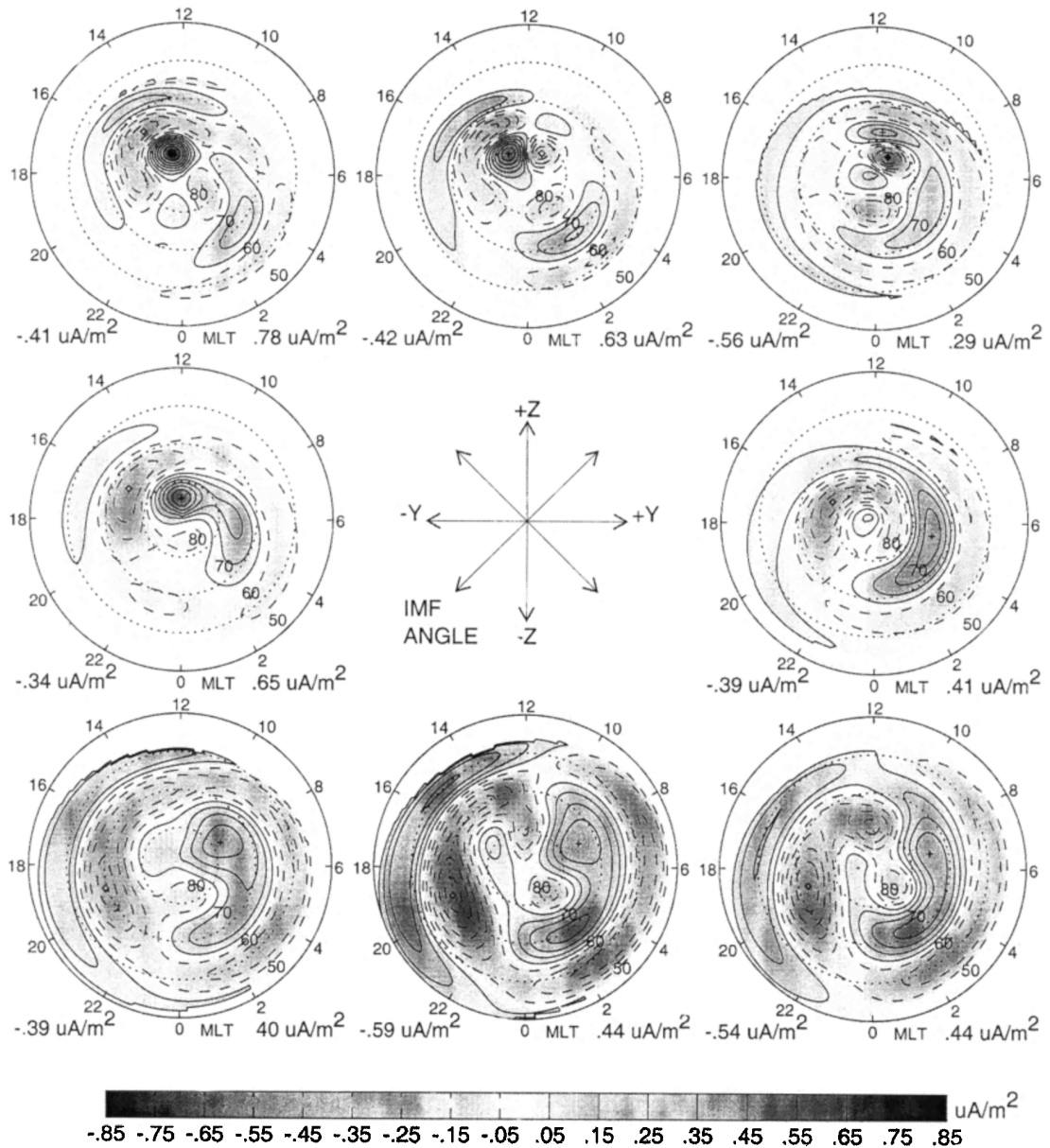


Figure 2.9: A diagram showing bins of Birkeland current patterns with $B_{\perp} = 10 \text{ nT}$. It can be seen that B_Y drives asymmetries in the current patterns, and that southward B_Z drives stronger currents. From Weimer (2001).

an increase in R2 intensity, and also noted that a model of the ring current developed by Fok *et al.* (2001) produced a dawn-dusk asymmetry in R2 currents during geomagnetically active times. This finding was linked to work by Anderson *et al.* (2005), who found that during geomagnetic storms the dusk currents were shifted equatorward compared to the dawn currents. Iridium data have also previously been used to verify estimates of the R2 Birkeland currents achieved by consideration of the ring current (Brandt *et al.*, 2004).

Gjerloev *et al.* (2011) suggested that dayside Birkeland current characteristics

were independent of both IMF B_Z and geomagnetic activity, whereas the nightside current amplitude was found to be driven by B_Z , using data from the ST-5 satellite constellation over a three-month period. This result is seemingly at odds with the currently understood picture of currents associated with ionospheric convection driven by reconnection, and also opposed by the overwhelming majority of other experimental findings which typically find dayside current magnitudes to be dependent on southward IMF. The conclusion is therefore drawn that this finding is flawed.

Work done by Anderson *et al.* (2008) using data from the Iridium satellite constellation demonstrated IMF control of field-aligned currents which came to similar conclusions to the work of Weimer (2001) and Papitashvili (2002); other work done with the same data found that Birkeland currents depended on the interplanetary electric field (IEF) for southward IMF, with a weak dependence on the solar wind pressure and no dependence on the Mach number (Korth *et al.*, 2010). Green *et al.* (2009) agreed with previous work but found that B_Y was not as important as had been thought. Later work done with AMPERE (a dataset consisting of processed Iridium data, described in Section 3.1) has demonstrated that when the IMF turns southward, R1 currents are observed on the dayside after about 20 minutes (as predicted by He *et al.* (2012)), before nightside reconnection begins and the currents begin to flow on the nightside (Anderson *et al.*, 2014). The authors theorised that this meant that R1 currents were being driven by the reconnection occurring at the magnetopause, with the ionospheric convection pattern becoming established and thus causing the formation of the rest of the Birkeland current system.

According to Rostoker *et al.* (1982), higher current strengths are driven by northward turnings in the IMF associated with substorms. However, it has been suggested by Freeman and Morley (2009) that the association between northward turnings of the IMF and substorms may be a misinterpretation of the data due to the requirement for southward IMF during the substorm growth phase. Consequently, it seems likely that the observations of Rostoker *et al.* (1982) are due to nightside reconnection driving a higher transpolar voltage and therefore higher current strengths (Milan, 2013).

Semiannual variations have been found in the latitude of the current oval and the intensity of the currents (Ohtani *et al.*, 2005b), with peaks in intensity found at the equinoxes and peaks in latitude found at the solstices (such that during summer and winter the ovals retreated to higher latitudes, indicating less open magnetic flux contained within the polar cap). This can be explained by the Russell and McPherron (1973b) effect, in which the geomagnetic activity is highest at equinox due to the dipole tilt being most conducive to magnetosphere-solar wind coupling. These effects are distinct from the seasonal and diurnal variation in Birkeland current

flow, which are due to conductance effects and discussed in Section 2.3.3.

2.3.3 Seasonal and diurnal variations

2.3.3.1 Solar zenith angle dependence of ionospheric conductance

There are two principal sources of E region ionisation (and therefore conductance): auroral particle precipitation, and solar extreme ultraviolet radiation, or EUV (Robinson and Vondrak, 1984). More auroral particle precipitation occurs during times when the aurora are more intense, and therefore the amount of auroral particle precipitation will be related to geomagnetic activity. The solar EUV contribution will be greater when the Sun is directly overhead, and is therefore expected to vary both seasonally and diurnally with the solar zenith angle.

Attempts have been made to quantify the Hall conductance Σ_H and the Pedersen conductance Σ_P in the ionosphere as a function of the solar zenith angle χ . The relationships found by these studies are as follows (Robinson and Vondrak, 1984):

$$\text{Mehta (1979): } \Sigma_P = 7.1 \cos(\chi)^{0.44} \quad \sim 0.52 \Sigma_H \quad (2.5a)$$

$$\text{Senior (1980): } \Sigma_P = 1.6 + 9.6 \cos(\chi) \quad \sim 0.56 \Sigma_H \quad (2.5b)$$

$$\text{Vickrey } et al. \text{ (1981): } \Sigma_P = 5 \cos(\chi)^{0.5} \quad = 0.5 \Sigma_H \quad (2.5c)$$

$$\text{de la Beaujardiere } et al. \text{ (1982): } \Sigma_P = 2 + 10 \cos(\chi) \quad \Sigma_H = 10 \cos^{0.5}(\chi) \quad (2.5d)$$

$$\text{Fujii and Iijima (1987): } \Sigma_P = 12.579 - 0.112\chi \quad (2.5e)$$

The above equations indicate that the Pedersen conductance is usually between 0.5 and 0.6 times the Hall conductance. After several studies had been performed it was postulated that differences between the functions found could be explained by a failure to take into account the UV flux, and the 10.7-cm solar flux $F_{10.7}$ was then used as a proxy for the UV flux. (The notation for the 10.7-cm solar flux was S_a in older papers (Baron *et al.*, 1983) but more recent papers have used $F_{10.7}$ (Ohtani *et al.*, 2014).) The E region ionisation was expected to be approximately proportional to the square root of the solar flux (Robinson and Vondrak, 1984), and therefore attempts were made to quantify the conductance with a factor of the solar

flux included. The attempts that include solar flux found:

$$\text{Robinson and Vondrak (1984): } \Sigma_P = 0.88 F_{10.7}^{0.5} \cos^{0.5}(\chi) = 0.59 \Sigma_H \quad (2.6a)$$

$$\begin{aligned} \text{Rasmussen } et al. (1988): \Sigma_P &= \frac{4.5}{B} \left(1 - \frac{0.85\chi^2}{90^\circ} \right) u \\ \Sigma_H &= \frac{5.6}{B} \left(1 - \frac{0.9\chi^2}{90^\circ} \right) u \end{aligned} \quad (2.6b)$$

$$\begin{aligned} \text{Moen and Brekke (1993): } \Sigma_P &= F_{10.7}^{0.49} (0.34 \cos(\chi) + 0.93 \cos^{0.5}(\chi)) \\ \Sigma_H &= F_{10.7}^{0.53} (0.81 \cos(\chi) + 0.54 \cos^{0.5}(\chi)) \end{aligned} \quad (2.6c)$$

In Equation 2.6b

$$u = 1 + 0.15 \frac{F_{10.7}}{90} + 0.05 \left(\frac{F_{10.7}}{90} \right)^2 \quad (2.7)$$

The result from Robinson and Vondrak (1984) supports the earlier inference regarding the relative values of Σ_H and Σ_P , but the later result from Moen and Brekke (1993) appears to contradict that conclusion. It should be noted that Robinson and Vondrak (1984) actually found a power of $\cos(\chi)$ equal to 0.46, but decided to round to 0.5 since they were unsure the accuracy of their experiment supported two significant figures and also because the peak ionisation for a Chapman layer varies with $\cos^{0.5}(\chi)$ for solar zenith angles up to 80° .

The studies above used varying methods to calculate the ionospheric conductance. Several authors made measurements of height-integrated electron density with incoherent-scatter radars during times when auroral precipitation was zero and thus the only contribution to ionisation was the solar EUV (Mehta, 1979; Senior, 1980; Vickrey *et al.*, 1981; de la Beaujardiere *et al.*, 1982; Robinson and Vondrak, 1984). Other authors have used the variation of the magnitudes of the Birkeland currents seasonally and diurnally to quantify the conductance (Fujii and Iijima, 1987).

2.3.3.2 Solar zenith angle dependence of Birkeland currents

The literature reviewed in Section 2.3.3.1 is useful in that Birkeland currents depend on the ionospheric conductance (Fujii and Iijima, 1987; Zheng *et al.*, 2006; Milan, 2013), but studies have also been conducted that show seasonal variations in the characteristics of the Birkeland currents themselves. Studies have shown that the current intensity increases during the summer, such that the intensity of both the R1 and R2 current systems is stronger in the summer (Fujii *et al.*, 1981; Ohtani *et al.*, 2005b). Studies have shown that the Birkeland currents increase both sea-

sonally and diurnally depending on the solar zenith angle χ (Fujii and Iijima, 1987; Chisham *et al.*, 2009; Wiltberger *et al.*, 2009). Chisham *et al.* (2009) reported that the vorticity in the ionospheric convection pattern also increased in summer, and interpreted this to mean caution should be taken when attributing this effect to conductance variations.

The disparity between R1 and R2 (which is generally referred to as the net Birkeland current (Fujii *et al.*, 1981; Christiansen *et al.*, 2002; Le *et al.*, 2010)) can be used to examine the amount of current flowing across the noon-midnight meridian (see Section 1.6.5), i.e. the Pedersen currents flowing from dawn to dusk across the polar cap. Yamamoto *et al.* (2003) reported that they did not see any link between combined or net Birkeland currents and χ and suggested that this was because the Pedersen conductance was not linked to χ . Although the result in terms of combined currents is disputed by the majority of the literature, it is true that authors have disagreed on the variation of the net Birkeland currents with χ : Fujii *et al.* (1981) found a link; Nakano *et al.* (2002) only reported a link for the net currents on the nightside; Christiansen *et al.* (2002) found no relation.

Evidence has been presented that only the dayside currents (Fujii *et al.*, 1981; Ohtani *et al.*, 2005b; Wang, 2005) are linked to χ . There is some agreement that the dayside Birkeland currents can be thought of as driven by a voltage generator (Watanabe *et al.*, 1998; Cattell *et al.*, 2003) and that the nightside currents are better explained by a combination of a voltage generator combined with a current generator (Fedder and Lyon, 1987; Wang, 2005; Lukianova and Christiansen, 2008; Chisham *et al.*, 2009).

It has been suggested that current intensity in the 20–02 MLT sector is stronger in the winter hemisphere than in the summer hemisphere (Ohtani *et al.*, 2005b,a, 2009), although it was noted that the same was not as obvious in the current density. Ohtani *et al.* (2005a) also noted that the width of the field-aligned current sheet was thicker in the summer hemisphere, which might indicate that the current is simply flowing in a larger area. The lack of supporting observations by Fujii *et al.* (1981) and Fujii and Iijima (1987) was attributed to a lack of observations in the 20–02 MLT sector. Higher particle energies were also observed in the winter hemisphere and it was hypothesised that this may be linked to a lower electron density in the acceleration region (Ohtani *et al.*, 2009). Since a given current either needs a large density and slower velocities or a low density and higher velocities, this would account for the observations. Ohtani *et al.* (2014) studied the effect of the solar flux $F_{10.7}$ on the Birkeland currents and showed that the effect of the solar flux put forward by Robinson and Vondrak (1984) and Moen and Brekke (1993) was separate to the seasonal effect; they theorised that an enhanced R1 current could lead to the

magnetotail being stretched which would drive further R1 enhancement.

Measurements of the currents have indicated that the Birkeland current ovals vary latitudinally with respect to the pole during solstice and equinox. During the summer, as the pole tilts sunward, the current ovals move antisunward, and vice versa in the winter (Ohtani *et al.*, 2005b). This is predicted by the T96 model (Tsyganenko, 1996), which shows that the footprints of the open field lines (and thus the polar cap) moves similarly with season. It was also reported by Ohtani *et al.* (2014) that the current ovals move equatorward across all MLT with higher values of $F_{10.7}$, which was attributed to an effect of the R1 current on the magnetospheric configuration. If this were true, it would indicate that the polar cap can change in size without magnetic reconnection, which is not physically possible. However, work has been done on the solar cycle dependence of the polar cap by Imber *et al.* (2013b), who showed that the size of the polar cap is associated with the solar cycle, as is the average dayside reconnection rate and the number of substorms in agreement with the ECPC paradigm; this means that the result of Ohtani *et al.* (2014) can be explained in the context of this result rather than by changes in magnetospheric configuration caused by R1 current flow. Ohtani *et al.* (2014) used data from DMSP F07 and F12–18, which cover the years 1983–1988 and 1995–2012; the data used by Imber *et al.* (2013b) covered 1996–2012 (see Figure 2.10).

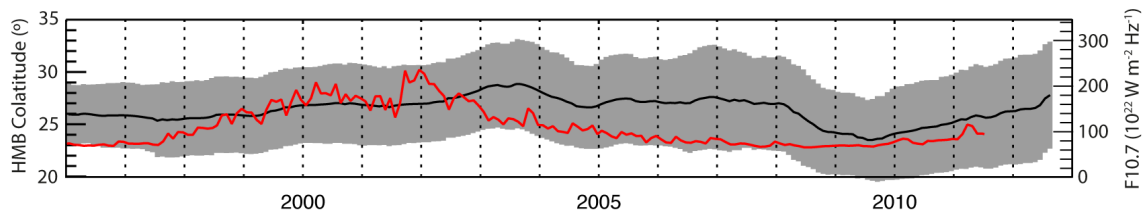


Figure 2.10: The black line and grey area is the colatitude of the Heppner-Maynard boundary (HMB) between 1996 and 2012, adapted from Imber *et al.* (2013b); the red line superimposed is the $F_{10.7}$ for the same period, adapted from Ohtani *et al.* (2014).

Chapter 3

Instrumentation

3.1 AMPERE

The Active Magnetosphere and Planetary Electrodynamics Experiment (AMPERE) was conceived to investigate the dynamics of the Birkeland currents using magnetometer data from the attitude control system of the Iridium telecommunications satellite network. It follows in the footsteps of work done to study the field-aligned current density using Iridium magnetometer data and validations of this technique (Anderson *et al.*, 2000; Waters *et al.*, 2001; Green *et al.*, 2006). The Iridium network of satellites is comprised of 66 active spacecraft that orbit the Earth in 6 circular, polar orbital planes (spaced by ~ 2 hours of MLT) at an altitude of 780 kilometres (Anderson *et al.*, 2000). The magnetic perturbation data from the Iridium constellation are subsequently processed using spherical harmonic basis function expansion methods such that the field-aligned currents can be inferred globally, resulting in the AMPERE dataset.

AMPERE consists of data from 1 January 2010 to 9 May 2013. After processing, the data are given on a grid which has spacing of 1° latitude and 1 hour of MLT. The data are made available in AACGM co-ordinates at an altitude of 780 km. Measurements are available for windows of ten minute intervals, evaluated every two minutes. The ten minute windows are due to the orbital spacing of the satellites: the satellites orbit with a period of 104 minutes (Anderson *et al.*, 2000), and so it takes 9.5 minutes for the next satellite to arrive at the same position. Initial work undertaken using the Iridium constellation concluded that the data were useful in characterising large-scale Birkeland currents in both hemispheres (Anderson *et al.*, 2000), but smaller-scale signatures cannot be explored due to the limitations of the dataset (Anderson and Christiansen, 2003).

3.1.1 The AMPERE processing method

AMPERE data is processed using magnetic perturbation data taken from Iridium satellites; each Iridium satellite has a triaxial fluxgate engineering magnetometer on-board which has a resolution of 29 nT (Waters, 2014, 2015). Iridium magnetometer data is sampled every 15 seconds by Anderson *et al.* (2000), but for AMPERE the data is sampled at a standard rate of 1 datum per 19.44s or a high rate of 2.16s (Anderson *et al.*, 2014). The Iridium satellites are not spinning and always face the nadir; the on-board three-axis magnetometer has axes pointing towards the nadir, along the spacecraft track and across the spacecraft track. Magnetic perturbations as a result of Birkeland currents (typically 100s of nT) can be measured in the cross-track component, which was the only component used in the initial treatment of Iridium. In AMPERE, all three components of the magnetometer readings are used.

The method for obtaining Birkeland currents from the magnetic perturbations measured by Iridium relies on Ampère’s law (Equation 1.4), which relates current density and magnetic fields in the relation $\nabla \times \mathbf{B} = \mu_0 \mathbf{j}$. Because \mathbf{j} is the field-aligned current density, it is parallel to the main magnetic field \mathbf{B} , and Equation 1.4 can be rearranged where \parallel and \perp indicate vectors parallel and perpendicular to the main field \mathbf{B} respectively.

$$\mathbf{j}_{\parallel} = \frac{\nabla \times \Delta \mathbf{B}_{\perp}}{\mu_0} \quad (3.1)$$

To process Iridium data from the raw satellite data into the magnetic perturbations for each satellite, an automated process is employed, as described by Anderson *et al.* (2000). Firstly, the IGRF-1995 magnetic field is transformed into the satellite co-ordinate system and subtracted from the data. Secondly, the variance-covariance matrix is derived from the residuals, which is used to correct for crosstalk (measurement errors as a result of spacecraft electronics); gain drift (measurement errors due to temperature-based changes in instrument accuracy); errors in the assumed spacecraft orientation; and fixed field offsets. The last step involves a high-pass filter to eliminate signals with a period longer than 26 minutes, corresponding to a quarter of an orbit; this was done to remove long-period residuals which were attributed primarily to errors in the IGRF-1995 model magnetic field (Anderson *et al.*, 2000). The length of time was chosen by examining periods in which the Birkeland currents could be identified over the polar cap and applying high-pass filters to that data, choosing the lowest period which did not distort the data. This process yields $\Delta \mathbf{B}$ from the \mathbf{B} measured by the spacecraft. The noise level was found to be 3.5 mul-

multiplied by the median of the processed $\Delta\mathbf{B}$, giving a total noise level of 70–100 nT, and the contamination of spurious points in the high-latitude region was found to be $< 1\%$.

The magnetic perturbation data processed by Anderson *et al.* (2000) is converted to a global map of magnetic perturbations via a method outlined in that paper, but an alternative method was given which uses spherical harmonics to produce a global map of the magnetic perturbations and the field-aligned currents (Waters *et al.*, 2001; Green *et al.*, 2006; Anderson *et al.*, 2014). Spherical harmonics can only be used to fit a scalar potential, meaning that the first part of the method is concerned with finding such a scalar potential that can be expressed in spherical harmonics.

Firstly, it is said that the total current flowing in the ionosphere can be split into a curl-free component, which Waters *et al.* (2001) calls the poloidal current \mathbf{I}_p , and a divergence-free component, which is called the toroidal current \mathbf{I}_q . The radial current density j_{\parallel} is equal to the divergence of the ionospheric current flowing. Assuming that the field-aligned current is radial, this means that the field-aligned current density is equal to the divergence of the curl-free current \mathbf{I}_p :

$$\mathbf{J}_{\parallel} = j_{\parallel}\hat{\mathbf{r}} = (\nabla \cdot \mathbf{I}_p)\hat{\mathbf{r}} \quad (3.2)$$

where $\hat{\mathbf{r}}$ is the radial unit vector. The $\nabla \times \mathbf{I}_p$ is by definition zero, and since the curl of a gradient is zero, \mathbf{I}_p can be said to be the gradient of some potential function Ψ , such that

$$\mathbf{I}_p = -\nabla\Psi, \quad (3.3)$$

$$\Delta\mathbf{B} = -\mu_0\hat{\mathbf{r}} \times \mathbf{I}_p, \quad (3.4)$$

$$\Rightarrow \Delta\mathbf{B} = \mu_0\hat{\mathbf{r}} \times \nabla\Psi \quad (3.5)$$

where the curl of Equation 3.4 yields Equation 3.1 and $\nabla\Psi$ can be expanded by spherical harmonics, as required.

Consequently, linking the field-aligned current density (assumed to be radial) to the divergence of the curl-free component of the ionospheric current means that the magnetic perturbations measured by the Iridium spacecraft can be expressed in terms of a scalar potential. This potential function can then be expanded:

$$\Psi(\theta, \phi) = \sum_{l,m} a_l^m Y_l^m(\theta, \phi) \quad (3.6)$$

$$Y_l^m(\theta, \phi) = \sqrt{\frac{2l+1(l-m)!}{4\pi(l+m)!}} P_l^m(\cos\theta) e^{im\phi}. \quad (3.7)$$

Y_l^m are the Laplacian spherical harmonic basis functions, constructed from the associated Legendre polynomials $P_l^m(\cos \theta)$ in latitude (θ) and sine/cosine functions in longitude (ϕ). The magnetic perturbations in the direction of latitude and the direction of longitudes are given by the relationship between Equation 3.5 and Equation 3.7, such that

$$\Delta B_\theta = -\frac{\mu_0}{r} \frac{1}{\sin \theta} \frac{\partial}{\partial \phi} \left[\sum_{l,m} a_l^m Y_l^m(\theta, \phi) \right] \quad (3.8a)$$

$$\Delta B_\phi = \frac{\mu_0}{r} \frac{\partial}{\partial \theta} \left[\sum_{l,m} a_l^m Y_l^m(\theta, \phi) \right] \quad (3.8b)$$

Then, to find a_l^m the least-squares merit function is formulated (Press *et al.*, 1986), where N is the number of data, $\Delta \mathbf{B}_d$ is a given datum and σ_d is the measurement error:

$$\chi^2 = \sum_{d=1}^N \left| \frac{\Delta \mathbf{B}_d - \mu_0 \hat{\mathbf{r}} \times \nabla \Psi}{\sigma_d} \right|^2 \quad (3.9)$$

This allows the function of $\nabla \Psi$ (and therefore the set of a_l^m) which gives the lowest χ^2 to be found by singular value decomposition algorithm (Press *et al.*, 1986), which allows the magnetic perturbation at any location (θ, ϕ) to be found using Equation 3.8.

The conditions necessary in order to model a vector field across a spherical cap where the edge is given by θ_c were given by Green *et al.* (2006):

$$Y_l^m(\theta_c, \phi) = 0 \quad (3.10a)$$

$$\frac{\partial}{\partial \theta} Y_l^m(\theta_c, \phi) = 0 \quad (3.10b)$$

The boundary of the polar cap was set at $\theta_c = 50^\circ$ (Waters *et al.*, 2001; Green *et al.*, 2006), the longitude order was set at 5, and the latitude order set to 20 (Anderson *et al.*, 2014), which yields a longitudinal resolution of 2.4 hours in MLT and a latitudinal resolution of 3° magnetic latitude. Anderson *et al.* (2014) noted that they did not use any currents under $0.16 \mu\text{A m}^{-2}$, as they were not confident that smaller signatures were not introduced by the fitting process; this is similar to the value of $0.2 \mu\text{A m}^{-2}$ which Clausen *et al.* (2012) concluded was the smallest physical signature.

An illustration that shows the stages of processing, from the raw magnetic perturbations detected along the six orbital tracks to the global current densities achieved using spherical harmonics, can be seen in Figure 3.1. Upward currents are shown in red (positive values) and downward currents in blue (negative). As discussed in

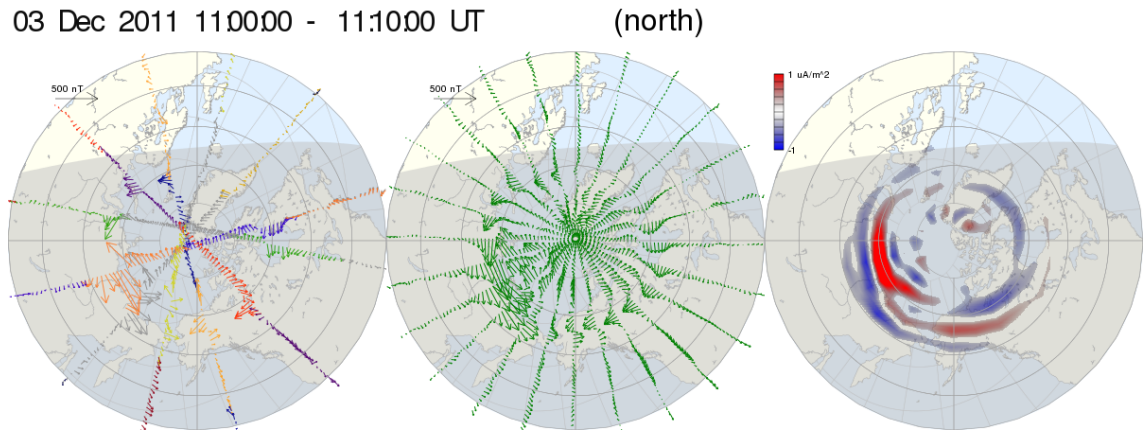


Figure 3.1: The three stages of AMPERE processing. Panel a shows the magnetic perturbations with the baseline (Anderson *et al.*, 2000) removed along the spacecraft tracks. Panel b shows the global magnetic perturbations inferred using spherical harmonics (Waters *et al.*, 2001), and panel c shows the global current densities (Green *et al.*, 2006). Data in this plot are from 3 December 2011 between 11:00 UT and 11:10 UT. Image taken from the AMPERE website.

Section 2.3.1, in general there are two rings of current: the inner region 1 current and the outer region 2 current.

3.1.2 Method for obtaining R1/R2 current magnitudes and locations

In this thesis, the topic of interest is the large-scale morphology of the R1/R2 system and therefore it is desirable to suppress small-scale, rapidly-varying features. To characterise the location and strength of the Birkeland current ovals, the fitting method described by Clausen *et al.* (2012) is implemented. This method determines the latitudes of the R1 and R2 currents along each meridian separately, before combining this information to determine the radii of the R1 and R2 current ovals.

Figure 3.2 presents a plot of current density j against latitude l for $\text{MLT} = 18$, and demonstrates the bipolar signature expected for adjacent upward and downward current sheets. Clausen *et al.* (2012) proposed a sinusoid with a gaussian envelope which can be fitted to the bipolar deflection to identify the R1 and R2 current systems. They also concluded that it was sensible to neglect small-scale current signatures below $0.2 \mu\text{A m}^{-2}$, shown by a broken line in Figure 3.2. Their equation is given by

$$j_{\text{fit}}(l) = o_0 + a_0 \exp\left(-\frac{(l - l_0)^2}{2\omega_0^2}\right) \sin\left(2\pi\frac{l - l_0}{2\sqrt{8 \ln 2}\omega_0} + \phi_0\right) \quad (3.11)$$

where o_0 is the zero offset, a_0 is the amplitude, and l_0 is the location of the centre of

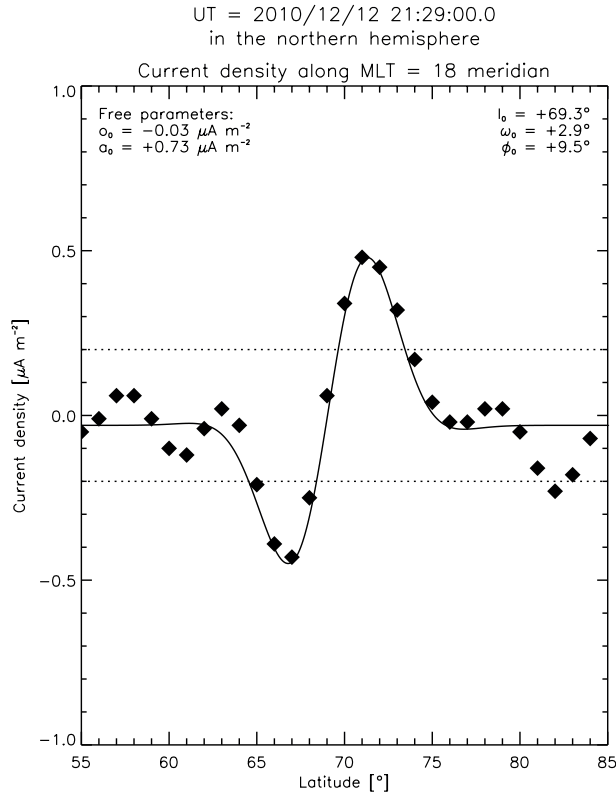


Figure 3.2: The current density data at a magnetic local time of 18:00 at 21:29 UT on 12 December 2010. The diamonds show the AMPERE data, the dotted lines show $\pm 0.2 \mu\text{A m}^{-2}$ and the solid line is a plot of Equation 3.11 given the parameters in the plot.

the function. The Full-Width-Half-Maximum (FWHM) of the Gaussian is given by $\sqrt{8 \ln 2} \omega_0$, and the wavelength of the sinusoid was chosen to be twice the FWHM. ϕ_0 is the phase shift of the sinusoid, such that the sinusoid crosses the line of $J = o_0$ at $l = l_0 - \sqrt{8 \ln 2} \omega_0 \phi_0 / \pi$. Figure 3.3 shows these parameters in relation to a sinusoid found using Equation 3.11.

An algorithm was created to automatically fit this equation to AMPERE data using a method outlined by Milan *et al.* (2012) in which a program starts with reasonable guesses for each parameter and iterates to find the best values of each. A fit line found by this algorithm is superimposed on Figure 3.2. A fit is not attempted where the maximum current density detected is less than $0.2 \mu\text{A m}^{-2}$. Fits are rejected on the dawn side where an upward current is detected poleward of a downward current, and vice versa on the dusk side, since these are inconsistent with the R1/R2 current system. Fits are also rejected if $\omega_0 < 1^\circ$, $|\phi_0| > 50^\circ$, or $l_0 > 85^\circ$.

However, there are meridians in which this bipolar signature is not seen: for instance, in Figure 3.4 at the 14 MLT meridian where two downward regions clearly flank a single upward region.

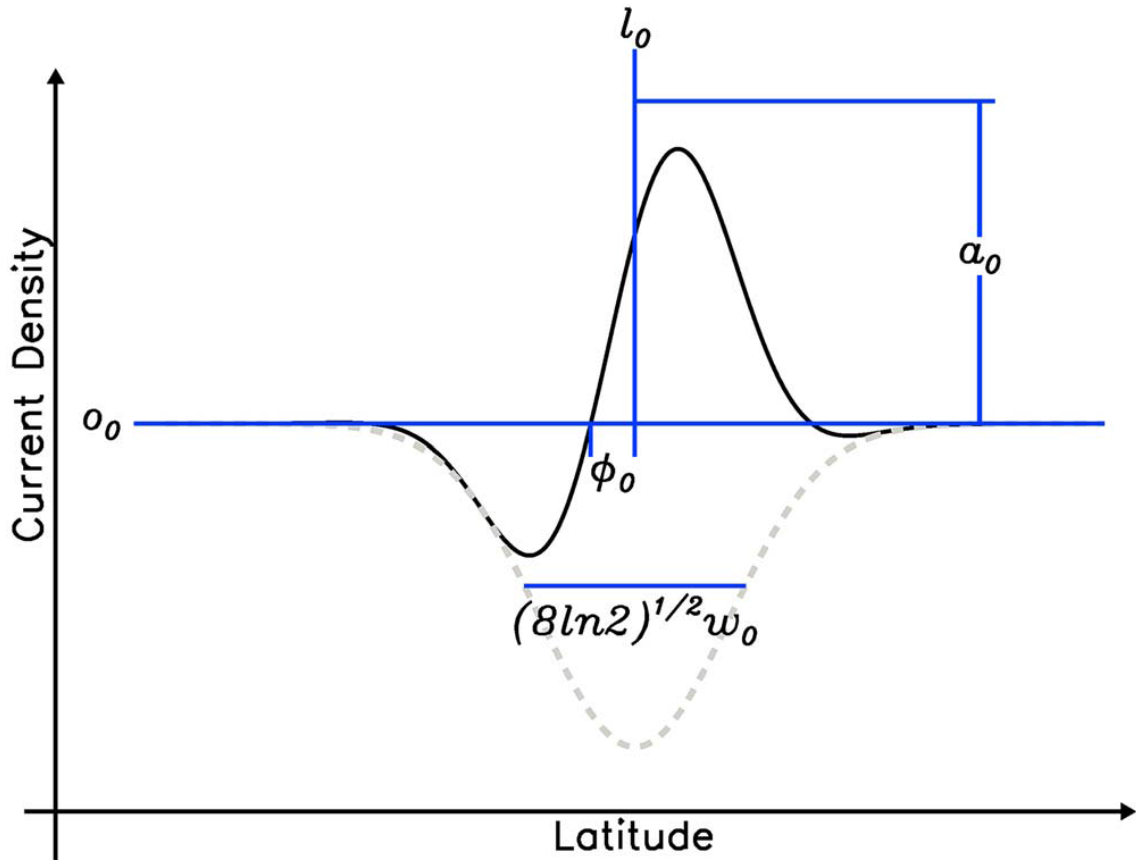


Figure 3.3: An example of the sinusoid generated by Equation 3.11 (in black) with the Gaussian envelope overplotted (in dashed grey). Shown are o_0 , which is the baseline of the function in y ; a_0 is the height of the Gaussian envelope; l_0 is the peak of the Gaussian envelope; $\sqrt{8 \ln 2} \omega_0$ is the Full-Width Half Maximum of the Gaussian envelope; and ϕ_0 refers to the offset of the centre of the sinusoid from the centre of the Gaussian envelope, such that the point at which the function crosses the line of $y = o_0$ is given by $x = l_0 - 2\sqrt{8 \ln 2} \omega_0 \phi_0 / 2\pi$. Taken from Clausen *et al.* (2012).

Figure 3.4 shows a map of AMPERE data (left) and the result of fitting to each of the local time meridians (right), where the dots indicate the locations of the upward and downward current peaks and the size of the dots depend on the a_0 parameter from Equation 3.11. It should be noted that red and blue are used to indicate upward and downward currents on the left but used to indicate R1 and R2 currents on the right. These fits can be used in turn to identify the size of the current rings. Clausen *et al.* (2012) gave an equation that can be used to get a fit to these points:

$$f(m) = l_1 + a_1 \cos\left(\frac{2\pi m}{24} + \phi_1\right) \quad (3.12)$$

where m is the MLT, l_1 is the mean latitude of the oval, a_1 is the amplitude of the deviation from the mean latitude and ϕ_1 is the oval's phase offset. This equation is fitted to the data using the same method as for Equation 3.11, and the result can be seen in the fit lines plotted in Figure 3.4. Note that Figure 3.4a shows that the bipolar R1 and R2 signature is not always seen as described above; for instance,

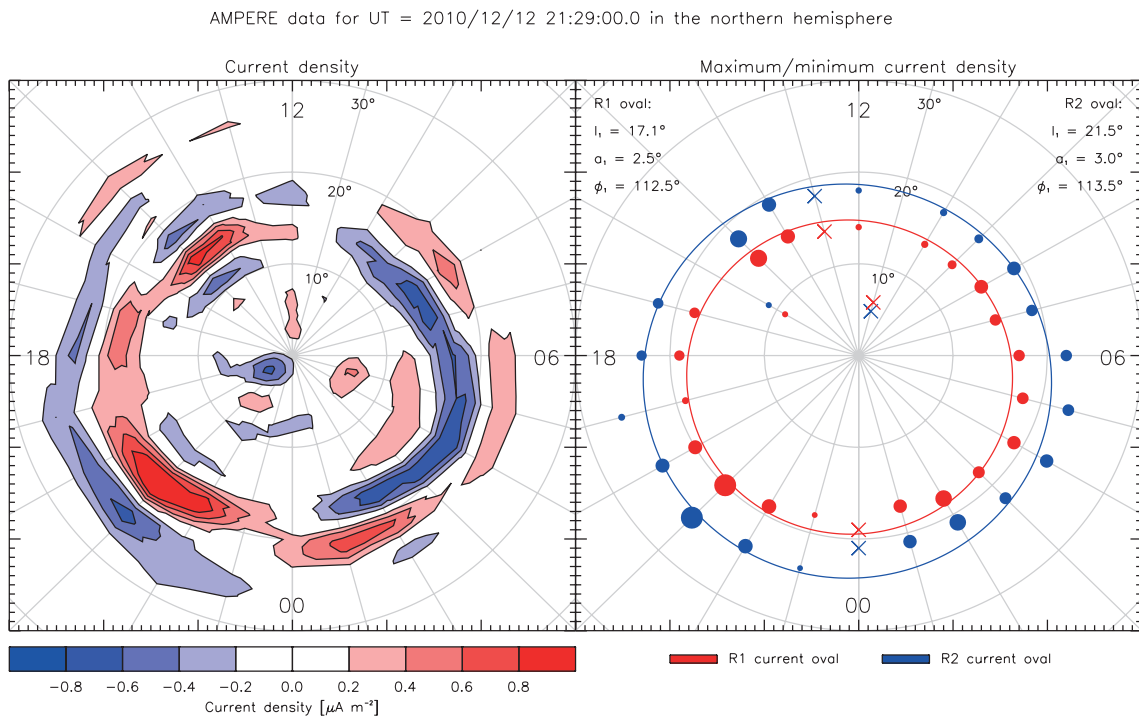


Figure 3.4: The same interval as shown in Figure 3.2. It should be noted that red and blue are used in panel a to show upward and downward current density respectively; but in panel b, red shows R1 current and blue shows R2 current. Panel a shows the current density from AMPERE across all MLT; panel b shows the maximum and minimum location of the solutions to Equation 3.11 as dots, where the size of the dot is proportional to a_0 . Crosses indicate the fit found for that magnetic local time was discarded and not used to fit Equation 3.12. The solid lines overlaid are the current ovals obtained by Equation 3.12.

at 14 MLT, two downward current regions clearly flank a single upward region. In places where there are three current sheets, Equation 3.11 will fit to the expected signature in order to identify R1 and R2.

The overall current magnitude flowing in each of the rings is calculated by integrating under the fitted curve of Figure 3.2 between the midpoint and the poleward edge (R1)/the equatorward edge (R2). The midpoint is given by $x = l_0 - 2\sqrt{8\ln 2}\omega_0\phi_0/2\pi$, and the equatorward and poleward edges are located at 0° and 60° colatitude (since the contribution of any colatitude at which $y = o_0$ is zero). This is multiplied by the area in m^2 described by a 0.1° by 1 MLT segment: For the case of Figure 3.2, the R1 and R2 currents integrated from 17:30 to 18:30 MLT have magnitudes of 105 and -107 kA respectively; summing the magnitude of both upward and downward currents across all the meridians seen in Figure 3.4 gives values of R1 current flowing $J_1 = 2.6$ MA and R2 current flowing $J_2 = 2.2$ MA, yielding a ratio $J_1/J_2 \sim 1.2$. It should be noted that the current magnitudes in the dawn and dusk sectors are normalised by dividing by the number of fitted meridians and multiplying by 12 in both before summing the two sectors, so the numbers presented may be slightly overestimated.

In order to calculate the total current flowing, the current calculated for each grid cell (1 hour of MLT by 0.1°) is summed. In order to avoid confusion, the current flowing in a single cell will be called $J_{l,m}$, as opposed to the total current J . Integrating the currents in each grid cell is achieved by the following integral, where $j = j_{\text{fit}}(l) - o_0$, m is the MLT and l is the magnetic colatitude. R is equal to $R_E + 780$ km. Data are available along each integer value of MLT, so the angle described by $m_1 - m_2$ is $\pi/12$. l_1 and l_2 , below, are separated by 0.1° colatitude. This is similar to a method to find the total current flowing utilised by Anderson *et al.* (2014).

$$J_{l,m} = Aj = \Omega R^2 j, \quad (3.13)$$

$$J_{l,m} = jR^2 \int_{l_2}^{l_1} \int_{m_2}^{m_1} \sin(l) \, dm \, dl, \quad (3.14)$$

$$J_{l,m} = jR^2 \frac{\pi}{12} \left[\cos(l) \right]_{l_2}^{l_1}. \quad (3.15)$$

This calculates the value of $J_{l,m}$ in each grid cell of 1 MLT and 0.1° ; these are then summed between $l_0 + \phi_0$ and the pole (to identify the poleward, R1 current) and between the edge of the cap θ_c and $l_0 + \phi_0$ (to identify the equatorward, R2 current). Once the current magnitude has been found along each value of MLT, the data is separated into the dawn and dusk flanks (dawn being $0 \leq \text{MLT} < 12$ and dusk being $12 \leq \text{MLT} < 24$). The magnitudes on one flank for one region are summed, and multiplied by $12/n$ where n is the number of successful fits on that flank. This is repeated for R1 and R2 in both dawn and dusk, and then the dawn and dusk currents can be summed to find the total R1 and R2 current flow in the given hemisphere, which are referred to as J_1 and J_2 .

Now, Figure 3.5 is presented. This figure shows three days of AMPERE data in order to show how the current vary temporally. The two uppermost panels, 3.5a and 3.5b, show the current density along the dawn-dusk meridian (MLT = 6 and MLT = 18) against time. The top panel shows northern hemisphere data and the bottom, southern hemisphere. Figure 3.5c shows the value of l_1 , the average latitude of the current oval, in the northern (top half) and southern (bottom half) hemispheres. In 3.5a-c, expansions and contractions of the polar cap are visible in the data. Figure 3.5d-e show the current magnitude calculated using the method outlined above for the same period, with 0.5–6 A flowing at any given point in the interval.

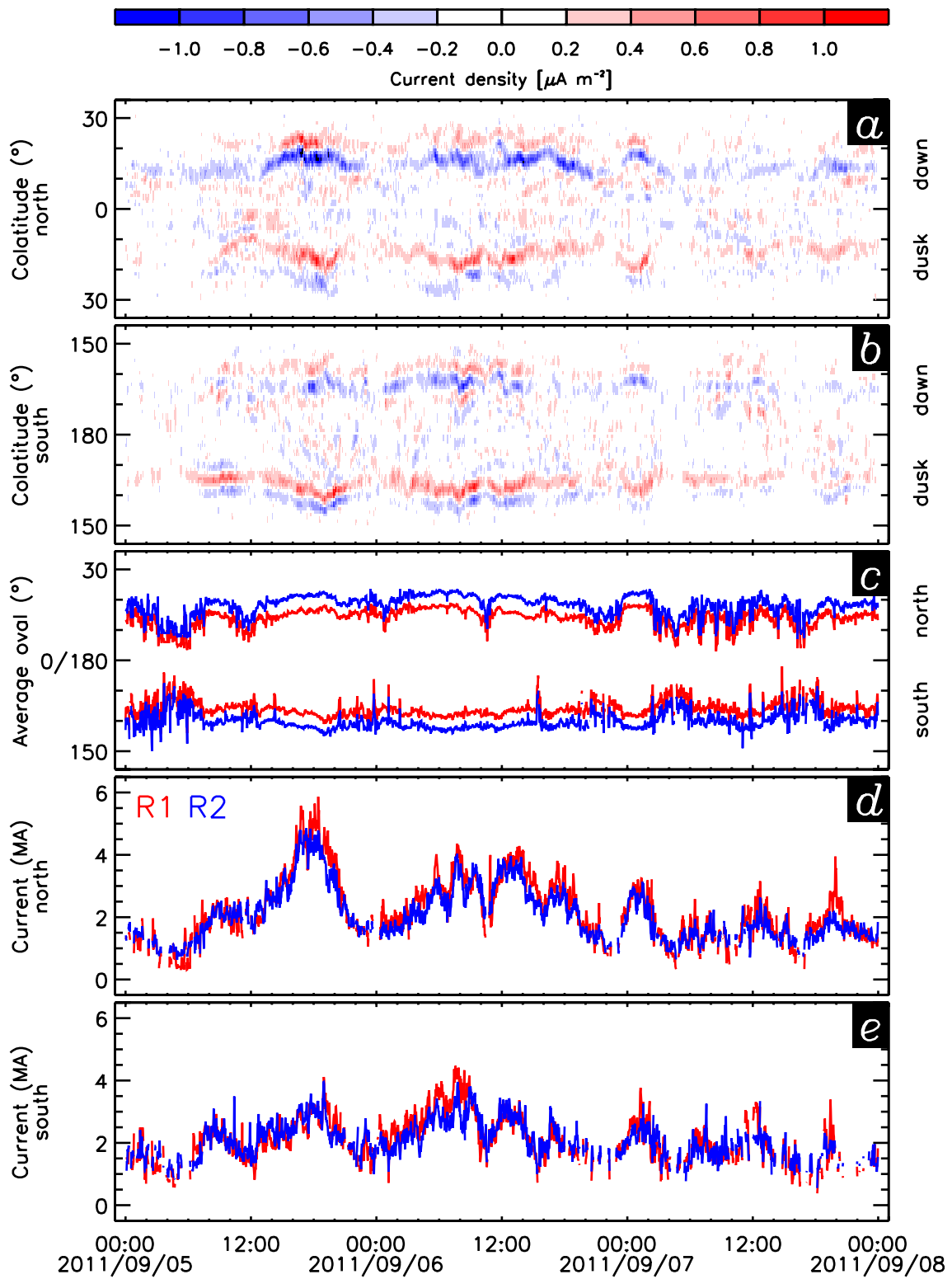


Figure 3.5: A plot showing 5–7 September 2011. Shown, from top to bottom, are the current density with respect to time as cuts through the dawn-dusk meridian in the a) northern and b) southern hemispheres; c) the value of l_1 calculated for both regions in the northern (top half) and southern (bottom half) hemispheres; and the current magnitudes for both regions in the d) northern and e) southern hemispheres.

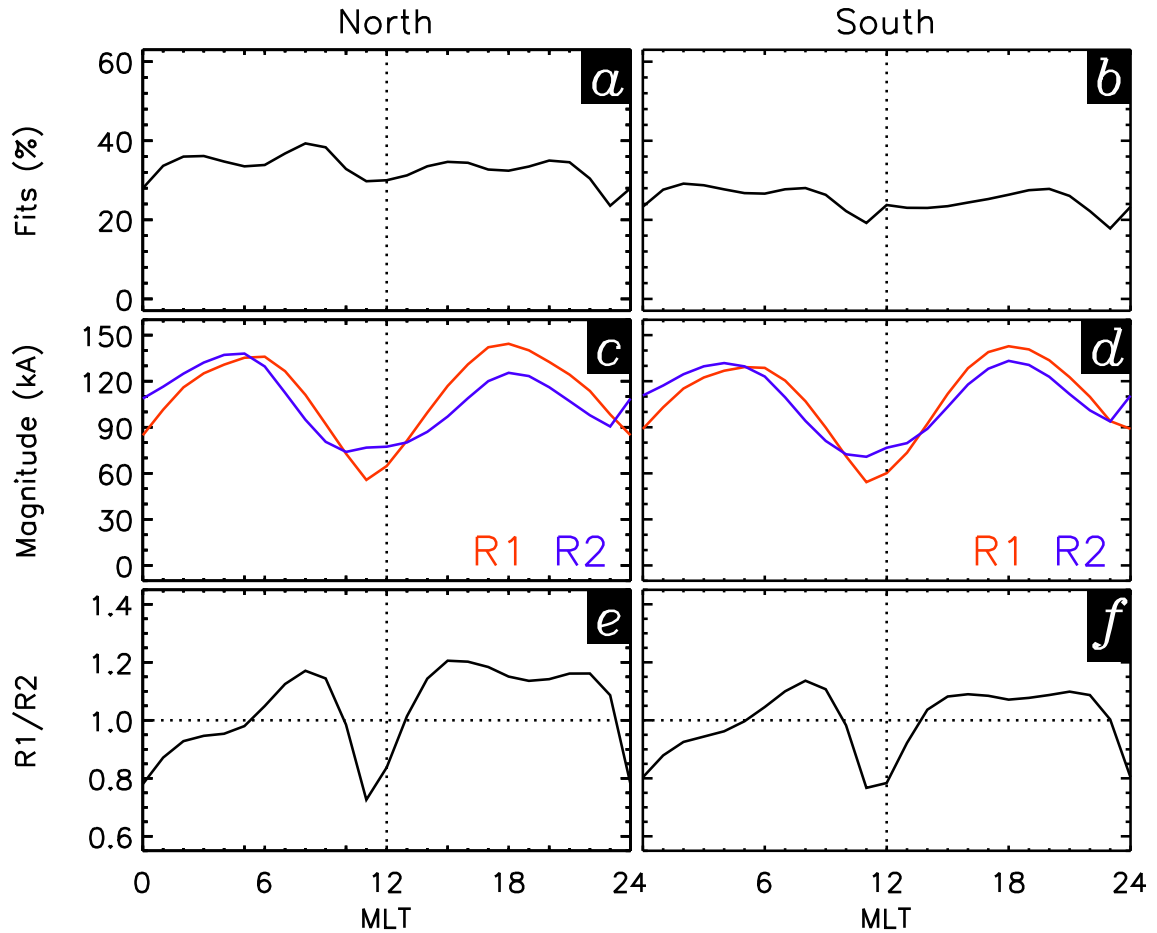


Figure 3.6: Panels showing MLT on the x -axis and a-b) the number of successful fits of Equation 3.11 for each hour of MLT as a percentage of the number of intervals, c-d) the average magnitude of the currents flowing in kA, and e-f) the ratio of R1 to R2 current magnitude. The northern hemisphere is shown on the left and the southern hemisphere is shown on the right; data in this plot extend from 1 January 2010 until 9 May 2013.

3.1.2.1 Success rates of this method

When the structure of the R1 and R2 current systems was first inferred (Iijima and Potemra, 1976a, 1978), it was found that they are most easily identified on the dawn and the dusk flanks. In the pre-midnight sector, the Harang discontinuity can lead to three current sheets, with a sheet poleward of the R1 current sheet; in the noon sector, there have been observations of three and even four current sheets, in opposition to the traditional R1/R2 current sheet picture (see Section 2.3.1). As such, it is necessary to consider under which conditions a successful fit of Equation 3.11 is likely to be made to the AMPERE data utilised. The success rate of this method is thus examined both with varying dayside reconnection rate and varying magnetic local time.

Figure 3.6 shows the number of fits of Equation 3.11 for each value of magnetic local time, alongside the average current magnitude in each magnetic local time.

The values plotted in Figure 3.6a and 3.6b are the percentage of intervals for which a successful fit was found for that MLT. The total number of successful fits in the northern hemisphere was 6525310 and in the southern hemisphere 4949875. The percentages are thus slightly lower in the southern hemisphere, indicating that the fitting technique has slightly more success in the northern hemisphere. Since the fitting technique works better at larger current densities, this may indicate that the AMPERE current densities in the northern hemisphere are systematically higher than those in the southern hemisphere.

Figure 3.6a and b show that the number of fits achieved is slightly lower at noon and pre-midnight, as dips are seen in both hemispheres at these local times. The number of fits peaks on either side of dawn in both hemispheres; the number of fits is slightly lower at dawn. The same phenomenon is seen in the northern hemisphere around dusk, but in the southern hemisphere there is no peak before dusk, only a peak after.

In Figure 3.6c and d, the current magnitude observed is plotted against MLT; in panels e and f, the ratio is plotted against MLT. These panels show that there are peaks in the current detected at dawn and dusk, with troughs observed at noon and midnight in both regions. It should be noted that the R1 current system has deeper troughs than the R2 current system, such that at noon and midnight the R2 current system is larger than R1. The R2 currents are also larger than the R1 currents through the post-midnight sector. This means that the ratio between R1 and R2 is less than 1 when the number of fits is lower, suggesting that at times when the fitting is less successful, the fitting also tends to report that R2 is larger than R1. Care must thus be taken when interpreting any observation of R2 magnitudes larger than R1.

The fitting employed assumes that the current systems will be well-described by an equation which finds a two-current-sheet system, thus assuming that the currents will be in two oppositely directed sheets (Region 1 and Region 2). Consequently, Equation 3.11 appears to be less successful at times when the two-region assumption breaks down. The fitting process is less successful at midnight (coincident with the Harang discontinuity) and at noon (coincident with Region 0 currents). Southward IMF is expected to drive R1 and R2 current systems, whereas northward IMF is expected to drive a somewhat different current system (Iijima and Potemra, 1978; Weimer, 2001): the percentage of fits is 30 – 40%, but the IMF will be northward approximately half of the time, which accounts for a large percentage of the failed fits.

R2 current magnitude is found to be higher than R1 when the fitting is less

successful. This may indicate that the fitting can misidentify the regions at times when more than two current sheets are present, resulting in apparently higher R2 currents when in actuality this might not be the case.

The number of successful fits with respect to the dayside reconnection rate Φ_D (calculated using Equation 2.3 and data from OMNI, described in Section 3.2) is determined and plotted for the northern and southern hemisphere (Figures 3.7 and 3.8 respectively). Since a fit is attempted along each value of MLT, the range of possible fits is $0 \leq N(\text{fits}) \leq 24$ where $N(\text{fits})$ is the number of fits achieved in an interval; the figures indicated describe the dependence of the number of possible fits on dayside reconnection rate.

In Figure 3.7a there are a large number of data for which a low number of fits occurs at a low dayside reconnection rate; it can thus be concluded that at low dayside reconnection rates, the fitting process works less well. 3.7b plots the number of fits divided by the number of fits in the respective bin of Φ_D ; this panel shows that the number of successful fits increases linearly with dayside reconnection rate until 30 kV, at which point the success rate saturates at approximately 70%. Since the fitting process only fits to signatures above $0.2 \mu\text{A m}^{-2}$, and since the work outlined in Section 2.3.2 indicates that current flow is larger when the IMF is southward, this is consistent with expectations based on previous work.

Figure 3.7c shows the number of data in each bin of Φ_D as a cumulative frequency diagram. There are approximately 3.5×10^5 data in the first bin of Φ_D , defined by $0 \text{ kV} \leq \Phi_D < 5 \text{ kV}$. There are 7.5×10^5 data across all the bins of Φ_D , meaning approximately half the data are in the first bin: this makes sense in the context of an IMF which is directed northward approximately half the time, and also provides context for the success rate plotted in Figure 3.6. Finally, for each bin, the percentage of the intervals for which more than 8 fits are achieved is calculated. This percentage is then plotted against Φ_D in Figure 3.7d: at least 8 fits are achieved more than half the time when dayside reconnection rate is greater than approximately 15 kV.

3.2 OMNI

The OMNI dataset is provided by NASA. The data obtained from the OMNI dataset were, at a cadence of 1 minute, the interplanetary magnetic field B_X , B_Y , B_Z in GSM co-ordinates, the solar wind velocity and density V_{sw} , and N_{sw} , and the auroral electrojet indices, AL and AU, derived from ground magnetometers as described in Section 3.2.2. Data were obtained for the period 2010–2012. The space-based

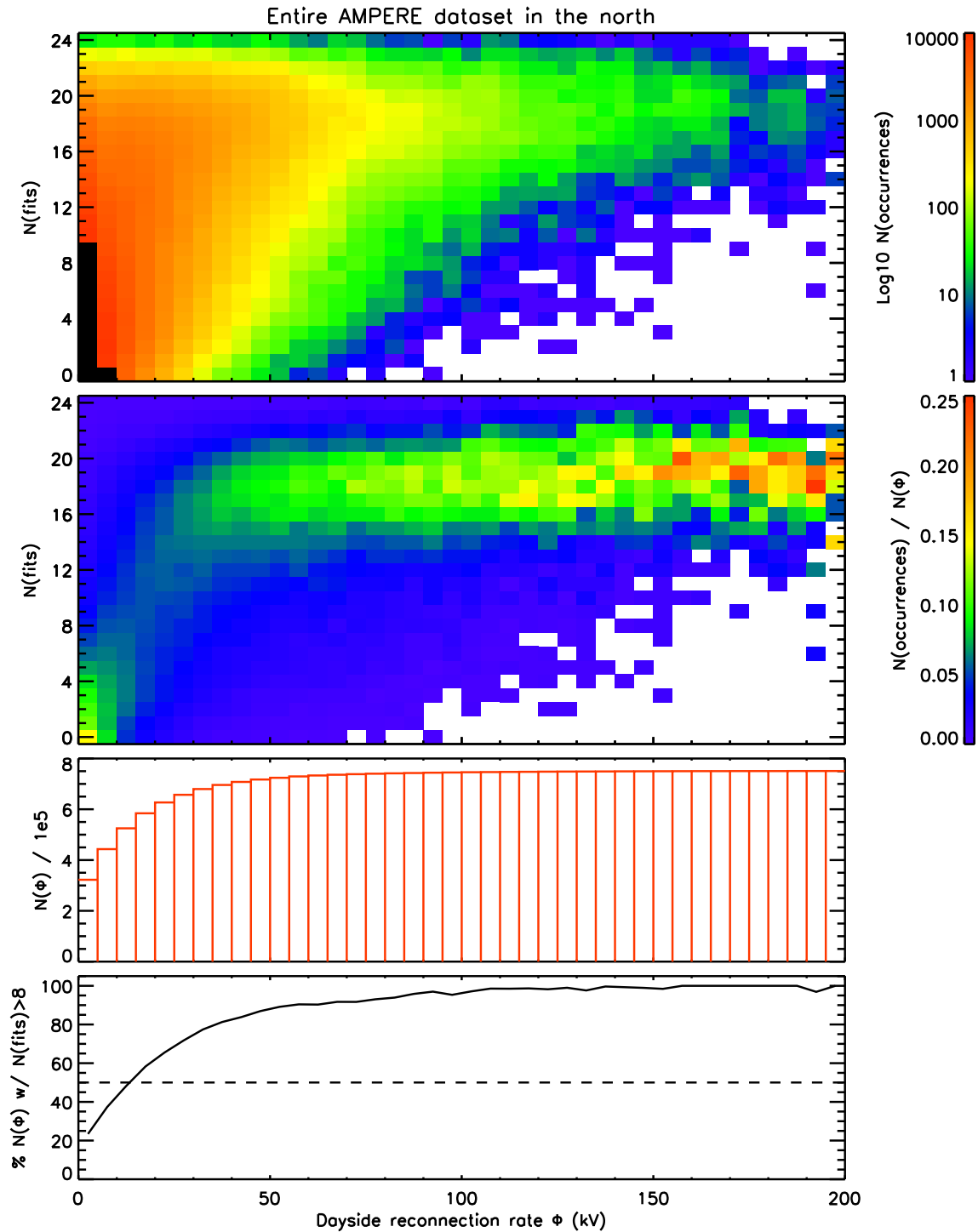


Figure 3.7: From top to bottom: a) the number of fits N colour-coded by the number of intervals for which that N was achieved, b) the same axis on y but colour-coded by the number of fits divided by the number of Φ_D data in the given bin, c) a cumulative frequency diagram of the number of Φ_D data in each bin, d) the percentage of the Φ_D data associated with a value $N > 8$. Φ_D is plotted on the x-axis; each bin is described by $\Phi_{D0} \leq \Phi_D < \Phi_{D0} + 5$ for a given lower bound Φ_{D0} . Data plotted is from Birkeland currents in the northern hemisphere. The colour code for panels a) and b) is plotted to the right of the respective panel, and black indicates that the value in a pixel is larger than the scale indicated, while white indicates no contribution to a pixel. Data in this plot extend from 1 January 2010 until 9 May 2013.

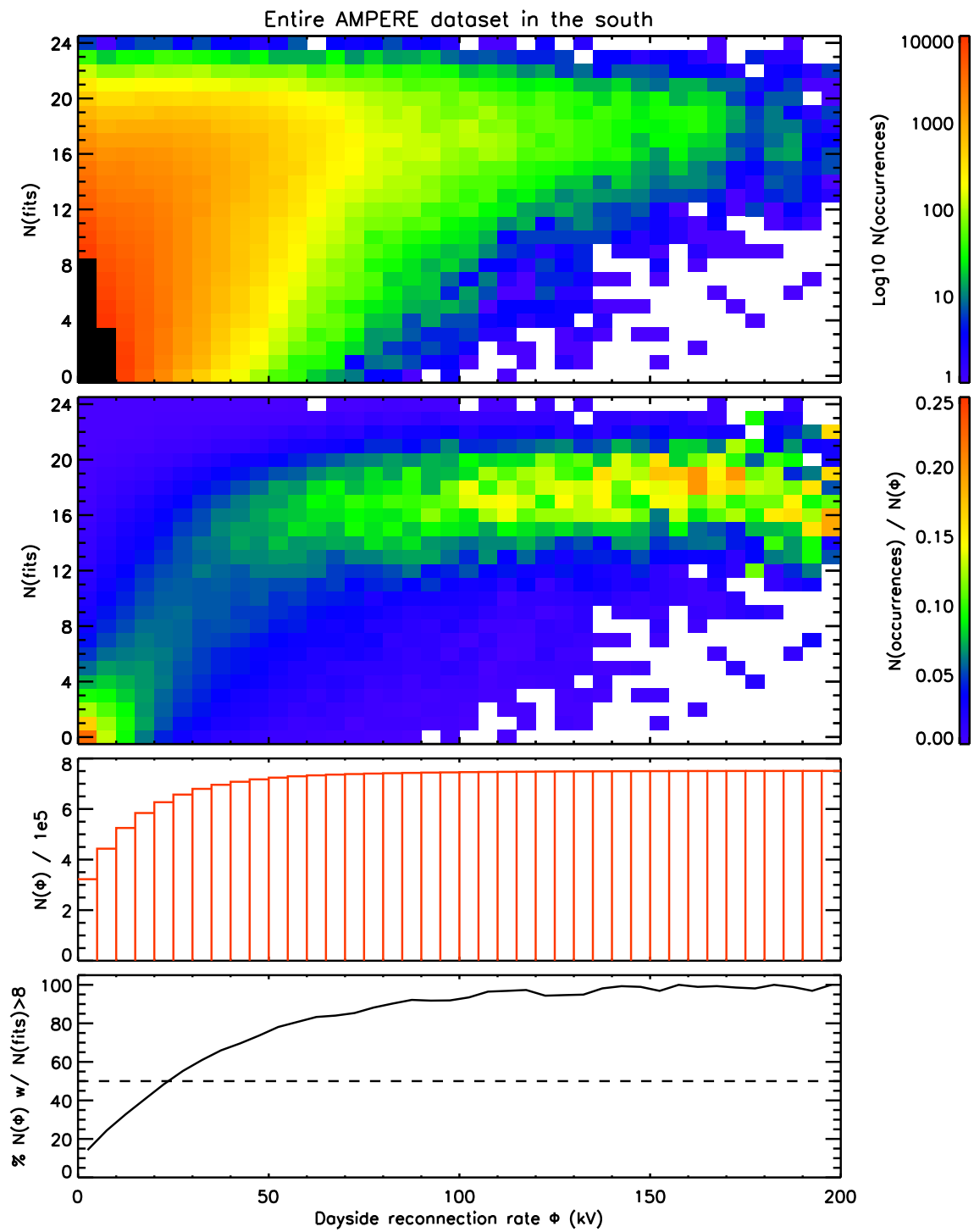


Figure 3.8: The same axes and colour codes as Figure 3.7, but with data from the southern hemisphere over the same period.

data from the OMNI dataset for the period of time considered in this thesis are constructed using measurements from three spacecraft: ACE, Geotail, and Wind. The indices are those maintained by the World Data Center C2 for Geomagnetism in Kyoto, Japan.

OMNI data of 1 minute cadence are referred to as High-Resolution OMNI (HRO) data and the processing that produces this dataset, including the method for deciding which spacecraft to use for data in a given interval, is described by King and Papitashvili (2014). The OMNI dataset is shifted from the point of measurement (which is often upstream of the magnetopause and not lying on the Sun-Earth line) to the nose of the bow shock located using the bow shock model of Farris and Russell (1994) and the magnetopause model of Shue *et al.* (1997). This shifting is performed under the assumption that variations in the solar wind parameters occur in phase fronts which propagate through the heliosphere at the velocity of the solar wind. The quality of the time shifting is examined by shifting data from ACE to Wind and comparing them with in-situ Wind data. The data is not shifted from the bow shock to the magnetopause.

Minimum variance analysis is employed to determine normals to discontinuity planes (phase fronts) in the IMF (Sonnerup and Cahill, 1968) in order that they may be shifted. Another method of finding phase fronts is to take the cross product of magnetic field vectors on either side of a discontinuity (Knetter *et al.*, 2004). If the cross-product is based on at least 46 points and the component of the mean magnetic field normal to the phase front is less than 0.035 nT, and if the cross-product finds an angle between the vectors on either side of the phase front which is larger than 13° , then this is the phase front used. If these criteria are not fulfilled, then minimum variance analysis is used. Minimum variance analysis is considered successful if it uses at least 77 points, and the angle between the minimum variance direction and the solar wind flow vector is less than 73° . If neither set of criteria are met then those data are flagged and later interpolated.

The work presented in this thesis does not filter out any OMNI data beyond those data that had been assigned error values when they were obtained.

3.2.1 Spacecraft

Each of the three spacecraft that have contributed to the OMNI data used in this thesis are still in operation at the time of writing. The first spacecraft is Geotail, which was launched on July 24, 1992. OMNI uses data from the Comprehensive Plasma Investigation (CPI), and the Magnetic Fields Measurement (MFM)

experiments (King and Papitashvili, 2014). CPI is comprised of an ion/electron three-dimensional velocity distribution instrument (1 eV–50 keV/q); a solar wind ions instrument (150 eV–7 keV/q); and an ion mass/energy spectrum instrument (1 eV–50 keV/q). MFM is comprised of a fluxgate magnetometer and a search coil magnetometer, both triaxial (Nishida, 1994; Acuña *et al.*, 1995).

Wind was launched as part of the Global Geospace Science Program on 1 November, 1994. The data that are used for OMNI come from the Solar Wind Experiment (SWE) and the Magnetic Field Investigation (MFI) instrumentation (King and Papitashvili, 2014). SWE measures the mass, energy and direction of ions and electrons in the 7 eV–22 keV range (Acuña *et al.*, 1995; Harten and Clark, 1995a), whilst MFI is comprised of two triaxial fluxgate magnetometers mounted on the two booms (Harten and Clark, 1995b).

ACE is the Advanced Composition Explorer and was launched on 25 August, 1997. The data that contribute to OMNI are taken from the Solar Wind Electron, Proton and Alpha Monitor (SWEPAM) and the magnetometer (King and Papitashvili, 2014). SWEPAM is able to measure the distribution of the energy to charge ratio of hydrogen, helium and electrons with a typical energy of ~ 1 keV/n, and two magnetometers are each mounted on a boom, as with Wind (Stone *et al.*, 1998).

3.2.2 Indices

Davis and Sugiura (1966) proposed three indices connected to the auroral electrojets: the AE index is the Auroral Electrojet index, and the AL and AU indices are the Auroral Lower and Auroral Upper indices respectively. Seven magnetometers were selected; the first criterion was whether they had made measurements in the timeframe under consideration. The second criterion was whether they were outside the polar cap, since the authors were concerned about complications due to transpolar currents. Five magnetometers outside the polar cap were selected, which left a gap in the spatial coverage of the magnetometers centred on the West Atlantic Ocean; two Southern Hemisphere magnetometers that were conjugate to this area were added, in order to improve the spatial coverage. The H component of each of these magnetometers was measured over time. The AU index was equal to the maximum positive perturbation in H (the envelope of the positive perturbations) and the AL index was equal to the maximum negative perturbation in H (the envelope of the negative perturbations) with time. The AE index was the AL index subtracted from the AU index. The modern AL and AU indices are constructed using data from twelve magnetometers in the northern hemisphere, but otherwise

follow the same method. These indices are the instantaneous maximum intensity of the magnetic perturbations observed at the surface as a result of the auroral electrojets depicted in Figure 1.18; AU measures the eastward electrojet and AL measures the westward electrojet. The substorm electrojet can thus be observed as a negative magnetic bay in the AL index, since it flows westward.

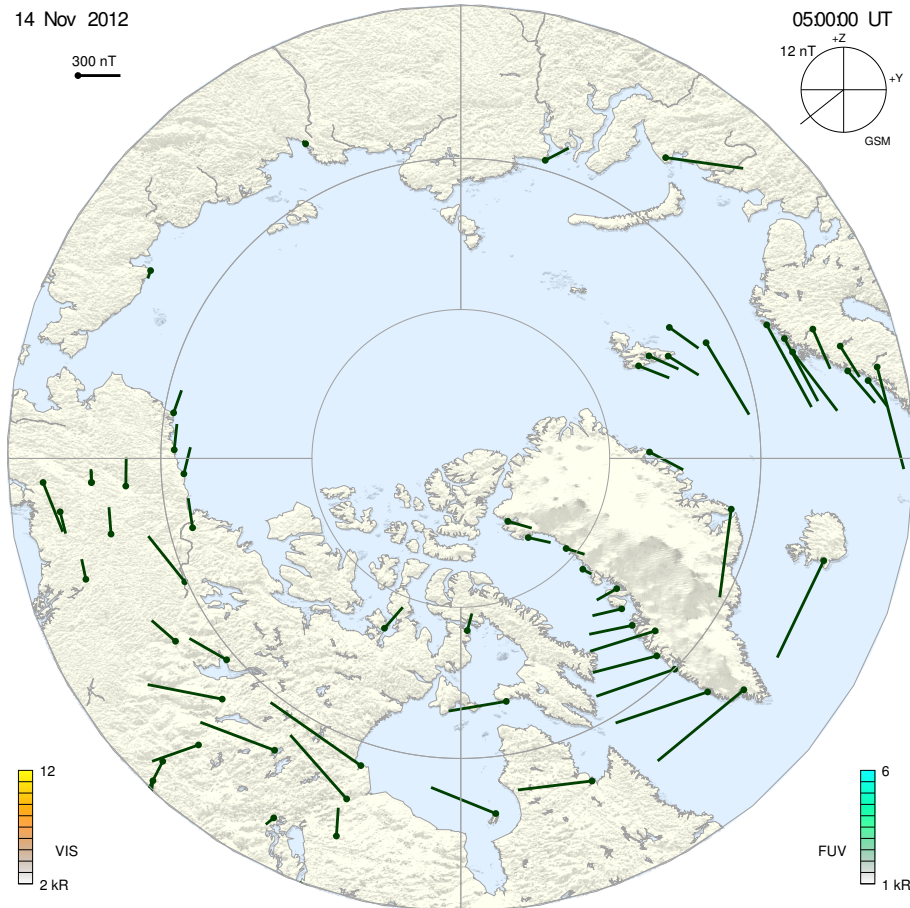


Figure 3.9: Plot showing magnetic perturbations observed by the SuperMAG experiment in the northern hemisphere on 14 November 2011 at 05:00 UT. Taken from the SuperMAG website.

3.3 SuperMAG

SuperMAG is a project which collates data from many magnetometers and chains of magnetometers worldwide, removing the baseline at each magnetometer to give the magnetic perturbation measured by each (Gjerloev, 2009, 2012). The SuperMAG indices of the maximum magnetic perturbation due to the eastward electrojet (SMU) and the maximum perturbation due to the westward electrojet (SML) were obtained and are utilised in this thesis. These indices are the upper and lower envelope of perturbations measured by observatories with latitudes 40–80° in the northern

hemisphere, and are the SuperMAG equivalent of the AU and AL indices described in Section 3.2.2 (it should be noted that the AU and AL indices are official geomagnetic indices, and the SML and SMU indices are not). Instead of being calculated with 12 magnetometers across the polar region, the SuperMAG indices are calculated using over 100 stations, meaning features that may be missed by the official indices will be shown in the equivalent SuperMAG-derived data (Newell and Gjerloev, 2011a). Figure 3.9 shows an example of the magnetic perturbations seen by SuperMAG magnetometers in the northern hemisphere.

The SuperMAG substorm list, which is also used in this thesis, is generated using an algorithm which examines the SML index (Newell and Gjerloev, 2011a,b). The onset of a substorm expansion phase is identified at $t = t_0$ (in minutes) when these criteria are satisfied:

$$\text{SML}(t_0 + i) - \text{SML}(t_0) < -15i \text{ nT} \quad i = 1, 2, 3 \quad (3.16a)$$

$$\sum_{i=4}^{29} \frac{\text{SML}(t_0 + i)}{26} - \text{SML}(t_0) < -100 \text{ nT} \quad (3.16b)$$

These criteria test for magnetic bays which are steep in the initial 3 minutes but sustained over a period of 30 minutes. Whenever this signature is observed, t_0 is recorded in the substorm list available from SuperMAG, alongside the latitude and MLT of the observatory which observed the magnetic bay. It should be noted that some SuperMAG substorms are recorded as having MLTs corresponding to the dayside of Earth; these substorms are eliminated from the list before it is used, leaving 2900 substorms for use in this thesis.

In order to perform the analysis of Chapter 5, the substorm list is subdivided by the colatitude of the region 1 Birkeland current oval l_1 at the time of substorm expansion phase onset t_0 . This allows investigation into how substorms are affected by the amount of open magnetic flux in the magnetosphere at the time of substorm onset. Consequently, it is useful to bin the substorm onsets by l_1 and then plot a histogram of the number of onsets in each bin.

The distribution of the onset colatitudes of the SuperMAG substorm list is presented in Figure 3.10, which shows substorms distributed between $\sim 10^\circ$ and $\sim 25^\circ$ and a peak measured at an onset colatitude of 18° . The number of substorms in each bin varies somewhat between the northern and southern hemisphere, with ~ 550 substorms seen at the peak in the northern hemisphere and ~ 500 substorms in the southern hemisphere. However, the distribution in both hemispheres is similar.

Five bins are defined into which substorms can be sorted by onset colatitude. These bins are denoted I-V, and defined as follows. I: $0^\circ < \phi \leq 15^\circ$; II: $15^\circ < \phi \leq$

17°; III: $17^\circ < \phi \leq 19^\circ$; IV: $19^\circ < \phi \leq 21^\circ$; V: $21^\circ < \phi \leq 30^\circ$. This categorisation is employed in Section 5.2.2.

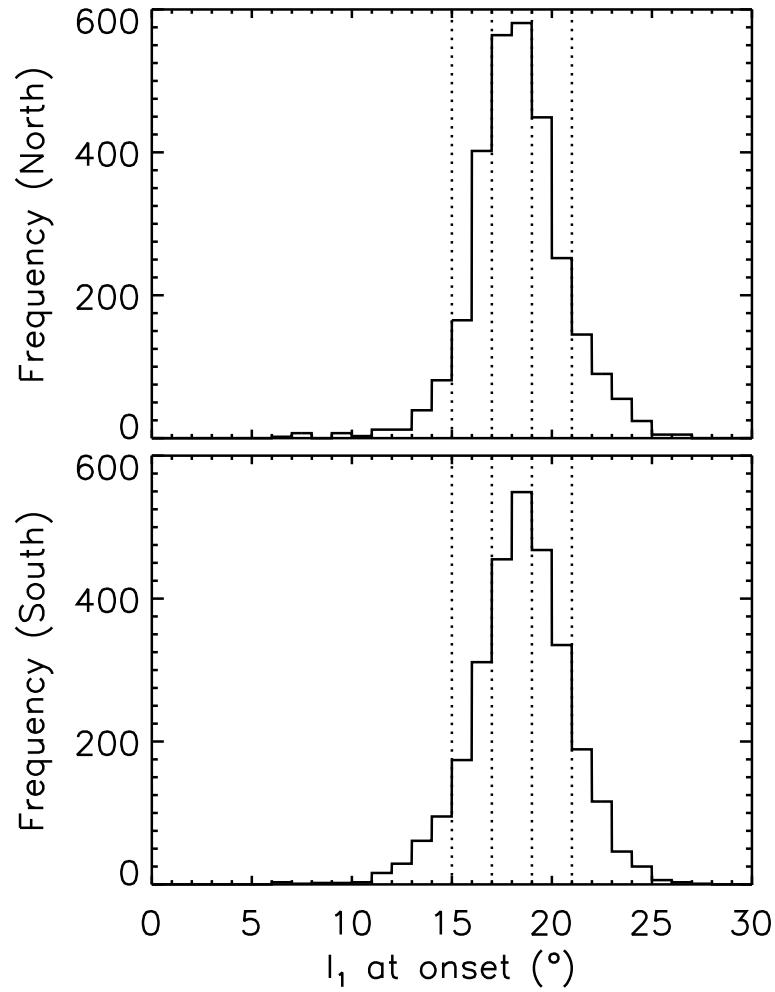


Figure 3.10: Histograms showing the value of l_1 for the Region 1 current oval at $t = 0$ min (substorm onset) for the northern (top) and southern (bottom) hemispheres. Larger values of l_1 at onset imply more active geomagnetic conditions prior to the onset of the substorm. The dotted lines show the boundaries of bins defined in Section 3.3.

Chapter 4

Birkeland currents and their role in solar wind - magnetosphere - ionosphere coupling

4.1 Introduction

As outlined earlier in this thesis, the magnitudes of the Birkeland currents are expected to be driven by a combination of dayside and nightside magnetic reconnection. As a result, it is desirable to examine the reaction of the Birkeland currents to both dayside and nightside reconnection rate. This is done by separating the currents into regions 1 and 2 currents using the technique in Section 3.1.2, before calculating their magnitudes over the three year period 2010–2012 and comparing them to Φ_D and AL index (as a proxy for Φ_N) for the same period. The correlation between the current amplitudes and these two variables is calculated, and the parameter space is explored to yield information about how current magnitudes vary with magnetic reconnection.

4.2 Four day example of reconnection driving the Birkeland currents

Figure 4.1a and 4.1b depict the Birkeland current density as a cut along the dawn-dusk meridian as observed by AMPERE in the northern and southern hemispheres respectively for a 4 day period in September 2010. This format shows the magnitudes of the currents as well as the latitudinal distribution, especially the variations in

latitude at which currents are observed. Panel c presents the magnitude of R1 and R2, J_1 and J_2 , calculated as before. Panel d shows the ratio J_1/J_2 . (Since there is a close correspondence between the northern and southern hemisphere throughout the data set, only the northern hemisphere is plotted; this will be the case throughout this chapter.) Panel e shows Φ_D as calculated by Equation 2.3 using OMNI data and panel f shows the AL and AU indices.

Figures 4.1a and b show that the current density varies significantly with time, and Figure 4.1c shows the same for current magnitude, including periods of quiescence (before 06:00 UT on 5 September and after 04:00 UT on 8 September) and periods of stronger current magnitudes seen throughout the rest of the interval. The current densities vary up to $1.2 \mu\text{A m}^{-2}$ both downwards (blue) and upwards (red). Stronger current magnitudes occur during periods of strong dayside reconnection and weaker magnitudes occur when dayside reconnection wanes (Figure 4.1e). This relationship is further demonstrated by plotting the current magnitudes against Φ_D in Figure 4.2a and 4.2c. The Pearson correlation coefficient $r = 0.60$ for Φ_D and J_1 , and $r = 0.61$ with J_2 , demonstrating a correlation during this period. Using the PCORRE function from the SolarSoftWare library to calculate the significance of both correlations yields significance levels below 10^{-15} . The AL and AU indices shown in panel f also have quiet periods at the start and end of the interval, with very little activity before 07:00 UT on day 1 and very little activity after 04:00 UT on day 4.

The current magnitudes in Figure 4.1c vary between 1 and 3 MA for most of the interval, with dips to 0.5 MA and peaks of 3.5 MA also observed. However, there are also periods in which the current densities are too low for the fitting technique to work. The first period falls within the first low current density interval, occurring between 00:00 UT and 04:00 UT on 5 September. The next periods occur between periods of stronger current density: at 00:00 UT and 23:00 UT on 6 September, and 10:00 UT and 14:00 UT on 7 September. The final period is after 04:00 UT on 8 September, in the final quiescent period.

The current ovals are located between colatitudes of 10° and 30° . These vary over time, with several excursions occurring in both hemispheres simultaneously, associated with expansions and contractions of the polar cap (Clausen *et al.*, 2013b). Substorm onsets are identified by characteristic negative bays in SML, marked by vertical dashed lines. It is observed that each substorm onset is preceded by a movement of the currents to lower latitude (substorm growth phase) and are followed by contractions to a higher latitude (substorm expansion phase). Substorms are in general associated with increases in current magnitude, and the current magnitudes are plotted against AL index in Figure 4.2b and 4.2d. The Pearson coefficient

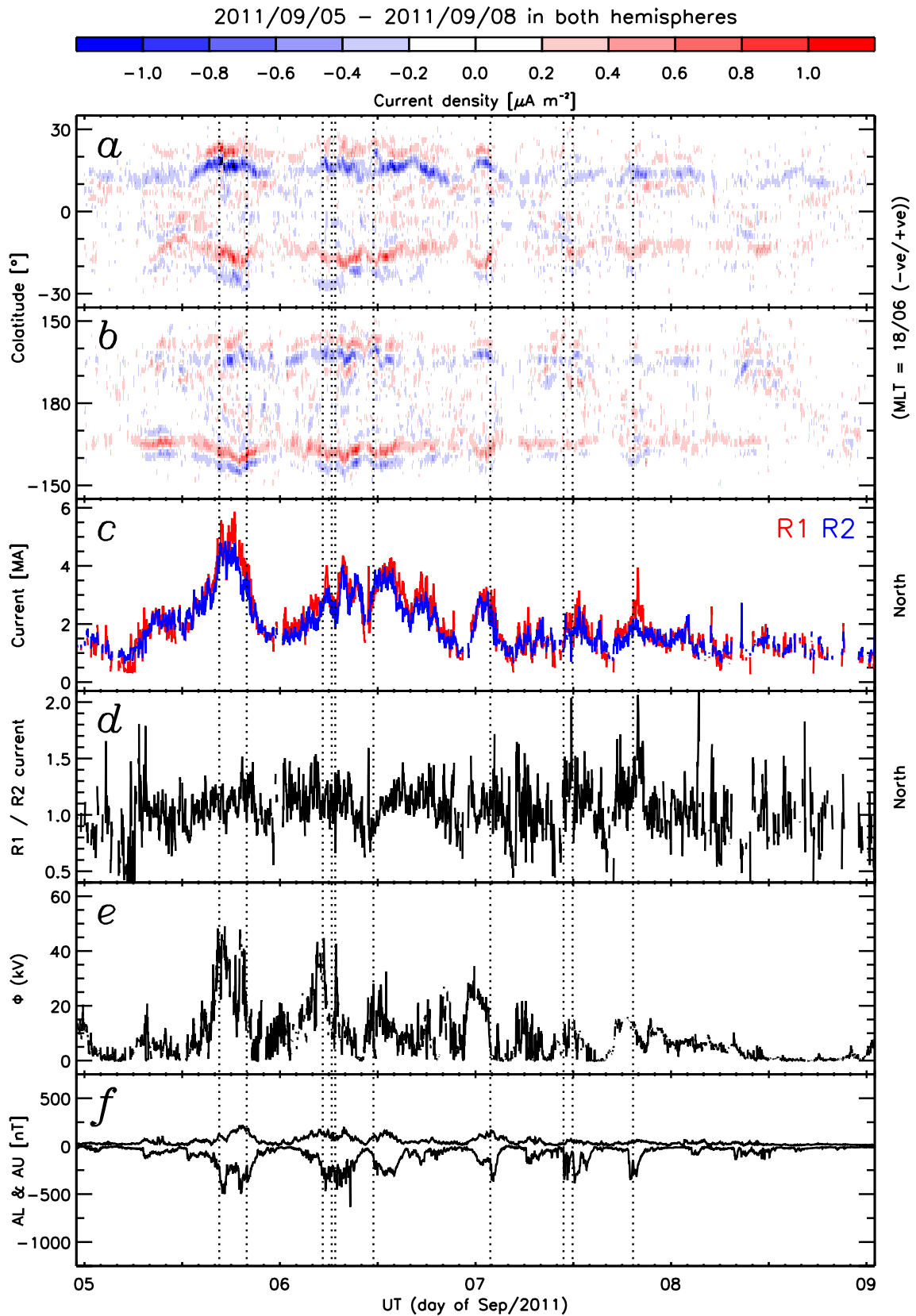


Figure 4.1: Diagram showing the 4 days beginning at UT = 2011-09-05 00:00:00. From top to bottom: Keograms showing the dawn-dusk meridian for a) the northern hemisphere and b) the southern hemisphere; c) the R1 current magnitude J_1 (red) and R2 current magnitude J_2 (blue) for the northern hemisphere; d) J_1/J_2 in the northern hemisphere; e) the dayside reconnection rate Φ_D ; f) the AL and AU indices. The southern hemisphere is not plotted due to the close correspondence between northern and southern hemisphere variations. Vertical dashed lines represent the times of substorms from the SuperMAG substorm list (Newell and Gjerloev, 2011a,b).

$r = -0.55$ between AL index and J_1 and between AL and J_2 ; the coefficient is the same to within two decimal points for the two, and the significance level for both is lower than 10^{-15} . These are slightly lower correlations than those seen with Φ_D .

4.3 Current magnitude variations with magnetic reconnection rates on the day and nightside

Now the temporal variation of the current systems has been described, the statistical relationship between R1 and R2 current magnitude and dayside and nightside driving is explored by employing three years of AMPERE data (2010–2012). The magnitudes of the Region 1 Birkeland currents have been plotted against the magnitudes of the Region 2 currents, shown in Figure 4.3a as an occurrence frequency diagram with bins of 0.2 MA.

The magnitudes of the Birkeland currents are strongly positively correlated, but the figure is asymmetrical about the white and blue dashed line which shows the line of equality. At low current magnitudes J_1 and J_2 are roughly equal, although J_1 begins to dominate over J_2 above 1 MA and J_2 seemingly dominates at very low magnitudes. At higher R1 currents, the ratio J_1/J_2 increases on average to about 1.15, as indicated by the red and black dashed line, which is a plot of the mean of J_2 in a series of bins of J_1 which are 0.25 MA wide, effectively giving the ratio between the two.

The colour-coding in Figure 4.3a shows the number of data in each of the plotted bins. This shows that the majority of the AMPERE dataset is made up of currents in both regions between approximately 0.2 MA and 4 MA. Figure 4.3b depicts the currents' magnitudes colour-coded by the mean of Φ_D in a given pixel, whereas in Figure 4.3c they appear colour-coded by the mean of AL index, since it has been shown that westward electrojet current is approximately proportional to the nightside reconnection rate (Holzer *et al.*, 1986). It is immediately obvious that the two are very similar; both day- and nightside reconnection are expected to drive Birkeland current magnitude.

Another feature visible in Figure 4.3b and 4.3c is the vertical stripes in the colour code. This indicates that R1 current is more strongly driven by the dayside and nightside reconnection rates than R2 current. Consequently, it is difficult to use Figure 4.3 to satisfactorily examine the dependence of the R2 current magnitudes on these drivers, and in Section 4.4, the two current systems will be plotted separately in order to better examine the behaviour of the R2 currents.

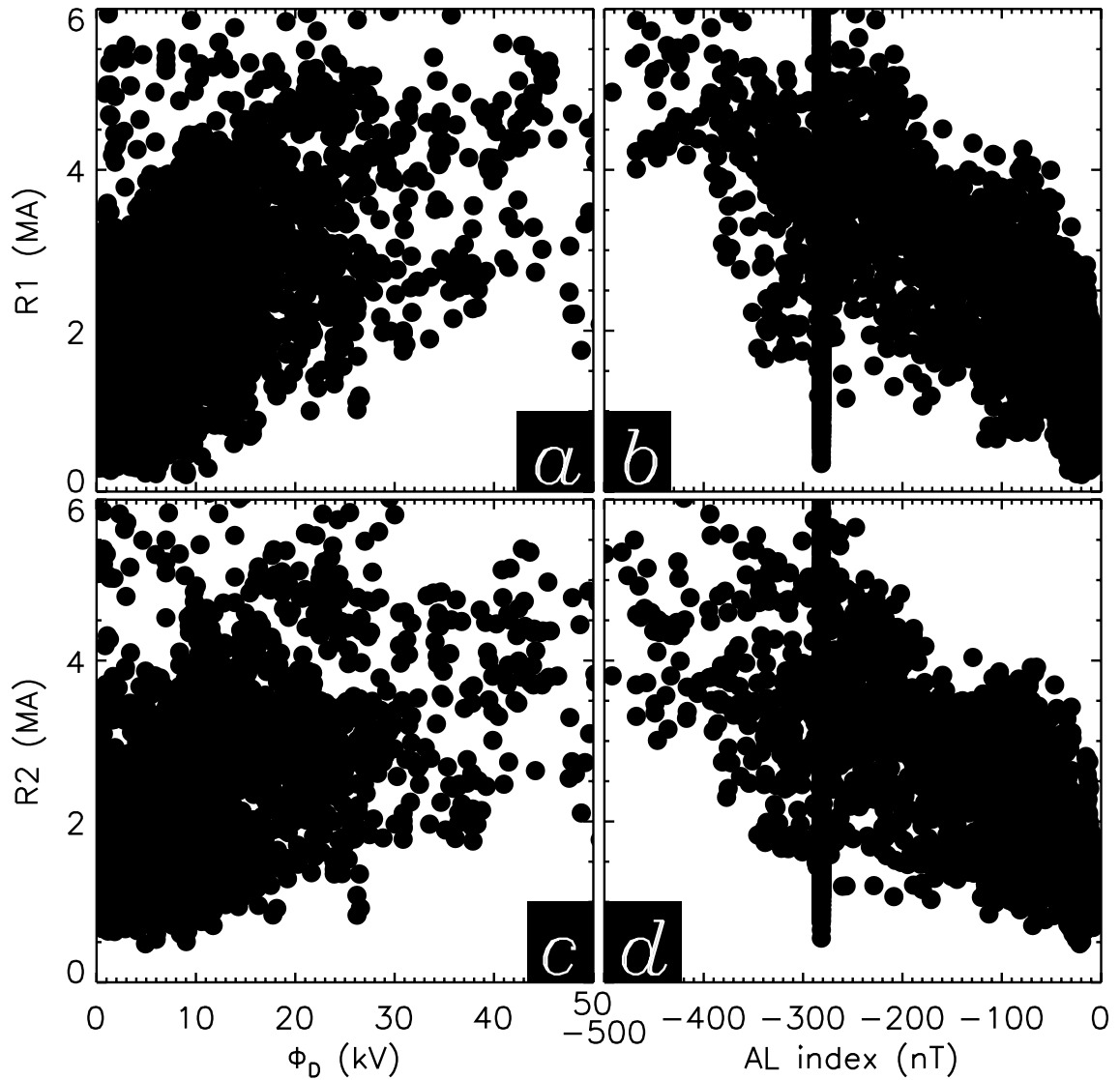


Figure 4.2: Diagram showing data from the 4 days plotted in Figure 4.1 beginning at UT = 2011-09-05 00:00:00. The top two panels show the R1 current magnitude J_1 plotted against a) Φ_D and b) AL index. The bottom two panels show the R2 current magnitude J_2 plotted against c) Φ_D and d) AL index. The correlation coefficients pertaining to each panel are detailed in the text.

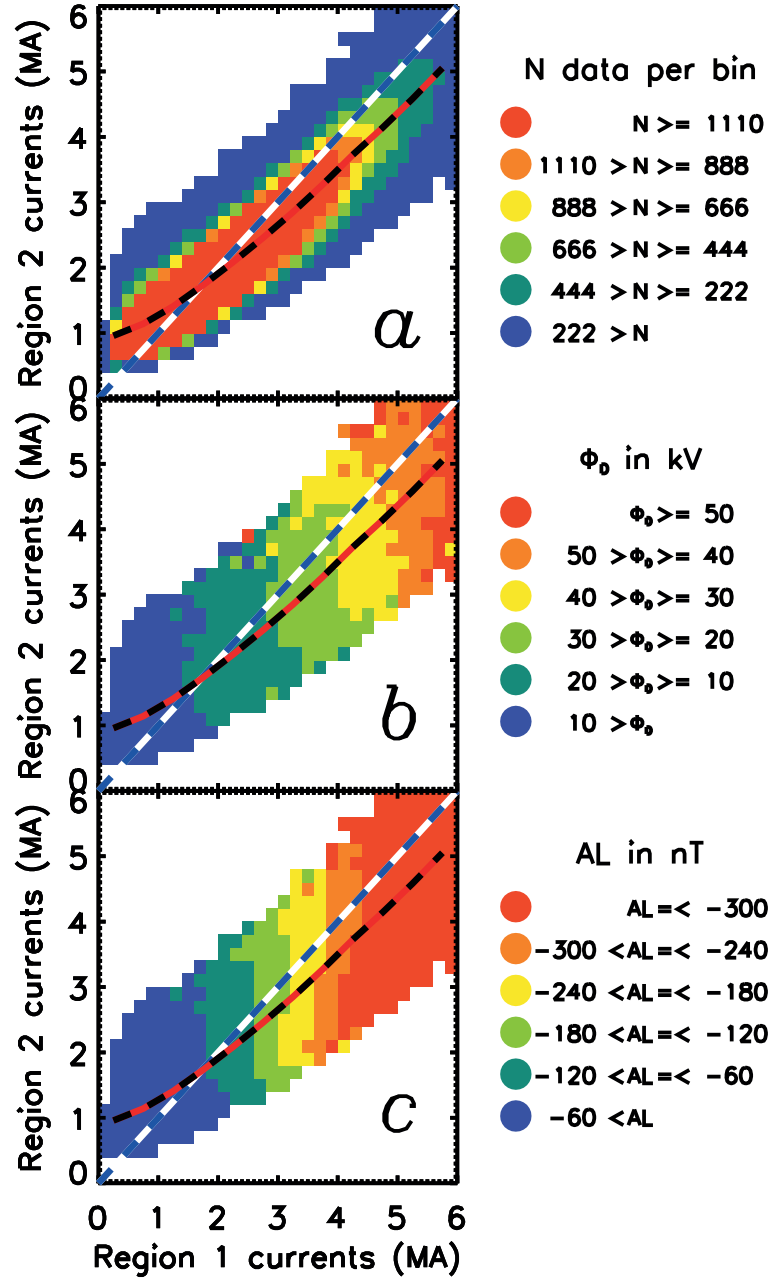


Figure 4.3: J_1 plotted on x and J_2 plotted on y , colour-coded by a) number of data per bin, b) dayside reconnection rate Φ_D in kV and c) AL index in nT. Where there are fewer than 10 points contributing to a bin, that bin is left white. The colour code for each panel is to the right of the panel. The white and blue line is the line of unity whilst the red and black line is the mean of J_2 in a series of bins of J_1 which are 0.25 MA wide. The standard deviations are plotted in Figure 4.4.

Higher currents are clearly correlated with faster reconnection. The Pearson coefficient $r = 0.64$ for Φ_D and J_1 and $r = 0.63$ in the case of J_2 , showing that R1 currents are slightly better correlated, consistent with the vertical stripes in Figure 4.3. Correlating the two with AL index, it is found that for J_1 , $r = -0.83$ and for J_2 , $r = -0.78$, showing that R1 currents are again better correlated. As in Section 4.2, these correlations are all significant at the 10^{-15} level.

The standard deviations of the values from Figure 4.3 are shown in Figure 4.4. The standard deviation is larger as the magnitudes of the currents increase, which is consistent with increasing values in the variables generally and also consistent with fewer points in each bin at larger current magnitudes. In the case of the dayside reconnection rate the standard deviation is over half the value of the mean; the standard deviation is below half the value of the mean for AL index. The high standard deviations can be interpreted to show that the spread in values of the two variables for a given combination of current magnitudes is high. Given that the two variables employed are estimates of the dayside and nightside reconnection rates, and given that high current magnitudes are expected to occur when either one is large, it makes sense that the spread of the points of one such variable in each bin would in turn be relatively large.

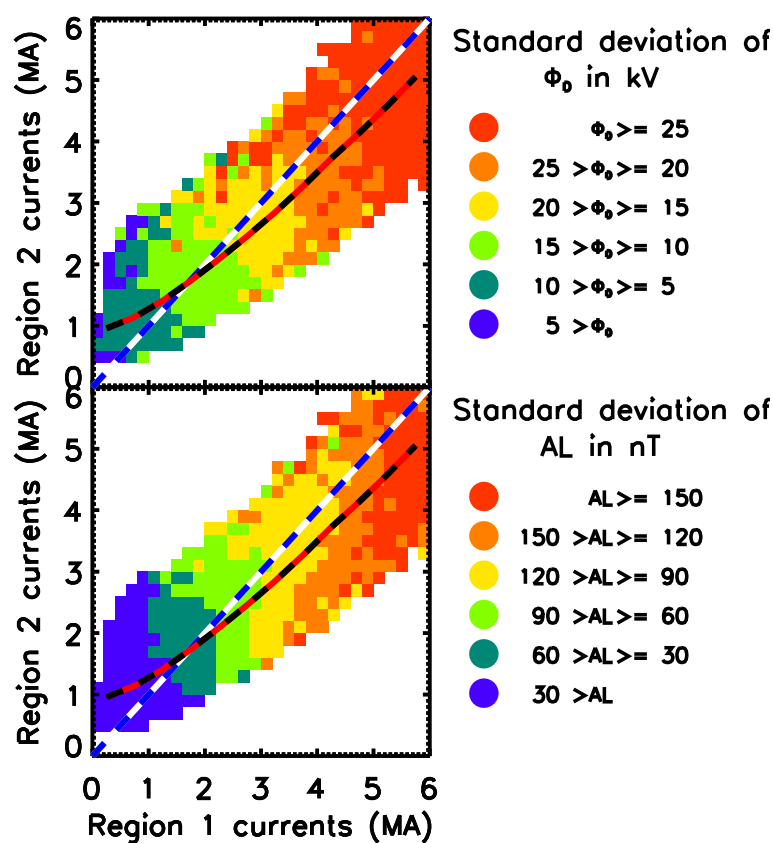


Figure 4.4: J_1 plotted on x and J_2 plotted on y , colour-coded by the standard deviation of (top) dayside reconnection rate Φ_D in kV and (bottom) AL index in nT. Where there are fewer than 10 points contributing to a bin, that bin is left white. The white and blue line is the line of unity whilst the red and black line is the mean of J_2 in a series of bins of J_1 which are 0.25 MA wide. The colour code for each panel is to the right of the panel: the colours are half the values of Figure 4.3.

4.4 R1 and R2 variations with reconnection rate examined separately

Figure 4.5 shows the Birkeland current magnitudes plotted against dayside reconnection rate Φ_D (panels a, c, e, g) and against the AL index (panels b, d, f, h), with R1 currents on the left of the figure and R2 currents on the right. The data is presented in this fashion in order to attempt to better examine the R2 currents, both in isolation and compared to the R1 currents. Figure 4.5a, b, e and f show this relationship colour-coded by the number of data per bin N (the colour-coding is the same between Figure 4.3 and Figure 4.5 for every variable). It can be seen that the majority of the points lie where $I < 4$ MA and either $\Phi_D < 50$ kV or $AL > -300$ nT, with small amounts of data elsewhere in the parameter space. The correlation between current magnitude and dayside reconnection rate can be seen in the main population (those bins not coloured blue), which clearly shows that higher current magnitudes are observed for higher values for Φ_D . A similar correlation can be seen for AL index.

Firstly, the relationship between the Birkeland currents and the dayside reconnection rate is focused upon. Figure 4.5a and 4.5e highlight that R1 is generally slightly more strongly correlated with Φ_D than R2 is. Figure 4.5c shows the same parameter space as in Figure 4.5a, but this time colour-coded by AL index. In R1, a given magnitude is strongly correlated with a specific value of AL index, as visible in the almost horizontal striations in the colour-coding by AL, with magnitudes of below 1.5 MA associated with an AL index of above -80 nT and magnitudes above 4 MA associated with an AL index of below -400 nT. In R2, as shown by Figure 4.5g, a given magnitude is associated with either a high dayside reconnection rate and high AL index, as seen by 2 MA currents occurring at $\Phi_D \simeq 90$ kV and an AL index of approximately -200 nT, or by a low dayside reconnection rate and slightly lower AL index, as seen by 2 MA currents occurring at $\Phi_D < 20$ kV and $AL \simeq -120$ nT.

Turning now to the AL index, Figure 4.5b and 4.5f shows that the R1 current is better correlated with AL index than R2 current is. Figure 4.5d is colour-coded by Φ_D , which shows striations in R1 currents similar to those in Figure 4.3. R1 currents of around 2 MA are driven by $\Phi_D \simeq 20$ kV whereas R1 currents of around 4 MA are driven by $\Phi_D \simeq 40$ kV. Figure 4.5h shows that R2 currents of 3 MA can be driven by high AL index and high dayside reconnection (~ 80 kV, ~ -400 nT) or by low dayside reconnection and a lower AL index (~ 20 kV, ~ -280 nT).

Figure 4.6 shows the parameter space of AL index versus Φ_D colour-coded by

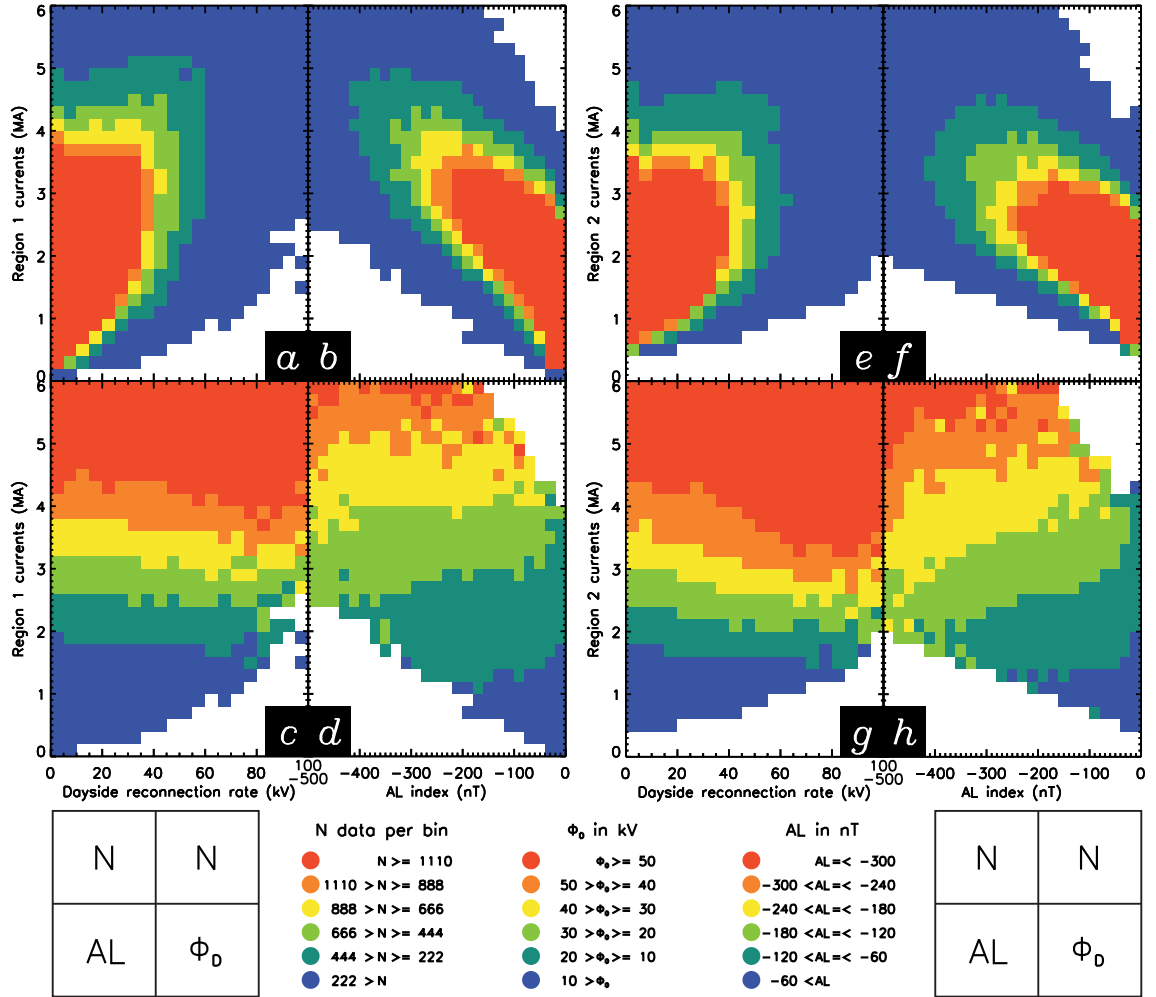


Figure 4.5: J_1 (a-d) and J_2 (e-h) plotted against Φ_D (a, c, e, g) and AL index (b, d, f, h). These are then colour-coded by number of data per bin (a, b, e, f), by AL index in nT (c, g) or by Φ_D in kV (d, h). Where there are fewer than 10 data contributing to a bin, that bin is left white. The colour codes are given underneath (and are the same as for Figure 4.3); the grids on either side describe the variable by which each panel is colour-coded.

R1 and R2 Birkeland current magnitude (panels a and b, respectively). This clearly indicates that for a given combination of Φ_D and AL index the R1 currents tend to be of higher magnitudes than R2. The diagram also demonstrates that R1, again, can be driven to higher magnitudes than R2 by the AL index, reinforcing the observed disparity in correlation between the two current systems and AL. At an AL index of -175 nT with no dayside reconnection, for example, $2.0 \text{ MA} \leq R1 < 2.5 \text{ MA}$, whereas $1.5 \text{ MA} \leq R2 < 2.0 \text{ MA}$.

At this point, it should be noted that the dayside reconnection rate Φ_D is responsible for driving the Hall current systems. Since the AL index measures magnetic perturbations due to the Hall currents, the two variables are not independent. The correlation coefficient between Φ_D and AL index $r = -0.59$ at a significance level of 10^{-15} . Figure 4.7 shows the number of data in each bin, both illustrating this

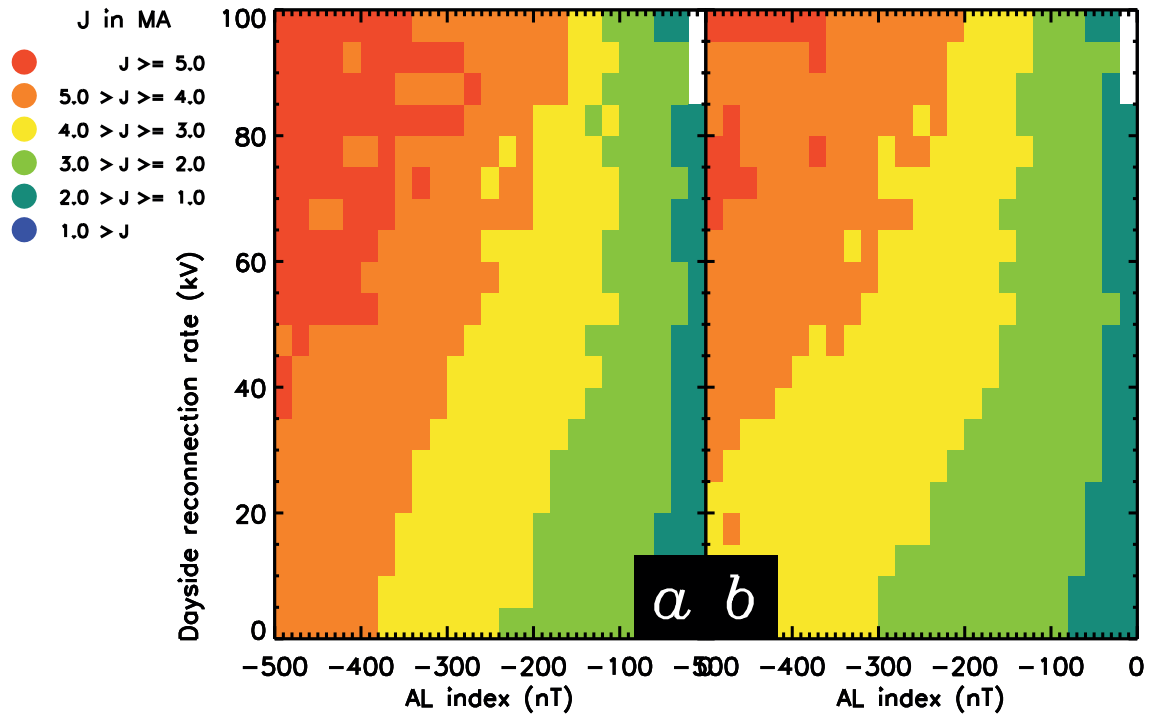


Figure 4.6: Panels showing AL index plotted against Φ_D , colour-coded by (a) J_1 and (b) J_2 . Where there are fewer than 10 data contributing to a bin, that bin is left white. The colour code is depicted on the left and is the same for both J_1 and J_2 .

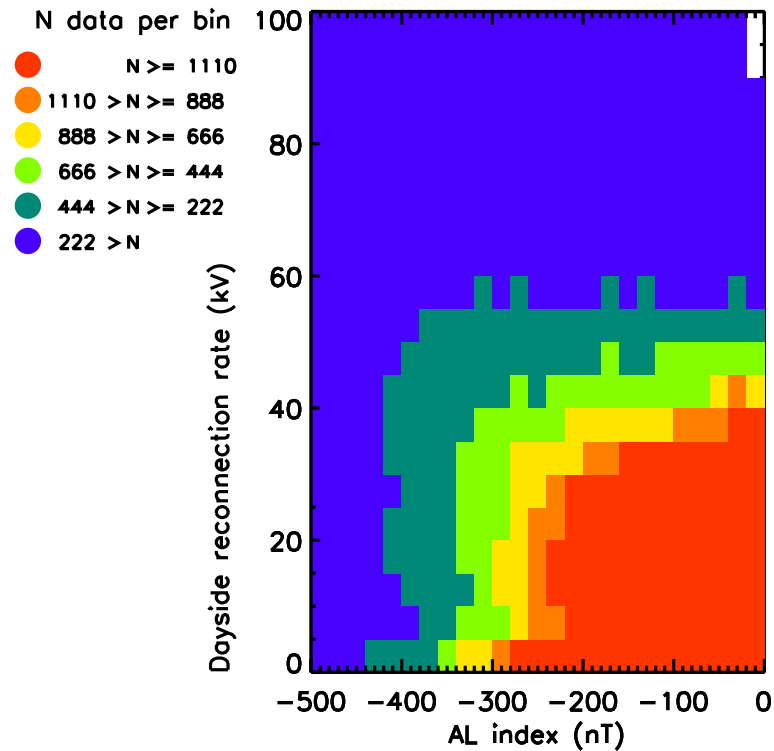


Figure 4.7: AL index plotted against Φ_D , colour-coded by the number of data in each bin. Where there are fewer than 10 data contributing to a bin, that bin is left white. The colour code is depicted on the left, and is the same as the one employed in Figures 4.3 and 4.5.

and providing context for the two panels in Figure 4.6. It can be seen that there is a trend in the data, with low dayside reconnection rates corresponding to low AL indices, and higher dayside reconnection rates present at higher AL indices. However, it should also be noted that there are also times at which AL index is large but dayside reconnection rate is small, and vice versa; this makes sense in terms of substorms driving larger AL index values when dayside reconnection is small.

4.5 Discussion

We have used observations from the AMPERE dataset to estimate the current magnitudes flowing in the regions 1 and 2 Birkeland current system. It has been demonstrated that these currents are dependent on the dayside reconnection rate, quantified by Φ_D , and nightside reconnection, for which the AL auroral geomagnetic index is used as a proxy. These findings are now discussed in more detail.

Comparing the magnitudes of the R1 and R2 currents, it is found that the currents are approximately equal at a magnitude of ~ 1 MA (Figure 4.3a). R1 currents begin to dominate above this point and the currents are, for values greater than ~ 1 MA, in the ratio $J_1/J_2 \simeq 1.15$ (which is slightly lower than in the interval shown in Figures 3.4 and 3.2). This is explained as R2 currents must close through ionospheric Pedersen currents to the R1 currents, whereas R1 currents can additionally close via Pedersen currents across the polar cap through R1 currents of the opposite polarity (see Figure 1.16). It is also possible that the R1 currents can close across the high-conductance auroral bulge. At times of low current magnitude and therefore low geomagnetic activity, the polar cap is likely to be of lower conductance due to the lack of particle precipitation, impeding the flow of Pedersen currents such that the R1 current system must close through the R2 current system, explaining the lack of R1 dominance at lower magnitudes. Times are also observed at which $J_1/J_2 < 1$, indicating more current flowing in the R2 current system (this can be seen in Figure 4.3 and also in Figure 4.1, particularly after substorms vi and vii). The R2 domination is observed during periods of low reconnection rate for which there are fewer data, possibly indicating this effect is not well-constrained. However, this may also indicate a relationship to the region 0 current system during periods of northward IMF. More work is required to assess the behaviour of FACs during such times.

During the four day period presented in Figure 4.1, eleven substorms have been identified from their characteristic negative perturbations in the AL index. These substorms tend to be preceded by periods of elevated dayside reconnection Φ_D . As

indicated by the measured correlation, the current systems intensify at these times and the current ovals move to lower latitudes as open magnetic flux accumulates in the magnetosphere (Milan *et al.*, 2003, 2007, 2012; Clausen *et al.*, 2012). At the time of substorm onset the current systems retreat to higher latitudes and the currents reintensify. At some points in the period presented in Figure 4.1, similar current magnitudes are observed at times of somewhat different levels in Φ_D and AL index. This indicates that although the reconnection rate plays an important role in driving these currents, other factors (such as ionospheric conductivity) may also influence the strength of the currents flowing: this is an area of further research. During the four day period the J_1/J_2 ratio appears to increase such that the R1 current is stronger than R2: it is probable that this is caused by a divergence of cross-tail current through the substorm current wedge (Clausen *et al.*, 2013b,a), but more work is needed to better quantify the temporal reaction of currents to substorms.

Further study of current changes through substorms, combined with observations of the convection pattern, and models which link these two phenomena (Milan, 2013) will play a crucial role in understanding solar wind-magnetosphere-ionosphere coupling. To this end, the relation of the reconnection rate to the current magnitudes has been studied statistically (Figures 4.3b and 4.3c). The reconnection rate is observed to be driving R1 current magnitude, as the highest values of Φ_D and AL index are well-correlated with the strongest current magnitudes. This can also be seen in the temporal presentation of the data (Figure 4.1): the low reconnection rates seen at the start and end of the interval appear to be driving low current densities and low current magnitudes seen in panels a, b and c. When Φ_D and AL index decrease after substorms vi and vii, the current density and magnitude respond by diminishing.

Previous studies have demonstrated that the ionospheric convection patterns observed in the ionosphere are driven by the direction of B_z being either north or south, with southward IMF driving a twin-cell convection pattern (Lockwood, 1991; Cowley and Lockwood, 1992) and northward IMF driving a more complex pattern (Imber *et al.*, 2006). The location of R1 and R2 field-aligned currents is related to the structure of the ionospheric convection pattern. The observations of higher Birkeland current magnitudes during periods of faster dayside reconnection imply that during periods of stronger ionospheric convection the Birkeland currents are enhanced, since dayside reconnection also drives ionospheric convection, and this is in agreement with previous work (Cowley, 2000; Milan, 2013; Juusola *et al.*, 2014).

Gjerloev *et al.* (2011) suggest that current amplitudes on the dayside are not driven by B_z . Because B_z is expected to drive Φ_D and therefore indirectly drive J , the correlation between B_z and J was examined (not shown). It was found that for

J_1 , $r = -0.46$ and, for J_2 , $r = -0.43$. This is not a strong correlation, indicating that Φ_D is clearly better correlated to the current magnitudes. However, previous studies have indicated observations of stronger currents on the dayside and on the nightside during periods of southward IMF (Rostoker *et al.*, 1982; Papitashvili, 2002; He *et al.*, 2012; Juusola *et al.*, 2014) and case studies performed using AMPERE also support this observation (Anderson *et al.*, 2014). Consequently the observed moderate correlation is interpreted as evidence for the role of B_z in current driving.

Rostoker *et al.* (1982) observed that, in addition to southward IMF, stronger field-aligned currents were driven by northward turnings in the IMF associated with substorms. There is some controversy on the exact mechanism by which a substorm is triggered, but the results suggest that current magnitude is enhanced alongside the AL index which is associated with substorm onset and nightside reconnection. In this case, the results of Rostoker *et al.* (1982) are interpreted as an indication that it is nightside reconnection, rather than northward IMF, that strengthens the current.

Figure 4.3b and c depict a strong correlation between Φ_D and AL index with R1 currents but imply that R1 is more strongly correlated than R2. This relationship is studied more closely with the aid of Figure 4.5. The correlations between Φ_D and J show only a 0.01 difference between R1 and R2, but R1 currents are more strongly correlated with AL index than R2 and AL, suggesting that any observed disparity in the magnitude of the two systems is more driven by periods of high AL index and high nightside reconnection rate.

Examining Figure 4.6 to further examine the reaction of currents to AL index, the R1 current is observed to be stronger at a given combination of Φ_D and AL index than R2, and that this effect is most pronounced during periods of low Φ_D . This further indicates that more R1 current closes through the R1 current system (on the other side of the polar cap) when nightside reconnection dominates, which requires a greater amount of current flow across the noon-midnight meridian. Since the AL index is a signature of the westward substorm electrojet, it is inferred that this increased current flow is made possible by the substorm electrojet across the noon-midnight meridian, and that this accounts for most of the observed R1-to-R1 current closure, explaining why AL is better correlated to J_1/J_2 than Φ_D is.

These results suggest that reconnection plays a dominant role in exciting the currents which transfer stress to the ionosphere to produce the ionospheric convection pattern, which is known to be excited during substorm growth phase and onset (Grocott *et al.*, 2009). It also suggests that tail dynamics and their electrical connection to the ionosphere can be monitored with this technique.

4.6 Conclusions

The work presented here gives an overview of the Birkeland currents on large scales in the AMPERE dataset and also their reaction to the solar wind, interplanetary magnetic field and day- and nightside reconnection rates. It has been shown that R1 tends to be stronger than R2 at current magnitudes above ~ 1 MA, with the peak of the ratio between R1 and R2 being ~ 1.15 at ~ 4 MA.

The results presented in this chapter can be interpreted in the context of R1 current being driven by ionospheric flows which are ultimately driven by reconnection on the dayside and the nightside. While R2 is also well-ordered by comparison to these drivers that current system is perhaps somewhat more complex, with R2 currents weaker than R1 by AL index during slow dayside reconnection rates. It is inferred that this is a signature of the westward electrojet allowing R1 currents to close across the polar cap and through the region 1 system on the other side.

Both dayside and nightside reconnection are key to driving the Birkeland currents, with both appearing to play a vital role in strong current magnitudes. This makes sense in the context of an R1 current that maps to the magnetopause and the magnetotail, and an R2 current that maps to the partial ring current on the nightside of the Earth.

Chapter 5

A superposed epoch analysis of the Birkeland currents during substorms

5.1 Introduction

Chapter 4 shows that Birkeland current magnitudes are consistent with the theory that currents are driven by ionospheric convection which is, in turn, driven by dayside and nightside magnetic reconnection. It was also shown that the region 1 current magnitudes tend to be higher than region 2. This chapter aims to expand upon these statements by performing a superposed epoch analysis of substorms observed by the SuperMAG experiment over the same three-year period as Chapter 4. The spatial evolution of the current ovals through a substorm is examined, as is the evolution of the regions 1 and 2 current magnitudes. This will allow the reaction of Birkeland currents to substorms, and therefore nightside reconnection, to be discussed.

5.2 Superposed epoch analysis

We use the substorm onset times identified by SuperMAG to form a superposed epoch analysis of the parameters of interest, including the R1 and R2 current magnitudes J_1 and J_2 , oval colatitudes l_1 and l_2 , dayside reconnection rate Φ_D , and geomagnetic indices SMU and SML. The analysis covered the period from 2 hours before substorm onset to 2 hours after. In the first instance, the analysis was performed on all 2900 substorms. Subsequently, the analysis was performed on subsets

of substorms binned by onset colatitude. There are cases in which substorm onsets occur within two hours of one another (so that the four-hour window would contain multiple substorms; a case which can clearly be seen around dawn on 6 September 2011 in Figure 4.1). No onsets were filtered out based on this criterion, however, such that the analysis presented includes some cases of substorm onsets occurring within two hours of one another. The window of two hours in each direction was selected as the window based on an average substorm periodicity of 2.5 hours (Parks and Winckler, 1968).

In Figures 5.1, 5.2, 5.3 and 5.4, solid lines are used to indicate the median of the data plotted, while shaded areas are drawn which describe the upper and lower quartiles of the data in each plot. In order to differentiate between R1 and R2 currents, red and blue are used respectively for both the solid lines and shaded areas. Purple shading is used to indicate the areas in which the quartiles overlap.

5.2.1 Quantifying the reaction of the coupled magnetosphere-ionosphere system to substorms

In Figure 5.1 the median response of the Birkeland currents to substorm onset is shown. From top to bottom: the variation of colatitude l_1 relative to the onset colatitude, the variation in l_1 , the variation in the R1 and R2 current magnitudes, the ratio R1/R2, the expected dayside reconnection rate Φ_D and the SML and SMU indices (Newell and Gjerloev, 2011a). For ease of reading, SML is described in terms of its magnitude, neglecting the sign of the perturbations it measures, which means that an increase in SML would indicate a transition to more negative magnetic perturbations.

In panels a-d, the change in position of the current ovals is observed. In panels a-b, Δl_1 is calculated by subtracting the value of l_1 at $t = 0$ min from l_1 , to examine the change in latitude with respect to the value at the substorm onset. In panels c-d, l_1 itself is plotted. It is seen that the current ovals expand to lower latitudes (higher colatitudes) as substorm onset approaches and then begin to contract again at $t \sim 10$ min. The R1 current oval starts at approximately 17° whereas R2 starts at approximately 21° – both ovals expand and then contract back to their pre-onset state. The change in the latitudinal extent of the current ovals varies over a range of 2° latitude during the four-hour period, as demonstrated by panel a, in which Δl_1 is seen to vary between -1.5 and 0.5 (with the latter value occurring ten minutes subsequent to onset). Both current ovals are seen to expand at the same rate until onset, at which point R2 continues to expand at the same rate while R1 does not, indicating a broadening in latitude of the current system. R2 is more sluggish than

Birkeland current parameters for 2576 substorms

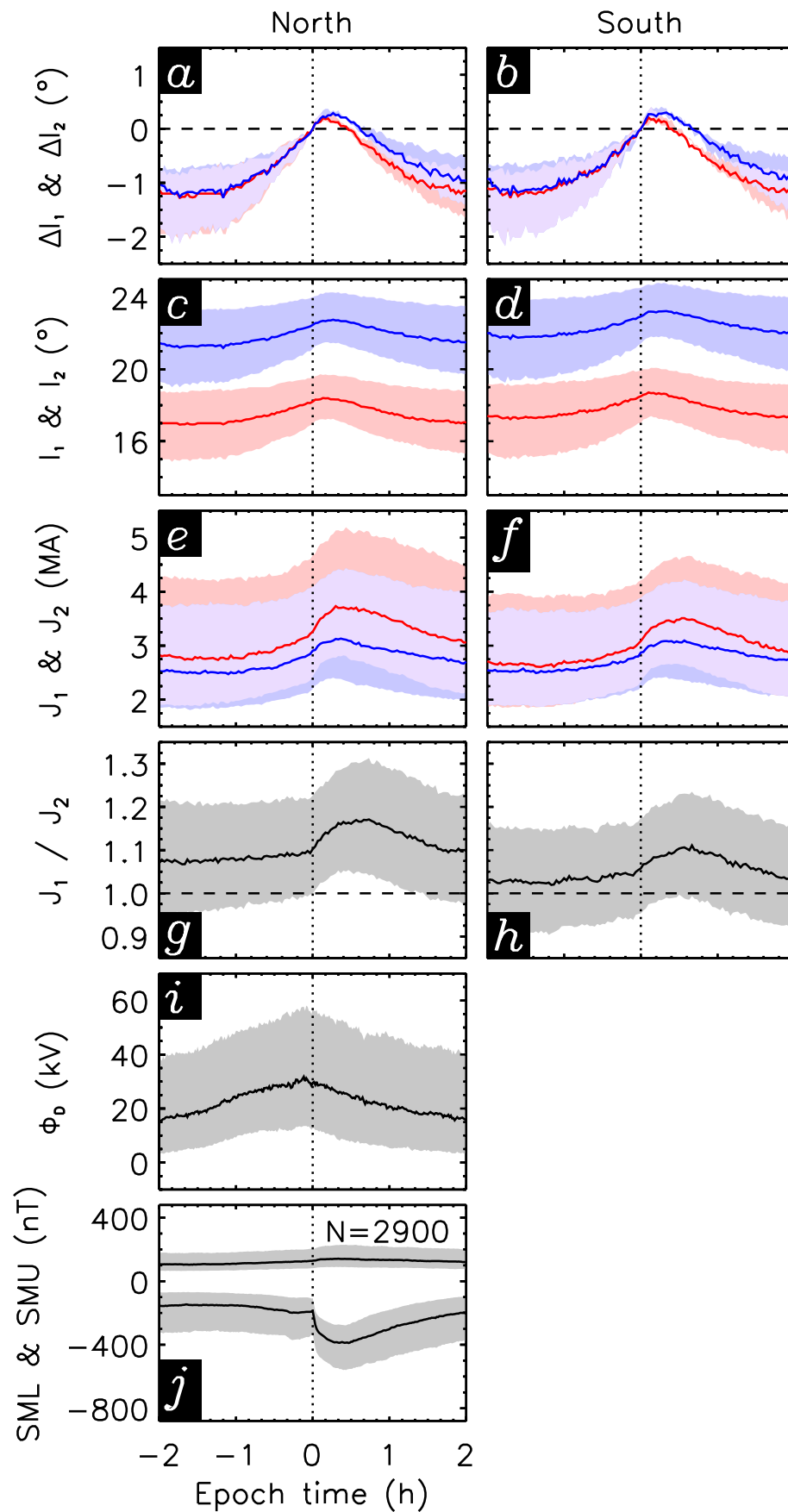


Figure 5.1: From top to bottom, a-b) Δl_1 and Δl_2 in degrees, c-d) l_1 and l_2 in degrees, e-f) J_1 and J_2 (MA), g-h) J_1/J_2 , i) Φ_D (kV), j) SML and SMU (nT) plotted against the epoch time t in minutes on the x -axis for the northern hemisphere (left) and southern hemisphere (right). R1 and R2 are denoted by red and blue respectively, and the shading denotes the quartiles in each panel.

R1 in its return to pre-substorm levels.

The current magnitudes as measured by AMPERE start, in the northern hemisphere, at $J_1 \sim 2.75$ MA and $J_2 \sim 2.25$ in panel e and a ratio R1/R2 of ~ 1.075 in panel g. The current magnitudes slowly increase between $t = -120$ min and $t = 0$ min, before substorm onset leads to a more rapid increase and a peak in current magnitude of $J_1 \sim 3.75$ MA and $J_2 \sim 3.25$ MA at $t \sim 20$ min. The current magnitudes observed then decrease through the period, returning almost to their initial levels. The ratio follows an almost identical pattern, with a slow increase observed until substorm onset, a rapid increase to a peak value of approximately 1.2 at $20 < t < 40$ min and then returning to pre-onset levels. The southern hemisphere follows a similar behaviour, but the current magnitude (f) and ratio (h) are lower throughout the epoch.

In panel i, the dayside reconnection rate $\Phi_D \sim 15$ kV at $t = -120$ min. It increases as time progresses, with a peak of $\Phi_D \sim 30$ kV slightly before substorm onset at $t = 0$ min. The level of dayside reconnection then falls, returning to its initial value at the end of the interval. In panel j, SMU ~ 100 nT at $t = -120$ minutes whereas SML ~ -150 nT at that time. SMU increases slightly from the start of the period, with a peak occurring at $t \sim 20$ min. The same is seen in SML until $t = 0$ min at which point a pronounced magnetic bay can be seen in SML at the time of substorm onset (Rostoker *et al.*, 1980). This bay also reaches a peak at $t \sim 20$ min, similar to the peak observed in the current magnitudes and ratio. This signature marks the formation of the substorm current wedge and is a recognised signature of substorm onset. Both SML and SMU then begin to decrease in magnitude through the epoch, returning to almost pre-onset levels at the end of the period.

5.2.2 The variation of reactions to substorms given different levels of activity

5.2.2.1 Reconnection rate and magnetic indices

As defined in Section 3.3, five bins are defined into which substorms can be sorted by onset colatitude. These bins are denoted I-V, and defined as follows. I: $0^\circ < \phi \leq 15^\circ$; II: $15^\circ < \phi \leq 17^\circ$; III: $17^\circ < \phi \leq 19^\circ$; IV: $19^\circ < \phi \leq 21^\circ$; V: $21^\circ < \phi \leq 30^\circ$. This categorisation is now employed, and Figure 5.2 shows the dayside reconnection rate Φ_D alongside SML and SMU averaged for the five categories outlined. These categories are defined by the colatitude of the R1 current oval at substorm onset. The plots corresponding to the smallest onset colatitudes (and thus the lowest level

of activity) are depicted at the top of the figure and the plots for the largest onset colatitudes depicted at the bottom.

In Bin I, it can be seen that at $t = -120$ min, $\Phi_D < 10$ kV and continues at that rate until $t = -20$ min. At this point, the reconnection rate begins to increase to a peak of approximately 15 kV located subsequent to the substorm onset. In Bin II, the reconnection rate increases from the initial value (~ 10 kV) to the peak (~ 20 kV), which is located at substorm onset. In Bins III-V, the initial and peak values increase until in Bin V, Φ_D varies between approximately 70 and 100 kV. The location of the peak in dayside reconnection rate becomes earlier with bin: in Bin I, the peak is seen just after substorm onset, whereas the peak in Bin V is as much as 25 minutes prior. The peak value is approximately 2 times the initial value in Bin I, whereas in Bin V the peak value is $\sim 1.4\%$ that of the initial value.

Turning to SML and SMU in Bin I, it is observed that both appear flat between the start of the interval (~ 90 nT) and the onset of the substorm. At substorm onset, SMU increases by 10 nT but returns to its initial magnitude relatively quickly. The familiar magnetic bay in SML is present at onset, with the SML magnitude increasing to ~ 200 nT and remaining higher than the initial magnitude for the rest of the interval. The sudden increase and then gradual decrease to a level higher than the initial magnitude is a common feature in every bin.

In Bin II, both SML and SMU remain steady at their initial values (100 nT and 90 nT respectively) until the substorm onset, at which point SMU increases slightly before quickly returning to its original level. SML again shows the signature magnetic bay, increasing to a higher magnitude of 300 nT. In Bins III-V, the magnitude of both indices increases slowly from $t = -120$ min to $t = 0$ min. At onset, the rate of increase of SMU climbs before the peak approximately 20 minutes later – it then returns to pre-substorm levels. The initial/peak magnitudes of SMU and SML increase with the onset colatitudes: in Bin V, the initial value of SML is approximately 500 nT, increasing to 750 nT just after onset. SMU starts at 250 nT and increases to 300 nT before dropping back down again. In all bins a decrease in SML magnitude is observed just prior to onset, although it is most pronounced in Bins IV and V.

5.2.2.2 Current magnitudes

Figure 5.3 shows J_1 , J_2 and J_1/J_2 . In Bin I, the observed current magnitudes remain constant at ~ 2 MA until onset which causes an increase in magnitude to a value of ~ 2.5 MA in R1 and ~ 2.25 MA in R2. The currents remain at this magnitude for the rest of the interval shown. Initially, R1 is higher than R2 at a ratio of 1.05;

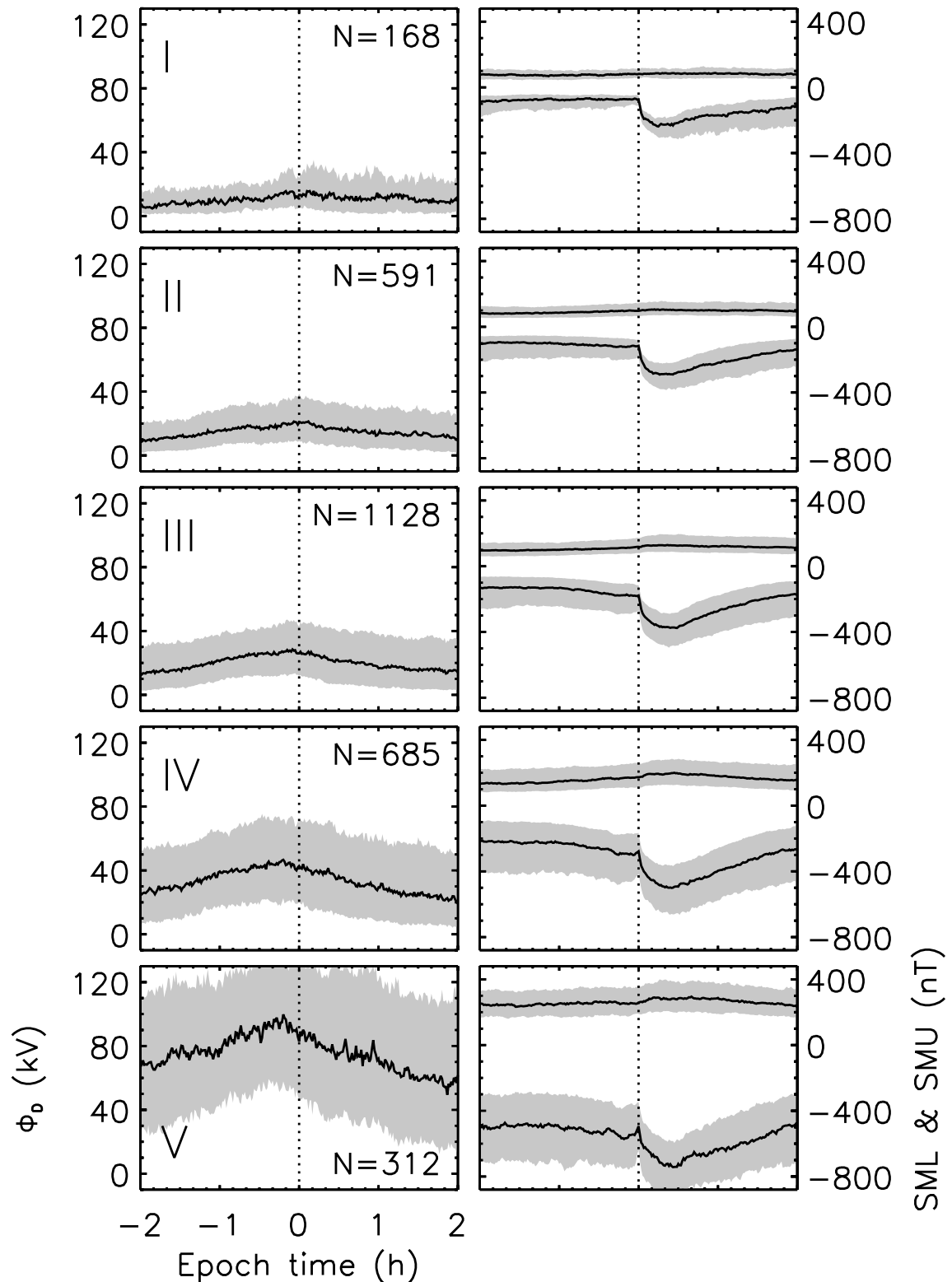


Figure 5.2: Φ_D (left) as calculated using OMNI data and SML and SMU (right) with respect to substorm onset at $t = 0$ min, binned by substorm onset colatitude (increasing from top to bottom). N is the number of substorms in the relevant bin, and the scales are the same as those for Figures 5.3 and 5.4. The bins are defined by onset colatitude. I: $0^\circ < \phi \leq 15^\circ$; II: $15^\circ < \phi \leq 17^\circ$; III: $17^\circ < \phi \leq 19^\circ$; IV: $19^\circ < \phi \leq 21^\circ$; V: $21^\circ < \phi \leq 30^\circ$.

at onset, the ratio between the two increases to a value of 1.2, and the ratio then decreases to 1.1 over the two hours subsequent to onset.

In Bin II, the initial values of the currents are just above 2 MA. The current systems remain steady until onset, when they relatively rapidly increase; R1 to $J \sim 3$ MA and R2 to $J \sim 2.5$ MA at $t = 20$ min. They then decrease gradually towards their initial value as time progresses. The ratio starts at a value of 1.05 and increases slightly until onset, at which point it climbs to a value of 1.15 and decreases slowly through the rest of the period.

In Bin III, the initial value of the currents is around 2.5 MA, with an increase at onset to 3.5 MA in R1 and 3 MA in R2. The slow decrease that subsequently occurs leads to values at $t = 120$ min that are between 0.25–0.5 MA higher than initially. The ratio starts above 1.05 and increases to 1.2 before decreasing, again to a value slightly higher than the initial value. In Bin IV, there is an initial R1 and R2 magnitude of just above 3.5 MA and 3 MA respectively, which increase to 4.75 MA and 4 MA at $t = 20$ min before decreasing to values comparable to those at the start. The ratio in this case starts between 1.05 and 1.1 before climbing to 1.2 and then returning. In Bin V, the R1 and R2 magnitudes are 6 and 5.5 MA respectively, and they increase to a peak magnitude of 7 MA and 6.5 MA, again at $t = 20$ min, before decreasing to values of 6 MA and 5.5 MA. The ratio starts at 1.1, decreases towards onset, and climbs very slightly at onset before returning to its original value.

The peak of the current magnitudes and ratios observed is consistently seen at $t = 20$ min, which does not appear to change with the variation in onset latitude and is the same as the peak in SML index. The increase in current magnitude coincidental with the substorm onset appears to be consistently larger for the Region 1 current than for the Region 2 current, matching the observed increase in ratio between the two at onset.

5.2.2.3 Latitude of current ovals

Figure 5.4 shows the value of l_1 and l_2 averaged per bin. In this case, Bin I shows that the current ovals get smaller by $0.5 - 1^\circ$ from the beginning of the interval depicted until the onset of the substorm at $t = 0$ min, with a sharp increase in oval colatitude seen at the onset of the substorm. The size of the current oval increases by 2° before decreasing throughout the period (at $t = 120$ min, they remain larger than their initial values). The two current ovals change in size similarly through the interval, but with l_1 decreasing in size more quickly than l_2 before the onset of the substorm and then increasing in size more quickly, reaching a higher Δl . The

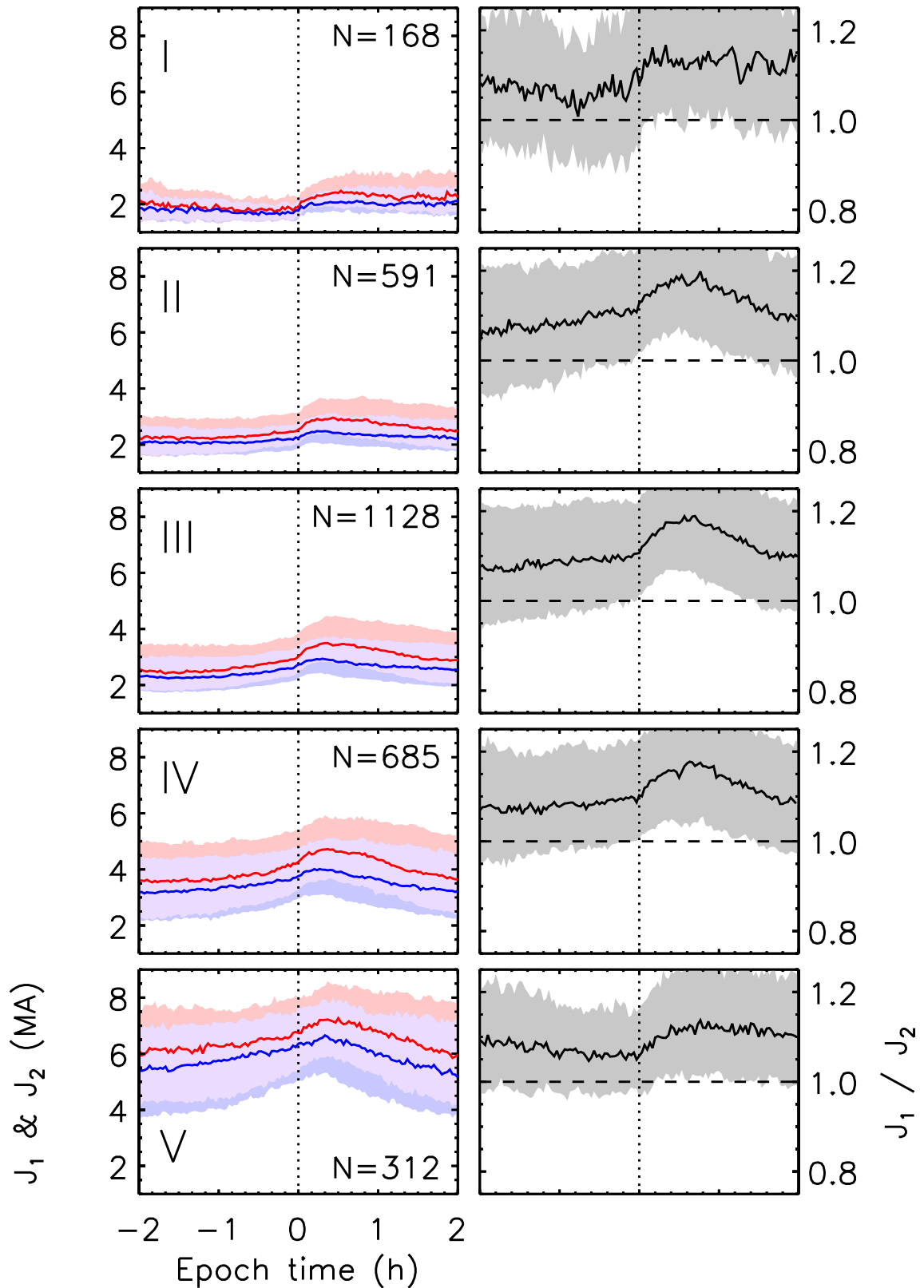


Figure 5.3: The magnitude in the northern hemisphere of the Region 1 (J_1 , red) and Region 2 (J_2 , blue) currents (left) and the ratio $\frac{J_1}{J_2}$ (right) with respect to substorm onset at $t = 0$ min, binned by substorm onset colatitude (increasing from top to bottom). N is the number of substorms in the relevant bin, and the scales are the same as those for Figures 5.2 and 5.4.

results from Bin I are discussed in detail in Section 5.3.2.1.

In Bin II, the two current ovals increase slowly in size by $\sim 1^\circ$ from the start of the period until substorm onset, both current ovals showing the same increase in size. After onset, both current systems increase more rapidly, until both current ovals reach a peak of $\sim 1^\circ$ larger at $t \sim 20$ min. The R2 current oval increases in size to a larger extent than R1, and Δl_2 remains larger than Δl_1 with the current ovals remaining $\sim 0.25^\circ$ larger at the end of the epoch than at the start.

Bin III exhibits a similar pattern prior to substorm onset, with both current systems increasing in tandem by 1.5° and the decrease in size after the peak being almost identical to Bin II. In this case, however, there is no increase in the rate of oval growth at the point of onset, with the peak in oval size occurring at $t \sim 10$ min. In Bin IV, the currents increase by 2° and the peak again moves earlier, to $t = 0$ min, with the ovals at the end of the epoch being approximately 0.25° larger than at the beginning, as in Bin II and III. In Bin V, the peak is also at $t = 0$ min but the ovals are 0.5° larger than their pre-substorm size at the end of the epoch, and the total increase is 2° .

As the onset colatitude increases with bin, the disparity between Δl_2 and Δl_1 increases. So too does the difference between l_1 and l_2 , with the two current ovals being separated by 4° in Bin I but by 5° in Bin V.

5.2.3 The variation of reactions to substorms with different seasons

Since the period of time for which data is available spans three years, the data can again be subdivided, but instead of using the subdivisions of Section 5.2.2 the subdivisions can be based on the month in which the substorm onset was observed. Substorms from the relevant months in 2010, 2011 and 2012 can be selected so as to examine the effects of season on a large-scale basis. Figure 5.5 shows the superposed epoch of all variables for substorms with expansion phase onsets observed in June, July and August; Figure 5.6 is the same, but shows onsets observed in December, January and February. In this way the differences between substorms occurring in the winter and in the summer can be examined.

Figure 5.5 shows the same variables as those in Figure 5.1, but in this case panels 5.5a, 5.5c, 5.5e and 5.5g show the substorms in the northern summer and panels 5.5b, 5.5d, 5.5f and 5.5h show the substorms in the southern winter. Panels 5.5a–d show that the current ovals react nearly identically in the two situations; the same is seen in panels 5.6a–d, for the southern summer.

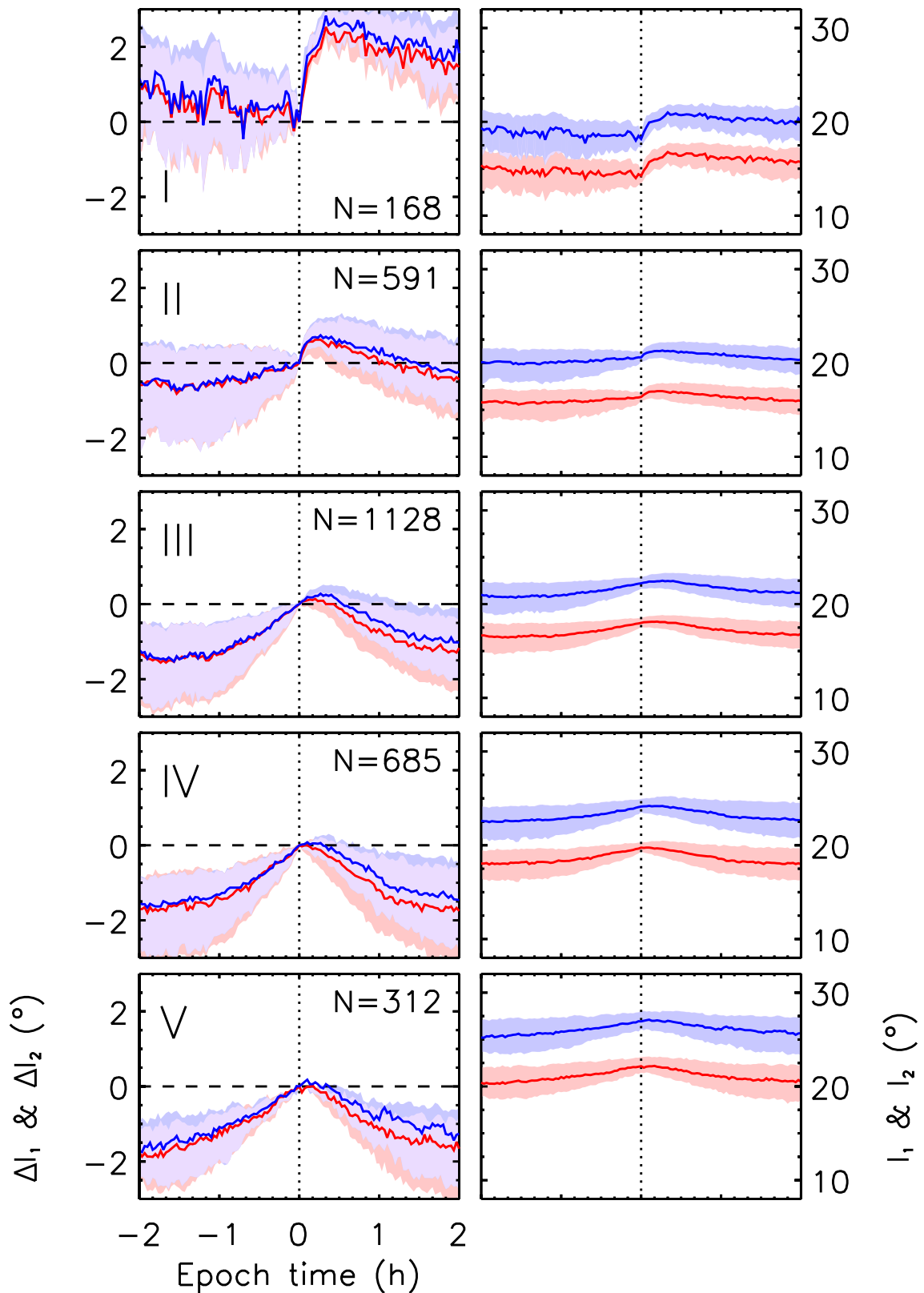


Figure 5.4: l_1 (red) and l_2 (blue) in the northern hemisphere with respect to substorm onset at $t = 0$ min, binned by substorm onset colatitude (increasing from top to bottom). The left-hand plots show Δl_1 and Δl_2 whereas the right-hand plots show the value of l_1 and l_2 . The units are equivalent to the average colatitude of the current oval. N is the number of substorms in the relevant bin, and the scales are the same as those for Figures 5.2 and 5.3.

In Figure 5.5e and 5.5f, the current magnitudes are driven differently in the two seasons. In the north, the current magnitudes J_1 and J_2 are driven from magnitudes of 3 MA and 2.5 MA to magnitudes of 4 MA and 3.25 MA approximately twenty minutes after the expansion phase onset. In the south, the currents are driven from magnitudes of approximately 2.5 MA to 3.5 MA and 3 MA, which is a smaller increase in magnitude from a smaller initial value. In the south, the currents return to their initial values by the end of the epoch; at the end of the epoch in the north, the magnitudes are 0.25 MA higher than their initial values.

Figure 5.5g shows that the ratio of R1 to R2 current is positive through the entire epoch, with J_1 being 10% stronger than R2 at the start of the interval, and increasing to 20% stronger after substorm onset before decreasing to the initial value. In Figure 5.5h, the two currents are very close to equal in magnitude, and the substorm onset triggers an increase such that R1 is 10% stronger before this situation resumes at the end of the epoch. It can be seen that the ratio is 0.1 larger throughout the epoch for the summer months as compared to the winter months.

Figure 5.6e and 5.6f show very similar situations to one another. Figure 5.6e, depicting the northern winter, shows current magnitudes starting at 2 MA for both regions, with J_1 increasing to 3 MA and J_2 increasing to 2.5 MA. The southern hemisphere, experiencing summer, shows an initial value that is 0.25 MA higher than the winter hemisphere, with J_1 increasing at a similar rate and J_2 increasing at a higher rate. The magnitudes in both hemispheres are 0.25 MA higher at the end of the epoch than at the start. Figure 5.6g and 5.6h show that in both hemispheres the currents are at parity at the start of the epoch. Both hemispheres show an increase in R1 relative to R2 with the substorm onset, with the northern hemisphere ratio increasing to 1.15 and the southern hemisphere increasing to 1.1.

The dayside reconnection rates for the summer and winter months are plotted in Figure 5.5i and 5.6i, showing that the reconnection rate varies between 20–40 kV in June–August and between 10–25 kV between December–February. The SML and SMU indices are plotted in Figure 5.5j and Figure 5.6j, showing a peak in SML of 400 nT in June–August and 300 nT in December–February. This phenomenon is discussed in more detail in Section 5.3.3.

5.3 Discussion

In the ECPC paradigm, substorm growth and expansion phases manifest themselves as the expansion and contraction of the polar cap (Cowley and Lockwood, 1992), and so follows a discussion of the spatial variation in the Birkeland current systems

in that context. Ionospheric convection is driven through first dayside and then nightside reconnection and the subsequent motion of flux tubes in the magnetosphere (Milan, 2013). These ionospheric motions are resisted by frictional coupling with the neutral atmosphere, requiring horizontal ionospheric currents and field-aligned currents. Hence, both phases are expected to be associated with FAC enhancements, as demonstrated in Chapter 4, and the relationship is explored in more detail. The categories outlined in Section 3.3 are utilised in order to discuss how the amount of open flux in the magnetosphere at onset affects the reaction of the Birkeland current system to substorms (Milan *et al.*, 2009a).

5.3.1 The reaction of the Birkeland currents to substorms

5.3.1.1 Spatial variations

As described by Cowley and Lockwood (1992), the polar cap expands as the amount of open flux in the magnetosphere increases. The R1 currents flow along the OCB and so the motion of the R1 current oval can be used as a proxy for the polar cap boundary, indicating that similar expansions and contractions to those seen in auroral data should be observed (Milan *et al.*, 2003; Clausen *et al.*, 2013b). In Figure 5.1 the extent of the current ovals expands through the growth phase as open flux is added by dayside reconnection. After substorm onset, the ovals maximise and then begin to contract again, which is consistent with open flux being closed in the magnetotail during the substorm expansion phase. Therefore the current ovals can be used as a proxy for the amount of open flux in the magnetosphere, and the time derivative of l_1 could be used to examine dayside and nightside reconnection rates.

The amount of open flux maximises at the same time as the extent of the current ovals, at $t \sim 20$ min, just after the onset of the substorm expansion phase. This indicates that, although the dayside reconnection rate begins to wane immediately prior to onset, Φ_D is still higher than the nightside reconnection rate Φ_N until the point that the open flux content begins to decrease again. This indicates that Φ_N becomes larger than Φ_D at the same point as the maximum of the magnetic bay observed in SML. It is therefore inferred that it marks the peak of Φ_N .

5.3.1.2 Magnitude variations

It can clearly be seen that field-aligned currents are strongly driven by substorms. The currents increase in magnitude as Φ_D increases, with rises in both clearly observed in Figure 5.1. This indicates that dayside reconnection drives currents

through the Birkeland current system during the substorm growth phase. It was previously shown in Chapter 4 that the magnitude of the Birkeland currents gets larger with increases in the value of Φ_D and also the AL index, consistent with the result here. The total increase in the current magnitude over the substorm cycle is 1 MA.

At substorm onset, the growth phase of the substorm is over, and the dayside reconnection rate on average begins to drop (Freeman and Morley, 2009), but the current magnitudes continue to increase. Since the onset of the substorm implies that magnetic reconnection has initiated in the magnetotail, it can be inferred that this is due to driving from the nightside reconnection increasing as the dayside reconnection rate decreases, and represents part of the expansion phase of the substorm. The inference is corroborated by an examination of the current densities over a two-hour epoch performed by Clausen *et al.* (2013a). The fact that the current magnitudes reach their peak coincident with the extent of the current ovals indicates that it is the point at which the sum of reconnection rates $\Phi_D + \Phi_N$, equal to twice the total cross polar cap potential (Milan, 2013), is at its peak.

The substorm current wedge also drives current through the Birkeland current system, causing the currents to increase more rapidly; the increase is a signature of the substorm expansion phase that can be seen in SML, which measures the magnetic perturbation associated with the substorm current wedge (SCW). As the SCW begins to decrease in magnitude so too does SML, coinciding with an expected decrease of the Birkeland currents. This is consistent with observations by Murphy *et al.* (2013) which show that both Region 1 and 2 are enhanced during the substorm cycle, but is inconsistent with observations that substorms are seen only in the R1 currents (Clausen *et al.*, 2013b).

It is clear that field-aligned currents are strongly driven by magnetic reconnection events in the solar wind-magnetosphere coupled system. The magnitude of the two current systems increases by up to 1 MA over the course of a substorm cycle, but the two current systems do not react identically to the onset of a substorm. The disparity in reaction can be seen by examination of the ratio J_1/J_2 , which increases to as much as 1.2 after substorm onset. The increase implies proportionally more current flowing through R1, even though both current systems are enhanced. This may explain why previous analyses of AMPERE data have differed on the role of R2 during the substorm cycle (Murphy *et al.*, 2013; Clausen *et al.*, 2013b). These observations suggest that, although R1 experiences a more notable enhancement, both current systems react to substorms. R1 experiencing larger enhancements than R2 is consistent with previous examinations of substorms (Sergeev *et al.*, 2014).

The high ratio suggests more R1 current closes across the noon/midnight meridian through the ionosphere during the substorm expansion phase, probably indicating significant current closure through the substorm auroral bulge. Usually, Hall currents flow sunward across the polar cap and antisunward around the flanks of the polar cap (also called the DP-2 current system), with Pedersen currents flowing in the auroral zone and also duskward across the polar cap. In this case, R1 currents can either close through R2 currents (via the auroral zone) or through R1 currents on the opposite side of the polar cap. During the substorm expansion phase, the substorm electrojet (also called DP-1) flows westward across midnight (from the dawn sector to the dusk sector), meaning that more R1 current can flow duskward and close through R1, explaining how the onset of expansion phase can increase the relative strength of R1 to R2.

Finally, the Birkeland currents decrease both in magnitude and in spatial extent after the expansion phase, as the recovery phase leads back into a quiescent magnetospheric state.

5.3.2 Reactions varying with geomagnetic conditions

Bins I-V show the change in the reaction of the Birkeland currents to substorms as the current ovals at onset are more equatorward (Figures 5.2, 5.3, 5.4). Bin I merits a separate discussion, presented in Section 5.3.2.1.

Within Bins II-V, it has been observed that the dayside reconnection rate is higher as the onset colatitude of the current ovals increases, which is also true of SML and SMU (Figure 5.2). In order for the current oval to reach high colatitudes, the dayside reconnection rate must be high to add enough open flux to expand the oval before the start of nightside reconnection at substorm onset. This is consistent with existing pictures of the ECPC paradigm.

Substorm onsets that occur with higher amounts of open magnetic flux are thought to be more intense due to the higher amount of energy contained within the magnetotail (Milan *et al.*, 2009a). This explains the larger magnetic bay in SML subsequent to substorm onset, as a more intense substorm is triggered. It also explains why the negative change in l_1 and l_2 is larger as the onset colatitude represented by the bins increases, since open magnetic flux is closed in the magnetotail at a higher rate and thus the polar cap will contract more quickly (Figure 5.4). It should be remembered, however, that l_1 and l_2 do not vary linearly with the open flux content of the magnetosphere.

The Birkeland current magnitudes become more enhanced at all points of the

epoch, per bin, as the onset colatitude increases. Since the current magnitudes are associated with higher reconnection rates, the higher Φ_D values observed with onset colatitude are evidently responsible for driving the increase. As described, the ratio J_1/J_2 at the start of the epoch is larger as the onset colatitudes increase, indicating that R1 currents are relatively larger than R2 currents with higher geomagnetic activity, consistent with the observations in Chapter 4. The enhancement in the ratio that occurs after substorm onset becomes less obvious from Bin II to Bin V, however. It is concluded that this indicates that the enhancement to the Birkeland currents is more evenly spread between R1 and R2 as conditions become more extreme or that the SCW intensity does not depend on onset latitude (Figure 5.3).

5.3.2.1 Signatures seen at small substorm onset colatitudes

Contrary to the other bins, Bin I shows a decrease in SML, SMU, l_1 , l_2 , J_1 , and J_2 prior to onset. At onset, there is a sudden increase in these values. Unlike the other bins, which show Φ_D increasing over the two hours preceding onset, the dayside reconnection rate begins to increase approximately twenty minutes prior to onset and remains high until after onset, which would result in the coupled solar wind-magnetosphere system experiencing the addition of open flux during the substorm. This would therefore lead to SMU increasing with enhanced ionospheric convection and an increase in the size of the current ovals, both of which are seen just after the dayside reconnection rate has increased.

Within the context of the ECPC paradigm, a decrease in the extent of the current ovals indicates that the amount of open flux contained within the polar cap decreases between the start of the epoch and the point of substorm onset. Such a decrease can only be explained by magnetic reconnection on the nightside causing the conversion of open to closed flux, which could imply reconnection at a distant neutral line in the magnetotail during extremely quiescent periods.

5.3.3 Reactions varying with season

Figure 5.5 shows a pronounced difference between substorm reactions in the summer and winter hemisphere during the northern summer, but during the southern summer, shown in Figure 5.6, the difference is much less pronounced. The dayside reconnection rate Φ_D is higher throughout the epoch in the northern summer than in the southern summer, which is a context in which this result can be explained. This leads to fewer substorms, as evidenced by the fact that 150 fewer substorms occurred during the northern winter.

The disparity in reconnection rates will lead to differences between the northern summer and the southern summer that are not a result of season but a result of higher dayside driving during the northern summer, leading to difficulties drawing conclusions regarding the reaction varying with season. The fact that the dayside reconnection rate was, on average, higher during the northern summer is a coincidence in the three years of data analysed; if the AMPERE dataset is extended beyond the three years currently available, it is possible seasonal variations will be easier to examine. The fact that the difference between Figure 5.5e and 5.5f is larger than the difference between Figure 5.6e and 5.6f is therefore probably related to the dayside reconnection rate being higher. It is also possible that this result could be explained by the bias of AMPERE towards larger northern magnitudes theorised in Chapter 3: this would exacerbate the enhancements during northern summer but obscure the enhancements during southern summer.

5.4 Conclusions

The work described in this chapter gives an overview of the reaction of the Birkeland current system (in both magnitude and spatial extent) to substorms within the context of the expanding/contracting polar cap paradigm. It has been demonstrated their reaction during various phases of the substorm, and shown that they become more intense in the growth phase, and reach a maximum during the expansion phase soon after onset, decreasing to pre-substorm levels in the recovery phase.

These results can be interpreted in the framework of currents being driven by ionospheric flows which are ultimately driven by magnetic reconnection. The magnitude of the two current systems increases by up to 1.25 MA over the course of a substorm cycle, and the ratio J_1/J_2 increases to as much as 1.2 after substorm onset, suggesting that the SCW enhances both Birkeland current systems but preferentially flows through the poleward Region 1 currents.

We categorise the data by colatitude and assume that larger current ovals imply a larger polar cap and therefore more open flux. The change in the size of the current ovals can be used to pinpoint the stage at which nightside reconnection begins to dominate over dayside reconnection, and this shows that nightside reconnection occurs at a higher rate after substorm onset when the current ovals (and therefore the amount of open magnetic flux) is higher.

The seasonal variation in the response of Birkeland currents to substorms is explored, but the disparity in the average dayside reconnection rate, combined with the potential bias of AMPERE toward larger northern hemisphere magnitudes, means

that it is hard to draw conclusions from the data presented. Conclusions regarding seasonal variation are drawn instead in Chapter 6.

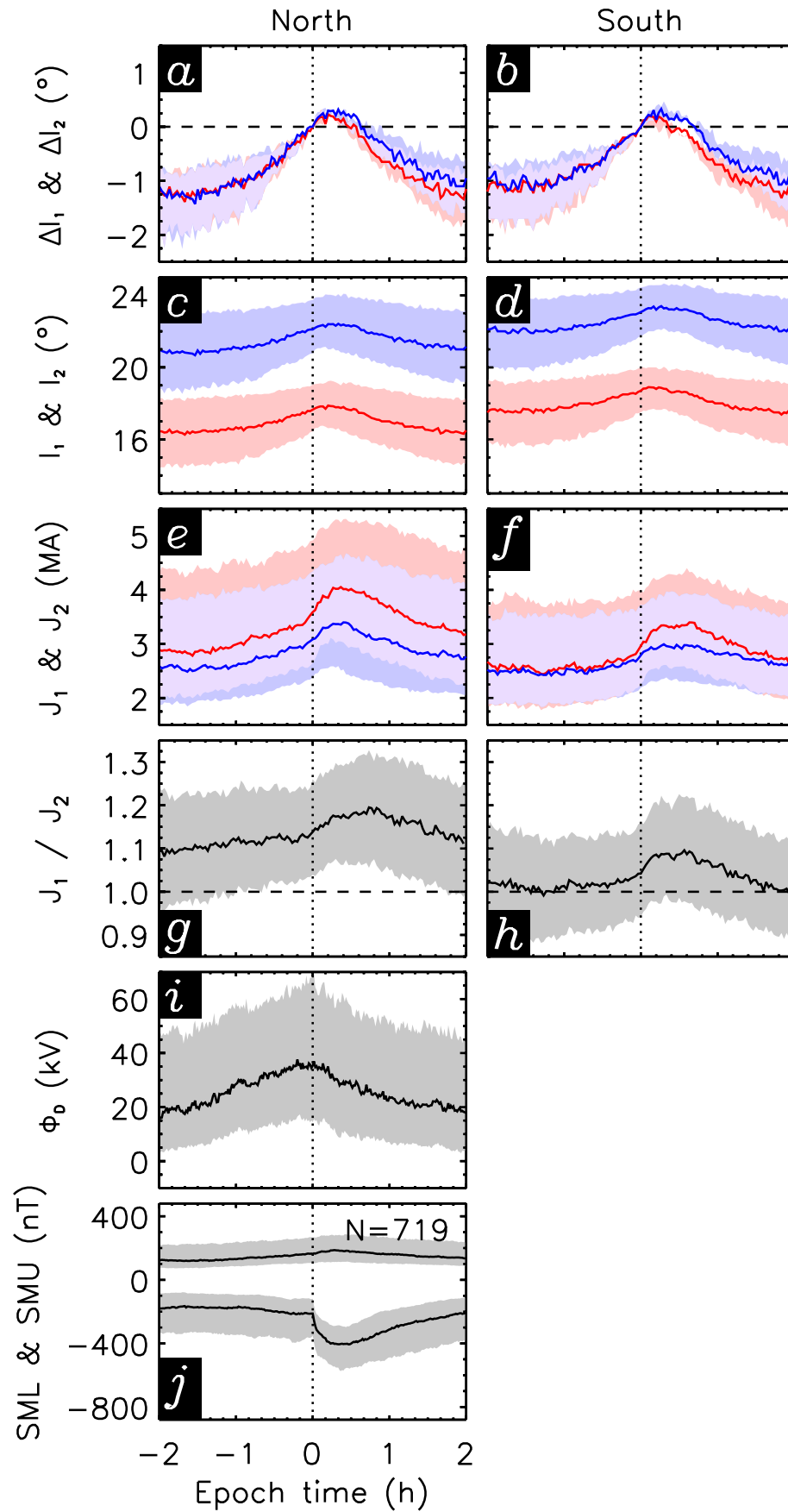


Figure 5.5: Substorms for the months of June, July and August. From top to bottom, a-b) Δl_1 and Δl_2 in degrees, c-d) l_1 and l_2 in degrees, e-f) J_1 and J_2 (MA), g-h) J_1/J_2 , i) Φ_D (kV), j) SML and SMU (nT) plotted against the epoch time t in minutes on the x -axis for the northern hemisphere (left) and southern hemisphere (right). R1 and R2 are denoted by red and blue respectively, the number of substorms is given on panel j, and the scale is the same as that used in Figure 5.1. The winter hemisphere plots are on the right in this figure.

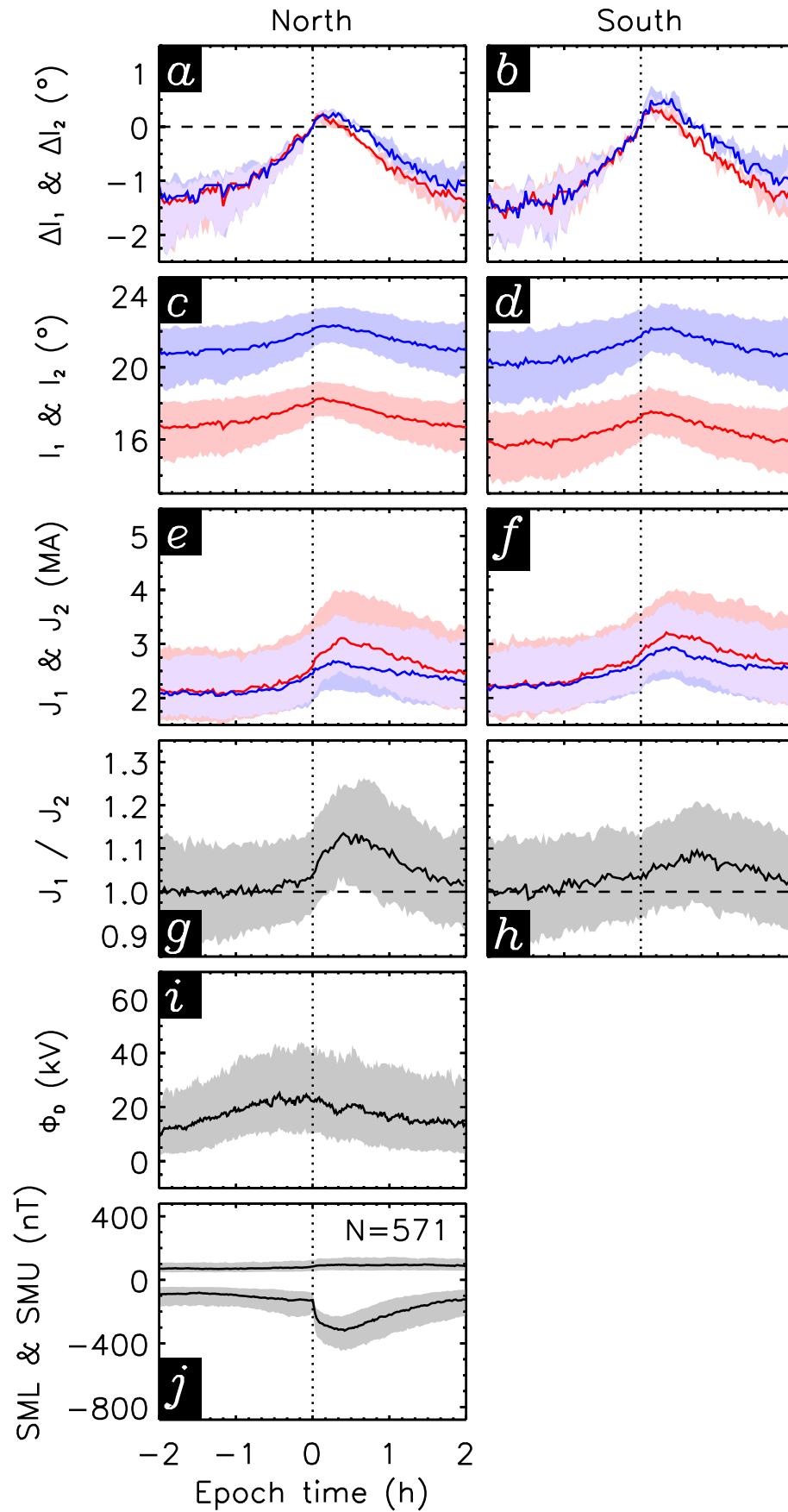


Figure 5.6: Substorms for the months of December, January and February. From top to bottom, a-b) Δl_1 and Δl_2 in degrees, c-d) l_1 and l_2 in degrees, e-f) J_1 and J_2 (MA), g-h) J_1/J_2 , i) Φ_D (kV), j) SML and SMU (nT) plotted against the epoch time t in minutes on the x -axis for the northern hemisphere (left) and southern hemisphere (right). R1 and R2 are denoted by red and blue respectively, the number of substorms is given on panel j, and the scale is the same as that used in Figure 5.1. The winter hemisphere plots are on the left in this figure.

Chapter 6

An analysis of seasonal and diurnal variations in conductance-related Birkeland current strengths

6.1 Introduction

Chapters 4 and 5 explored the effect of magnetic reconnection on Birkeland current magnitudes, but the work in Chapter 5 suggested more work was necessary to understand seasonal variations in the data (due to the high dayside reconnection rates during summer in the northern hemisphere for the three years of AMPERE data). This chapter explores the seasonal variation in the current magnitudes measured for the same three year period as Chapters 4 and 5, in order to quantify the effect of season and ionospheric conductance variations on the currents flowing measured by AMPERE. This is done by first taking the mean current magnitude in each month of the period, and then subdividing these means by the hours of UT. For this chapter, the distinction between regions 1 and 2 Birkeland currents is not drawn, and instead the total upward and downward current along each hour of MLT is integrated (Equation 3.13), ignoring any value for which $j < |0.2 \mu\text{A m}^{-2}|$ and any current signature at a magnetic colatitude $l > 30^\circ$. It should be noted that this means a move away from considering the R1 and R2 current systems and their magnitudes J_1 and J_2 , and a move toward considering J , which is the total Birkeland current flowing. In the following chapter, this total current is subdivided between hemispheres, yielding J_N and J_S , the total current in the northern and southern hemispheres respectively.

6.2 Birkeland current strengths 2010 – 2012

6.2.1 Mean monthly Birkeland current strengths

Figure 6.1a shows the monthly mean Birkeland current strengths measured by AMPERE plotted against the number of days since 1 January 2010 in the northern and southern hemispheres, plotted in red and blue respectively). Diurnal and seasonal variations in solar illumination controlled by the solar zenith angle will give rise to variations in ionospheric conductance. The dayside reconnection rate Φ_D , which controls the ionospheric convection has a semiannual variation (Russell and McPherron, 1973b) which leads to more activity at the equinoxes; other than this, Φ_D is not expected to have a seasonal or diurnal variation. Thus it is proposed that there will be a seasonal and diurnal variation of the Birkeland currents which is solely due to the solar illumination effect on the ionospheric conductance. The presence of such an effect can be verified by plotting $J_N - J_S$ in Figure 6.1c. J_N is up to 2 MA higher than J_S during summer in the northern hemisphere (indicated by the light red stripes) whereas J_S is approximately 0.5 MA higher than J_N during summer in the southern hemisphere (indicated by the light blue stripes).

Figure 6.1b shows the monthly mean dayside reconnection rate Φ_D (calculated as in Section 2.1.3), for the period 2010 – 2012. It can be seen that the mean Φ_D varies significantly during this time. Peaks are located in May 2010; July 2011 and July 2012, whereas troughs are located in January 2010, December 2011 and December 2012. In order to identify the seasonal variation in the Birkeland currents, the change in the conductance with season is considered. Instead of using the local conductance Σ (Robinson and Vondrak, 1984; Fujii and Iijima, 1987), it is instead assumed that the total amount of Birkeland current flowing can be described by the dayside reconnection rate (a voltage) multiplied by some term Ξ . This assumption is made because Birkeland current strength has been previously shown to be well-correlated with Φ_D . Ξ is so called to differentiate it from Σ , and will vary with season and will have units of conductance; this assumes that the seasonal effect on the Birkeland currents can be quantified by a single number. This assumption yields the following relation describing total Birkeland current:

$$J = \Phi_D \Xi. \quad (6.1)$$

If the data are averaged over a long enough period of time, Φ_D can be employed in isolation without explicitly considering Φ_N , because on the timescale of a month, $\Phi_D = \Phi_N$ (Cowley and Lockwood, 1992). As mentioned in the introduction, the subdivision of currents into R1 and R2 is no longer used, such that Equation 6.1

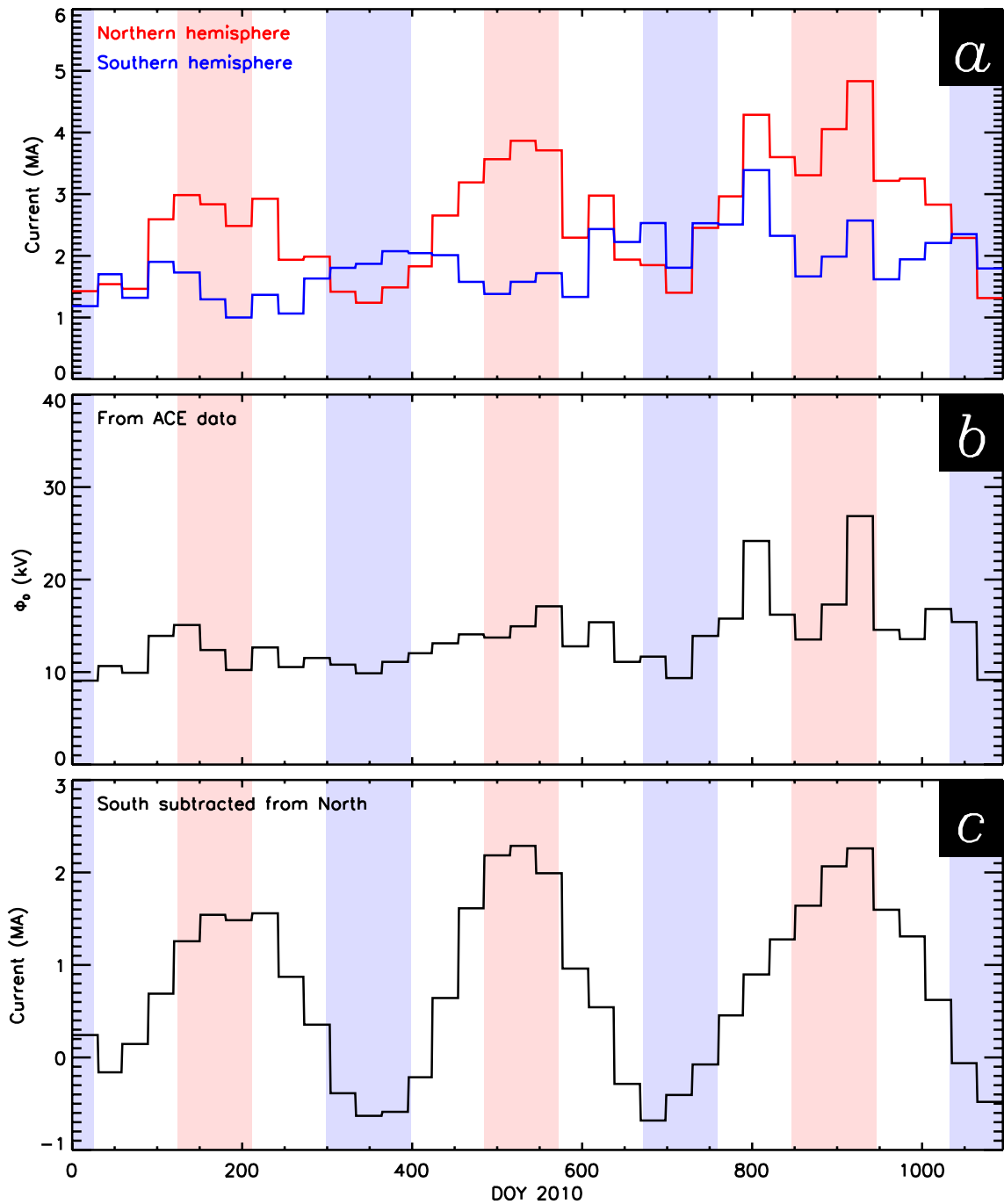


Figure 6.1: A diagram showing the day of 2010 on the x -axis. Plotted on the y -axis, from top to bottom: a) the current magnitude J_N (in red) and J_S (in blue); b) the dayside reconnection rate Φ_D ; c) the difference in current magnitude $J_N - J_S$. Each variable is plotted as a monthly mean. A light red background indicates May – July, and a light blue background indicates November – January.

does not refer to R1 or R2 but instead to total Birkeland current (which can then be subdivided into northern and southern hemisphere current flow J_N and J_S respectively).

We assume that the conductance Ξ can be quantified as a sinusoid that has a period of one year, equal to zero on the 79th day of 2010, which was the vernal equinox in that year. Thus,

$$t = \frac{2\pi(d - 79)}{365.25} \quad (6.2)$$

$$\Xi(t) = y_0 \pm y_a \sin(t) \quad (6.3)$$

can be written where y_0 is the background conductance, y_a is the variation in conductance due to seasonal effects (the amplitude of the sinusoid), and d is the number of days since 1 January 2010. In the southern hemisphere, y_a is expected to be negative, as opposed to the positive amplitude expected in the northern hemisphere.

Equation 6.1 implies that $\Phi_D = J/\Xi(t)$. Consequently, the estimate of Φ_D from OMNI data can be compared with an estimated Φ_D^* calculated by dividing current magnitude J by the sinusoid $\Xi(t)$, and this means that the form of $\Xi(t)$ that provides the best correlation between the two can be determined using Equation 6.3. The reconnection rate is estimated in order to make the graphs slightly simpler to interpret. By exploring values of y_0 and y_a , the form of Equation 6.3 that gives the best fit between Φ_D and $J/\Xi(t)$ can be found for each hemisphere to find the conductance in the north Ξ_N and the south Ξ_S .

To this end, the values of y_a and y_0 that give the best correlation coefficient were obtained using a brute force approach, trying different values of $y_a = ry_0$ where $0 \leq r \leq 1$ in steps of r of 0.001. Then, once the best value of r is identified, different values of y_0 are attempted between 0 and 200 in steps of 0.2 to find the one which minimises the difference of the squares. The results were

$$\Xi_N(t) = 189.8 + 36.8 \sin(t) \text{ mho} \quad (6.4)$$

$$\Xi_S(t) = 143.2 - 44.3 \sin(t) \text{ mho} \quad (6.5)$$

Figure 6.2 shows the result of Φ_D^* . Figure 6.2a shows the mean values of Φ_D previously plotted in Figure 6.1b with the northern and southern estimates of Φ_D (using the solutions presented in Equations 6.4 and 6.5) overlaid in red and blue respectively. Figure 6.2 also shows the measured Φ_D plotted against the estimated Φ_D in the northern (6.2b) and southern (6.2c) hemispheres. In both hemispheres, a Pearson correlation coefficient of above 0.9 is measured, indicating a strong correlation.

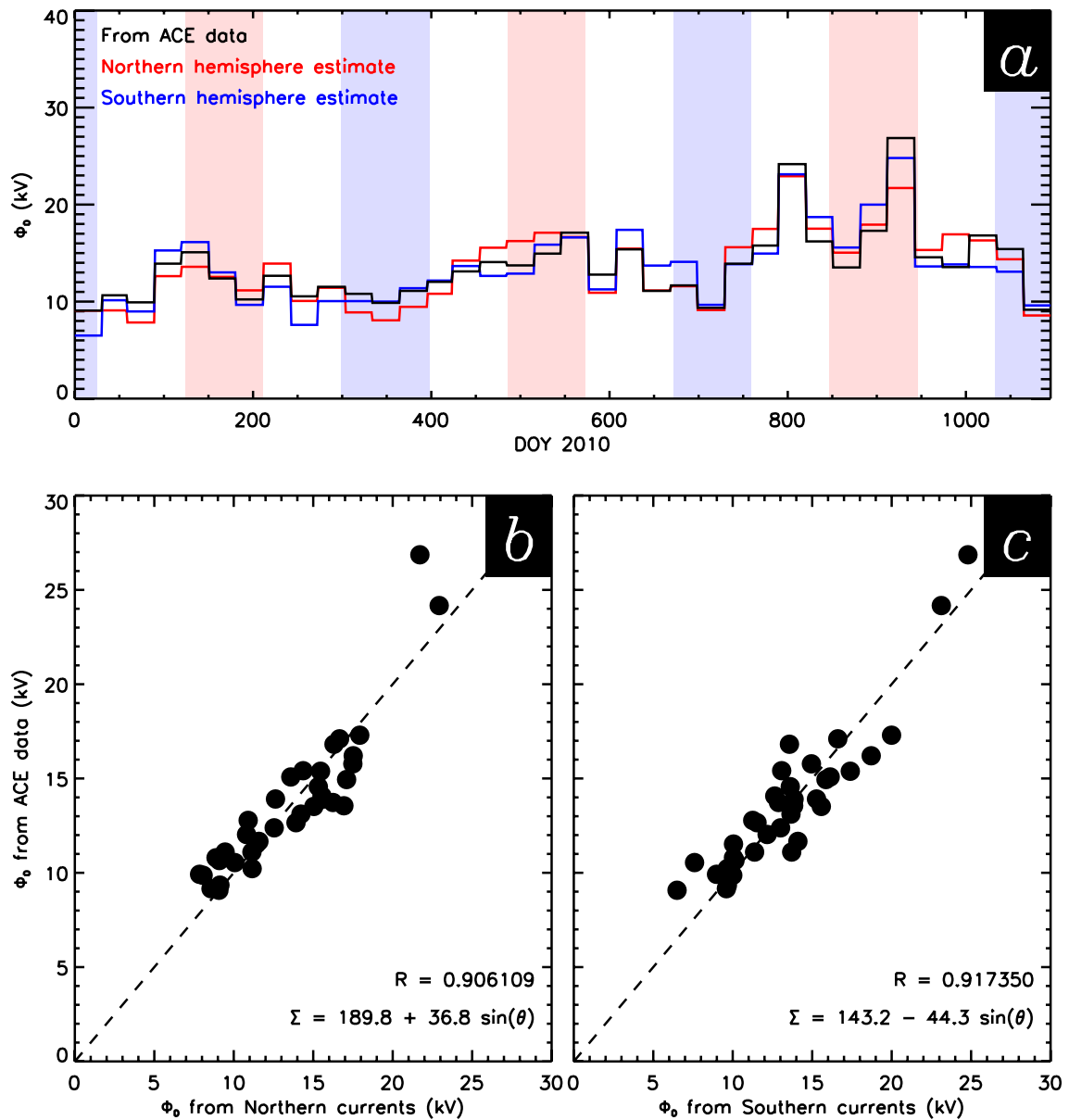


Figure 6.2: a) A diagram showing the Φ_D plot shown in Figure 6.1b (day of 2010 vs. Φ_D) with the estimated Φ_D based on J_N (red) and J_S (blue) overplotted. b) A plot of Φ_D showing the AMPERE-based prediction against the ACE measurement for the northern hemisphere. c) For the southern hemisphere.

6.2.2 Mean diurnal Birkeland current strengths

Examining diurnal variations expected due to solar zenith variations, Figure 6.3 shows mean Birkeland current magnitudes J_N (6.3a) and J_S (6.3b), plotted as colours on a graph of the number of months since January 2010 (on the x -axis) against the hour of UT (on the y -axis). In order to make the diurnal variation more clear, the hourly mean variation in the current magnitudes over the three year period (6.3d and 6.3e) is also plotted (to the right of these plots).

In order to split the data into the 24 hours of the day, the Birkeland current magnitudes are binned by taking the intervals which have start times in a given hour (i.e. $00 : 00 \leq \text{UT} < 01 : 00$). Each of these 24 bins is then used to take the mean average across every day in a given month to find the magnitude of the Birkeland currents for a given combination. The bin which contains data from 00:00 until 00:58 UT will be referred to as the 00-01 UT bin (and so forth), for ease of discussion.

The seasonal variation observed in section 6.2.1 is present in Figure 6.3, this method of presenting the data also shows a diurnal variation, which is highlighted by the right-hand plots. In the northern hemisphere, the maximum current strength is observed at 16-17 UT whereas the minimum current strength is observed at 00-01 UT. In the southern hemisphere, the maximum current strength is observed at 05-06 UT whereas the minimum is at 16-17 UT. In addition to the current magnitudes, Φ_D is plotted on the same axes in Figure 6.3c and 6.3f: there is not an apparent diurnal variation, indicating that any observed diurnal explanation cannot be explained by dayside reconnection driving the system.

In order to quantify the diurnal variations observed in Figure 6.3, calculations of the solar zenith angle χ at the geomagnetic pole are considered. An estimate of the position of the geomagnetic pole in 2010 is used, with geographic latitude $\phi = 80.1^\circ$ in both hemispheres, and longitude $\lambda_N = -72.2^\circ$ in the northern hemisphere and $\lambda_S = 107.8^\circ$ in the southern hemisphere (Finlay *et al.*, 2010). The value of χ at the geomagnetic pole across the years 2010 – 2012 is shown in Figure 6.4, with the diurnal variations plotted on the right-hand-side and the variation with month of 2010 depicted to the top and to the bottom. The top half of the figure shows the solar zenith angle in the northern hemisphere χ_N whereas the bottom half shows the southern hemisphere χ_S . Turning points in χ are seen at June and December in each year, as well as at 04-05 UT and 16-17 UT.

Comparing Figure 6.4 with Figure 6.1a, it can be seen that the hemispheric current magnitudes are higher during months in which the solar zenith angle χ is

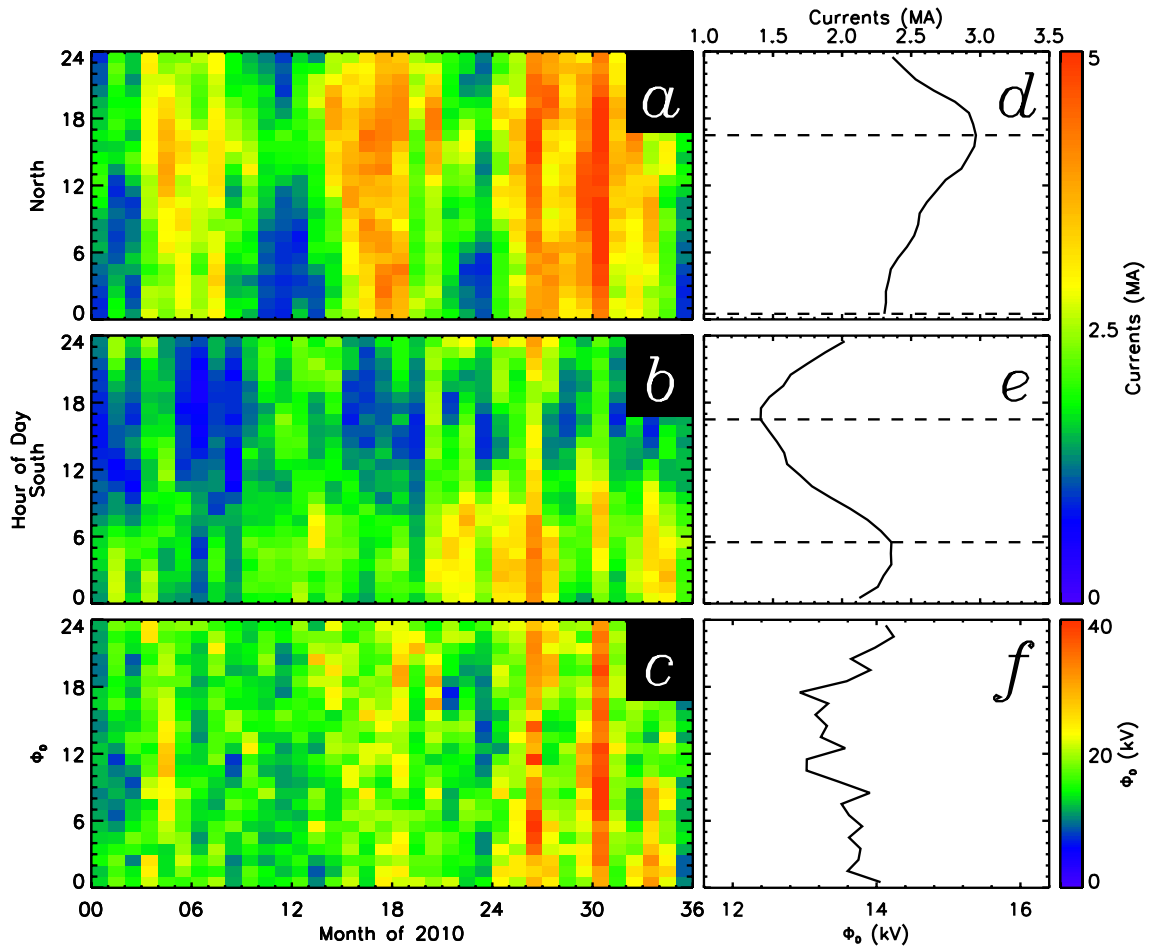


Figure 6.3: To the left: diagrams plotted with month of 2010 on the x -axis and hour of day on the y -axis. On the z -axis, from top to bottom: a) the northern current magnitude J_N ; b) the southern current magnitude J_S ; c) the dayside reconnection rate Φ_D . To the right: diagrams with hour of day on the y -axis and, on the x -axis, d) J_N , e) J_S , and f) Φ_D averaged over all months.

Table 6.1: Maxima and minima observed in Figure 6.1 and Figure 6.4, and their differences.

Year	Month		J (MA)		J (MA)	
	Maximum	Minimum	Maximum	Minimum	June	December
2010	Aug	Dec	1.2	-0.5	1.2	-0.5
2011	Jun	Nov	1.8	-0.5	1.8	-0.3
2012	Jul	Dec	1.8	-0.4	1.6	-0.4

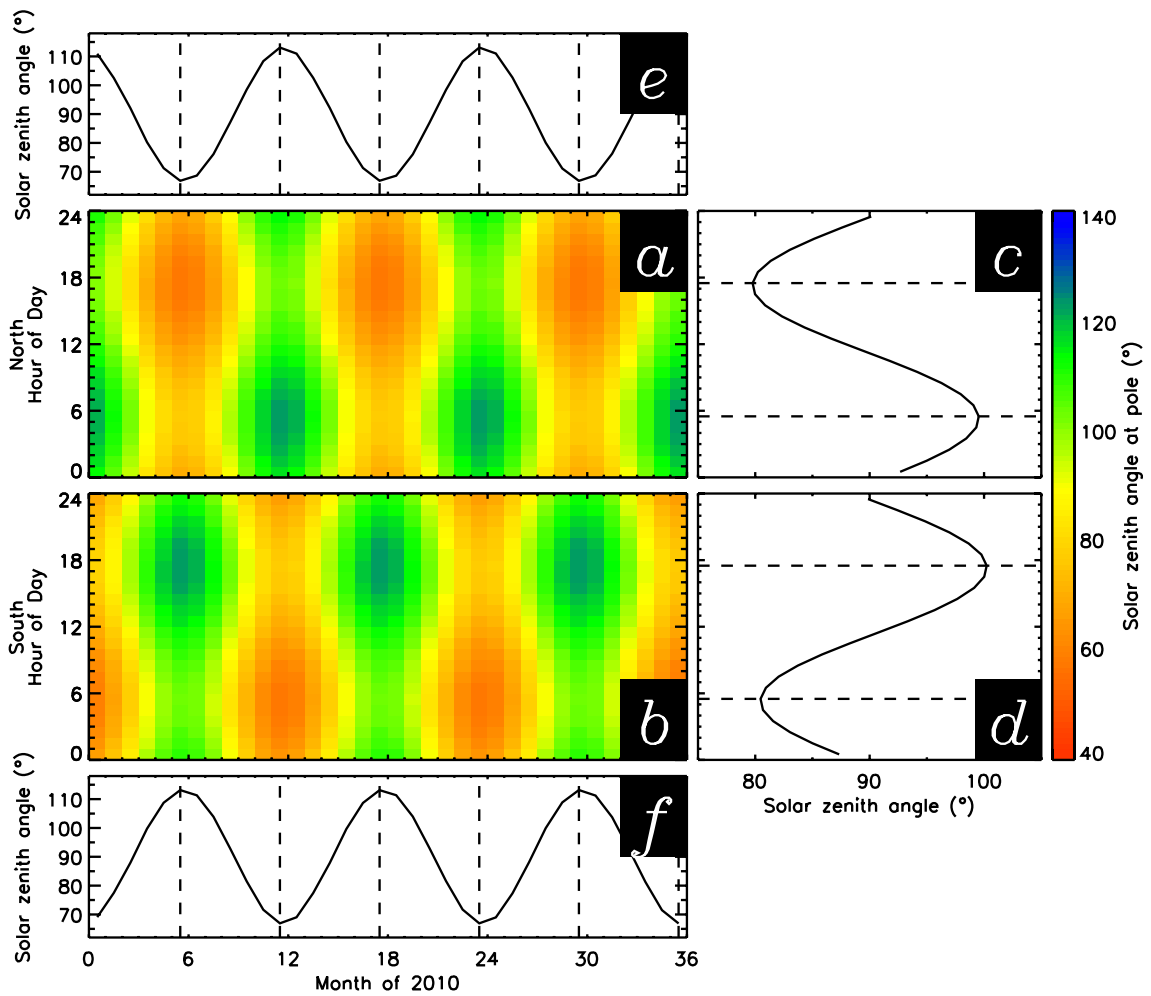


Figure 6.4: In the middle, to the left: diagrams plotted with month of 2010 on the x -axis and hour of day on the y -axis. On the z -axis, solar zenith angle χ at the geomagnetic pole in the northern and southern hemispheres (a and b). To the right: plots of χ against hour of day for the northern and the southern hemispheres (c and d). To the top and bottom: plots of χ against month of 2010 for the northern and southern hemispheres (e and f).

lower (indicating more sunlight incident on the pole). Examining Figure 6.1c, there are maxima located at August 2010, June 2011 and July 2012 whereas minima are seen at December 2010, November 2011 and December 2012. The expected maxima and minima would be located in June and December every year, based on observation of χ . The difference between the current magnitude at the observed turning point and the current magnitude at the theorised turning point is less than 10% of the total seasonal variation in current magnitude in all cases (approximately 0.2 MA); the values at both the observed and theorised turning points are tabulated in Table 6.1.

Comparing Figure 6.4 with Figure 6.3, it can again be seen that the solar zenith angle is lower during hours in which the current magnitudes are higher. In both hemispheres, a turning point is observed at 16-17 UT which is coincident with a turning point of the opposite sense observed in the value of χ . Examining the other turning points, the southern hemisphere's maximum current strength is observed an hour later than the minimum seen in χ_S , whereas the minimum J_N MA is observed at 00-01 UT, 4 hours earlier than the corresponding maximum in χ_N . The difference between the current magnitude at the expected turning point and the magnitude at the observed turning point is less than 0.1 MA and as such has not been tabulated.

6.2.3 Mean Birkeland current strengths as a function of solar zenith angle χ

In this section, the response of the Birkeland current magnitude J to the variation of the conductance $\Sigma(\chi)$ across the polar regions is explored. Note that here, the conductance $\Sigma(\chi)$ varies with the co-ordinate on the surface of the Earth. As a result, Equation 6.1 is modified to use the mean of $\Sigma(\chi)$ instead of using Ξ , such that

$$J = \Phi_D \langle \Sigma \rangle. \quad (6.6)$$

6.2.3.1 Solar zenith angle χ over the auroral zone

In order to calculate $\Sigma(\chi)$ it is necessary to consider the value of χ across the polar cap and auroral zone, rather than just at the position of the geomagnetic pole (as plotted in Figure 6.4). As such, a $40^\circ \times 40^\circ$ rectilinear grid is employed in which the x -axis and y -axis are aligned with the dawn-dusk and noon-midnight local time meridians respectively. Each cell is 2° of magnetic latitude in both directions (approximately 222 km in both directions). This grid is placed such that it extends to 40° in both directions of x . Since the geomagnetic pole is offset from the rotational

pole by 10° , the range of y is offset such that it the grid goes from 50° to 30° . The solar zenith angle χ is calculated at every co-ordinate across the defined grid, and then the conductance $\Sigma(\chi)$ is calculated for each co-ordinate. An algorithm is employed to find the best $\Sigma(\chi)$ by calculating $\langle \Sigma \rangle$ and using Equation 6.6 with global J and Φ_D . The rectilinear grid used is similar to that used in Milan *et al.* (2014).

The colatitude ϕ and the longitude λ are calculated with the equations below:

$$\phi = \sqrt{x^2 + y^2} \quad (6.7)$$

$$\lambda = \tan^{-1}(x, -y) + \lambda_P \quad (6.8)$$

where the offset between $\lambda = 0^\circ$ and the longitude of the pole $\lambda_P = -72.2^\circ$ in the northern hemisphere and $\lambda_P = 107.8^\circ$ in the southern hemisphere in 2010 (Finlay *et al.*, 2010).

6.2.3.2 Different relations between Birkeland current strengths and conductance

Functional forms of $\Sigma(\chi)$ are averaged across the polar regions such that the best fits to the observed Birkeland currents may be contrasted. In all cases, it is assumed that

$$\Sigma(\chi \geq 90^\circ) = y_0, \quad (6.9)$$

i.e. that regions in darkness have a low residual conductance, whereas sunlit regions have conductances proportional to combinations of χ , $\cos \chi$ and $\sqrt{\cos \chi}$ and $F_{10.7}$. For each of these functional forms, the value of $\Sigma(\chi)$ across the polar cap is calculated and then the mean taken to achieve $\langle \Sigma(\chi) \rangle$, which is used instead of Ξ as a number which represents the global variation in conductance due to changes in solar illumination. The mean of the calculated conductances is calculated using only co-ordinates which lie no more than 30° from the geomagnetic pole on the rectilinear grid.

The first form explored is one in which the ionospheric conductance is related to the cosine of the solar zenith angle where

$$\Sigma(\chi < 90^\circ) = F_{10.7}^{\frac{1}{2}} \left(y_0 + y_a \cos^{\frac{1}{2}}(\chi) + y_b \cos(\chi) \right). \quad (6.10)$$

This has a term $F_{10.7}^{\frac{1}{2}} y_0$ added to an equation similar to that proposed by Moen and Brekke (1993); this addition is made because of the presence of a y_0 term in the work of Fujii and Iijima (1987).

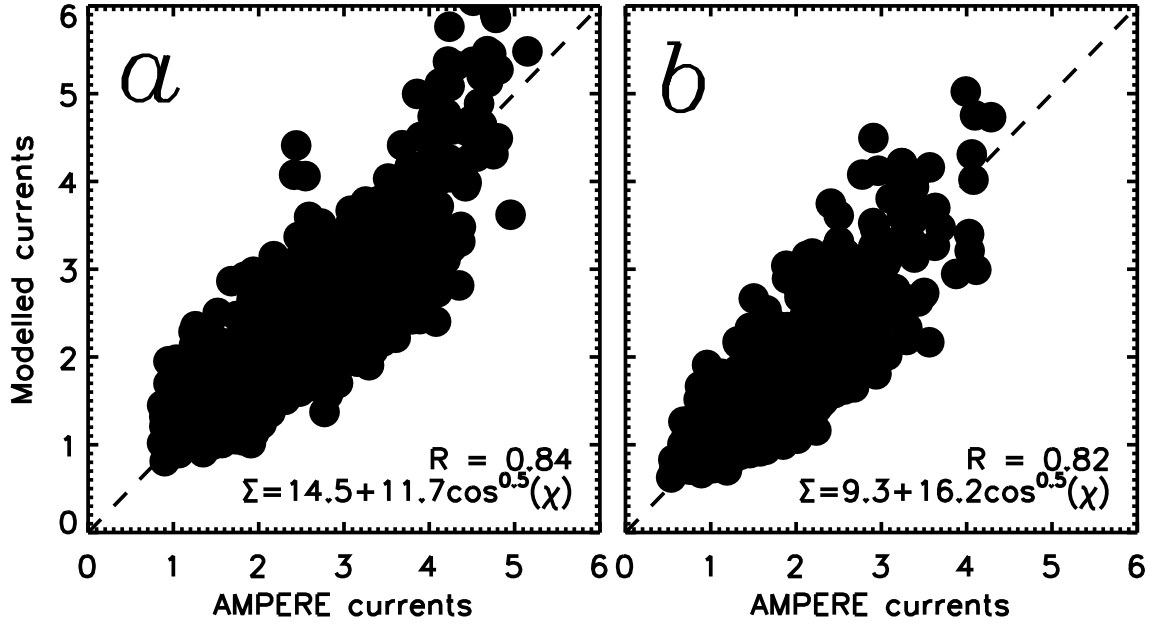


Figure 6.5: Figures to show the relationship between J and $\Phi_D\langle\Sigma(\chi)\rangle$ using a cosine model in the northern hemisphere (top) and the southern hemisphere (bottom).

The IDL function MPFIT (Moré, 1978; Markwardt, 2009) is employed to solve Equation 6.1 using Equation 6.10 using the Levenberg-Marquardt algorithm, calculating $\Phi_D\langle\Sigma(\chi)\rangle$ and comparing it to J to solve for y_0 , y_a and y_b . Each of the coefficients is constrained such that it is positive. The results achieved by the fitting process are shown in Figure 6.5. The solution to Equation 6.10 is found to be

$$\begin{aligned}\Sigma_N(\chi) &= F_{10.7}^{\frac{1}{2}} \left(14.5 + 11.7 \cos^{\frac{1}{2}}(\chi) \right) \text{ mho} \\ \Sigma_S(\chi) &= F_{10.7}^{\frac{1}{2}} \left(9.3 + 16.2 \cos^{\frac{1}{2}}(\chi) \right) \text{ mho}\end{aligned}\quad (6.11)$$

achieving a Pearson correlation coefficient $R = 0.84$ in the northern hemisphere and $R = 0.82$ in the southern hemisphere. The value of y_b was found to be zero in both fits, yielding functions which are comprised of the result of Robinson and Vondrak (1984) plus $F_{10.7}^{\frac{1}{2}}y_0$. The values of y_0 and y_a found in Equation 6.11 indicate that the variation of current with respect to the background level is significantly larger in the southern hemisphere than in the northern hemisphere, with $y_a = 0.81y_0$ in the northern hemisphere and $y_a = 1.74y_0$ in the southern hemisphere. This is because the background level is consistently larger in the northern hemisphere than in the southern hemisphere, consistent with the previously observed bias towards larger northern current magnitudes (Section 6.2.1).

A function was also attempted which was a linear relationship between the solar

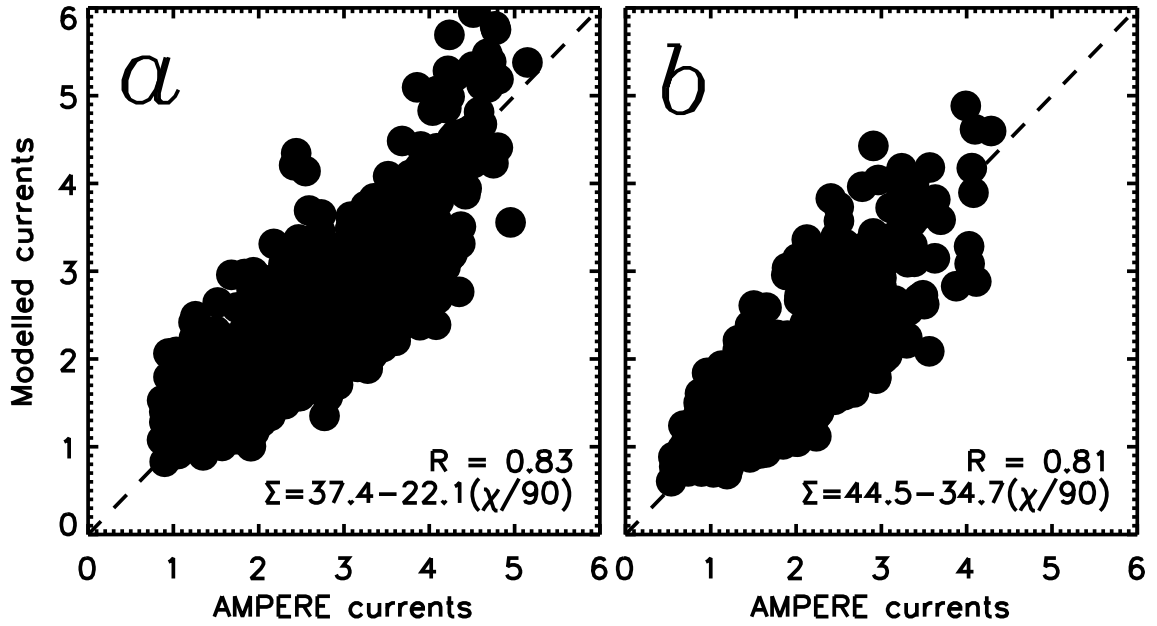


Figure 6.6: Figures to show the relationship between J and $\Phi_D\langle\Sigma(\chi)\rangle$ using a linear model in the northern hemisphere (top) and the southern hemisphere (bottom).

zenith angle (normalised by dividing it by 90°) and $\Sigma(\chi)$, such that

$$\Sigma(\chi) = F_{10.7}^{\frac{1}{2}} (y_0 - y_a(\chi/90^\circ)). \quad (6.12)$$

This is similar to the function used by Fujii and Iijima (1987), but multiplied by $F_{10.7}^{\frac{1}{2}}$. (It should be noted that neither of the functions used by Robinson and Vondrak (1984) and Moen and Brekke (1993) include a constant term y_0 , but the one used in Fujii and Iijima (1987) does.) The effect of fitting Equation 6.12 to the current magnitudes is shown in Figure 6.6. The solution to this equation is found to be

$$\begin{aligned} \Sigma_N(\chi) &= 37.4 - 22.1(\chi/90^\circ) \text{ mho} \\ \Sigma_S(\chi) &= 44.5 - 34.7(\chi/90^\circ) \text{ mho} \end{aligned} \quad (6.13)$$

achieving a Pearson correlation coefficient $R = 0.83$ in the northern hemisphere and $R = 0.81$. The correlation decreases with this form, suggesting that the result of Robinson and Vondrak (1984) is a better description of the phenomena considered. Therefore, Equation 6.10 is the function employed when examining subsets of the data in the rest of this chapter.

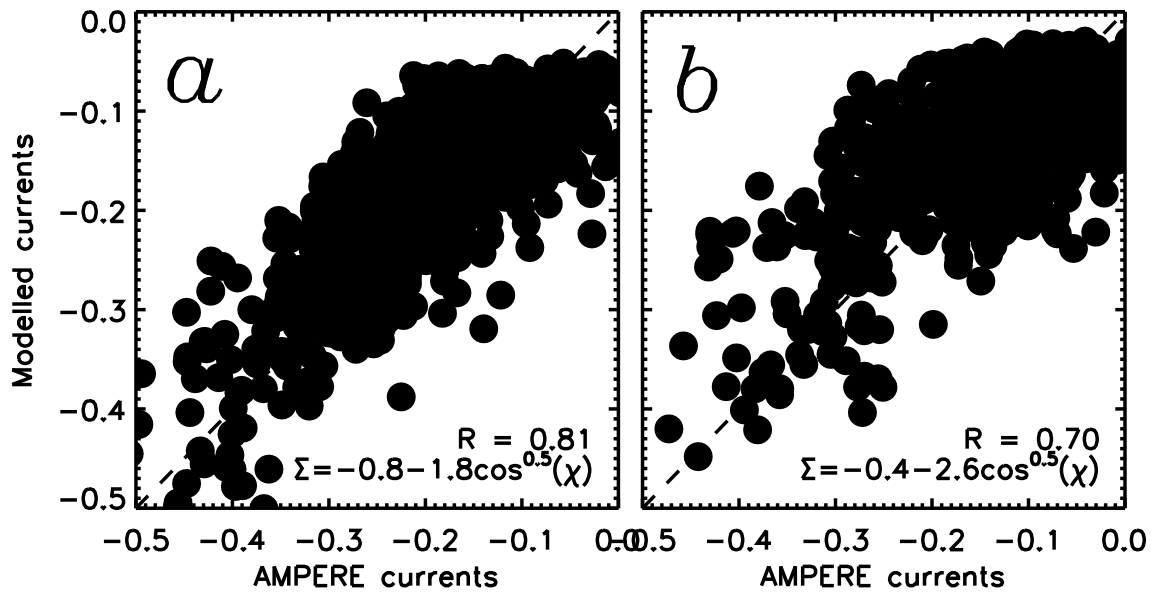


Figure 6.7: Figures to show the relationship between the dawnside net current magnitude J_A and $\Phi_D\langle\Sigma(\chi)\rangle$ for Equation 6.10 in the northern hemisphere (top) and the southern hemisphere (bottom).

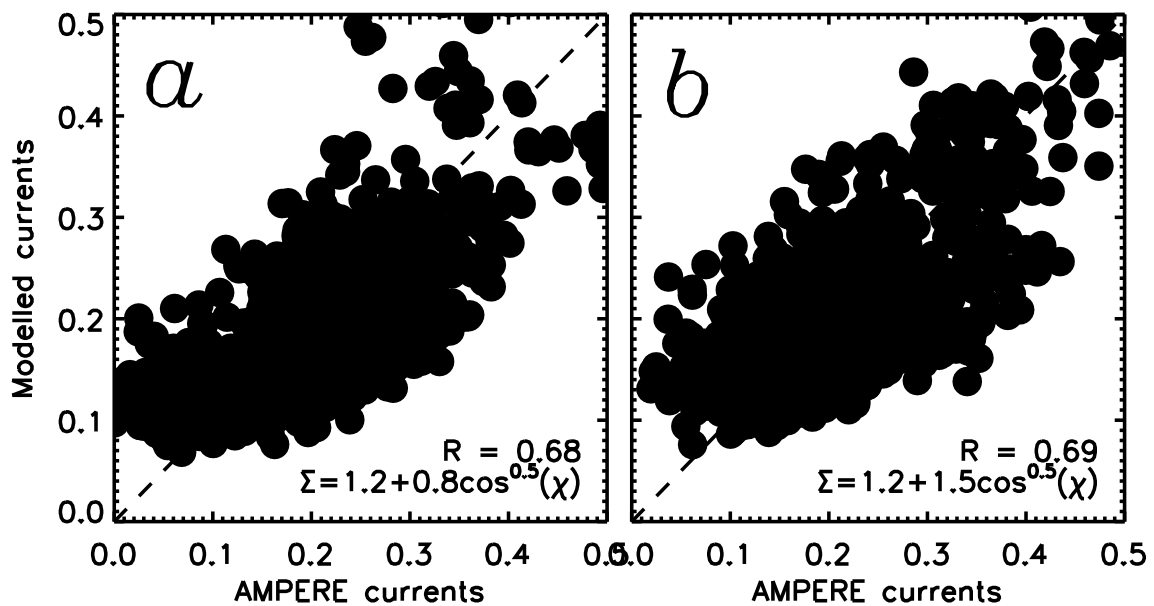


Figure 6.8: Figures to show the relationship between the duskside net current magnitude J_U and $\Phi_D\langle\Sigma(\chi)\rangle$ for Equation 6.10 in the northern hemisphere (top) and the southern hemisphere (bottom).

6.2.4 Comparison of net Birkeland current strengths with conductance

So far in this section, the total Birkeland currents have been measured. The net Birkeland currents are now considered, split into the dawnside currents $J_{A,h}$ ($0 \leq \text{MLT} < 12$) and the duskside currents $J_{U,h}$ ($12 \leq \text{MLT} < 24$). This is done in order

to investigate the Pedersen currents which cross the polar cap in order to close R1 Birkeland currents on either side.

Figure 6.7 shows the result of fitting Equation 6.10 to the net Birkeland currents on the dawnside $J_{A,h}$, with Pearson correlation coefficients $R_{A,N} = 0.81$ and $R_{A,S} = 0.70$:

$$\begin{aligned}\Sigma_{A,N}(\chi) &= -(0.8 + 1.8 \cos(\chi)) \text{ mho} \\ \Sigma_{A,S}(\chi) &= -(0.4 + 2.6 \cos(\chi)) \text{ mho}\end{aligned}\tag{6.14}$$

Figure 6.8 shows the result of fitting Equation 6.10 to the net Birkeland currents on the duskside $J_{U,h}$, with correlations $R_{U,N} = 0.68$ and $R_{U,S} = 0.69$.

$$\begin{aligned}\Sigma_{U,N}(\chi) &= 1.2 + 0.8 \cos(\chi) \text{ mho} \\ \Sigma_{U,S}(\chi) &= 1.2 + 1.5 \cos(\chi) \text{ mho}\end{aligned}\tag{6.15}$$

Any imbalance between the upward and downward Birkeland currents must be due to Pedersen currents flowing across the polar cap, and so the net current flows allow these Pedersen currents to be quantified, suggesting that the cross polar-cap Pedersen current flowing is between 0.05 MA and 0.5 MA.

6.3 Discussion

Chapters 4 and 5 have shown that Birkeland current magnitude J is consistent with driving by dayside reconnection rate Φ_D , and is also related to substorm processes in the magnetotail. Previous studies have linked conductance to Birkeland current strengths (Fujii and Iijima, 1987) and examined the conductances of other current systems (Moen and Brekke, 1993). In the discussion below, the significance of the inclusion of a conductance term to the relationship between J and Φ_D is quantified to illustrate the improvement yielded by the method described in this chapter.

6.3.1 Seasonal variation in conductance $\Xi(t)$

Figure 6.1 shows a clear seasonal variation in the current magnitude in the northern hemisphere J_N and in the southern hemisphere J_S . This seasonal variation is a total of 3.1 MA, with $J_N - J_S = 2.3$ MA at the height of the northern summer and $J_N - J_S = -0.8$ MA during the southern equivalent. This apparently suggests that the northern hemisphere enjoys proportionally larger current magnitudes as a result

of season, compared to the southern hemisphere. The observed larger northern currents might be a coincidental bias over the period of data shown, but would also be consistent with a bias towards larger northern hemisphere values in the AMPERE dataset. This would be in agreement with some of the conclusions drawn in Section 6.2.1. However, the peaks in the mean Φ_D are located during northern summers and the troughs located in southern summers, which might also provide an explanation for why stronger currents are found in the northern hemisphere. Note that there are two large reconnection signatures in March and July 2012, which are consistent with reports of intense periods of geomagnetic activity in those months (Wang *et al.*, 2013; Tsurutani *et al.*, 2014).

Comparing the Pearson correlation coefficient between J and Φ_D assuming no seasonal variation in conductance (the null hypothesis) allows insight into the variation of J with season. In the northern hemisphere, $R = 0.86$, and in the southern hemisphere $R = 0.61$, providing more evidence of the coincidentally high Φ_D during northern summer (and vice versa). The correlation coefficients measured for the data are $R = 0.91$ and $R = 0.92$ in the northern and southern hemisphere respectively, yielding improvements $\Delta R = 0.05$ in the north and $\Delta R = 0.31$ in the south. This difference is small in the northern hemisphere but much more pronounced in the southern hemisphere. Conducting an F-test on the data demonstrates that this improvement is statistically significant for both hemispheres, showing a clear seasonal effect in the data. To examine the dependence of the FACs on conductance more generally, zenith angles are considered.

6.3.2 Variation in conductance $\Sigma(\chi)$

The relationship of the conductance with solar zenith angle, and the related dependence of the current magnitudes, is now discussed. Previous work has established a link between J and $\Sigma(\chi)$ (e.g Robinson and Vondrak, 1984; Fujii and Iijima, 1987; Chisham *et al.*, 2009; Wiltberger *et al.*, 2009, and references therein), whilst some others have disagreed (Yamamoto *et al.*, 2003). This relationship is quantified for the AMPERE data under consideration. The correlation of J with Φ_D was found to be $R = 0.64$ in Chapter 4: by binning the data with hour of day and month of year, the correlations are 0.75 and 0.54 in the northern and southern hemisphere respectively.

First, the results of the cosine model outlined in Equation 6.11 are discussed. Correlation coefficients are found in the northern hemisphere of $R = 0.84$ and in the southern hemisphere $R = 0.82$. These correlations are high, indicating that the model under testing fits the data well. The current magnitude J is therefore inferred

to be dependent on conductance $\langle \Sigma \rangle$, with this dependence being well-described by a variation of Σ with the solar zenith angle χ . Different functions could be tried by using different functions of $\Sigma(\chi)$ (Robinson and Vondrak, 1984; Rasmussen *et al.*, 1988), but the small differences achieved in correlation coefficient between the two models fitted in this chapter implies that any such attempt would not increase the correlation achieved by a large amount. It should be noted that the function Robinson and Vondrak (1984) does not have a y_0 term; this is because they only considered periods of low geomagnetic activity; this analysis does not restrict itself to quiet times and as such the y_0 term is due to the average current flowing.

Previous studies have also concluded that dayside currents are responsive to variations in the conductance (Fujii *et al.*, 1981; Ohtani *et al.*, 2005b; Wang, 2005). Some authors have indicated that dayside Birkeland currents can be thought to be driven by a voltage generator (Watanabe *et al.*, 1998; Cattell *et al.*, 2003), which is consistent with the proposal that $J = \langle \Sigma \rangle \Phi_D$. Previous authors have also found that the nightside Birkeland currents are consistent with driving from a combination of a voltage generator (nightside reconnection) and a current generator (Fedder and Lyon, 1987; Wang, 2005; Lukianova and Christiansen, 2008; Chisham *et al.*, 2009).

6.3.3 Differences in net currents

Having discussed the dependence of the total current flowing on $\langle \Sigma(\chi) \rangle$, the net currents (on the dawnside and on the duskside) are now discussed. The magnitude of the net currents can be used to quantify the amount of current flowing across the noon-midnight meridian, since if there is a net downward current on the dawnside, the current must be closed via net upward current on the duskside. Previous work has shown that much of the current which flows across in this manner can be attributed to effects from substorms but currents can also close across the polar cap via Pedersen currents, which have been estimated to be approximately 0.1 MA in magnitude (Le *et al.*, 2010). Previous work has disagreed on the presence of a seasonal dependence of net currents (Fujii *et al.*, 1981; Christiansen *et al.*, 2002; Nakano *et al.*, 2002).

Figure 6.7 and Figure 6.8 show the net currents on the dawnside and duskside respectively. The correlation coefficients are lower than those observed for the total currents in the two hemispheres, but are still indicative of good correlations, with the net dawnward currents in the northern hemisphere achieving $R = 0.81$ and each other combination having a correlation $R \sim 0.70$. This indicates that net currents are dependent on solar zenith angle, and more current will flow across the polar cap during periods of larger $\langle \Sigma(\chi) \rangle$. Examining the net currents observed, the Pedersen

currents across the polar cap are $0 < J_P < 0.5$ MA, with higher Pedersen current flow during periods of higher conductivity and higher dayside reconnection rate. Substorms, which also play a significant role in the current flow across the noon-midnight meridian via the substorm electrojet (Chapter 5), are not thought to be associated with χ ; this is why the correlations are lower than for the total current.

6.4 Conclusions

We have estimated current magnitudes using the relation $J = \Phi_D \Xi$, demonstrating that Birkeland currents measured by AMPERE are seasonally dependent, with both hemispheres observed to have seasonal variations in the three years under discussion. These seasonal variations take the form $y_0 + y_a \sin(t)$, and they have been quantified as a variation in conductance of $0.19y_0$ in the northern hemisphere and $0.31y_0$ in the southern hemisphere, with correlation coefficients $R \sim 0.9$ in both hemispheres.

Furthermore, it has been shown that, over the three years, J also displays diurnal variations consistent with a dependence on solar zenith angle χ . It has been demonstrated that Birkeland currents are well-described by the function $J = \Phi_D \langle \Sigma(\chi) \rangle$, where $\Sigma(\chi)$ is given by $y_0 + y_a \cos(\chi)$. In the northern hemisphere, the total variation in conductance is $0.81y_0$ and the correlation coefficient is 0.84. In the southern hemisphere, the total variation in conductance is $1.74y_0$ and the correlation is 0.82. The larger background level in the northern hemisphere may indicate a bias in the AMPERE dataset towards higher current densities in the northern hemisphere.

The net Birkeland current flow has been examined in the same manner, and a conductance variation has been found with correlation coefficients of $R \sim 0.7$. The magnitude of the Pedersen currents flowing across the polar cap therefore also appears to depend on $\langle \Sigma(\chi) \rangle \Phi_D$, with Pedersen currents measured to be up to 0.5 MA in magnitude across the noon-midnight meridian. The lower correlation coefficients are attributed to effects from substorms (Chapter 5).

Chapter 7

Conclusion and future work

7.1 Conclusion

In this thesis, a picture has been outlined of the relationship between the Birkeland field-aligned currents which flow in the magnetosphere and magnetic reconnection on both the dayside and nightside of the magnetosphere. The currents over a three-year period (2010–2012) observed by AMPERE have been quantified in order to shed new light on this picture of the magnetosphere.

An overview of the reaction of the Birkeland currents to the dayside magnetic reconnection rate, and their reaction to the AL index, was presented in Chapter 4. The results were consistent with the explanation that R1 current is driven by ionospheric flows which are themselves driven by magnetic reconnection on the dayside and nightside. R2 is also well-ordered by comparison to these drivers, but seems to display somewhat more complex behaviour, with R2 weaker than R1 at given values of AL index.

It was shown that R1 currents generally tend to be stronger than R2 currents, with the ratio between R1 and R2 observed to be approximately 1.15 at higher current magnitudes. This can be explained by Pedersen currents flowing across the polar cap, allowing current to flow down through the dawn R1 current, cross the polar cap and then flow upward through R1 currents on the dusk side. However, the higher R1 current magnitudes may actually be a result of the westward electrojet which occurs during substorms, which allows current to close across the noon-midnight meridian, and would explain the observed change in relative R1 and R2 current strength with AL index.

The evolution during substorms of the spatial extent and the magnitude of the Birkeland currents is explored in Chapter 5. This is in order to better quantify

the behaviour of Birkeland currents in the context of the ECPC paradigm, but also to more fully explore the change in the magnitudes of the current systems during dayside and nightside reconnection. It was shown that the currents begin to become larger in magnitude as dayside reconnection rate becomes higher, and peak shortly after the onset of the expansion phase, decreasing through the rest of the epoch. This is consistent with the theory that the currents are driven by magnetic reconnection, with the maximum total reconnection rate coming shortly after the onset of the expansion phase, at which time dayside reconnection is waning but still occurring and the nightside reconnection rate has increased sharply.

The observed disparity in the magnitudes of the two current systems that was described in Chapter 4 can now be seen to be affected by the substorm process, with the onset of a substorm resulting in more current flowing across the polar cap and thus resulting in a larger ratio of R1 to R2 current magnitude. The results suggest that the substorm leads to more current flowing through both regions 1 and 2 current systems, but that the R1 current system is more enhanced by the substorm.

The data is categorised by colatitude, under the assumption that larger current ovals imply a larger polar cap and therefore more open magnetic flux. The current oval increases in size due to dayside reconnection prior to the substorm, and begins to decrease in size after the onset of the expansion phase; the change in the size of the current ovals can be used to pinpoint the stage at which nightside reconnection begins to dominate over dayside reconnection. When the current ovals are larger (and therefore the amount of open magnetic flux is higher) at the time of the substorm onset, this results in a faster nightside reconnection rate.

The analysis of seasonal variations in the reaction of the Birkeland currents to substorms presented in Chapter 5 led to the more detailed analysis of solar illumination effects presented in Chapter 6. Current magnitudes are estimated using the relation $J = \Phi_D \Xi$, where Ξ is a number which describes the change in conductance due to season for the global system. This demonstrates that Birkeland currents measured by AMPERE are seasonally dependent, with the seasonal variation found to be well-described by a sinusoid and the resulting correlation coefficient between the estimated and observed Φ_D of $R \sim 0.9$.

It is also shown in Chapter 6 that the Birkeland currents vary diurnally, consistent with a reliance on the solar illumination as a result of the solar zenith angle χ , and this is quantified, with currents in both hemispheres showing increases in magnitude at times of larger solar illumination. Calculation of the correlation between the observed current magnitudes and the current magnitudes estimated using

$J = \Phi_D < \Sigma(\chi) >$ shows $R > 0.8$, indicating that the Birkeland current magnitudes can be well-described by multiplication of the dayside reconnection rate by a measure of the variation of conductance with solar illumination.

The net Birkeland current flow has been examined in the same manner, and a conductance variation has been found with correlation coefficients of $R \sim 0.7$. The magnitude of the Pedersen currents flowing across the polar cap therefore also appears to depend on $\Sigma(\chi)\Phi_D$, with Pedersen currents measured to be up to 0.5 MA in magnitude across the noon-midnight meridian. The lower correlation coefficients are thought to be due to effects from substorms (Chapter 5).

Results from chapters 3, 5 and 6 show that northern hemisphere current magnitudes are consistently larger than their southern hemisphere counterparts across the three-year period examined in this thesis. This may be due to dayside reconnection dominating during the northern summers, as described in Chapter 6, but may also be indicative of a systematic bias in the AMPERE dataset itself which either overestimates northern hemisphere current density or underestimates southern hemisphere current density. This would better account for the observations, in Chapter 3, that fewer fits are found in the southern hemisphere than in the northern hemisphere for the period under examination; the AMPERE dataset needs to be compared with other spacecraft observations in both hemispheres on a statistical basis in order to quantify whether this effect is physical or whether it is due to a bias in the dataset employed.

7.2 Future work

In the future, the seasonal analysis performed in this thesis can be expanded upon; work should be done to better explore the relationship between variations in ionospheric conductance due to solar illumination and the Birkeland currents. One potential avenue for more detailed investigation would be to combine the Birkeland current model of Milan (2013) with models of the ionospheric conductance (Robinson and Vondrak, 1984; Moen and Brekke, 1993) in order to estimate the Birkeland current magnitudes and compare them with the AMPERE data described in Chapter 6.

In order to more finely separate the effects on the Birkeland current magnitude of magnetic reconnection and ionospheric conductance, a study might be imagined in which the AMPERE data are binned by dayside reconnection rate and by the mean ionospheric conductance in the polar region (as employed in Chapter 6) before being analysed. This would allow the analysis of Chapter 5 to be performed on each

bin, thus allowing for seasonal effects on the reaction to a substorm to be better quantified; such a thing could also be done to create averaged maps of the observed currents for each bin, similar to work that has been done with bins of different IMF components.

Another avenue of future potential research concerns the way in which the Birkeland currents are related to the position of the magnetopause. The Chapman-Ferraro currents which flow in the magnetopause close through the Birkeland current system, and there are many unanswered questions regarding the precise nature of this process. If a database could be compiled of magnetopause crossings in the period of time from the start of 2010, the location of the magnetopause could be compared with the Birkeland current magnitudes and locations at the time of each crossing, allowing for the link between the two to be better quantified.

In conclusion, AMPERE is a novel dataset which has allowed, for the first time, large-scale studies comparing the magnitude and spatial extent of the Birkeland currents with driving by magnetic reconnection as part of the expanding/contracting polar cap paradigm. This thesis has shown that observations of the Birkeland currents are consistent with the theory that magnetic reconnection on the dayside and the nightside drives larger Birkeland current magnitudes; causes the current ovals to expand and contract in the same sense as the polar cap, and that substorms lead to the magnitude of R1 increasing relative to R2. This thesis has also shown, for the first time, that observations are consistent with a picture in which the ionospheric conductance affects the Birkeland current magnitudes driven by magnetic reconnection.

References

- Acuña, M., Ogilvie, K., Baker, D., Curtis, S., Fairfield, D., and Mish, W.: The Global Geospace Science Program and its investigations, *Space Science Reviews*, **71**, 5–21, doi: 10.1007/BF00751323, 1995.
- Akasofu, S.-I.: The development of the auroral substorm, *Planetary and Space Science*, **12**, 273 – 282, doi: [http://dx.doi.org/10.1016/0032-0633\(64\)90151-5](http://dx.doi.org/10.1016/0032-0633(64)90151-5), 1964.
- Akasofu, S.-I.: The roles of the north-south component of the interplanetary magnetic field on large-scale auroral dynamics observed by the DMSP satellite, *Planetary and Space Science*, **23**, 1349 – 1354, doi: [http://dx.doi.org/10.1016/0032-0633\(75\)90030-6](http://dx.doi.org/10.1016/0032-0633(75)90030-6), 1975.
- Akasofu, S.-I.: Where is the magnetic energy for the expansion phase of auroral substorms accumulated?, *Journal of Geophysical Research: Space Physics*, **118**, 7219–7225, doi: 10.1002/2013JA019042, 2013.
- Akasofu, S.-I. and Chapman, S.: The ring current, geomagnetic disturbance, and the Van Allen radiation belts, *Journal of Geophysical Research*, **66**, 1321–1350, doi: 10.1029/JZ066i005p01321, 1961.
- Akasofu, S. I. and Meng, C. I.: A study of polar magnetic substorms, *Journal of Geophysical Research*, **74**, 293–313, doi: 10.1029/JA074i001p00293, 1969.
- Akasofu, S.-I., Meng, C.-I., and Kimball, D.: Dynamics of the aurora–IV: Polar magnetic substorms and westward traveling surges, *Journal of Atmospheric and Terrestrial Physics*, **28**, 489 – 496, doi: [http://dx.doi.org/10.1016/0021-9169\(66\)90058-4](http://dx.doi.org/10.1016/0021-9169(66)90058-4), 1966.
- Anderson, B. J. and Christiansen, F.: What features of field aligned currents might global scale fits miss?, *AGU Fall Meeting Abstracts*, p. D5, 2003.
- Anderson, B. J., Takahashi, K., and Toth, B. A.: Sensing global Birkeland currents with Iridium engineering magnetometer data, *Geophysical Research Letters*, **27**, 4045–4048, doi: 10.1029/2000GL000094, 2000.

- Anderson, B. J., Ohtani, S.-I., Korth, H., and Ukhorskiy, A.: Storm time dawn-dusk asymmetry of the large-scale Birkeland currents, *Journal of Geophysical Research: Space Physics*, **110**, n/a–n/a, doi: 10.1029/2005JA011246, 2005.
- Anderson, B. J., Korth, H., Waters, C. L., Green, D. L., and Stauning, P.: Statistical Birkeland current distributions from magnetic field observations by the Iridium constellation, *Annales Geophysicae*, **26**, 671–687, doi: 10.5194/angeo-26-671-2008, 2008.
- Anderson, B. J., Korth, H., Waters, C. L., Green, D. L., Merkin, V. G., Barnes, R. J., and Dyrud, L. P.: Development of large-scale Birkeland currents determined from the Active Magnetosphere and Planetary Electrodynamics Response Experiment, *Geophysical Research Letters*, **41**, 3017–3025, doi: 10.1002/2014GL059941, 2014.
- Araki, T., Kamei, T., and Iyemori, T.: Polar cap vertical currents associated with northward interplanetary magnetic field, *Geophysical Research Letters*, **11**, 23–26, doi: 10.1029/GL011i001p00023, 1984.
- Armstrong, J. C. and Zmuda, A. J.: Field-aligned current at 1100 km in the auroral region measured by satellite, *Journal of Geophysical Research*, **75**, 7122–7127, doi: 10.1029/JA075i034p07122, 1970.
- Armstrong, J. C. and Zmuda, A. J.: Triaxial magnetic measurements of field-aligned currents at 800 kilometers in the auroral region: Initial results, *Journal of Geophysical Research*, **78**, 6802–6807, doi: 10.1029/JA078i028p06802, 1973.
- Armstrong, J. C., Akasofu, S. I., and Rostoker, G.: A comparison of satellite observations of Birkeland currents with ground observations of visible aurora and ionospheric currents, *Journal of Geophysical Research*, **80**, 575–586, doi: 10.1029/JA080i004p00575, 1975.
- Axford, W. I. and Hines, C. O.: A unifying theory of high-latitude geophysical phenomena and geomagnetic storms, *Canadian Journal of Physics*, **39**, 1433–1464, doi: 10.1139/p61-172, 1961.
- Bahnsen, A.: Recent techniques of observations and results from the magnetopause regions, *Journal of Atmospheric and Terrestrial Physics*, **40**, 235 – 256, doi: [http://dx.doi.org/10.1016/0021-9169\(78\)90042-9](http://dx.doi.org/10.1016/0021-9169(78)90042-9), 1978.
- Baker, D. N., Anderson, R. C., Zwickl, R. D., and Slavin, J. A.: Average plasma and magnetic field variations in the distant magnetotail associated with near-Earth substorm effects, *Journal of Geophysical Research: Space Physics*, **92**, 71–81, doi: 10.1029/JA092iA01p00071, 1987.

- Baker, D. N., Pulkkinen, T. I., Angelopoulos, V., Baumjohann, W., and McPherson, R. L.: Neutral line model of substorms: Past results and present view, *Journal of Geophysical Research: Space Physics*, **101**, 12975–13010, doi: 10.1029/95JA03753, 1996.
- Baker, K. B. and Wing, S.: A new magnetic coordinate system for conjugate studies at high latitudes, *Journal of Geophysical Research: Space Physics*, **94**, 9139–9143, doi: 10.1029/JA094iA07p09139, 1989.
- Barfield, J. N., Saffelos, N. A., Sheehan, R. E., Carovillano, R. L., Potemra, T. A., and Knecht, D.: Three-dimensional observations of Birkeland currents, *Journal of Geophysical Research: Space Physics*, **91**, 4393–4403, doi: 10.1029/JA091iA04p04393, 1986.
- Baron, M. J., Heinselman, C. J., and Petrieks, J.: Solar cycle and seasonal variations of the ionosphere observed with the Chatanika incoherent scatter radar, *Radio Science*, **18**, 895–900, doi: 10.1029/RS018i006p00895, 1983.
- Baumjohann, W. and Treumann, R. A., eds.: Basic Space Plasma Physics, Imperial College Press, London, UK, 1997.
- Berchem, J. and Russell, C. T.: The thickness of the magnetopause current layer: ISEE 1 and 2 observations, *Journal of Geophysical Research: Space Physics*, **87**, 2108–2114, doi: 10.1029/JA087iA04p02108, 1982.
- Biermann, L.: Solar corpuscular radiation and the interplanetary gas, *The Observatory*, **77**, 109–110, 1957.
- Birkeland, K.: The Norwegian Aurora Polaris Expedition 1902-1903, vol. 1, H. Aschelhoug & Co., Christiania, Norway, 1908.
- Birkeland, K.: The Norwegian Aurora Polaris Expedition 1902-1903, vol. 2, H. Aschelhoug & Co., Christiania, Norway, 1913.
- Bonnevier, B., Boström, R., and Rostoker, G.: A three-dimensional model current system for polar magnetic substorms, *Journal of Geophysical Research*, **75**, 107–122, doi: 10.1029/JA075i001p00107, 1970.
- Borovsky, J. E. and Birn, J.: The solar wind electric field does not control the dayside reconnection rate, *Journal of Geophysical Research: Space Physics*, **119**, 751–760, doi: 10.1002/2013JA019193, 2014.
- Boström, R.: A model of the auroral electrojets, *Journal of Geophysical Research*, **69**, 4983–4999, doi: 10.1029/JZ069i023p04983, 1964.

- Boström, R.: Auroral electric fields, Tech. Rep. 66-15, KTH, Alfvén Laboratory, qC 20120420, 1966.
- Brandt, P., Roelof, E. C., Ohtani, S.-I., Mitchell, D. G., and Anderson, B. J.: IMAGE/HENA: Pressure and current distributions during the 1 October 2002 storm, *Advances in Space Research*, **33**, 719 – 722, doi: [http://dx.doi.org/10.1016/S0273-1177\(03\)00633-1](http://dx.doi.org/10.1016/S0273-1177(03)00633-1), 2004.
- Burton, R. K., McPherron, R. L., and Russell, C. T.: An empirical relationship between interplanetary conditions and D_{st} , *Journal of Geophysical Research*, **80**, 4204–4214, doi: [10.1029/JA080i031p04204](https://doi.org/10.1029/JA080i031p04204), 1975.
- Carlson, H. C. and Egeland, A.: The aurora and the auroral ionosphere, in Introduction to Space Physics, edited by M. G. Kivelson and C. T. Russell, chap. 14, pp. 459–502, Cambridge University Press, Cambridge, UK, 1995.
- Carrington, R. C.: Description of a singular appearance seen in the Sun on September 1, 1859, *Monthly Notices of the Royal Astronomical Society*, **20**, 13–15, 1859.
- Cattell, C., Dombeck, J., Peria, W., Strangeway, R., Elphic, R., and Carlson, C.: Fast Auroral Snapshot observations of the dependence of dayside auroral field-aligned currents on solar wind parameters and solar illumination, *Journal of Geophysical Research: Space Physics*, **108**, n/a–n/a, doi: [10.1029/2001JA000321](https://doi.org/10.1029/2001JA000321), 2003.
- Cauffman, D. P. and Gurnett, D. A.: Satellite measurements of high latitude convection electric fields, *Space Science Reviews*, **13**, 369–410, doi: [10.1007/BF00219164](https://doi.org/10.1007/BF00219164), 1972.
- Chapman, S. and Bartels, J.: Geomagnetism, International series of monographs on physics, Clarendon Press, Oxford, UK, URL <http://books.google.co.uk/books?id=NQgAAAAMAAJ>, 1940.
- Chapman, S. and Ferraro, V. C. A.: A new theory of magnetic storms, *Terrestrial Magnetism and Atmospheric Electricity*, **36**, 77–97, doi: [10.1029/TE036i002p00077](https://doi.org/10.1029/TE036i002p00077), 1931a.
- Chapman, S. and Ferraro, V. C. A.: A new theory of magnetic storms, *Terrestrial Magnetism and Atmospheric Electricity*, **36**, 171–186, doi: [10.1029/TE036i003p00171](https://doi.org/10.1029/TE036i003p00171), 1931b.
- Chisham, G., Freeman, M. P., Abel, G. A., Bristow, W. A., Marchaudon, A., Ruohoniemi, J. M., and Sofko, G. J.: Spatial distribution of average vorticity in the

- high-latitude ionosphere and its variation with interplanetary magnetic field direction and season, *Journal of Geophysical Research: Space Physics*, **114**, n/a–n/a, doi: 10.1029/2009JA014263, 2009.
- Christiansen, F., Papitashvili, V. O., and Neubert, T.: Seasonal variations of high-latitude field-aligned currents inferred from Ørsted and Magsat observations, *Journal of Geophysical Research: Space Physics*, **107**, SMP 5–1–SMP 5–13, doi: 10.1029/2001JA900104, 2002.
- Clauer, C. R. and McPherron, R. L.: Mapping the local time-universal time development of magnetospheric substorms using mid-latitude magnetic observations, *Journal of Geophysical Research*, **79**, 2811–2820, doi: 10.1029/JA079i019p02811, 1974.
- Clausen, L. B. N., Baker, J. B. H., Ruohoniemi, J. M., Milan, S. E., and Anderson, B. J.: Dynamics of the region 1 Birkeland current oval derived from the Active Magnetosphere and Planetary Electrodynamics Response Experiment (AMPERE), *Journal of Geophysical Research*, **117**, A06 233, 2012.
- Clausen, L. B. N., Baker, J. B. H., Ruohoniemi, J. M., Milan, S. E., Coxon, J. C., Wing, S., Ohtani, S., and Anderson, B. J.: Temporal and spatial dynamics of the regions 1 and 2 Birkeland currents during substorms, *Journal of Geophysical Research: Space Physics*, **118**, 3007–3016, doi: 10.1002/jgra.50288, 2013a.
- Clausen, L. B. N., Milan, S. E., Baker, J. B. H., Ruohoniemi, J. M., Glassmeier, K.-H., Coxon, J. C., and Anderson, B. J.: On the influence of open magnetic flux on substorm intensity: Ground- and space-based observations, *Journal of Geophysical Research: Space Physics*, **118**, 2958–2969, doi: 10.1002/jgra.50308, 2013b.
- Coleman, P. J., Davis, L., and Sonett, C. P.: Steady component of the interplanetary magnetic field: Pioneer V, *Phys. Rev. Lett.*, **5**, 43–46, doi: 10.1103/PhysRevLett.5.43, 1960.
- Cowley, S. W. H.: The causes of convection in the Earth’s magnetosphere: A review of developments during the IMS, *Reviews of Geophysics*, **20**, 531–565, doi: 10.1029/RG020i003p00531, 1982.
- Cowley, S. W. H.: Solar wind control of magnetospheric convection, in Achievements of the International Magnetospheric Study (IMS), edited by B. Battrock and E. Rolfe, vol. 217 of *ESA Special Publication*, pp. 483–494, 1984.

- Cowley, S. W. H.: Magnetosphere-ionosphere interactions: A tutorial review, in Magnetospheric Current Systems, vol. 118 of *Geophysical Monograph Series*, pp. 91–106, American Geophysical Union, Washington, DC, USA, URL <http://www.agu.org/books/gm/v118/GM118p0091/GM118p0091.shtml>, 2000.
- Cowley, S. W. H.: Current-voltage and kinetic energy flux relations for relativistic field-aligned acceleration of auroral electrons, *Annales Geophysicae*, **24**, 325–338, doi: 10.5194/angeo-24-325-2006, 2006.
- Cowley, S. W. H. and Lockwood, M.: Excitation and decay of solar wind-driven flows in the magnetosphere-ionosphere system, *Annales Geophysicae*, **10**, 103–115, 1992.
- Cowley, S. W. H., Morelli, J. P., and Lockwood, M.: Dependence of convective flows and particle precipitation in the high-latitude dayside ionosphere on the x and y components of the interplanetary magnetic field, *Journal of Geophysical Research: Space Physics*, **96**, 5557–5564, doi: 10.1029/90JA02063, 1991.
- Cramoysan, M., Bunting, R., and Orr, D.: The use of a model current wedge in the determination of the position of substorm current systems, *Annales Geophysicae*, **13**, 583–594, doi: 10.1007/s00585-995-0583-0, 1995.
- Cummings, W. D. and Coleman, P. J.: Magnetic fields in the magnetopause and vicinity at synchronous altitude, *Journal of Geophysical Research*, **73**, 5699–5718, doi: 10.1029/JA073i017p05699, 1968.
- Cummings, W. D. and Dessler, A. J.: Field-aligned currents in the magnetosphere, *Journal of Geophysical Research*, **72**, 1007–1013, doi: 10.1029/JZ072i003p01007, 1967.
- Cummings, W. D., Barfield, J. N., and Coleman, P. J.: Magnetospheric substorms observed at the synchronous orbit, *Journal of Geophysical Research*, **73**, 6687–6698, doi: 10.1029/JA073i021p06687, 1968.
- Davis, T. N. and Sugiura, M.: Auroral electrojet activity index AE and its universal time variations, *Journal of Geophysical Research*, **71**, 785–801, doi: 10.1029/JZ071i003p00785, 1966.
- de la Beaujardiere, O., Baron, M. J., Wickwar, V. B., Senior, C., and Evans, J. V.: The MITHRAS: A program of simultaneous radar observations of the high-latitude auroral zone, Tech. rep., Southwest Research Institute, 1982.
- de la Beaujardiere, O., Watermann, J., Newell, P., and Rich, F.: Relationship between Birkeland current regions, particle precipitation, and electric fields, *Journal*

- of Geophysical Research: Space Physics*, **98**, 7711–7720, doi: 10.1029/92JA02005, 1993.
- Doyle, M. A. and Burke, W. J.: S3-2 measurements of the polar cap potential, *Journal of Geophysical Research: Space Physics*, **88**, 9125–9133, doi: 10.1029/JA088iA11p09125, 1983.
- Dungey, J.: Conditions for the occurrence of electrical discharges in astrophysical systems, *Philosophical Magazine Series 7*, **44**, 725–738, doi: 10.1080/14786440708521050, 1953.
- Dungey, J. W.: Interplanetary magnetic field and the auroral zones, *Physics Review Letters*, **6**, 47–48, 1961.
- Dungey, J. W.: The length of the magnetospheric tail, *Journal of Geophysical Research*, **70**, 1753–1753, doi: 10.1029/JZ070i007p01753, 1965.
- Egeland, A., Holter, Ø., and Omholt, A., eds.: *Cosmical Geophysics*, Universitetsforlaget, Oslo, Norway, 1973.
- Elvey, C. T.: Problems in auroral morphology, *Proceedings of the National Academy of Sciences*, **43**, 63–75, URL <http://www.pnas.org/content/43/1/63.short>, 1957.
- Farris, M. H. and Russell, C. T.: Determining the standoff distance of the bow shock: Mach number dependence and use of models, *Journal of Geophysical Research: Space Physics*, **99**, 17 681–17 689, doi: 10.1029/94JA01020, 1994.
- Fedder, J. A. and Lyon, J. G.: The solar wind-magnetosphere-ionosphere current-voltage relationship, *Geophysical Research Letters*, **14**, 880–883, doi: 10.1029/GL014i008p00880, 1987.
- Feldstein, Y. I. and Levitin, A. E.: Solar wind control of electric fields and currents in the ionosphere, *Journal of Geomagnetism and Geoelectricity*, **38**, 1143–1182, doi: 10.5636/jgg.38.1143, 1986.
- Finlay, C. C., Maus, S., Beggan, C. D., Bondar, T. N., Chambodut, A., Chernova, T. A., Chulliat, A., Golovkov, V. P., Hamilton, B., Hamoudi, M., Holme, R., Hulot, G., Kuang, W., Langlais, B., Lesur, V., Lowes, F. J., Lhr, H., Macmillan, S., Manda, M., McLean, S., Manoj, C., Menvielle, M., Michaelis, I., Olsen, N., Rauberg, J., Rother, M., Sabaka, T. J., Tangborn, A., Tffner-Clausen, L., Thbault, E., Thomson, A. W. P., Wardinski, I., Wei, Z., and Zvereva, T. I.: International Geomagnetic Reference Field: The eleventh generation, *Geophysical*

- Journal International*, **183**, 1216–1230, doi: 10.1111/j.1365-246X.2010.04804.x, 2010.
- Fok, M.-C., Wolf, R. A., Spiro, R. W., and Moore, T. E.: Comprehensive computational model of Earth's ring current, *Journal of Geophysical Research: Space Physics*, **106**, 8417–8424, doi: 10.1029/2000JA000235, 2001.
- Forsyth, C., Fazakerley, A. N., Rae, I. J., J. Watt, C. E., Murphy, K., Wild, J. A., Karlsson, T., Mutel, R., Owen, C. J., Ergun, R., Masson, A., Berthomier, M., Donovan, E., Frey, H. U., Matzka, J., Stolle, C., and Zhang, Y.: In situ spatiotemporal measurements of the detailed azimuthal substructure of the substorm current wedge, *Journal of Geophysical Research: Space Physics*, **119**, 927–946, doi: 10.1002/2013JA019302, 2014.
- Foster, J. C.: An empirical electric field model derived from Chatanika radar data, *Journal of Geophysical Research: Space Physics*, **88**, 981–987, doi: 10.1029/JA088iA02p00981, 1983.
- Freeman, M. and Southwood, D.: The effect of magnetospheric erosion on mid- and high-latitude ionospheric flows, *Planetary and Space Science*, **36**, 509 – 522, doi: [http://dx.doi.org/10.1016/0032-0633\(88\)90110-9](http://dx.doi.org/10.1016/0032-0633(88)90110-9), 1988.
- Freeman, M. P. and Morley, S. K.: No evidence for externally triggered substorms based on superposed epoch analysis of IMF B_z , *Geophysical Research Letters*, **36**, n/a–n/a, doi: 10.1029/2009GL040621, 2009.
- Freeman, M. P., Southwood, D. J., Lester, M., and Waldock, J. A.: Measurement of field-aligned currents by the SABRE coherent scatter radar, in Physics of Magnetic Flux Ropes, vol. 58 of *Geophysical Monograph Series*, pp. 575–580, American Geophysical Union, Washington, DC, USA, doi: 10.1029/GM058p0575, 1990.
- Friis-Christensen, E., Kamide, Y., Richmond, A. D., and Matsushita, S.: Interplanetary magnetic field control of high-latitude electric fields and currents determined from Greenland Magnetometer Data, *Journal of Geophysical Research: Space Physics*, **90**, 1325–1338, doi: 10.1029/JA090iA02p01325, 1985.
- Fujii, R. and Iijima, T.: Control of the ionospheric conductivities on large-scale Birkeland current intensities under geomagnetic quiet conditions, *Journal of Geophysical Research: Space Physics*, **92**, 4505–4513, doi: 10.1029/JA092iA05p04505, 1987.
- Fujii, R., Iijima, T., Potemra, T. A., and Sugiura, M.: Seasonal dependence of large-scale Birkeland currents, *Geophysical Research Letters*, **8**, 1103–1106, doi: 10.1029/GL008i010p01103, 1981.

- Fukushima, N.: Equivalence in ground geomagnetic effect of Chapman-Vestine's and Birkeland-Alfven's electric current-systems for polar magnetic storms, *Report of Ionosphere and Space Research in Japan*, **23**, 219–227, 1969.
- Fukushima, N.: Generalized theorem for no ground magnetic effect of vertical currents connected with Pedersen currents in the uniform-conductivity ionosphere, *Report of Ionosphere and Space Research in Japan*, **30**, 35–40, 1976.
- Gjerloev, J. W.: A global ground-based magnetometer initiative, *Eos, Transactions American Geophysical Union*, **90**, 230–231, doi: 10.1029/2009EO270002, 2009.
- Gjerloev, J. W.: The SuperMAG data processing technique, *Journal of Geophysical Research: Space Physics*, **117**, n/a–n/a, doi: 10.1029/2012JA017683, 2012.
- Gjerloev, J. W., Ohtani, S., Iijima, T., Anderson, B., Slavin, J., and Le, G.: Characteristics of the terrestrial field-aligned current system, *Annales Geophysicae*, **29**, 1713–1729, doi: 10.5194/angeo-29-1713-2011, 2011.
- Gonzalez, W. D. and Mozer, F. S.: A quantitative model for the potential resulting from reconnection with an arbitrary interplanetary magnetic field, *Journal of Geophysical Research*, **79**, 4186–4194, doi: 10.1029/JA079i028p04186, 1974.
- Grant, I. S. and Phillips, W. R.: Electromagnetism, John Wiley & Sons, Chicester, UK, 2 edn., 1990.
- Green, D. L., Waters, C. L., Anderson, B. J., Korth, H., and Barnes, R. J.: Comparison of large-scale Birkeland currents determined from Iridium and SuperDARN data, *Annales Geophysicae*, **24**, 941–959, doi: 10.5194/angeo-24-941-2006, 2006.
- Green, D. L., Waters, C. L., Anderson, B. J., and Korth, H.: Seasonal and interplanetary magnetic field dependence of the field-aligned currents for both northern and southern hemispheres, *Annales Geophysicae*, **27**, 1701–1715, doi: 10.5194/angeo-27-1701-2009, 2009.
- Grocott, A., Wild, J. A., Milan, S. E., and Yeoman, T. K.: Superposed epoch analysis of the ionospheric convection evolution during substorms: Onset latitude dependence, *Annales Geophysicae*, **27**, 591–600, doi: 10.5194/angeo-27-591-2009, 2009.
- Grocott, A., Milan, S. E., Imber, S. M., Lester, M., and Yeoman, T. K.: A quantitative deconstruction of the morphology of high-latitude ionospheric convection, *Journal of Geophysical Research: Space Physics*, **117**, n/a–n/a, doi: 10.1029/2012JA017580, 2012.

- Harten, R. and Clark, K.: The design features of the GGS Wind and Polar spacecraft, *Space Science Reviews*, **71**, 23–40, doi: 10.1007/BF00751324, 1995a.
- Harten, R. and Clark, K.: The WIND magnetic field investigation, *Space Science Reviews*, **71**, 207–229, doi: 10.1007/BF00751330, 1995b.
- He, M., Vogt, J., Lhr, H., Sorbalo, E., Blagau, A., Le, G., and Lu, G.: A high-resolution model of field-aligned currents through empirical orthogonal functions analysis (MFACE), *Geophysical Research Letters*, **39**, n/a–n/a, doi: 10.1029/2012GL053168, 2012.
- Heppner, J. P.: Polar-cap electric field distributions related to the interplanetary magnetic field direction, *Journal of Geophysical Research*, **77**, 4877–4887, doi: 10.1029/JA077i025p04877, 1972.
- Heppner, J. P.: Empirical models of high-latitude electric fields, *Journal of Geophysical Research*, **82**, 1115–1125, doi: 10.1029/JA082i007p01115, 1977.
- Hoffman, R. A., Fujii, R., and Sugiura, M.: Characteristics of the field-aligned current system in the nighttime sector during auroral substorms, *Journal of Geophysical Research: Space Physics*, **99**, 21 303–21 325, doi: 10.1029/94JA01659, 1994.
- Holzer, R. E. and Slavin, J. A.: Magnetic flux transfer associated with expansions and contractions of the dayside magnetosphere, *Journal of Geophysical Research: Space Physics*, **83**, 3831–3839, doi: 10.1029/JA083iA08p03831, 1978.
- Holzer, R. E., McPherron, R. L., and Hardy, D. A.: A quantitative empirical model of the magnetospheric flux transfer process, *Journal of Geophysical Research: Space Physics*, **91**, 3287–3293, doi: 10.1029/JA091iA03p03287, 1986.
- Hones, E. W., Baker, D. N., Bame, S. J., Feldman, W. C., Gosling, J. T., McComas, D. J., Zwickl, R. D., Slavin, J. A., Smith, E. J., and Tsurutani, B. T.: Structure of the magnetotail at 220 R_E and its response to geomagnetic activity, *Geophysical Research Letters*, **11**, 5–7, doi: 10.1029/GL011i001p00005, 1984.
- Horning, B. L., McPherron, R. L., and Jackson, D. D.: Application of linear inverse theory to a line current model of substorm current systems, *Journal of Geophysical Research*, **79**, 5202–5210, doi: 10.1029/JA079i034p05202, 1974.
- Huang, C.-S., Sofko, G. J., Koustov, A. V., Andre, D. A., Ruohoniemi, J. M., Greenwald, R. A., and Hairston, M. R.: Evolution of ionospheric multicell convection during northward interplanetary magnetic field with $|B_z/B_y| > 1$, *Jour-*

- Journal of Geophysical Research: Space Physics*, **105**, 27 095–27 107, doi: 10.1029/2000JA000163, 2000.
- Hughes, W. J.: The magnetopause, magnetotail and magnetic reconnection, in Introduction to Space Physics, edited by M. G. Kivelson and C. T. Russell, chap. 9, pp. 227–287, Cambridge University Press, Cambridge, UK, 1995.
- Hundhausen, A. J.: The solar wind, in Introduction to Space Physics, edited by M. G. Kivelson and C. T. Russell, chap. 4, pp. 91–128, Cambridge University Press, Cambridge, UK, 1995.
- Iijima, T. and Potemra, T. A.: The amplitude distribution of field-aligned currents at northern high latitudes observed by Triad, *Journal of Geophysical Research*, **81**, 2165–2174, 1976a.
- Iijima, T. and Potemra, T. A.: Field-aligned currents in the dayside cusp observed by Triad, *Journal of Geophysical Research*, **81**, 5971–5979, 1976b.
- Iijima, T. and Potemra, T. A.: Large-scale characteristics of field-aligned currents associated with substorms, *Journal of Geophysical Research*, **83**, 599–615, 1978.
- Iijima, T., Potemra, T. A., Zanetti, L. J., and Bythrow, P. F.: Large-scale Birkeland currents in the dayside polar region during strongly northward IMF: A new Birkeland current system, *Journal of Geophysical Research: Space Physics*, **89**, 7441–7452, doi: 10.1029/JA089iA09p07441, 1984.
- Imber, S. M., Milan, S. E., and Hubert, B.: The auroral and ionospheric flow signatures of dual lobe reconnection, *Annales Geophysicae*, **24**, 3115–3129, doi: 10.5194/angeo-24-3115-2006, 2006.
- Imber, S. M., Milan, S. E., and Lester, M.: The Heppner-Maynard boundary measured by SuperDARN as a proxy for the latitude of the auroral oval, *Journal of Geophysical Research: Space Physics*, **118**, 685–697, doi: 10.1029/2012JA018222, 2013a.
- Imber, S. M., Milan, S. E., and Lester, M.: Solar cycle variations in polar cap area measured by the SuperDARN radars, *Journal of Geophysical Research: Space Physics*, **118**, 6188–6196, doi: 10.1002/jgra.50509, 2013b.
- Juusola, L., Kauristie, K., Amm, O., and Ritter, P.: Statistical dependence of auroral ionospheric currents on solar wind and geomagnetic parameters from 5 years of CHAMP satellite data, *Annales Geophysicae*, **27**, 1005–1017, doi: 10.5194/angeo-27-1005-2009, 2009.

- Juusola, L., Milan, S. E., Lester, M., Grocott, A., and Imber, S. M.: Interplanetary magnetic field control of the ionospheric field-aligned current and convection distributions, *Journal of Geophysical Research: Space Physics*, pp. n/a–n/a, doi: 10.1002/2013JA019455, 2014.
- Kamide, Y. and Akasofu, S.-I.: The auroral electrojet and field-aligned current, *Planetary and Space Science*, **24**, 203 – 213, doi: [http://dx.doi.org/10.1016/0032-0633\(76\)90017-9](http://dx.doi.org/10.1016/0032-0633(76)90017-9), 1976.
- Kamide, Y., Burch, J. L., Winningham, J. D., and Akasofu, S. I.: Dependence of the latitude of the cleft on the interplanetary magnetic field and substorm activity, *Journal of Geophysical Research*, **81**, 698–704, doi: 10.1029/JA081i004p00698, 1976.
- Kamide, Y., Richmond, A. D., and Matsushita, S.: Estimation of ionospheric electric fields, ionospheric currents, and field-aligned currents from ground magnetic records, *Journal of Geophysical Research: Space Physics*, **86**, 801–813, doi: 10.1029/JA086iA02p00801, 1981.
- Kamide, Y., Kokubun, S., Bargatze, L., and Frank, L.: The size of the polar cap as an indicator of substorm energy, *Physics and Chemistry of the Earth, Part C: Solar, Terrestrial & Planetary Science*, **24**, 119 – 127, doi: [http://dx.doi.org/10.1016/S1464-1917\(98\)00018-X](http://dx.doi.org/10.1016/S1464-1917(98)00018-X), 1999.
- Kan, J. R. and Lee, L. C.: Energy coupling function and solar wind-magnetosphere dynamo, *Geophysical Research Letters*, **6**, 577–580, doi: 10.1029/GL006i007p00577, 1979.
- Kern, J. W.: Analysis of polar magnetic storms, *Journal of Geomagnetism and Geoelectricity*, **18**, 125–131, doi: 10.5636/jgg.18.125, 1966.
- Kikuchi, T., Lhr, H., Kitamura, T., Saka, O., and Schlegel, K.: Direct penetration of the polar electric field to the equator during a $D_P 2$ event as detected by the auroral and equatorial magnetometer chains and the EISCAT radar, *Journal of Geophysical Research: Space Physics*, **101**, 17 161–17 173, doi: 10.1029/96JA01299, 1996.
- King, J. H. and Papitashvili, N. E.: One min and 5-min solar wind data sets at the Earth's bow shock nose, <http://omniweb.gsfc.nasa.gov/html/HROdocum.html>, accessed on 16 October 2014, 2014.
- Kivelson, M. G.: Physics of space plasmas, in *Introduction to Space Physics*, edited by M. G. Kivelson and C. T. Russell, chap. 2, pp. 27–57, Cambridge University Press, Cambridge, UK, 1995.

- Kivelson, M. G. and Russell, C. T., eds.: Introduction to Space Physics, Cambridge University Press, Cambridge, UK, 1995.
- Knetter, T., Neubauer, F. M., Horbury, T., and Balogh, A.: Four-point discontinuity observations using Cluster magnetic field data: A statistical survey, *Journal of Geophysical Research: Space Physics*, **109**, n/a–n/a, doi: 10.1029/2003JA010099, 2004.
- Knight, S.: Parallel electric fields, *Planetary and Space Science*, **21**, 741 – 750, doi: [http://dx.doi.org/10.1016/0032-0633\(73\)90093-7](http://dx.doi.org/10.1016/0032-0633(73)90093-7), 1973.
- Korth, H., Anderson, B. J., and Waters, C. L.: Statistical analysis of the dependence of large-scale Birkeland currents on solar wind parameters, *Annales Geophysicae*, **28**, 515–530, doi: 10.5194/angeo-28-515-2010, 2010.
- Lanchester, B. S., Rees, M. H., Lummerzheim, D., Otto, A., Sedgemore-Schulthess, K. J. F., Zhu, H., and McCrea, I. W.: Ohmic heating as evidence for strong field-aligned currents in filamentary aurora, *Journal of Geophysical Research: Space Physics*, **106**, 1785–1794, doi: 10.1029/1999JA000292, 2001.
- Le, G., Slavin, J. A., and Strangeway, R. J.: Space Technology 5 observations of the imbalance of regions 1 and 2 field-aligned currents and its implication to the cross-polar cap Pedersen currents, *Journal of Geophysical Research: Space Physics*, **115**, n/a–n/a, doi: 10.1029/2009JA014979, 2010.
- Lockwood, M.: On flow reversal boundaries and transpolar voltage in average models of high-latitude convection, *Planetary and Space Science*, **39**, 397 – 409, doi: [http://dx.doi.org/10.1016/0032-0633\(91\)90002-R](http://dx.doi.org/10.1016/0032-0633(91)90002-R), 1991.
- Lockwood, M. and Cowley, S. W. H.: Ionospheric convection and the substorm cycle, in *Substorms 1: Proceedings of the First International Conference on Substorms*, vol. 1, pp. 99–109, European Space Agency, Kiruna, Sweden, 1992.
- Luhmann, J. G.: Ionospheres, in *Introduction to Space Physics*, edited by M. G. Kivelson and C. T. Russell, chap. 7, pp. 183–202, Cambridge University Press, Cambridge, UK, 1995.
- Lukianova, R. and Christiansen, F.: Modeling the UT effect in global distribution of ionospheric electric fields, *Journal of Atmospheric and Solar-Terrestrial Physics*, **70**, 637 – 645, doi: <http://dx.doi.org/10.1016/j.jastp.2007.08.047>, 2008.
- Lyons, L.: Generation of large-scale regions of auroral currents, electric potentials, and precipitation by the divergence of the convection electric field, *Journal of*

- Geophysical Research: Space Physics*, **85**, 17–24, doi: 10.1029/JA085iA01p00017, 1980.
- Markwardt, C. B.: Non-linear least-squares fitting in IDL with MPFIT, in *Astronomical Data Analysis Software and Systems XVIII*, edited by D. A. Bohlander, D. Durand, and P. Dowler, vol. 411 of *Astronomical Society of the Pacific Conference Series*, p. 251, 2009.
- McDiarmid, I. B., Burrows, J. R., and Wilson, M. D.: Large-scale magnetic field perturbations and particle measurements at 1400 km on the dayside, *Journal of Geophysical Research: Space Physics*, **84**, 1431–1441, doi: 10.1029/JA084iA04p01431, 1979.
- McPherron, R.: Substorm related changes in the geomagnetic tail: The growth phase, *Planetary and Space Science*, **20**, 1521 – 1539, doi: [http://dx.doi.org/10.1016/0032-0633\(72\)90054-2](http://dx.doi.org/10.1016/0032-0633(72)90054-2), 1972.
- McPherron, R. L.: Growth phase of magnetospheric substorms, *Journal of Geophysical Research*, **75**, 5592–5599, doi: 10.1029/JA075i028p05592, 1970.
- McPherron, R. L.: Magnetospheric dynamics, in *Introduction to Space Physics*, edited by M. G. Kivelson and C. T. Russell, chap. 13, pp. 400–458, Cambridge University Press, Cambridge, UK, 1995.
- McPherron, R. L., Russell, C. T., and Aubry, M. P.: Satellite studies of magnetospheric substorms on august 15, 1968: 9. phenomenological model for substorms, *Journal of Geophysical Research*, **78**, 3131–3149, doi: 10.1029/JA078i016p03131, 1973.
- McWilliams, K. A., Yeoman, T. K., Sigwarth, J. B., Frank, L. A., and Brittnacher, M.: The dayside ultraviolet aurora and convection responses to a southward turning of the interplanetary magnetic field, *Annales Geophysicae*, **19**, 707–721, doi: 10.5194/angeo-19-707-2001, 2001.
- Mehta, N. C.: Ionospheric electrodynamics and its coupling to the magnetosphere, Ph.D. thesis, University of California, San Diego, California, USA, 1979.
- Meng, C. I. and Akasofu, S. I.: A study of polar magnetic substorms: 2. three-dimensional current system, *Journal of Geophysical Research*, **74**, 4035–4053, doi: 10.1029/JA074i016p04035, 1969.
- Milan, S. E.: Dayside and nightside contributions to the cross polar cap potential: Placing an upper limit on a viscous-like interaction, *Annales Geophysicae*, **22**, 3771–3777, doi: 10.5194/angeo-22-3771-2004, 2004.

- Milan, S. E.: Modeling Birkeland currents in the expanding/contracting polar cap paradigm, *Journal of Geophysical Research: Space Physics*, **118**, 5532–5542, doi: 10.1002/jgra.50393, 2013.
- Milan, S. E.: The proposed modification of Borovsky and Birn (2014) reduces the correlation of the function proposed by Milan *et al.* (2012), private communication, received on 9 July, 2014.
- Milan, S. E., Lester, M., Cowley, S. W. H., Oksavik, K., Brittnacher, M., Greenwald, R. A., Sofko, G., and Villain, J.-P.: Variations in the polar cap area during two substorm cycles, *Annales Geophysicae*, **21**, 1121–1140, doi: 10.5194/angeo-21-1121-2003, 2003.
- Milan, S. E., Provan, G., and Hubert, B.: Magnetic flux transport in the Dungey cycle: A survey of dayside and nightside reconnection rates, *Journal of Geophysical Research: Space Physics*, **112**, A01 209, doi: 10.1029/2006JA011642, 2007.
- Milan, S. E., Boakes, P. D., and Hubert, B.: Response of the expanding/contracting polar cap to weak and strong solar wind driving: Implications for substorm onset, *Journal of Geophysical Research: Space Physics*, **113**, doi: 10.1029/2008JA013340, 2008.
- Milan, S. E., Grocott, A., Forsyth, C., Imber, S. M., Boakes, P. D., and Hubert, B.: A superposed epoch analysis of auroral evolution during substorm growth, onset and recovery: Open magnetic flux control of substorm intensity, *Annales Geophysicae*, **27**, 659–668, doi: 10.5194/angeo-27-659-2009, 2009a.
- Milan, S. E., Hutchinson, J., Boakes, P. D., and Hubert, B.: Influences on the radius of the auroral oval, *Annales Geophysicae*, **27**, 2913–2924, 2009b.
- Milan, S. E., Gosling, J. S., and Hubert, B.: Relationship between interplanetary parameters and the magnetopause reconnection rate quantified from observations of the expanding polar cap, *Journal of Geophysical Research*, **117**, A03 226, 2012.
- Milan, S. E., Imber, S., and Lester, M.: ECLAT SuperDARN user guide, <http://www2.le.ac.uk/departments/physics/research/rspp/missions/eclat/eclat-data-products>, accessed on 6 November 2014, 2014.
- Milone, E. F. and Wilson, W. J. F.: *Solar System Astrophysics: Planetary Atmospheres and the Outer Solar System*, Springer, Berlin, Germany, 2008.
- Moen, J. and Brekke, A.: The solar flux influence on quiet time conductances in the auroral ionosphere, *Geophysical Research Letters*, **20**, 971–974, doi: 10.1029/92GL02109, 1993.

- Moré, J.: The Levenberg-Marquardt algorithm: Implementation and theory, in Numerical Analysis, edited by G. Watson, vol. 630 of *Lecture Notes in Mathematics*, pp. 105–116, Springer Berlin Heidelberg, doi: 10.1007/BFb0067700, 1978.
- Murphy, K. R., Man, I. R., Jonathan Rae, I., Waters, C. L., Frey, H. U., Kale, A., Singer, H. J., Anderson, B. J., and Korth, H.: The detailed spatial structure of field aligned currents comprising the substorm current wedge, *Journal of Geophysical Research: Space Physics*, pp. n/a–n/a, doi: 10.1002/2013JA018979, 2013.
- Nakano, S., Iyemori, T., and Yamashita, S.: Net field-aligned currents controlled by the polar ionospheric conductivity, *Journal of Geophysical Research: Space Physics*, **107**, SMP 4–1–SMP 4–6, doi: 10.1029/2001JA900177, 2002.
- Newell, P. T. and Gjerloev, J. W.: Evaluation of SuperMAG auroral electrojet indices as indicators of substorms and auroral power, *Journal of Geophysical Research: Space Physics*, **116**, n/a–n/a, doi: 10.1029/2011JA016779, 2011a.
- Newell, P. T. and Gjerloev, J. W.: Substorm and magnetosphere characteristic scales inferred from the SuperMAG auroral electrojet indices, *Journal of Geophysical Research: Space Physics*, **116**, n/a–n/a, doi: 10.1029/2011JA016936, 2011b.
- Newell, P. T., Sotirelis, T., Liou, K., Meng, C.-I., and Rich, F. J.: A nearly universal solar wind-magnetosphere coupling function inferred from 10 magnetospheric state variables, *Journal of Geophysical Research: Space Physics*, **112**, n/a–n/a, doi: 10.1029/2006JA012015, 2007.
- Nishida, A.: Geomagnetic D_P 2 fluctuations and associated magnetospheric phenomena, *Journal of Geophysical Research*, **73**, 1795–1803, doi: 10.1029/JA073i005p01795, 1968.
- Nishida, A.: The Geotail mission, *Geophysical Research Letters*, **21**, 2871–2873, doi: 10.1029/94GL01223, 1994.
- Nishida, A. and Cahill, L. J.: Sudden impulses in the magnetosphere observed by Explorer 12, *Journal of Geophysical Research*, **69**, 2243–2255, doi: 10.1029/JZ069i011p02243, 1964.
- Obayashi, T.: The interaction of the solar wind with the geomagnetic field during disturbed conditions, in *Solar-Terrestrial Physics*, p. 107, Academic Press, London, UK, 1967.
- Ohtani, S., Potemra, T. A., Newell, P. T., Zanetti, L. J., Iijima, T., Watanabe, M., Blomberg, L. G., Elphinstone, R. D., Murphree, J. S., Yamauchi, M., and

- Woch, J. G.: Four large-scale field-aligned current systems in the dayside high-latitude region, *Journal of Geophysical Research: Space Physics*, **100**, 137–153, doi: 10.1029/94JA01744, 1995.
- Ohtani, S., Ueno, G., and Higuchi, T.: Comparison of large-scale field-aligned currents under sunlit and dark ionospheric conditions, *Journal of Geophysical Research: Space Physics*, **110**, n/a–n/a, doi: 10.1029/2005JA011057, 2005a.
- Ohtani, S., Ueno, G., Higuchi, T., and Kawano, H.: Annual and semiannual variations of the location and intensity of large-scale field-aligned currents, *Journal of Geophysical Research: Space Physics*, **110**, n/a–n/a, doi: 10.1029/2004JA010634, 2005b.
- Ohtani, S., Wing, S., Ueno, G., and Higuchi, T.: Dependence of premidnight field-aligned currents and particle precipitation on solar illumination, *Journal of Geophysical Research: Space Physics*, **114**, n/a–n/a, doi: 10.1029/2009JA014115, 2009.
- Ohtani, S., Wing, S., Merkin, V. G., and Higuchi, T.: Solar cycle dependence of nightside field-aligned currents: Effects of dayside ionospheric conductivity on the solar wind-magnetosphere-ionosphere coupling, *Journal of Geophysical Research: Space Physics*, **119**, 322–334, doi: 10.1002/2013JA019410, 2014.
- Otto, A., Lummerzheim, D., Zhu, H., Lie-Svendsen, ., Rees, M. H., and Lanchester, B. S.: Excitation of tall auroral rays by ohmic heating in field-aligned current filaments at F region heights, *Journal of Geophysical Research: Space Physics*, **108**, n/a–n/a, doi: 10.1029/2002JA009423, 2003.
- Papitashvili, V. O.: A new model of field-aligned currents derived from high-precision satellite magnetic field data, *Geophysical Research Letters*, **29**, 1683, doi: 10.1029/2001GL014207, 2002.
- Parker, E. N.: Sweet’s mechanism for merging magnetic fields in conducting fluids, *Journal of Geophysical Research*, **62**, 509–520, doi: 10.1029/JZ062i004p00509, 1957.
- Parker, E. N.: Dynamics of the interplanetary gas and magnetic fields, *Astrophysical Journal*, **128**, 664, doi: 10.1086/146579, 1958.
- Parks, G. K. and Winckler, J. R.: Acceleration of energetic electrons observed at the synchronous altitude during magnetospheric substorms, *Journal of Geophysical Research*, **73**, 5786–5791, doi: 10.1029/JA073i017p05786, 1968.

- Perreault, P. and Akasofu, S. I.: A study of geomagnetic storms, *Geophysical Journal International*, **54**, 547–573, doi: 10.1111/j.1365-246X.1978.tb05494.x, 1978.
- Petschek, H. E.: Magnetic field annihilation, *NASA Special Publication*, **50**, 425, 1964.
- Petschek, H. E.: The mechanism for reconnection of geomagnetic and interplanetary field lines, in *The Solar Wind*, edited by R. J. Mackin, Jr. and M. Neugebauer, p. 257, 1966.
- Press, W. H., Flannery, B. P., Teukolsky, S. A., and Vetterling, W. T.: Numerical recipes. The art of scientific computing, Cambridge University Press, Cambridge, UK, 1986.
- Rasmussen, C. E., Schunk, R. W., and Wickwar, V. B.: A photochemical equilibrium model for ionospheric conductivity, *Journal of Geophysical Research: Space Physics*, **93**, 9831–9840, doi: 10.1029/JA093iA09p09831, 1988.
- Reiff, P. H. and Burch, J. L.: IMF B_y -dependent plasma flow and Birkeland currents in the dayside magnetosphere: 2. A global model for northward and southward IMF, *Journal of Geophysical Research: Space Physics*, **90**, 1595–1609, doi: 10.1029/JA090iA02p01595, 1985.
- Reiff, P. H., Spiro, R. W., and Hill, T. W.: Dependence of polar cap potential drop on interplanetary parameters, *Journal of Geophysical Research: Space Physics*, **86**, 7639–7648, doi: 10.1029/JA086iA09p07639, 1981.
- Robinson, R. M. and Vondrak, R. R.: Measurements of E region ionization and conductivity produced by solar illumination at high latitudes, *Journal of Geophysical Research: Space Physics*, **89**, 3951–3956, doi: 10.1029/JA089iA06p03951, 1984.
- Rostoker, G., Anderson, C. W., Oldenburg, D. W., Camfield, P. A., Gough, D. I., and Porath, H.: Development of a polar magnetic substorm current system, *Journal of Geophysical Research*, **75**, 6318–6323, doi: 10.1029/JA075i031p06318, 1970.
- Rostoker, G., Akasofu, S.-I., Foster, J., Greenwald, R., Kamide, Y., Kawasaki, K., Lui, A., McPherron, R., and Russell, C.: Magnetospheric substorms—definition and signatures, *Journal of Geophysical Research: Space Physics*, **85**, 1663–1668, doi: 10.1029/JA085iA04p01663, 1980.
- Rostoker, G., Mareschal, M., and Samson, J. C.: Response of dayside net downward field-aligned current to changes in the interplanetary magnetic field and

- to substorm perturbations, *Journal of Geophysical Research*, **87**, 3489, doi: 10.1029/JA087iA05p03489, 1982.
- Rothwell, P. L., Silevitch, M. B., and Block, L. P.: A model for the propagation of the westward traveling surge, *Journal of Geophysical Research: Space Physics*, **89**, 8941–8948, doi: 10.1029/JA089iA10p08941, 1984.
- Russell, C. and McPherron, R.: The magnetotail and substorms, *Space Science Reviews*, **15**, 205–266, doi: 10.1007/BF00169321, 1973a.
- Russell, C. T. and McPherron, R. L.: Semiannual variation of geomagnetic activity, *Journal of Geophysical Research*, **78**, 92–108, doi: 10.1029/JA078i001p00092, 1973b.
- Sandahl, I., Brndstrm, U., and Sergienko, T.: Fine structure of aurora, *International Journal of Remote Sensing*, **32**, 2947–2972, doi: 10.1080/01431161.2010.541507, 2011.
- Scholer, M., Gloeckler, G., Hovestadt, D., Klecker, B., and Ipavich, F. M.: Characteristics of plasmoid-like structures in the distant magnetotail, *Journal of Geophysical Research: Space Physics*, **89**, 8872–8876, doi: 10.1029/JA089iA10p08872, 1984.
- Schunk, R.: The terrestrial ionosphere, in *Solar-Terrestrial Physics*, edited by R. Carovillano and J. Forbes, vol. 104 of *Astrophysics and Space Science Library*, pp. 609–676, Springer Netherlands, doi: 10.1007/978-94-009-7194-3_22, 1983.
- Scurry, L. and Russell, C. T.: Proxy studies of energy transfer to the magnetosphere, *Journal of Geophysical Research: Space Physics*, **96**, 9541–9548, doi: 10.1029/91JA00569, 1991.
- Senior, C.: Les conductivites ionospheriques et leur role dans la convection magnetospherique: Une etude experimentale et theorique, Ph.D. thesis, L'Univ. Pierre et Marie Curie, Paris, France, 1980.
- Sergeev, V. A., Tsyganenko, N. A., Smirnov, M. V., Nikolaev, A. V., Singer, H. J., and Baumjohann, W.: Magnetic effects of the substorm current wedge in a spread-out wire model and their comparison with ground, geosynchronous, and tail lobe data, *Journal of Geophysical Research: Space Physics*, **116**, n/a–n/a, doi: 10.1029/2011JA016471, 2011.
- Sergeev, V. A., Nikolaev, A. V., Tsyganenko, N. A., Angelopoulos, V., Runov, A. V., Singer, H. J., and Yang, J.: Testing a two-loop pattern of the substorm current

- wedge (SCW2L), *Journal of Geophysical Research: Space Physics*, **119**, 947–963, doi: 10.1002/2013JA019629, 2014.
- Shue, J.-H., Chao, J. K., Fu, H. C., Russell, C. T., Song, P., Khurana, K. K., and Singer, H. J.: A new functional form to study the solar wind control of the magnetopause size and shape, *Journal of Geophysical Research: Space Physics*, **102**, 9497–9511, doi: 10.1029/97JA00196, 1997.
- Siscoe, G. L. and Huang, T. S.: Polar cap inflation and deflation, *Journal of Geophysical Research: Space Physics*, **90**, 543–547, doi: 10.1029/JA090iA01p00543, 1985.
- Siscoe, G. L., Sibeck, D. G., Slavin, J. A., Smith, E. J., Tsurutani, B. T., and Jones, D. E.: ISEE 3 magnetic field observations in the magnetotail: Implications for reconnection, in *Magnetic Reconnection in Space and Laboratory Plasmas*, vol. 30 of *Geophysical Monograph Series*, pp. 240–248, American Geophysical Union, Washington, DC, USA, URL <http://www.agu.org/books/gm/v030/GM030p0240/GM030p0240.shtml>, 1984.
- Slavin, J. A., Smith, E. J., Tsurutani, B. T., Sibeck, D. G., Singer, H. J., Baker, D. N., Gosling, J. T., Hones, E. W., and Scarf, F. L.: Substorm associated traveling compression regions in the distant tail: ISEE-3 Geotail observations, *Geophysical Research Letters*, **11**, 657–660, doi: 10.1029/GL011i007p00657, 1984.
- Slavin, J. A., Smith, M. F., Mazur, E. L., Baker, D. N., Iyemori, T., Singer, H. J., and Greenstadt, E. W.: ISEE 3 plasmoid and TCR observations during an extended interval of substorm activity, *Geophysical Research Letters*, **19**, 825–828, doi: 10.1029/92GL00394, 1992.
- Sofko, G. J., Greenwald, R., and Bristow, W.: Direct determination of large-scale magnetospheric field-aligned currents with SuperDARN, *Geophysical Research Letters*, **22**, 2041–2044, doi: 10.1029/95GL01317, 1995.
- Sonnerup, B. U. .: Magnetopause reconnection rate, *Journal of Geophysical Research*, **79**, 1546–1549, doi: 10.1029/JA079i010p01546, 1974.
- Sonnerup, B. U. . and Cahill, L. J.: Explorer 12 observations of the magnetopause current layer, *Journal of Geophysical Research*, **73**, 1757–1770, doi: 10.1029/JA073i005p01757, 1968.
- Stauning, P.: Field-aligned ionospheric current systems observed from Magsat and Ørsted satellites during northward IMF, *Geophysical Research Letters*, **29**, ORS 6–1–ORS 6–4, doi: 10.1029/2001GL013961, 2002.

- Stone, E. C., Frandsen, A. M., Mewaldt, R. A., Christian, E. R., Margolies, D., Ormes, J. F., and Snow, F.: The Advanced Composition Explorer, in *The Advanced Composition Explorer Mission*, edited by C. Russell, R. Mewaldt, and T. Von Rosenvinge, pp. 1–22, Springer Netherlands, doi: 10.1007/978-94-011-4762-0_1, 1998.
- Sweet, P. A.: The neutral point theory of solar flares, in *Electromagnetic Phenomena in Cosmical Physics*, edited by B. Lehnert, vol. 6 of *IAU Symposium*, p. 123, 1958.
- Tsurutani, B. T., Echer, E., Shibata, K., Verkhoglyadova, O. P., Mannucci, A. J., Gonzalez, W. D., Kozyra, J. U., and Ptzold, M.: The interplanetary causes of geomagnetic activity during the 7–17 March 2012 interval: A CAWSES II overview, *J. Space Weather Space Clim.*, **4**, A02, doi: 10.1051/swsc/2013056, 2014.
- Tsyganenko, N. A.: Effects of the solar wind conditions in the global magnetospheric configurations as deduced from data-based field models, in *International Conference on Substorms*, edited by E. J. Rolfe and B. Kaldeich, vol. 389 of *ESA Special Publication*, p. 181, 1996.
- Tsyganenko, N. A. and Stern, D. P.: Modeling the global magnetic field of the large-scale Birkeland current systems, *Journal of Geophysical Research: Space Physics*, **101**, 27 187–27 198, doi: 10.1029/96JA02735, 1996.
- Vasyliunas, V. M.: Large-scale morphology of the magnetosphere, in *Solar-Terrestrial Physics*, edited by R. Carovillano and J. Forbes, vol. 104 of *Astrophysics and Space Science Library*, pp. 243–254, Springer Netherlands, doi: 10.1007/978-94-009-7194-3_11, 1983.
- Vasyliunas, V. M., Kan, J. R., Siscoe, G. L., and Akasofu, S.-I.: Scaling relations governing magnetospheric energy transfer, *Planetary and Space Science*, **30**, 359 – 365, doi: [http://dx.doi.org/10.1016/0032-0633\(82\)90041-1](http://dx.doi.org/10.1016/0032-0633(82)90041-1), 1982.
- Vickrey, J. F., Vondrak, R. R., and Matthews, S. J.: The diurnal and latitudinal variation of auroral zone ionospheric conductivity, *Journal of Geophysical Research: Space Physics*, **86**, 65–75, doi: 10.1029/JA086iA01p00065, 1981.
- Volland, H.: A model of the magnetospheric electric convection field, *Journal of Geophysical Research: Space Physics*, **83**, 2695–2699, doi: 10.1029/JA083iA06p02695, 1978.
- Vorobjev, V., Starkov, G., and Feldstein, Y.: The auroral oval during the substorm development, *Planetary and Space Science*, **24**, 955 – 965, doi: [http://dx.doi.org/10.1016/0032-0633\(76\)90007-6](http://dx.doi.org/10.1016/0032-0633(76)90007-6), 1976.

- Wang, H.: Solar zenith angle and merging electric field control of field-aligned currents: A statistical study of the Southern Hemisphere, *Journal of Geophysical Research*, **110**, A03 306, doi: 10.1029/2004JA010530, 2005.
- Wang, M., Lou, W., Li, P., Shen, X., and Li, Q.: Monitoring the ionospheric storm effect with multiple instruments in North China: July 15–16, 2012 magnetic storm event, *Journal of Atmospheric and Solar-Terrestrial Physics*, **102**, 261 – 268, doi: <http://dx.doi.org/10.1016/j.jastp.2013.05.021>, 2013.
- Watanabe, M., Iijima, T., Nakagawa, M., Potemra, T. A., Zanetti, L. J., Ohtani, S.-i., and Newell, P. T.: Field-aligned current systems in the magnetospheric ground state, *Journal of Geophysical Research: Space Physics*, **103**, 6853–6869, doi: 10.1029/97JA03086, 1998.
- Waters, C. L.: Corrections to AMPERE numbers, private communication, received on 27 November, 2014.
- Waters, C. L.: Iridium magnetometers are Ithaco vector fluxgate instruments, private communication, received on 4 March, 2015.
- Waters, C. L., Anderson, B. J., and Liou, K.: Estimation of global field-aligned currents using the Iridium System magnetometer data, *Geophysical Research Letters*, **28**, 2165–2168, doi: 10.1029/2000GL012725, 2001.
- Weimer, D. R.: Maps of ionospheric field-aligned currents as a function of the interplanetary magnetic field derived from Dynamics Explorer 2 data, *Journal of Geophysical Research: Space Physics*, **106**, 12 889–12 902, doi: 10.1029/2000JA000295, 2001.
- Wiltberger, M., Weigel, R. S., Lotko, W., and Fedder, J. A.: Modeling seasonal variations of auroral particle precipitation in a global-scale magnetosphere-ionosphere simulation, *Journal of Geophysical Research: Space Physics*, **114**, n/a–n/a, doi: 10.1029/2008JA013108, 2009.
- Wolf, R.: The quasi-static (slow-flow) region of the magnetosphere, in *Solar-Terrestrial Physics*, edited by R. Carovillano and J. Forbes, vol. 104 of *Astrophysics and Space Science Library*, pp. 303–368, Springer Netherlands, doi: 10.1007/978-94-009-7194-3_14, 1983.
- Wolf, R. A.: Magnetospheric configuration, in *Introduction to Space Physics*, edited by M. G. Kivelson and C. T. Russell, chap. 10, pp. 288–329, Cambridge University Press, Cambridge, UK, 1995.

- Wygant, J. R., Torbert, R. B., and Mozer, F. S.: Comparison of S3-3 polar cap potential drops with the interplanetary magnetic field and models of magnetopause reconnection, *Journal of Geophysical Research: Space Physics*, **88**, 5727–5735, doi: 10.1029/JA088iA07p05727, 1983.
- Yamamoto, T., Ozaki, M., and Inoue, S.: Relationship between ionospheric conductivity and intensity of the daytime region 1 field-aligned current in geomagnetically quiet conditions, *Journal of Geophysical Research: Space Physics*, **108**, n/a–n/a, doi: 10.1029/2002JA009607, 2003.
- Yang, J., Toffoletto, F. R., Wolf, R. A., Sazykin, S., Ontiveros, P. A., and Weygand, J. M.: Large-scale current systems and ground magnetic disturbance during deep substorm injections, *Journal of Geophysical Research: Space Physics*, **117**, n/a–n/a, doi: 10.1029/2011JA017415, 2012.
- Zanetti, L. J., Potemra, T. A., Iijima, T., Baumjohann, W., and Bythrow, P. F.: Ionospheric and Birkeland current distributions for northward interplanetary magnetic field: Inferred polar convection, *Journal of Geophysical Research: Space Physics*, **89**, 7453–7458, doi: 10.1029/JA089iA09p07453, 1984.
- Zheng, Y., Lui, A. T. Y., Fok, M.-C., Anderson, B. J., Brandt, P. C., Immel, T. J., and Mitchell, D. G.: Relationship between Region 2 field-aligned current and the ring current: Model results, *Journal of Geophysical Research: Space Physics*, **111**, n/a–n/a, doi: 10.1029/2006JA011603, 2006.
- Zmuda, A. J. and Armstrong, J. C.: The diurnal variation of the region with vector magnetic field changes associated with field-aligned currents, *Journal of Geophysical Research*, **79**, 2501–2502, doi: 10.1029/JA079i016p02501, 1974a.
- Zmuda, A. J. and Armstrong, J. C.: The diurnal flow pattern of field-aligned currents, *Journal of Geophysical Research*, **79**, 4611–4619, doi: 10.1029/JA079i031p04611, 1974b.
- Zmuda, A. J., Martin, J. H., and Huring, F. T.: Transverse magnetic disturbances at 1100 kilometers in the auroral region, *Journal of Geophysical Research*, **71**, 5033–5045, 1966.
- Zmuda, A. J., Armstrong, J. C., and Huring, F. T.: Characteristics of transverse magnetic disturbances observed at 1100 kilometers in the auroral oval, *Journal of Geophysical Research*, **75**, 4757–4762, doi: 10.1029/JA075i025p04757, 1970.
- Zmuda, A. J., Potemra, T. A., and Armstrong, J. C.: Transient parallel electric fields from electromagnetic induction associated with motion of field-aligned currents,

Journal of Geophysical Research, **79**, 4222–4226, doi: 10.1029/JA079i028p04222, 1974.